INVESTIGATION OF A RESISTIVE ANODE DETECTOR FOR ASTRONOMICAL SPECTROSCOPY

Mark Clampin

A Thesis Submitted for the Degree of PhD
at the
University of St Andrews

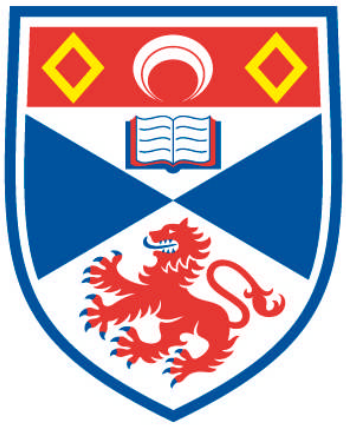

1986

Investigation of a Resistive Anode Detector for Astronomical Spectroscopy.

by

M. Clampin

A dissertation submitted for the degree of Doctor of Philosophy at the University of St Andrews.

St Andrews December 1985

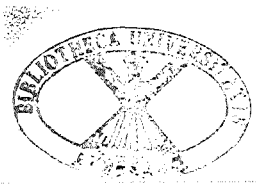

CERTIFICATE

I certify that Mark Clampin has spent nine terms in research work at the University Observatory, St. Andrews, that he has fulfilled the conditions of Ordinance General No. 12 and Senate Regulations under resolution of the University Court, 1967, No. 1, and that he qualified to submit the accompanying dissertation in application for the degree of Ph.D.

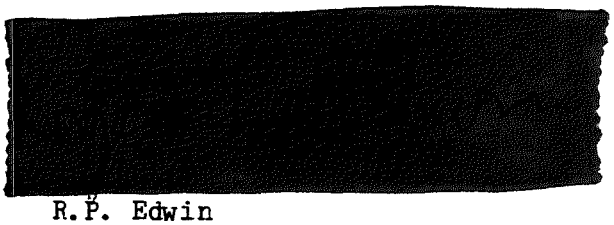

R.P. Edwin

DECLARATION

Except where reference is made to the work of others the research described in this thesis and the composition of the thesis are my own work. No part of this thesis has previously been submitted in application for a higher degree. I was admitted to the Faculty of Science of the University of St. Andrews as a research student under Ordinance General No. 12 on the 1st October, 1982. I was accepted as a candidate for the degree of Ph.D. on the 1st October, 1983, under Resolution of the University Court, 1967, No. 1.

Mark Clampin

In submitting this thesis to the University of St. Andrews I understand that I am giving permission for it to be made available for use in accordance with the regulations of the University Library for the time being in force, subject to any copyright vested in the work not being affected thereby. I also understand that the title and abstract will be published, and that a copy of the work may be made and supplied to any bona fide library or research worker.

ACKNOWLEDGEMENTS

I am indebted to my supervisor Dr R.P. Edwin for his invaluable help and guidance throughout this project. I should like to thank Dr P.W. Hill for his advice and assistance and Dr R.W. Hilditch for his help and for suggesting an investigation of SV Cam. I wish to extend my thanks to Professor D.W.N. Stibbs for making available the use of the University Observatory facilities and for his interest in this work. I extend my thanks to the staff of the University Observatory for their help. I would like to thank Dr A.J. Adamson for his advice on the darker corners of REDUCE, David Carr for his help with the electronic hardware, Roger Stapleton for his assistance with the software and Dr I. Skillen for the use of PULSAR. The contributions of research students past and present are gratefully acknowledged. Many thanks are due to Mr F. Barlow and the staff of ITL for making me welcome during my visits and in particular to Dr A. Lyons for his advice and help on the project. I should like to express my thanks to Dr F. Paresce, Dr I. van Breda, Dr P. Read, Dr H. Schwartz and Dr J. Allington-Smith for their contributions and suggestions during the course of this work.

I should like to thank the University of St Andrews Computing Laboratory and the Royal Observatory Edinburgh Starlink node for the use of computing facilities and the University of St Andrews Photographic Laboratory for their assistance with the photographic

material. I gratefully acknowledge the Science and Engineering Research Council for financial support in the form of a CASE studentship and the allocation of travel funds.

Finally I should like to thank my parents and Doreen for their support and encouragement during this work.

ABSTRACT

A large format two dimensional photon counting detector has been evaluated as a detector for astronomical spectroscopy. The design comprises an S20 photocathode, a tandem MCP gain stage and a circular arc terminated resisitive anode to provide positional coordinates of detected events. The system is run from an LSI 11/23 computer operating under FORTH control.

The micro-channel plate operating characteristics and the detector's resolution, quantum efficiency and imaging performance have been studied. The principal areas requiring design improvement are found to be the micro-channel plate gain, electronic signal processing and photocathode quality.

The detector has been employed in a observing program on a 0.5 m telescope. Spectra of IAU faint radial velocity standards and the eclipsing binary system SV Cam have been obtained and analysed to assess the system's performance.

Table of contents

Chapter 1

1.1) Detectors for Small Telescopes

Much of the development of astronomical spectroscopic detectors has been aimed towards obtaining optimum performance from the larger optical telescopes. Thus many of the most successful detectors are in one way or another unsuitable for installation and operation on small optical telescopes. In recent years detectors designed for applications in spaceborne astronomy and nuclear physics, which are especially suited to small telescopes in size and simplicity, have begun to appear. These new detectors have broadened the choices available to astronomers seeking to extend the capability of smaller telescopes.

At St. Andrews there is considerable research interest in the spectroscopic study of binary and variable systems with periods less than a few days. An efficient detector on a small telescope can provide an important contribution to these fields in the gap between systems which are photographically observable and those suitable for observation with the larger telescopes. Ideally a detector designed for use on a small telescope should possess the following properties.

A high value of detective quantum efficiency (DQE) and wide spectral response of the detector are of particular importance in order that it may record the maximum amount of signal information from the telescope over a wide spectral range, (typically 300 nm to 800 nm).

A format which allows two dimensional spectroscopy and direct imaging is required, with larger format active areas than the usual 18 mm to 25 mm. High spatial resolution is necessary and combined with a large active area, demands large pixel formats (such as 1024 x 1024 pixels over a 40 mm diameter active area).

Ideally the detector should detect individual photons with every photon arrival weighted equally, noise being limited to quantum photon statistics; detector dark current and other system noise should be kept to a minimum. The detector should be able to cover a wide dynamic range of count rates without loss of linearity, caused perhaps by crosstalk and coincidence losses between pixels, or saturation of the readout system. The detector system should be stable with time and orientation, to avoid repeated calibrations and minimise performance uncertainties.

The readout system for the detector should allow real time analysis of data collected and detailed subsequent post-analysis after data storage. Most astronomical detectors are interfaced to computers with magnetic tape or hardware storage of data and consequently as pixel formats increase in size, storage requirements

will make increasingly heavy demands on memory and storage media. Geometric image distortion is also important, since the correction of effects such as 'pin-cushion' or 'S' distortion require additional computer resources.

The size of the detector and its accompanying instruments should be compatible with mounting on a smaller telescope. In practice, this will usually be the detector head assembly plus any electronic processing units required to be in close proximity to the detector head. The head assembly should be of a size and weight that it may be mounted on the telescope cameras without placing excessive strain on the instrument itself, or give rise to any significant telescope flexure.

The commercial availability of detectors and integral components is also an important consideration. Detectors which may be bought commercially or assembled from commercially available components are more readily replaceable in the case of damage or failure, an important factor for general user instruments. There are many advantages, in terms of initial investment, for the development of devices which will have wider applications in academic research or industry.

Therefore, in view of the many factors affecting the choice of such a detector, it is not only important to consider the current status of ground based instruments, but also that of spaceborne and nuclear instrumentation not directly related to the field. A brief review of the current detector types now follows.

1.2) Photographic Techniques.

Photographic emulsion has been the main detector in astronomical spectroscopy for decades and this popularity is largely due to several important properties. The large amount of information that can be recorded on one plate and easily stored (eg. 10^5 pixels cm^{-2} of plate), maintains photography as an important detector for spectrograms. For applications such as objective prism plates it remains the principle detection medium. The resolution of photographic plates is currently unsurpassed by other detectors and ranges from 80 lp/mm to 200 lp/mm (Eccles et al. 1983). In addition they are readily available and they are relatively cheap and easy to use.

As astronomical detectors they have, however, several problems. The most important is their low sensitivity, typically a DQE of less than one percent in the visible waveband (Baum 1962), which is also dependant on the rate of arrival of photons (reciprocity failure). They have a non-linear response and their dynamic range is limited to 100 or less. Real time assessment of images is also complicated, since they cannot be examined as the image is integrated. Digitisation of images is necessary before data can be analysed and the costly nature of the equipment required may offset the low cost advantage of the plates.

There are a wide range of photographic emulsions available for spectroscopy covering a broad range of spectral sensitivity, from ~300 nm to 1100 nm. Techniques of hypersensitisation can improve the sensitivity of emulsions to DQE values of up to two to four percent (Smith and Hoag 1979).

A procedure applied to many photographic emulsions involves baking plates in a stream of gas, such as nitrogen, hydrogen or forming gas. Chemical bathing can be applied to certain emulsions and preflashing is appropriate for high signal to noise (class 1) situations. Hypersensitisation has been extensively reviewed by many authors (Smith and Hoag 1979, Eccles et al. 1983). Reciprocity failure may also be reduced at low light levels by the use of special emulsions (Smith and Hoag 1979).

The chemistry and physics of the photographic process are still not well understood and so further improvements may be anticipated in the future.

In the late fifties several workers (Hiltner 1962) investigated the possibilities of improving photographic performance using image tube technology then under development and photoelectronic astronomical detectors have evolved from these first attempts.

1.3) Electronographic Detectors.

Electronographic cameras originally developed by Lallemand (Lallemand, Duchesne and Wlerick 1960) overcome many of these problems and extend the limitations of photographic imaging and spectroscopy. In these cameras photoelectrons emitted from a photocathode are accelerated to energies of up to 40 kV to impact a nuclear photographic emulsion sensitive to electrons.

There are two major problems associated with the design and operation of electronographic cameras. Outgassing from the photographic emulsion leads to contamination of the tube photocathodes shortening their useful lifetimes. In addition there is the difficulty of placing the emulsions into the high vacuum environment of the electronographic tube.

Lallemand's camera consisted of a refrigerated glass cylinder with an encapsulated photocathode and plate magazine. The photocathode, opened with a magnetic hammer, was lost upon opening the system to remove the emulsion plates.

Hiltner and Niklas (1962) improved photocathode protection with an aluminium oxide foil to isolate the relatively contaminated emulsion vacuum from the photocathode vacuum. A modified Lallemand camera with bakeable vacuum valves enables the plates to be changed whilst preserving the photocathode, which is formed in situ (Kron

1962, Kron et al. 1969).

The Spectracon (McGee et al. 1966) employed high voltages to accelerate electrons through a thin mica window which was able to withstand atmospheric pressure. This design and subsequent Spectracon designs (McMullan and Powell 1979) have proved to be the most versatile form of the electronographic camera.

Electronographic cameras reduce the photographic problems of non-linearity and reciprocity failure, while retaining good resolution. DQE's of the order of 85% to 75% of the photocathode's responsive quantum efficiency (RQE) are reported (Walker 1976). Their spectral sensitivity will be determined by the performance of the camera's photocathode.

Electronographic cameras remain specialised instruments requiring considerable care both in their preparation and operation and so have not found widespread use. These instruments are still, however, in active use, both in imaging and spectroscopy (Lelievre 1983, Wlerick et al. 1983, Petrov 1982) and also in spaceborne instruments (Carruthers 1976, Heckathorn and Carruthers 1982).

1.4) Image Intensifier Tubes.

Inverter intensifiers and first generation diode intensifiers were also used to improve the performance of photographic spectroscopy, by providing intensified images that could be recorded photographically. A simple first generation intensifier consists of

a photocathode, an electrostatic acceleration stage across a short gap (~1 mm) and a back-aluminised phosphor output screen. These are known as proximity-focussed diode intensifiers and they were originally operated for astronomy with a lens system to image the phosphor onto a photographic plate. In practice it was found that the low gain figures in the region of 10 to 100 (Ford 1968), combined with losses from the lens systems, made them inadequate for low light level work with overall gains of the order of one (Ford 1968).

Improved performance has been obtained using a fibre optic output to couple the phosphor to the photographic plate (Johnson et al. 1978). This technique gives overall gains of the order of 10, although there is some degradation of resolution in comparison with photography (Edwin 1985).

Cascade and transmission secondary emission (TSE) were two designs of intensifiers developed with improved gain characteristics. Cascaded Intensifiers (Stoudenheimer 1960, Ford 1966) consisted of cascaded stages of phosphor-photocathode sandwiches. Devices comprising up to four stages were manufactured providing gains of 10^3 to 10^7. Many variations are now available with both electrostatic and magnetic focussing and have been extensively reviewed in the literature (eg. Cromwell and Dyvig 1972). These intensifiers in general, however, combine high gain performance with good resolution, typically up to 80 lp/mm (Cromwell and Dyvig 1972) and ruggedness. In common with most electromagnetically focussed tubes they give some degree of

geometric distortion, magnetically focussed tubes usually giving better performance.

Proximity focussed diode tubes have also been used recently, either as the input (front end) of a conventional cascade intensifier (Cromwell et al. 1985), or in a cascade as one of a number of tubes coupled together by lenses or fibre optics.

The gain in TSE intensifiers is achieved by using several stages of dynodes, with magnetic focussing to maintain the resolution of the system (Wachtel et al. 1960, Emberson et al. 1962). Typical gains for designs with up to five dynode stages are of the order of 10^3 to 10^6. The dynode arrangement of these tubes makes them rather fragile and in addition the QE is low since a large proportion of the primary photoelectrons are lost in the dynode structure (Hiltner 1962). For these reasons the high gain cascaded intensifier has become the most widespread design.

While they were originally used as intensifiers for photographic plates, the most successful applications of intensifiers have been as photon counting first stages, utilising a second detector system to provide electronic readout of the phosphor scintillations. These systems are usually classified by their readout method and so will be considered later after discussion of the relevant readout detectors.

1.5) Television camera systems.

Television systems have also found a wide application in astronomical spectroscopy, being one of the first classes of detectors to provide electronic output of data and thus allow real time monitoring and direct computer access to the images. Most of the impetus for their development came from evolving commercial requirements.

Vidicon camera tubes having photoconductive targets are in general unsuitable for low light level astronomical use. Their lack of intrinsic gain severely limits the detectable signal level. The mechanism of storage target operation also gives rise to limitations in their photometric accuracy and dynamic range (Livingston 1973).

In secondary emission conduction (SEC) vidicons, photoelectrons are emitted from a photocathode and accelerated and focussed onto a target with a high secondary emission coefficient (Goetze 1966, Boerio et al. 1966). The secondary electrons then discharge the target by conduction and alter the target's charge distribution produced by the scanning electron beam. This gives one stage of intensification providing gains of up to 10^2 (Ford 1979).

The tubes need no cooling, other than that for the photocathode, and are normally used in integration mode. In common with vidicons there are problems with the photometric accuracy of the targets due to the dependence of gain upon the target potential (Crane 1973, Zucchino 1976).

SEC vidicons have, though, found several applications in the field of astronomical spectroscopy. Lowrance (1972) and Morton and Andereck (1976) employed an SEC vidicon as the integrating detector for a coude spectrograph installed on the Hale telescope to obtain spectra of 18th magnitude galaxies. Boksenberg et al. (1982) have described the use of an SEC vidicon detector on the IUE space telescope for ultraviolet spectroscopy.

Silicon target cameras are an extension of these television camera designs, where silicon diode arrays are used as the photosensing targets. The large dark current means that they need cooling usually to $-80^{\circ}C$ (McCord and Westphal 1972). The silicon vidicon (Crowell and Labuda 1969) has been used primarily for spectroscopy out to the near-infrared (110 nm). Its photometric properties are very good (Diner and Westphal 1977), having a dynamic range of the order of 10^3. In common with other vidicons, the silicon vidicon possesses no internal gain mechanism, limiting its use to relatively high signal levels.

Silicon intensified tubes (SIT) (Westphal 1973) provide gains of the order of 10^3 (Ford 1979), by the mechanism of accelerated photoelectrons discharging target diodes by the production of electron-hole pairs. These tube targets also have a charge storage capability allowing long integrations and their photometric performance is excellent (Westphal and Kristian 1976). SIT cameras have been used to obtain galactic redshifts and for spectrophotometry on several telescopes (Westphal et al. 1975, Osmer 1977).

1.6) Hybrid systems.

Some of the most successful systems so far have been hybrid systems, composed of two or more coupled stages in some intensifier-detector configuration. The Robinson-Wampler scanner (Robinson and Wampler 1972) consists of an image intensifier tube coupled to an image dissector. With this design an image on the photocathode will be intensified on the phosphor output with a gain of 10^5. The phosphor acts as a temporary storage element having a decay time of a few milliseconds and this allows time for the dissector to scan the whole phosphor.

This system has shown itself to give good performance, having a resolution of 60 μm FWHM, good linearity and stability and its performance approaches the photon counting limit. Scanners have been used successfully at several observatories, on large telescopes at Lick (Miller et al. 1976), KPNO (Goad 1979) and at the Anglo

Australian Telescope.

Mende (1971) conducted a study of the performance of a four stage magnetically focussed intensifier, lens coupled to a Plumbicon television tube. One of the main limiting problems was found to be the sampling of scintillations which often fell between adjacent lines and consecutive frames of the television scanning.

Boksenberg's Image Photon Counting System (IPCS) consisted of a similar system with several unique solutions to the problems (Boksenberg 1972, Boksenberg and Burgess 1972, Boksenberg 1976). The IPCS is a four stage magnetically focussed cascade intensifier with a gain of 10^7, lens coupled to a Phillips Plumbicon television tube by an f/2 lens. It employs processing electronics to digitise the video signal from the camera, find the centroid of phosphor scintillations detected and produce addresses of the event locations. It gives a resolution of 2048 channels, twice the number of scan lines.

Several important features have made this system particularly successful. It is built from commercially available components which are easily replaceable, giving system modularity. The system employs high gain, so that all photon events can be recorded easily because they are well above the level of the detector noise. The detector centroiding unit gives an increase in resolution over analogue methods and weights events equally without noise. Thus in principle the performance of the tube should be limited only by quantum photon statistics and the photocathode dark noise.

The major limitation of the detector is its dynamic range. It is limited to relatively low light level work because the persistence of the phosphor sets an upper limit to the count rate that can be handled linearly without loss of DQE (Fort et al. 1976).

IPCS systems employing cascaded intensifiers are very heavy and tend to be of a size incompatible with mounting on smaller telescopes. There have also been problems with instrument flexure, partly due to the internal component arrangements in the intensifiers.

The system has proved very successful having been in use at the Anglo Australian Telescope for several years and similar systems have also been installed and used at other observatories (Lynds 1975, Gilbert et al. 1976). Machetto et al. (1982, 1985) have employed a similar system for the two detectors on the Faint Object Camera to be deployed on the Hubble Space Telescope.

1.7) Silicon Array Devices.

In recent years a class of photoconductive device with readout systems based on silicon arrays have found increasing prominence as astronomical detectors, both for direct imaging and spectroscopic applications.

1.7.1) Silicon Diode Arrays.

The simplest silicon detector is a one dimensional array of PN junction photodiodes. Minority carriers are generated in the depletion layer and accumulate in the thin layer along the interface. In operation the diodes are usually reverse biassed to 5 V and left floating. Electron-hole pairs created in the junction by photoevents will slowly discharge the diode. Thus the accumulated signal may be obtained from the degree of charge required to rebias the diode. The charge on the diodes is clocked out via a shift register onto the video output lines.

The most notable commercial development of these devices has been undertaken by E.G. & G. Reticon and they are available in a number of array formats of up to 4096 array elements (Timothy 1983), with typical pixel sizes of 15 μm to 30μm. Their wide commercial availability has been an important factor in their rapid spread as spectroscopic detectors.

Reticon arrays have very high quantum efficiencies in the visible and near infra-red, Talmi and Simpson (1980) report a value of ~70% at 600 nm and 60% at 400 nm, the highest blue response of all the silicon array detectors. Resolution is defined by the pixel width which ranges from 15 μm to 30 μm (Vogt 1981) depending on the size of the array. These devices are usually operated at temperatures of -150^{o}C since at room temperature the thermal

generation of charge carriers becomes excessive for integrations greater than a few seconds and the diodes quickly saturate. The full well capacity of a Reticon is of the order of 10^7 electrons, the highest of all the currently available photoconductive detectors.

The main disadvantages of these devices are their large readout noise due to the relatively high (~70 pF) capacitance of the video output line. Walker (1985) reports a value of 370 e^- rms, obtained using correlated double sampling techniques. More typically values have been of the order of 500 e^- rms (Vogt et al. 1978). This in practice means that the use of Reticons in this mode is limited to integration of relatively high signal levels, since a large amount of signal is required to approach photon noise limited performance. Fixed pattern noise is often seen in Reticon flat field responses (Latham 1982). This is caused by the varying levels of capacitative coupling of transients from the clock driver signals into the separate output video lines. This may, in most cases, be removed by flat fielding of the spectra (Davis and Latham 1979, Goad and Reed 1983).

Livingston (1976) has reviewed many of the spectroscopic detectors employing Reticons as the readout device. Tull and Nather (1973), Vogt et al. (1978) and Vogt (1981) have used Reticon detectors to obtain high resolution spectra with signal to noise ratios sufficient for accurate spectrophotometry.

1.7.2) Intensified Silicon Diode Arrays.

In order to overcome the effects of high Reticon readout noise several workers have coupled a high gain cascaded intensifier to a Reticon array (Schectman and Hiltner 1976, Davis and Latham 1979, Latham 1982, Jorden et al. 1982).

This front-end configuration, similar to the IPCS detectors, offers the advantage of photon counting performance. Event centroiding of the scintillations which fall over several diodes can also be applied to the video signal from the arrays to locate events to a high accuracy, giving resolutions of the order of a 0.25 of a diode (Allen et al. 1983). This translates to a resolution of typically 25 μm to 30 μm FWHM at the photocathode.

Frame subtraction checking is used to ensure that events are not recorded more than once due to the long persistence of the intensifier's phosphors. The system's dynamic range, in common with the IPCS, remains limited due to the coincidence losses incurred at higher count rates from the phosphor and the video readout time of the array.

The necessity for cooling of the intensifier, which operates at high voltages, to $-30^{o}C$ produces difficulties in operation (Latham 1982) such as the danger of surface leakage and corona. Careful potting of high voltage components is therefore very important.

The DQE of these systems is primarily determined by the photocathode and subsequent losses due to the intensifier's counting efficiency and the array's RQE (Allen et al. 1983). Thus operating silicon arrays in systems such as this means that a large proportion of their intrinsic quantum efficiency is lost. For maximum efficiency, the output phosphor should be matched to the response of the diode array.

1.7.3) Charge Coupled Devices.

Charge Coupled Devices (CCD) may be regarded as two dimensional arrays of MOS capacitors. A single cell of a surface channel CCD is illustrated in figure 1-1 and consists of a p-type doped silicon substrate with a silicon oxide (SiO_2) insulating layer grown into it. This in turn is etched away and a metal electrode, known as a gate, placed on its surface.

When the gate is positively biased a depletion layer forms at the $Si-SiO_2$ layer and as the gate voltage increases the depletion layer moves deeper into the substrate. At a gate voltage of a few volts an inversion layer of free electrons will form at the $Si-SiO_2$ junction. If the cell is uncooled, thermal electrons will flow into the junction. If it is cooled, an inversion layer will not form unless free electrons are generated by photon bombardment. The depletion layer may therefore be conceptually regarded as a potential well for the storage of charge.

Figure 1-1: Schematic diagram illustrating the configuration and operating principles of a MOS capacitor charge coupled cell.

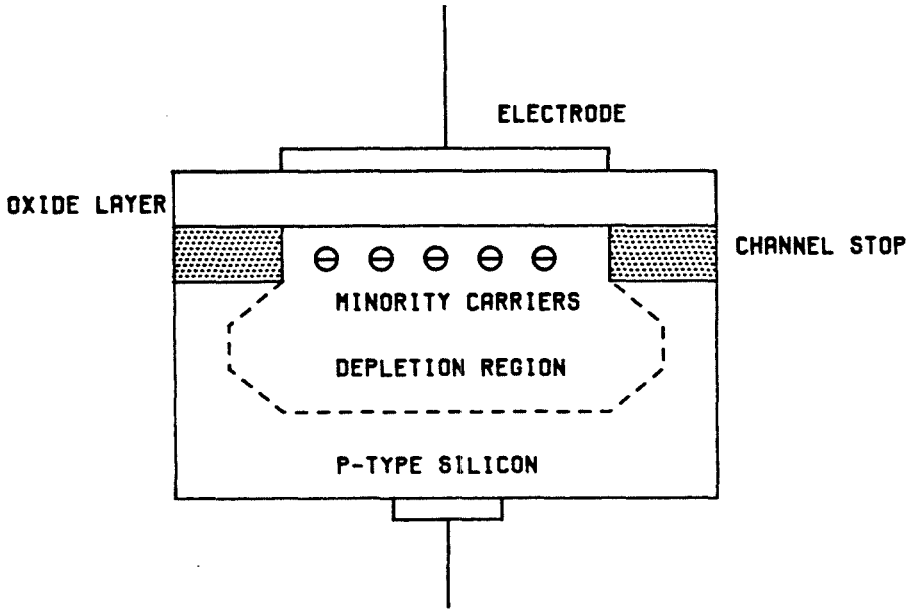

Figure 1-2: Schematic diagram illustrating the operating modes of a charge injection device (after Barbe 1975).

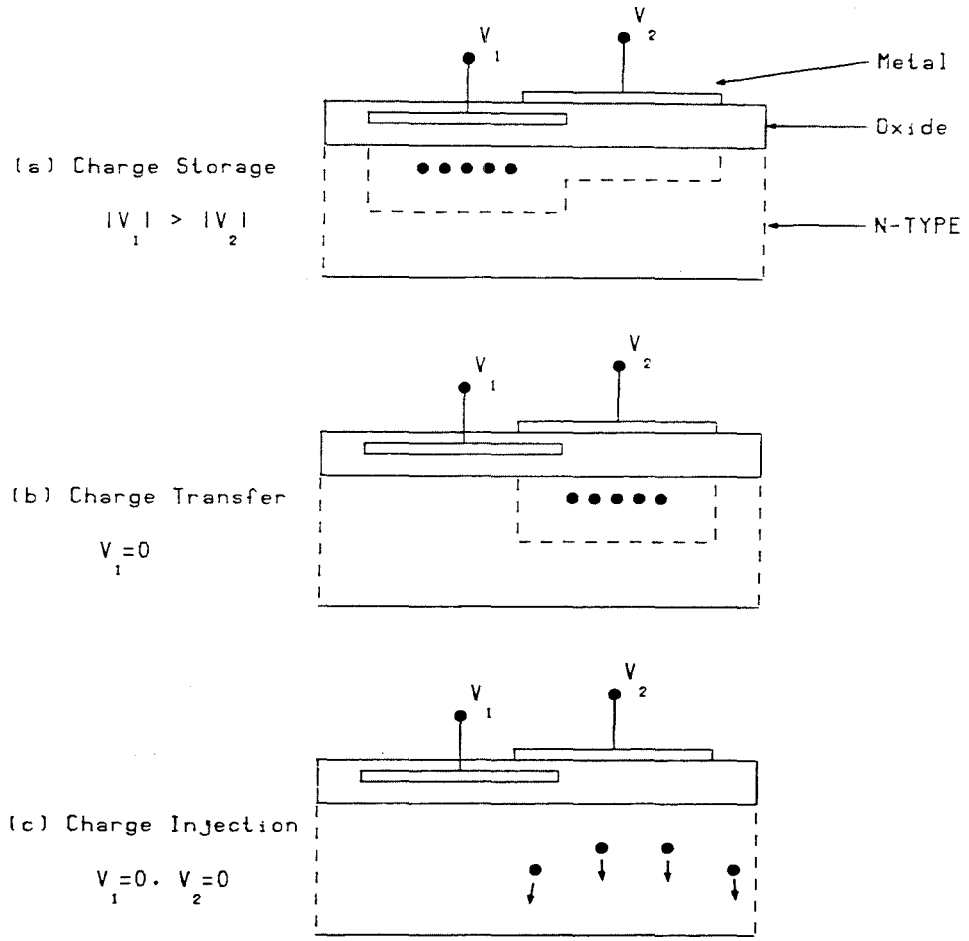

Charge leakage between adjacent cells is prevented by channel stops, which operate by reducing the depth of the potential well. This may be achieved by either increased doping or an increased thickness of the SiO_2 marking cell boundaries.

In charge coupled devices a two dimensional array of MOS capacitors are coupled so that charge can be transferred from one capacitor to another and finally out to an amplifier, each capacitor representing a pixel. In astronomical imaging applications CCD exposures are usually controlled by a shutter mechanism which isolates the chip from illumination while the chip is read out. There are several readout methods such as the three phase, uniphase and virtual phase techniques and these are comprehensively discussed by Timothy (1983) and Livingston (1976). Associated with all these methods however there is a readout noise, usually of the order of 10 to 100 e^- rms (Timothy 1983), a figure lower than that of Reticons. With typical array sizes of 500 x 500 pixels, charge transfer efficiency must be very high, of the order of 99.999%, in order to avoid charge smearing during a charge transfer.

With the surface channel CCD, charge transfer is inefficient at low light levels due to trapping states associated with the $Si-SiO_2$ interface. It is often overcome by filling cells with a small amount of initial charge, known as fat zero or pre-flashing. This technique improves linearity at low light levels but adds to the readout noise of the device. A solution to this problem is the buried channel CCD (Howes and Morgan 1979), which stores and moves

the charge packets below the $Si-SiO_2$ interface. The substrate below the SiO_2 layer is doped n-type which causes the depletion layer to be formed at the P-N junction away from $Si-SiO_2$ interface area. This technique results in less trapping and also more efficient charge transfer (~99.998%), since carrier mobility in the bulk material is higher. Charge transfer with this technique is also more rapid since field lines between adjacent electrodes in the bulk material are almost parallel to the direction of movement.

Full well capacities for CCDs are of the order of 10^4 to 10^5 electrons. In order to reduce dark current to acceptable levels the chips are usually cooled to temperatures of -100 ^{o}C to -120 ^{o}C, giving dark currents of $< 10^{-2}$ electrons pixel^{-1} second^{-1}.

Resolution is determined by the pixel size, with typical values ranging from 30 μm to 15 μm (Timothy 1983). In common with other detectors having discrete anode arrays, some care is required to avoid aliasing at spatial sampling frequencies greater than those allowed by the pixel size.

The detective quantum efficiency of CCDs varies according to the design. Front illuminated chips tend to have lower quantum efficiencies of the order of ~30% eg. Goad (1982), due to absorption within the configuration of metal electrodes on the surface. Some chips combine the use of transparent polysilicon as the electrode material with uniphase readout, requiring one electrode per cell at the chip surface.

The highest quantum efficiencies have been obtained with devices having their reverse side thinned to depletion depth and are illuminated from the back. Geary and Kent (1981) report ~80% at 700nm for an RCA SID53612 chip. This also decreases the response to cosmic rays, the events being confined to one or two pixels. Thinned chips, can however cause problems with handling and mounting due to their fragility.

The high quantum efficiency of CCDs in the near infrared surpasses that of most other spectroscopic detectors. York et al. (1981) and Goad (1982) report the performance of CCDs used for echelle coudé spectroscopy. The two dimensional format coupled with high DQE make them especially suitable for high dispersion work on faint objects. For the same reason CCDs have also been used for medium dispersion work on very faint objects. Typical examples of CCD systems for this purpose are Oke (1981), Lauer (1983) and Mackay (1983).

For most CCDs the quantum efficiency drops drastically towards 400 nm. Two techniques for improving this figure are under investigation. Coating CCDs with a blue sensitive phosphor has been reported by Blouke el al. (1981) and in the same context, Mackay (1983) discusses the performance of a near IR phosphor. An alternative method is 'UV flashing' which causes changes in the energy band structure of the chip and improves the blue response.

The advantages of CCDs are, however, often offset by other considerations. Most chips available currently have relatively small formats, typical pixel formats are 312 x 512 (RCA), 500 x 500 (TI), 385 x 576 (GEC) and 488 x 380 (Fairchild). This can lead to problems in matching the chip formats to imaging or spectrographic instruments and some form of imaging onto the chip is required. Some spectrographic systems have been designed especially for CCD detectors, a typical example being the FOS system at the AAO (Gillingham 1983). Another solution is to use fibre-optics to couple the CCD to the the imaging instrument, such as an aperture plate for multiple object spectroscopy (Gray 1982). For many applications requiring large format detectors, CCD detectors remain unsuitable, unless assembled into mosaics of larger dimensions (Lockhart 1982). In common with unintensified Reticons there is also the size and weight of the cryostat assembly to consider.

Larger TI uniphase chips having 800 x 800, 15 μm pixels have been fabricated for the Space Telescope wide field camera (Lockhart 1982) and the Galileo project (Klaasen et al. 1982). Van Breda (1984) has reported GEC 1500 x 1500 pixel and Tektronix 2048 x 2048 pixel chips under development. Currently there is a problem with the availability of suitable CCDs, and consequently their cost can be very high. The problem of data storage and access can also be expected to grow as these instruments evolve to larger pixel formats.

CCDs have readout noise associated with the detector and this means that it is not possible to obtain true photon counting performance. Noise figures are, however, improving, the GEC P8600 has a readout noise of the order of 10 e^- rms (Timothy 1983). CCD images often suffer from cosmetic problems such as bad pixels, blocked columns and hot pixels. Most of these defects can be treated in the subsequent reduction of the images. Non-uniform flat field response and interference fringes are both features of many chips, which require careful calibration to minimise their effects. The interference with the electrode structure, which is similar in dimension to that of visible light is the cause of fringes. Djorgovski (1985) has reviewed many of the current problems associated with the operation of CCDs.

1.7.4) Intensified Charge Coupled Devices.

Stapinski et al. (1981) have described a photon counting detector comprised initially of six electrostatic-focus intensifiers coupled by fibre optics to a CCD. The CCD is read out in video mode and phosphor scintillations arising from photon events are detected by the CCD and the event location determined by event centering. Similar frame processing to that of Reticon systems is employed to ensure events are not recorded twice. The performance of this detector is reported for a second intensifier design and will be discussed later.

1.7.5) Charge Injection Devices.

These devices are very similar in principle to CCDs with the exception that each pixel has two adjacent electrodes, as illustrated in figure 1-2 (Barbe 1975), and may be regarded as a double capacitor. Charge may therefore be switched between them by alternating the voltages on the electrodes. In a two dimensional array, one of the two electrodes is connected to others in its row and the other to those in its column. This allows single pixel addressing of the array and non-destructive readout. This has several advantages compared to CCDs, allowing non-destructive multiple readouts to minimise the readout noise and monitoring for cosmic ray events. Problems encountered in CCDs with charge transfer efficiencies at low signal levels are also removed with this readout method and the full well capacity is greater than CCDs by a factor of 10 to 100.

CIDs have been mainly used for imaging applications such as surface photometry (Aikens et al. 1976), planetary imaging (Wattson et al. 1975) and star tracking (Jones et al. 1979). Spectroscopic observations have been reported by Aikens et al. (1976) and Jorden and van Breda (1981), who have investigated the performance of a GE TN2000 chip. Typical readout noise levels of 2500 e^- rms are reported, with 2^7 multiple readouts reducing this figure to 250 e^- rms.

CID formats have been the limiting factor, most chips having about 100 x 100 pixels, together with high readout noise figures. The DQE of these chips is also inferior to that of thinned CCD chips. Michon (Timothy 1983) reports the development of 400 x 400 CIDS by General Electric with an expected low readout noise of 25 e^- rms and this may result in more use of CID chips as optical detectors.

1.7.6) Electron Bombarded Silicon Arrays.

Electron bombarded silicon tubes (EBS) such as the Digicon (Beaver and McIlwain 1971) usually consist of discrete one dimensional silicon diode arrays enclosed in the high vacuum of a magnetically focussed tube. Photoelectrons from a semitransparent photocathode are accelerated to energies of typically 20-25 kV to bombard the diodes which are read out in parallel, each diode having its own pre-amplifier and processing electronics. With the performance limited only by processing electronics, this architecture gives a very high count rate performance and a dynamic range of 10^7 (Ginaven et al. 1981). The pre-amplifier circuits of each individual diode may also be adjusted so that each pixel has the same relative sensitivity.

The array size in parallel readout systems is currently limited to a maximum of 512 diodes by the need to bring one electrode per diode through the high vacuum wall of the tube. The high resolution obtainable with magnetic focussing effectively limits resolution in

these tubes to that of the individual diode dimensions eg. 50 μm (Ginaven et al. 1981).

The magnetic focussing also allows deflection of different parts of the photocathode image onto the array and also allows the image to be laterally stepped sideways in order to remove the effects of aliasing. Geometric distortion often found in magnetically focussed tubes can be minimised to an acceptable level for the one dimensional arrays.

Typically these tubes need cooling to reduce the dark count from the bialkali or trialkali photocathode. The DQE of these tubes has been found to be typically 80% of the photocathode RQE (Harms et al. 1982).

A self-scanned tube incorporating a Reticon array allows the number of pixels to be increased to 1024 (Tull et al. 1975) with a resultant increase in resolution and some designs also incorporate dual arrays (Tull et al. 1979). This is made possible by the serial readout of these arrays which means that only a few electrodes are required to pass through the tube walls.

This method of reading out the array places an overhead on the maximum count rate that the instrument can handle without a loss of linearity due to coincidence effects. Typical results from the use of these detectors are presented by Vogt et al. (1979).

The main problems associated with Digicons are their complexity, long term reliability (Timothy 1983) and photocathode stability (Ford 1979). The short lifetime of these tubes is thought to be due to bombardment of the diodes and amplifiers by heavy ions released by the photocathode. Eck et al. (1985), however, have recently reported lifetimes of the order of 10^{12} $e^{-}diode^{-1}$ for digicons chosen as detectors on the Hubble Space Telescope. The high cost of these instruments has, in general, limited them to such projects to date.

The possibility of using CCD chips in self scanned Digicons has also been investigated experimentally (Everett et al. 1982) although this work remains in its early stages. The lifetime of CCDs under electron bombardment is uncertain and the use of rear-illuminated thinned chips has been investigated (Choisser 1976). Processing of the tubes also presents a problem since the photocathode processing procedure requires that the whole assembly including the CCD must undergo bakeout at $300^{o}C$.

1.8) Micro-channel Plate Arrays.

The evolution of micro-channel plate arrays (MCPs) has led to the development of compact intensifiers and detectors which are ideally suited to both spaceborne and ground-based astronomical spectroscopy.

MCPs are an extension of the principle of the Channel Electron Multiplier (CEM) originally developed at the Bendix Research Laboratories (Goodrich and Wiley 1962, Wiley and Hendee 1962) and the Mullard Laboratories (Adams and Manley 1962). CEMs are glass tubes with a high secondary electron emission coefficient, operated with a high potential across their terminals. Input electrons entering the CEM are accelerated and collide with the tube wall producing secondary electrons which are also accelerated and collide with the tube walls. Thus at the output end of the CEM there will be a cascade of electrons.

In order to allow replenishment of electronic charge lost from the wall due to collisions, the channel wall must be slightly conductive. This is achieved using lead oxide doped glass treated to give a semiconductive surface (Trap 1971).

The electron gain of a CEM has been found to be dependant on V, the applied voltage and l/d, the length to diameter ratio of the tube (Schmidt and Hendee 1966, Manley et al. 1969). Typical gains from CEMs are of the order of 10^5 to 10^8, for V = 2000 V and l/d = 100:1 (Timothy 1983). Thus in principle CEM designs can be reduced to very small dimensions while retaining their high gains.

CEMs have been used for a large variety of applications including the detection of electrons, ions, ultraviolet and X-ray radiation (Lampton 1976). For applications such as the detection of ultraviolet radiation, a hollow, conical photocathode can be

employed to enhance the detection efficiency.

Since very small CEMs giving high gain can be constructed, in principle it should be possible to construct an array of CEMs suitable for various imaging operations. The Bendix laboratories produced the first arrays of CEMs during the early sixties by bonding together thousands of CEMs and obtained promising results (Wiley and Hendee 1962). Since then the development of MCP technology has been very rapid and due especially to the impetus provided by military night vision intensifier requirements.

MCPs are fabricated from lead oxide tubes with etchable glass cores. These are heated and drawn to a uniform diameter, then stacked and fused into an array. The process of heating and drawing is repeated to produce a boule from which wafers of the required dimensions are cut. The core glass is then etched away and the wafers reduced in hydrogen at 250^{o}C to 450^{o}C to produce the semiconductive surface (Washington 1971, Millar 1972).

The physical principles of MCPs will be discussed in the next chapter, this chapter limiting itself to discussion of their applications. MCPs are used in compact image intensifiers and as the gain stage in detectors with a variety of electronic readout systems.

Table 1-1 (Schagen 1971) shows the MCP detection efficiencies for a range of different types of radiation. MCPs considered in the context of astronomical detectors find application in three main waveband regions, ultraviolet, X-Ray and the optical, where input electrons are produced at a photoemissive surface (photocathode). Ultraviolet and X-ray photons have sufficient energy to generate electrons from the channel walls without a photocathode. In systems where incident electrons are accelerated from a photocathode, optimum detection efficiency will be achieved.

In the ultraviolet and X-Ray regions the instruments will often be spaceborne and so the need to seal the tube in a high vacuum environment, to prevent contamination, is removed. The MCP will either be used directly to detect and amplify a signal, or for maximum detection efficiency will have a suitable thin photocathode deposited on its front surface. Typical photocathode materials for X-Ray and EUV such as caesium flouride, are reviewed by Siegmund and Malina (1983). These detectors are usually constructed in what is known as a demountable configuration, since it is relatively simple to replace components or rearrange the configuration of the tube during the laboratory evaluation stage of development.

In optical tubes, a photoemissive surface provides photoelectrons which are electromagnetically or proximity focussed onto the MCP. Usually the components are assembled to the prescribed configuration and then sealed in a high vacuum tube with a photocathode processed onto its glass window. This process is

TABLE 1-1

Detection efficiency of channnel multipliers.

Type of Radiation		Efficiency (%)
Electrons	0.2 - 2 kev	50-85
	2.0 - 50 kev	10-60
Positive Ions	0.5 - 2 kev	5-85
(H^+ , He^+ , A^+)	2.0 - 50 kev	60-85
	50 - 200 kev	4-60
UV Radiation	300 - 110 nm	5-15
	110 - 150 nm	1-5
Soft X-Rays	0.2 - 5 nm	5-15
	0.012 - 0.02 nm	~1

somewhat traumatic since the unit is usually baked out at a high temperature prior to sealing in order to remove possible photocathode and MCP contaminants. Such an arrangement cannot be modified once the tube has been sealed without repeating the processing of the photocathode and degrading the performance of the MCPs. In addition several extra parameters need to be considered in evaluating the performance of the tube.

1.8.1) MCP Readout Techniques: Intensifiers.

MCPs are used as the primary gain stage in second generation and the new third generation image intensifiers currently under development, the difference being the change from multialkali to III-IV photocathodes such as gallium arsenide (Spicer and Bell 1972). Second generation tubes have either proximity or electromagnetic focussing arrangements, while third generation tubes are usually proximity focussed.

Proximity focussed tubes consist of a photocathode in close proximity to the input MCP with a large electric field across the gap to maintain the resolution. The output consists of a phosphor screen in close proximity to the output MCP, again with a high field across the gap. In electromagnetically focussed tubes the arrangement is usually that of a short magnetic or electrostatic focus region, imaging onto an MCP configuration. The MCP output is either in close proximity to the phosphor output screen or imaged onto it via another electrostatic or magnetic focus region. Choice depends on the required resolution, distortion level and simplicity

of operation. In general, the electromagnetic tubes have higher resolution with some image distortion common to electromagnetic focussing systems. Proximity focussed tubes are virtually distortionless and relatively simple to operate.

Second generation MCP image intensifiers have recently started to replace first generation intensifiers as the photon counting front ends for intensified silicon arrays and for television systems.

Boulesteix (1978) coupled an electrostatically focussed MCP intensifier to a SIT vidicon by fibre optic. With event centering a resolution of 55 μm at the photocathode, over an active area of 25 mm was achieved. Rosier and Polaert (1978) achieved similar results with a curved MCP dual proximity focussed intensifier.

The same principle may be applied to CCD chips where the phosphor of the intensifier is imaged onto the CCD either via a fast lens system or directly by a fibre optic taper (Coleman 1985). The CCD is read out in a video mode and events centroided to increase the resolution.

Airey et al. have integrated a Fairchild CCD via a fast lens with a magnetically focussed MCP intensifier (1978) and a proximity focussed intensifier (1985). The resulting system, designed to be portable, has been used for imaging applications. Stapinski et al. (1981) demonstrated an intensified Fairchild SL62925 CCD chip used for long slit spectroscopy of a Planetary Nebula. The intensifier,

coupled via two f/1.2 lens, consisted of a proximity focussed MCP intensifier with a fibre optic coupling to a one stage electrostatic intensifier.

This configuration is under active development for large format (40 mm) intensifiers employing a fibre optic taper to reduce the image size to a format suitable for a single CCD (Lyons and Read 1983). Beavais et al. (1985) have integrated 18 mm third generation intensifiers with Thompson TH7861 CCD chips via a fibre optic taper for military television imaging applications.

Several very large format detectors are under development, consisting of an MCP intensifier linked by fibre optics to an array of CCD chips. The Starlab detector (Gorham et al. 1982) will be a 90 mm diameter active area device intended for a 1 m spaceborne telescope facility. It is proposed that the device will have 12.5 μm resolution with a wavelength coverage of 120 nm to 800 nm. Hobbs et al. (1983) have tested several small scale prototypes with some success. The MOSAIC detector (Williams and Weistrop 1983) is a similar, currently demountable detector, with 8000 x 8000 pixels covering an active area of 70 x 70 mm and is intended for photon counting spectroscopy and imaging in the ultraviolet.

1.8.2) MCP Readout Techniques: Multiwire Anodes

Multiwire readout techniques were first used with proportional counters (Bokowski and Kopp 1970, Charpak 1977). Crossed wire grids have been used as readout systems for MCPs in detectors intended for X-ray imaging. One dimensional detectors were built for X-ray applications with capacitatively coupled wire readouts by Gott et al. (1970) and a two dimensional readout system has been built by Kellogg et al. (1976).

The wires (typically 0.1 mm in diameter) are interconnected by resistors with every eighth wire connected to a pre-amplifier. Position events are obtained by centroiding around the amplifier with the largest signal for an event. Resolution of 10 μm FWHM has been reported by Kellogg for such a detector with an active area of 26 x 26 mm, indicating that greater than 1000 x 1000 pixels are possible. Stability up to count rates of 10^4 without coincidence losses was obtained with the system.

A version of this detector was flown as the High Resolution Imager on the Einstein satellite (Henry et al. 1977). This design of readout system has been incorporated in a sealed tube by Kellogg et al. (1979) with a reported resolution of 50-70 μm FWHM.

1.8.3) MCP Readout Techniques: Multi-Anode

Several designs of multi-anode readout system have also been proposed and tested in recent years. The Quadrant Anode detector (Lampton and Malina 1976) has an anode consisting of a metal disc split into four separate anodes each connected to a pre-amplifier. In operation the tube produced a resolution of 10 μm FWHM and a count rate capability of up to 10^5 counts per second. The detector is subject to very severe distortion and gives active areas of only 1 x 1 mm to 3 x 3 mm, with typically 100 x 100 pixels.

Two designs of multi-anode micro-channel array (MAMA) readout systems have been extensively discussed by Timothy and Bybee (1979, 1981). Discrete anode readout systems have been reported with 2 x 2, 10 x 10 and 1 x 160 pixel format anodes. Each discrete anode requires an individual pre-amplifier and this limits the maximum number of pixels ultimately achievable. The resolution is therefore relatively poor, since is it limited by anode size. The high count rate capability of these detectors means that applications such as auto-guiders, low resolution photometers and star trackers have been proposed.

The multilayer coincidence array readout consists of two sets of orthogonal thin (10 μm) strips sandwiched together but insulated from each other with exposed metal left bare to the output of the MCP. They are connected together such that for a 512 x 512 pixel

array, 96 amplifiers would be required (Timothy and Bybee 1981). Charge from the MCP is spread over two or three metal strips and the position is determined by centroiding in the pulse processing electronics.

Multilayer anodes have been used in MAMA detectors by Timothy and Bybee (1979). Reported performance is excellent, with resolution of the order of 20 μm FWHM for active areas of 10 x 10 mm. Count rates of the order of 10^6 are possible with good photometric accuracy and minimal image distortion.

MAMA detectors have been proposed for a variety of spaceborne applications in the X-Ray, UV and EUV wavebands (Timothy and Bybee 1981). They have been used for high resolution optical spectroscopy with promising results (Timothy and Joseph 1981) and are also being proposed for other ground based applications (Butcher 1981). To date, one of the main limitations of this type of detector have been their high cost, a 1024 x 256 pixel MAMA detector system was quoted as costing $200,000 by Timothy (1982), which make them too costly for many observatories.

Another multi-anode readout system currently under development is the CODACON (Lillie et al. 1979, McClintlock et al. 1982) This type of anode consists of 15 μm wide strips mounted on a 10 μm thick substrate. On the reverse side are pairs of binary code tracks. The configuration is mounted so that the anode is in close proximity to the MCPs in order that an event will deposit charge onto one metal strip.

An incident electron cloud will cause charge to be capacitatively induced onto the binary tracks at the position of the event. The amplifiers will then switch to the appropriate state resulting in a binary position, usually in Gray code. In the one dimensional case, n amplifiers will be required for 2^n pixels, making the readout electronics simple and reducing the number of feedthroughs required for a sealed tube design.

Resolution of 20 μm FWHM is reported for a one dimensional device used for the UV spectroscopy of Jupiter (McClintlock et al. 1982). Siegmund and Malina (1983) report the construction of a 32 x 32 pixel anode utilising this principle. The manufacture of large arrays for CODACONS and MAMA type devices involves the complex multilayer technology used for the production of integrated circuits.

The precision analogue photon address (PAPA) detector (Papaliolios 1985) employs the same principle as the CODACON except in an analogue form. The output image from an MCP intensifier is sent to a number of photomultiplier (PMT) tubes by means of an array of individual imaging systems. Each PMT receives an image of the intensifier output passed through a Gray coded mask. If a photoevent is registered, then the appropriate binary address is incremented by the system. Nine PMTs for X and similarly nine for Y, with a strobe channel provide 512 x 512 resolvable pixels over a 25 mm active diameter. The system can currently operate at rates up to 200 kHz. The system is, however fairly complex in terms of its

mechanical construction. This in combination with its size and weight, will make it suitable for the larger telescopes only.

1.8.4) MCP Readout Techniques: Resistive Anode

Resistive anodes are resistive discs where the centroid of a charge cloud produced from an MCP may be determined by analysis of the charge at its terminals. The anode consists of a resistive coating or ink deposited on an insulating substrate base. Resistive anodes can have one or two dimensional geometries, with the two dimensional anodes being either circular, square or of a specially shaped design for low distortion. Resistive anodes are extensively discussed in the literature and have been used in demountable configurations in nuclear physics and UV astronomy. Recently the principle has been applied to sealed tubes having semi-transparent photocathodes (Rees et al. 1980, 1981, 1982), with resolutions of down to 100 μm reported. Fermani et al. (1982) report a potential resolution of 50 μm for a 25 mm active diameter sealed tube and have recently reported similar resolution for a sealed tube (1984).

1.8.5) MCP Readout Techniques: Wedge and Strip Anode

A close relative of the resistive anode is the wedge and strip anode (Martin et al. 1981), which consists of three conductive electrodes with their areas dependant upon spatial location. Figure 1-3 shows a typical design for a three strip pattern and gives its position algorithm. Siegmund et al. (1983) have recently reported the performance of a demountable and sealed wedge and strip imaging

Figure 1-3: Portion of a three electrode Wedge and Strip pattern and the position algorithm.

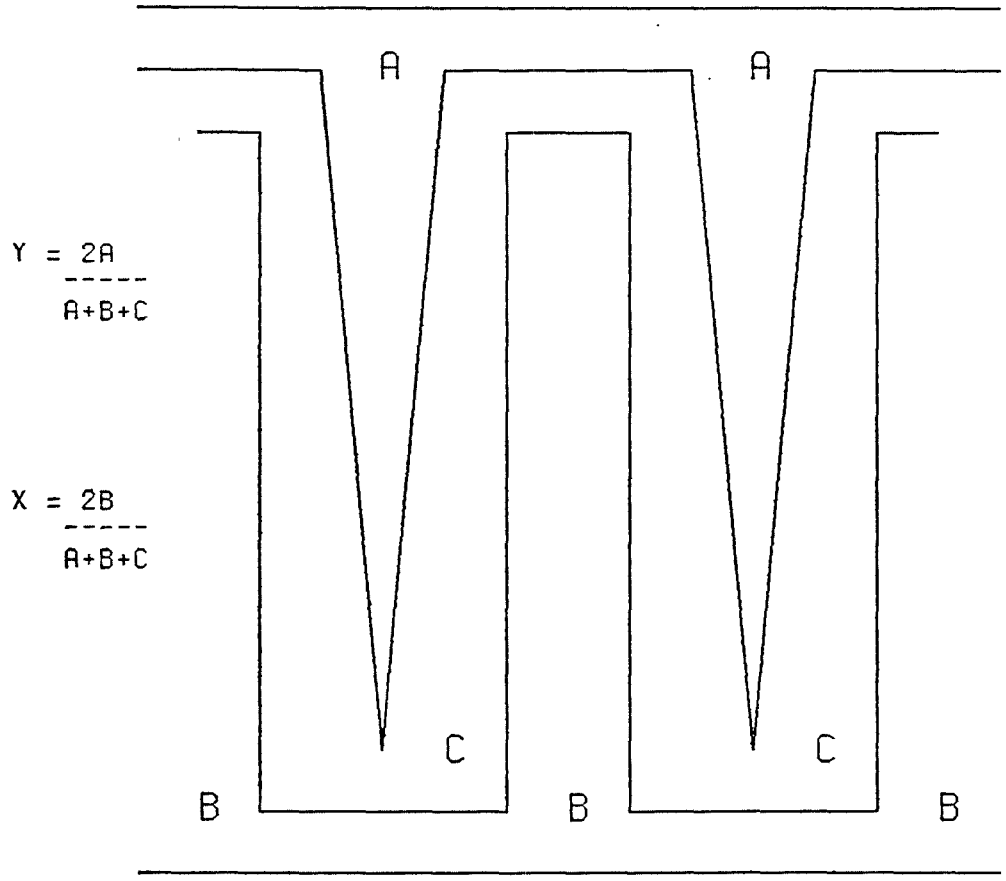

WEDGE AND STRIP THREE ELECTRODE PATTERN

detector. The demountable configuration gave a resolution of 40 μm, the sealed tube's resolution however, was in the region of 100 μm. Distortion characteristics are claimed to be better than that of resistive anodes, although some 'S' distortion was apparent.

In these detectors the charge cloud must fall over several elements of the anode pattern to obtain correct charge division. It is therefore necessary to have a field ring assembly between the output MCP and the anode to ensure a uniform field in the drift region where the charge cloud is allowed to spread. This drift region means that the device is also susceptible to magnetic fields with ~1 Gauss able to cause up to 100 μm event deflection (Siegmund and Malina 1983).

1.9) Conclusions

The main considerations in choosing a spectroscopic detector were performance, compatibility with the existing spectrograph and cost. The resolution desired was in the region of 60 μm to 40 μm FWHM, with the spectral response and sensitivity of a typical S20 photocathode. A 40 mm active diameter photocathode, together with a compact size, was required for compatibility with the spectrograph format. While a two dimensional format was desirable, since it allows greater flexibility, it was not considered crucial to the application.

Most of the intensified television and Reticon systems are of excessive size and beyond the financial resources of a small observatory. The financial constraint similarly applied to CCD systems and in addition there is the problem of mounting heavy cryostats on a relatively small spectrograph. Both CCD and television systems were unable to meet the format requirements of a 40 mm diameter window.

In terms of typical cost and size, the obvious choice was an MCP based device employing resistive anode or wedge and strip readout. A resistive anode design was chosen in view of the problems experienced by Rees (1983) in the fabrication of large format tubes with wedge and strip anodes. Fabrication of an operational 25 mm diameter sealed wedge and strip detector has since been achieved by Siegmund et al. (1983). Prior to this study a limited number of 40 mm sealed resistive anode detectors had been fabricated at Instrument Technology Limited, but none had been systematically evaluated. In addition, few resistive anode detectors have been used for ground based optical astronomy and none with a larger format have been reported.

The aim of this study can be defined, therefore, as an investigation of the potential of large format resistive anode detectors for astronomical spectroscopy on small optical telescopes. The investigation included both laboratory and astronomical testing of the instrument. The project was conducted in collaboration with Dr Rees of University College, London and

Instrument Technology Limited.

This study should allow improvements to be suggested for the design of future tube and processing electronics. Furthermore, information regarding the wider properties of the tube may contribute to the development of 40 mm active diameter intensifiers for the next generation CCD detectors. These intensifiers have similar design characteristics to sealed resistive anode detectors, but use a different readout technique.

Chapter 2

2.1) Resistive Anode Theory

Resistive anodes evolved from the attempts to obtain two dimensional images with proportional counters in nuclear physics. Early developments using multi-wire counters were limited to one dimension, with positional resolution determined by the number of wires (Charpak et al. 1968). Borkowski and Kopp (1970) obtained two dimensional images by using resistive wires and the pulse risetime of an event to determine the position. They further refined this technique (1972) using two wire wound cathode planes, placed either side of the anode. An event location could then be determined from the risetime of induced currents in these planes resulting from an anode event. Similar detectors have been discussed by Hough and Drever (1972), Charpak and Sauli (1973) and Sims et al. (1981). Extension of these concepts leads to the resistive anode, where the multi-wire design becomes a continuous planar sheet. The anode may be used in either one or two dimensions. Fraser et al. (1981b, 1981c) have reviewed the general principles of capacitatively terminated RC lines, for both risetime and charge ratio methods of position encoding.

The general theory of two dimensional resistive anode operation has been extensively discussed by Fraser et al. (1981a, 1981e), Lampton and Paresce (1974), and Rees et al. 1980. Resolution is limited by the thermionic noise of the anode and will discussed for the linear anode design. Square and circular two dimensional anodes exhibit pincushion or barrel image distortion. The degree of distortion is dependant upon the anode shape, signal processing technique, the electrode lengths and their connection points (Fraser et al. 1981a, 1981e).

The circular arc terminated (CAT) anode is an alternative resistive anode geometry based on a suggestion by Gear (1969), which virtually eliminates image distortion. The anode design is shown in figure 2-1(a), with figure 2-1(b) illustrating the geometrical parameters necessary for discussion of the design. Gear noted that for an infinite resistive sheet of resistance per unit area $R_{\square}$, a uniform potential gradient will be unaffected by the removal of a circular section radius a, if the hole boundary is terminated by a linear line resistance r_L per unit length where

$$r_L = R_{\square}/a. \qquad (2.1)$$

Since this theorem applies for any number of circular holes, it may be applied to the case of a finite planar resistive sheet bounded by four concave circular areas with terminating boundary line resistors (figure 2-1). In this configuration if terminals 1 and 4 were raised to a potential and terminals 2 and 3 grounded, there would be a uniform potential gradient in the X direction.

Figure 2-1(a): Circular arc terminated (CAT) resistive anode design, showing circular concave border resistive strips and terminal connections.

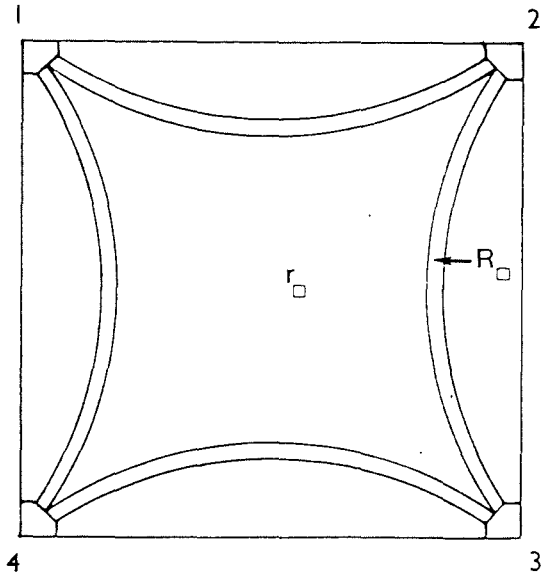

$r_\square$ = anode surface resistivity

$R_\square$ = Border Resistors

Figure 2-1(b): Diagram showing main anode dimensional nomenclature and parameters (Fraser and Mathieson 1981d).

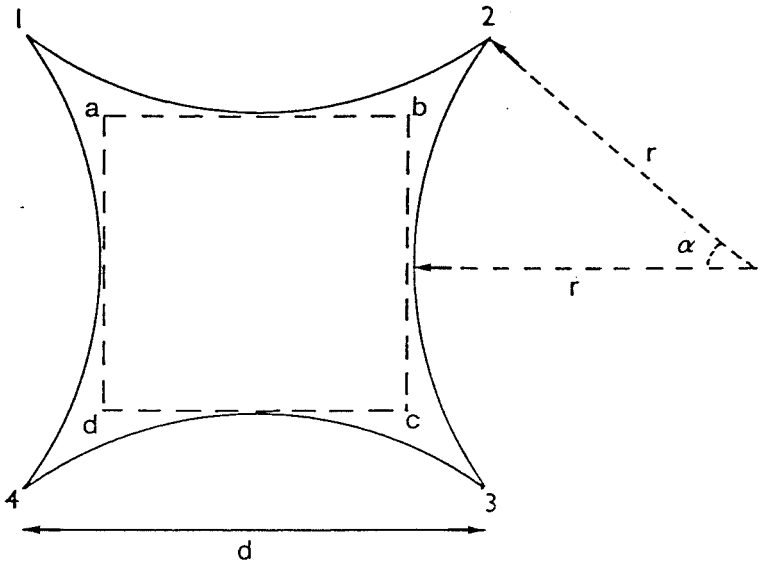

w = width of border resistor.

$$A_g = d^2 \left[1 - \frac{2\alpha - \sin 2\alpha}{2 \sin^2 \alpha} \right] \quad \text{(Total Anode Area)}$$

$$A_w = d^2 \left[1 - \frac{1 - \cos\alpha}{\sin\alpha} \right]^2 \quad \text{(Work Area - abcd)}$$

$$A_s = d^2 \cdot \frac{4\alpha}{\sin\alpha} \cdot \left[\frac{w}{d} \right] \quad \text{(Border Resistor Strip Area)}$$

Maxwell's reciprocal theorem states that the current in a detector divided by the voltage at source remains constant when source and detector are interchanged (Lorraine and Corson 1962). Thus if the anode terminals are earthed, for a steady current i_o into the anode at point (x,y) then the terminal currents are related to the position by

$$x/d = (i_1 + i_2)/i_o \tag{2.2}$$

$$y/d = (i_1 + i_4)/i_o \tag{2.3}$$

The value of i_o is then given by the sum of currents at the four anode terminals. Signal processing to implement the above algorithms is necessary for successful application of this technique. A condition for linear operation is that the anode is operated in the DC limit (Fraser and Mathieson 1981d), which corresponds to the limit of vanishing anode capacitance to ground, or a long shaping filter time constant with respect to the anode time constant $R_\square C/\pi^2$. This condition ensures that the total charge from a pulse is measured by the pre-amplifiers.

Fraser and Mathieson (1981d) have noted that the assumption of a line resistance is unrealistic in practice, where the border will always have a finite width. For a border resistance of width w they derive the relation;

$$r_\square = \frac{w/a[2-w/a]}{(2-w/a)[2-w/a]} R_\square \tag{2.4}$$

where $r_{\square}$ is the resistance per unit area of the border resistances. Thus equation 2.1, which for a finite border width w may be written

$$r_{\square} = wR_{\square}/a, \tag{2.5}$$

is a special case of equation 2.4 for the assumption that w/a << 1. In addition equipotential symmetry considerations are important since the theorem only applies to complete non-intersecting border resistors. In the limit when $\alpha = \pi/4$, the configuration should give negligible distortion as long as w/d << 1. The authors attribute slight boundary distortion effects noted by Rees et al. (1980) and Lampton and Carlson (1979), either to 'extended' electrodes, or to the matching of anode sheet resistances using equation 2.1 instead of 2.4.

The resolution achieved is mainly determined by anode thermionic noise, but pre-amplifier noise and diffusion-line delay also provide a contribution. Thermionic noise is anti-correlated between opposite terminals of the anode and is determined by the resistance between them R_2. The mean square error in x is given by Fraser and Mathieson (1981d) as

$$\frac{(\Delta x)^2}{d^2} = \frac{1}{Q^2} \frac{(2kT_e)\gamma^2 T_a}{\pi} \frac{}{R_2} \tag{2.6}$$

where T_e is the anode temperature, k is Boltzmann's constant, T_a is the shaping filter time constant and γ is the filter noise form factor. Q is the total injected charge and in MCP devices this will

be the MCP gain. R_2 is called the double terminal resistance by Fraser et al. (1981a) and is determined from the potential solution for an anode with two opposite terminals at unit potential with the others grounded. For a CAT anode Fraser and Mathieson (1981d) derive

$$R_2 = R_{\square}/(1 + \cot\alpha). \qquad (2.7)$$

This relationship together with that of equation 2.4 implies that there will have to be a compromise between the thermionic noise of the anode and the useful area available for imaging. The increased thermal noise for a given size of CAT anode compared to a normal anode of the same dimensions is the penalty incurred for obtaining image linearity. Fraser and Mathieson (1981d) state that ideally $d/2a > 0.2$ and that for $w/d \ll 1$ the value of α is not critical.

The other two contributions to noise are not correlated and will therefore produce a spatially dependant degradation to the resolution. The magnitude of these noise factors has often been estimated as minimal by most authors to date, and will be discussed further in later chapters. Since resolution is determined by the signal to thermionic noise in the anode, a high gain output from the MCP stage of a resistive anode detector is highly desirable. The techniques and theory of MCP operation will therefore be discussed in the context of resistive anode detector requirements.

2.2) Micro-Channel Plates

The basic principle of a CEM was discussed in Chapter 1, together with a brief description of MCPs and their manufacture. The applications of MCPs discussed in Chapter 1 highlight their increasing application in astronomical detectors. This section will discuss the MCP operating characteristics of particular relevance to resistive anode detectors, although the principles may be equally applied to other MCP based detectors.

2.2.1) High Gain Configurations

MCPs operate in two different regimes. At low voltages (eg. 600 V) a single channel may be considered as a series of discrete evenly spaced dynodes. The gain, defined as the number of output electrons per input photon or particle according to the method of illumination, is given by Ruggieri (1972) as

$$G \sim \delta^{N D_{es}^{-1}} \tag{2.8}$$

where N is the number of channel collisions , D_{es} is the output electrode penetration depth into the channel wall, known as the endspoiling factor and δ is the secondary emission coefficient of the channel walls. Expressions for N will differ according to the assumptions made regarding electron trajectories and ballistics inside the channel. Thus there are many similar expressions for MCP

gain in the literature based on different models. eg. Eberhardt (1979), Wiza (1979). Considering diametric electron trajectories only, Ruggieri finds

$$N \sim \delta^{(l/d)^2 V_0 V_m^{-1}} \tag{2.9}$$

where l/d is the length to diameter ratio of the MCP, V_m is the applied voltage and V_o is the initial energy of the secondary electrons as they leave the channel wall. Since

$$\delta \sim V_m^2 (l/d)^{-2}, \tag{2.10}$$

then

$$G \sim \left[\frac{V_m^2}{(l/d)^2}\right]^{(l/d)^2 V_o V_m^{-1}} \cdot D_{es}^{-1} \tag{2.11}$$

A single MCP with l/d = 40 will give typical gains of 10^3 to 10^5 (Ruggieri 1972) with a negative exponential output pulse height distribution. In this regime the increase of channel gain with applied voltage is rapid, but then with increasing voltage starts to level off as the saturation regime is reached. Saturation occurs at high gains (10^5 to 10^6) and arises from space charge effects near channel outputs, due to the charge density on the channel walls reducing the electrostatic field. Thus as secondary electrons lose kinetic energy the secondary emission yield from wall collisions falls to ~1. In addition, at high current levels failure to replace extracted charge will lower channel wall charge levels and contribute to channel saturation.

In the saturated regime, the output pulse height distribution becomes quasi-Gaussian and is suitable for use in photon counting applications, since all detected electrons should receive approximately equal weighting. In the saturated regime, MCP gain is linearly proportional to the normalised field strength E_n and is thus directly related to the the applied voltage (Schmidt and Hendee 1966).

Figure 2-2 illustrates the appearance of a typical saturated pulse height distribution with the low gain negative exponential noise tail and the quasi-Gaussian saturation peak. The two parameters used to provide a qualitative evaluation of the pulse height distribution quality are also shown. The pulse height resolution (PHR) is a measure of the spread of the pulse heights around the peak of the distribution. For photon counting applications the PHR should be narrow ideally with values of < 100% for optimal electronic discrimination and processing of pulses. In cases where the peak is not fully resolved the PHR is defined as twice the half width at the half maximum value. The peak to valley ratio (PVR) is a measure of the signal to noise of the distribution and a high PVR is required in order that the saturated pulse be discriminated from the negative exponential noise tail.

When MCPs are run at these high gains the presence of ion feedback becomes a problem. Ion feedback is caused by positive ions released by collisions with the channel walls and residual gas molecules being accelerated back along the channel. Collisions with

Figure 2-2: Diagram showing the main parameters associated with the chararacterisation of MCP pulse height distributions.

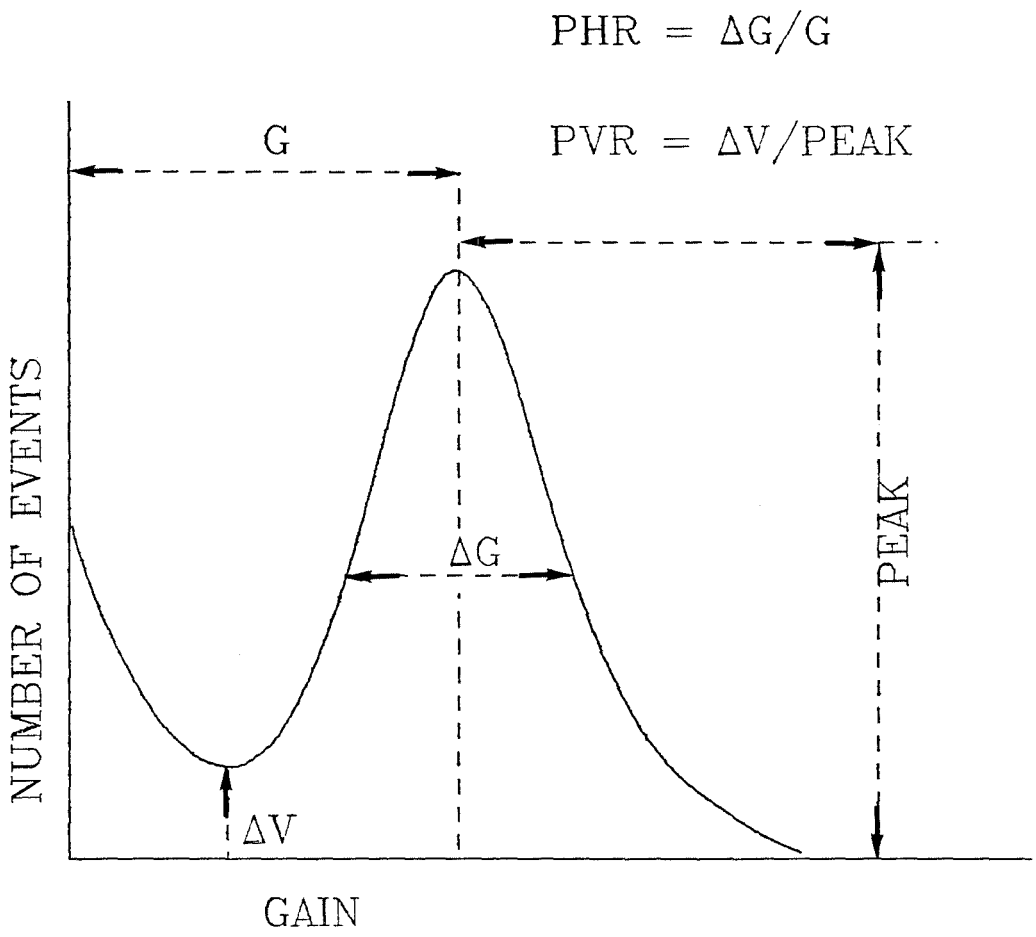

residual gas molecules are only a problem at pressures above 10^{-6} torr and usually occurs in demountable systems operating at inadequate vacuum pressures. If the flux of ions increases, collisions near the input of the channels lead to further secondary electron avalanches, causing afterpulses and distortion of pulse height distribution. Ion feedback, if unchecked in sealed tubes, will damage the photocathode, reducing its sensitivity and useful lifetime.

The number of ions released in wall collisions may be significantly reduced by vacuum baking and 'scrubbing' the MCPs prior to operation to reduce the levels of adsorbed gas in the channel walls. Typical preparation involves vacuum baking at $\sim 300\ ^{o}C$ and with a suitable irradiation source operating the plates at high current levels, known as plate 'scrubbing'. The removal of adsorbed gas from the channel walls also reduces the damage to semitransparent photocathodes in sealed tubes caused by raised gas pressure as molecules are desorbed from the channel walls (Rees et al. 1980).

The useful gains obtainable from operating single plates are insufficient for applications where a combination of high gain, up to 10^{8} and a saturated pulse height distribution are required. The need to reduce the ion feedback resultant from high gains is a major consideration in obtaining this performance.

MCPs can be stacked, usually in twos or threes, to give high saturated gain values of up to 10^8 (Rees et al. 1981, Johnson and Blank 1979). The problem of ion feedback may be reduced by inhibiting the path of ions released near the channel outputs from travelling down the channels. At plate interfaces the channels may be oriented so that there is a bias angle of up to 20^o between respective channels. Ions travelling back up channels re-collide with the channel wall at the interface and are thus trapped before reaching the plate input. Tandem plates are known as 'V' or 'chevron' plate configurations, while a triple stack is known as a 'Z' plate. Although larger stacks are not common, Johnson and Blank (1979) have tested a four plate stack and Fermani et al. (1982) have evaluated a 5 plate 'Z-V' configuration consisting of two clamped MCP stacks separated by a 1 mm gap.

In these stack configurations, stable saturated gains of the order of 10^6 to 10^8 have been obtained both in tandem (Kellogg et al. 1976, Wiza 1979) and triple (Eberhardt 1981, Armentrout 1985) configurations. The interface gap is of some importance in these stacks and determines the overall gain and pulse height distribution achievable. If the plates are clamped together, electrons will spread over only a few channels (Eberhardt 1981) of the next plate at the interface. The gain in these configurations will not be much in excess of that from a single plate, of the same l/d.

MCP stacks are therefore often constructed with an interplate gap which may vary from 20 μm (Timothy and Bybee 1975) to 3 mm (Rogers and Malina 1982). While these configurations produce high gains, the pulse height distributions are poor and typically range from 100% to 200% FWHM (Wiza 1979, Rogers and Malina 1982, Fermani et al. 1982). The application of a bias potential across the gap can be used to vary the spread of the electron cloud incident on the following plate and sweep out any space charge buildup. In principle the spread of the cloud will determine the number of channels with incident electrons in the second plate and thus the overall gain. Rogers and Malina (1982) have found that PHR decreases with higher intergap voltages and levels out to a plateau region, with the final value being higher for a larger intergap spacing. eg. 100% at 150 μm to 400% at 3 mm.

Recently a PHR of 50% at a gain of 10^8 has been reported with a large format (60 cm^2) 'Z' plate configuration with the interspace gap determined by 25 μm thick electrodes (Armentrout 1985). Armentrout highlights problems with gain variation across the field caused by intergap space charge effects, and plate arching which may be the source of poor PHRs in these systems. Operation of such high gain assemblies is complicated by dangers of plate damage from transients, thermal runaway and breakdown leading to arcing.

Increasing the l/d ratio of MCPs from 40:1 to 80:1 also gives improved performance. Increasing the l/d ratio will reduce the gain a plate will give, compared to a similar plate with a lower l/d ratio at the same voltage. Thicker plates with a larger l/d ratio, however, allow a higher maximum voltage to be applied to the plate giving higher gain (Ruggieri 1972). Clamped tandem and triple MCPs with large l/d ratios of 80:1 give pulse height distributions of the order of 30% to 50% with gains of 10^7 (Siegmund et al. 1983, 1984, Lyons and Read 1983).

Curved channel plates (Timothy 1981) are MCPs in which the channels are curved in order to reduce ion feedback. With curved channels, ions will have short travel paths before colliding with the channel wall. Another advantage of the short travel paths is the reduction of pulse height distribution distortion due to afterpulses. With l/d ratios of typically 140:1 these plates have been shown to give very high gains ($>10^6$) with narrow PHRs of 30% to 40% FWHM for single plates at potentials of 2000 V (Timothy 1981). A similar concept is employed to inhibit feedback in 'J' plates.

MCPs have vacuum deposited nichrome or iconel electrodes covering the front and rear faces of the plate. The degree of electrode penetration, at the output face into the channels can have an important effect on the overall performance (Ruggieri 1972). If the channel penetration is relatively deep, ie. ~1 channel diameter then the output pulse height distribution is narrowed, at the

expense of a reduction in gain (Koshida and Hosobuchi 1985).

In sealed tubes the presence of any ion feedback at high gain is such that some means of stopping ions from damaging ('etching') the photocathode is essential. Deposition of a thin (~5 nm to 8 nm) layer of Al_2O_3 on the face of the input MCP (eg. Millar et al. 1972) will prevent ions from impacting the photocathode and the technique has become standard practice.

2.2.2) MCP Resolution

The resolution of an MCP considered in isolation is determined from a single channel diameter which is typically of the order of 15 μm to 12.5 μm (Mullard 1985, Galileo 1985), although 8 μm diameter channel MCPs are under development (Wiza 1979). Endspoiling collimates the output electron cloud and may be optimised to increase resolution, usually in MCP intensifiers (Ruggieri 1972, Koshida and Hosobuchi 1985). In general the intrinsic MCP resolution will usually be degraded by the method used to detect the output pulse.

2.2.3) Count Rate Performance.

A typical transit time for a pulse to pass through an MCP is of the order of 180 ps-270 ps with a spread 30 ps-60 ps, for 40:1 (l/d) MCPs (Eberhardt 1981, Yamazaki et al. 1985). For 'V' and 'Z' configurations this will be longer eg. 360 ps with a 750 ps spread for a tandem plate (Wiza 1979). Thus count rate performance is not

usually limited by transit time considerations.

The recovery time of a single MCP channel is determined by considering the channel as a distributed RC network where $\tau = R_c C_c$. Wiza (1979) has calculated a typical value to be 20 ms for a 300 MΩ, 25 mm diameter (40:1) MCP and implies a single channel count rate ceiling of 50 cs^{-1}. Gatti et al. (1983) considered the resistive paths between adjoining channels and calculated the recovery time to be 5x longer than $R_c C_c$. If the event rate in a channel exceeds the rate given by the reciprocal of the channel recovery time, there will be a consequent decrease in gain. The saturation limit for a single channel is usually defined as being when the output current exceeds 10% of the channel wall (strip) current through the plate (Wiza 1979), although again this figure varies. Higher count rates with localised sources may be achieved by the use of low resistance plates, with a consequent drop in the time constant (Fermani et al. 1982).

For 'V' and 'Z' plate configurations, the overall count rate will be lowered by a factor dependant on the number of channels activated in the following plates. Armentrout has found higher count rates than predicted without loss of gain, for a large format 'Z' plate configuration. This he attributed to heating of the innermost plate, causing a drop in resistance which allows the plate to take more current.

2.2.4) Background Noise

MCP background noise arises from two main sources: intrinsic dark noise characterised by the negative exponential tail seen in pulse height distributions, and noise due to MCP irregularities. Contributions due to the latter include effects such as 'switched on channels', dead channels, hot spots and field emission due to the mounting hardware. Siegmund and Malina (1983) attribute most common MCP noise problems of this nature to hotspots, with the others having been almost eliminated by quality control. The origin of hotspots is uncertain, but they may be caused by dust or damage on the front surface of a plate, or sometimes from the bakeout of a sealed tube (Siegmund 1984). When hotspots do occur they usually produce lower gains in the pulse height distribution than a true event (Bowyer et al. 1981) and so may often be removed by electronic discrimination.

Henry et al. (1977) have proposed that intrinsic dark noise in an MCP is caused mainly by defects in the channel walls giving rise to field emission, with less then 5% of dark noise arising from other causes. eg. thermionic emission. MCP dark count rates are low with typical figures being of the order of 0.01 $cs^{-1}mm^{-2}$ (Timothy 1981) for curved plates and a 'V' plate configuration (Wiza 1979). Siegmund et al. (1984) have obtained lower values of 0.002 $cs^{-1}mm^{-2}$ with a 'Z' plate configuration. In general, low values of intrinsic noise can be obtained by the selection of

plates.

2.2.5) Detection Efficiency

Table 1.1 shows that the detection efficiency of a CEM for electrons is very high. Hill (1976) has shown that the optimum detection efficiency is obtained for primary electron energies in the range 200-600 eV. When MCPs are operated in proximity focussed sealed tubes, the problem is complicated by the presence of an Al_2O_3 film on the input plate. The transmission of this layer is proportional to the incident electron energy and has a lower threshold corresponding to 150-200 eV.

Detection efficiencies for MCPs are limited by several additional factors and are dependent upon the particular application. The open area ratio of MCPs, that is the ratio of open channel area to the interchannel web area, is usually quoted at around 55% to 60%. In principle this should then lower the detection efficiency by a considerable fraction. Studies by Panitz and Froesch (1976) and Taylor et al. (1983) have shown that this factor can be raised for demountable systems by placing a weak electric field above the MCP input. This field has the effect of returning secondary electrons produced from collisions with the interchannel web back into the channels of the MCP. The proximity focussing potential in a sealed MCP has a similar effect. Another solution is to funnel the inputs to MCP channels in order to increase the effective open area ratio of the plate (Lampton 1974).

2.2.6) MCP Lifetimes

MCP useful lifetimes are determined essentially by Q, the total charge that may be extracted per unit area of the plates (C cm^{-2}) with a stable gain. Sandel et al. (1977) reported that lifetimes of a sample of several plates from different manufacturers were relatively short compared to channeltrons and fell when operated at high current levels. Such analysis of MCPs is obviously influenced by differences in manufacturing procedure and this appears to be the case with the lifetime tests of Rees et al. (1980), who find improved MCP lifetime characteristics. The reduction of plate contamination in a sealed device is also highlighted as a possible contributory factor. Sandel et al. (1977) also note that continual irradiation of one section of a plate will lead to a loss of gain in this area with respect to the rest of the plate. In general MCP lifetimes are still poorly understood and are very much a function of the required application and the operating environment.

The plate preparation techniques discussed for a required application usually result in an associated initial drop in gain. When MCPs are prepared for sealed tube devices they are usually baked and 'scrubbed' to remove adsorbed gases in the channel walls. Both these processes give rise to a loss of gain in the plates, Siegmund et al. (1983) report a factor of ~8 drop for a pair of plates at a given voltage after scrubbing and baking. The loss of gain with scrubbing is due to outgassing of the channel walls and

is to a certain extent reversible with re-exposure to air. Panitz and Foesch (1976) suggest that the irreversible gain loss due to baking may be a result of a change in the composition of the channel walls. Using a microprobe they found the surface layers of channel walls to be alkali-rich. This layer was shown to determine secondary emission properties of the channels rather than lead oxide as previously thought. They therefore attributed gain loss to the desorption of these alkalis during baking. Siegmund and Malina (1983) have further speculated that continued desorption of these alkalis under electron bombardment may ultimately determine the lifetime of a plate.

2.3) Resistive Anode Detector Systems

The main applications of resistive anodes have been mainly in the fields of particle detection in nuclear physics and as ultraviolet and X-ray detectors in astronomy. Only in the last five years have they been used in sealed tubes for optical applications. The literature on resistive anode work breaks down into one and two dimensional systems. Although this work is concerned with two dimensional anodes, important considerations associated with general anode operation and signal processing have arisen from one dimensional anode research.

Several one-dimensional resistive anodes designs have been investigated for applications in spaceborne X-ray and ultraviolet astronomy. Carruthers and Opal (1974) report a resistive strip interfaced to a rectangular MCP stack giving a gain of 10^7. A

resolution of 1% of the anode length was obtained from this detector.

Parkes et al. (1974) described a one dimensional anode with two MCPs separated by 75 μm in a 'V' plate configuration. With an MCP channel diameter of 20 μm, a resolution of 42 μm was obtained over an active area of 27 mm, at a gain of 10^7. The resolution of the anode was not spatially linear, deteriorating towards the anode terminals. The detector was designed for charge particle and X-ray detection applications.

Laurence and Stone (1975) and Weiser et al. (1976) both detail one dimensional demountable MCP-anode configurations for spaceborne ultraviolet spectroscopy. Both systems employed photocathode coated input MCPs with typical resolutions of the order of 100 μm. Hartig et al. (1980) report a similar system for spaceborne ultraviolet spectroscopy with a resolution of 200 μm at a gain of 10^6. A degradation of performance due to the system's processing electronics will be discussed in chapter three.

Augustyniak et al. (1972) pioneered the use of a (CAT) resistive anode in a demountable configuration to detect magnetically focussed secondary electrons from a silicon surface barrier detector. A resolution of 0.23 mm FWHM was obtained for this device with an active diameter of 10 mm, operating at a micro-channel plate gain of 10^7. A major factor limiting the achievable resolution in this case was the MCP channel diameter of 0.2 mm. The use of a diffusion delay signal processing technique

while not a limitation with this design, was unsuitable for this type of anode, since charge ratio signal processing is required for optimum linearity.

Lampton and Paresce (1974) evaluated a 65 x 40 mm active diameter demountable configuration for particle detection and a 75 mm active area one dimensional anode for UV spectrometry. The resolutions obtained respectively were 0.50 to 0.25 mm and 0.3 mm.

A two dimensional system for ultraviolet imaging (Opal et al. 1979) involved using an anode truncated by four parabolas, to reduce distortion, coupled with an MCP having an ultraviolet sensitive photocathode deposited on its front end. The system achieved 80 μm resolution over a 5 mm diameter active area, with some severe distortion at the edge of the field. Event processing speeds in this case were complicated by telemetry considerations.

Lampton and Carlson (1979) investigated the properties of CAT anodes in a demountable MCP-anode configuration. With 40 μm channel diameter MCPs operating at a gain of 5×10^6, a resolution of 100 x 100 pixels was obtained for a 25 mm active diameter device. The authors also reported the improvement in anode linearity compared with other anode designs. Values of $w/d = 0.1$, $d/2a = 0.25$ and $R_{\square} = 200\ k\Omega$ are quoted by the authors for their anode.

A 75mm CAT anode was used by Stair (1982) in a demountable configuration for low-energy electron diffraction experiments. Using MCPs with a channel diameter of 25 μm in a chevron configuration producing a gain of 10^7, a resolution of 400 μm was obtained. No apparent image distortion was observed with this large format CAT anode.

A high gain demountable configuration consisting of a cascaded pair of MCP stacks, discussed earlier, with a CAT anode were investigated by Fermani et al. (1982). A resolution of 50 μm was obtained with this detector over an active diameter 25 mm, this resolution being due to the very high gains obtained with the system ($>10^7$).

Rees et al. (1980) discuss the development of two dimensional resistive anode detectors in sealed tube configurations designed for optical imaging applications. Two designs with opaque and transparent photocathodes were initially tested. Tubes with a transparent photocathode deposited on the input window were found to have short lifetimes of the order of 0.01-0.1 $mCmm^{-2}$, due to ion feedback damage to the photocathode. Depositing opaque photocathodes onto the input MCP was found to be a solution to this problem, although there is a penalty incurred in the loss of cathode sensitivity.

The 20 mm active diameter systems tested, were found to have a resolution of 200 μm attributable solely to the anode at a gain of 4×10^6 rising to a predicted 100 μm at a gain of 10^7. The resolution was found to be proportional to gain over a limited range of $1\text{-}5 \times 10^6$. The 100 μm resolution predicted is confirmed by Rees et al. (1981) using an 18 mm diameter device with a 'Z' plate MCP configuration. These later devices have transparent photocathodes and thus increased sensitivity. The problem of ion feedback was resolved with the increase in availability of MCPs with Al_2O_3 films on their input surfaces.

Mertz et al. (1982) discuss the performance of an 18 mm diameter Surface Science Laboratories sealed tube for astronomical imaging. The device was found to give 100 x 100 resolvable pixels at 50% modulation. Slight barrel distortion was found, with the maximum occurring at the periphery of the field. The authors also demonstrate the spatial aliasing effect due to the arrival of coincident events at high count rates (2×10^3 cps). This arises from the simultaneous arrival of pulses within the deadtime of the anode, ie. at rates in excess of the reciprocal of the anode time constant. While the detector electronics is not discussed, the authors note that most of the dark counts occur on or near the rim of the detector field. This is probably due to the dynamic range of the electronics being exceeded and consequently saturating during signal division.

The most recent published application of a resistive anode detector to astronomy has been that of Fermani et al. (1983), who report the performance of a high gain (10^8) 25 mm diameter sealed tube. Resolution of 42 μm at 600 nm was obtained, with the proximity focussing being the limiting factor. Cooling to $-30^{\circ}C$ reduced the dark count rate to 30 cs^{-1} from the 2000 cs^{-1} found at room temperature. Using low resistance plates a point image count rate of 100 $cs^{-1}pixel^{-1}$ is claimed, where the pixels are 25 x 25 μm in size.

2.4) Detector Design

The detector design chosen was that of a 40 mm active diameter S20 photocathode, with a tandem double thickness MCP arrangement and a CAT resistive anode readout. The tube was of a design used by Dr Rees's group at UCL, with whom we collaborated at this stage of the project, and was manufactured and processed by Instrument Technology Limited. These detectors are called imaging photon detectors (IPD) by ITL, although this name can also be applied to other compact MCP based detectors. A schematic of the detector design is shown in figure 2-3(a) illustrating the principle components of the IPD. Figure 2-3(b) shows the principle component spacing dimensions of the design. The internal layout of the tube is shown in figure 2-4, showing the arrangements of the tube components and the method of achieving a vacuum seal.

Figure 2-3(a): Schematic diagram illustrating detector configuration.

(a)

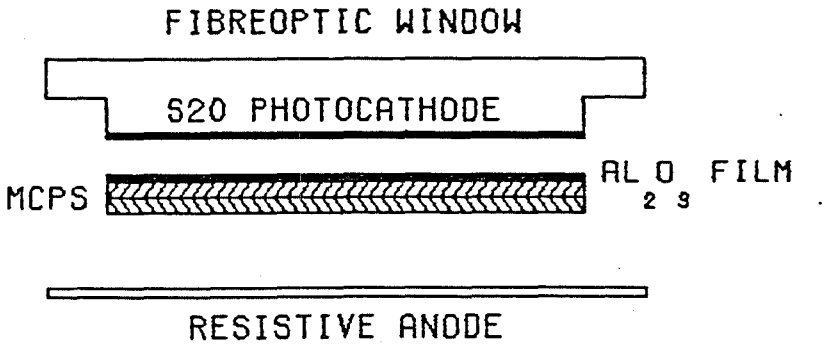

Figure 2-3(b): Schematic diagram illustrating main detector component separation dimensions.

(b)

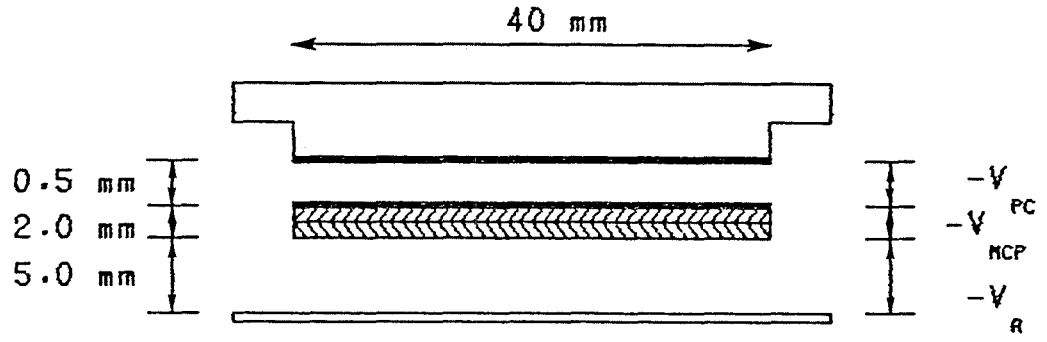

Figure 2-4: Diagram showing internal arrangement of detector tube.

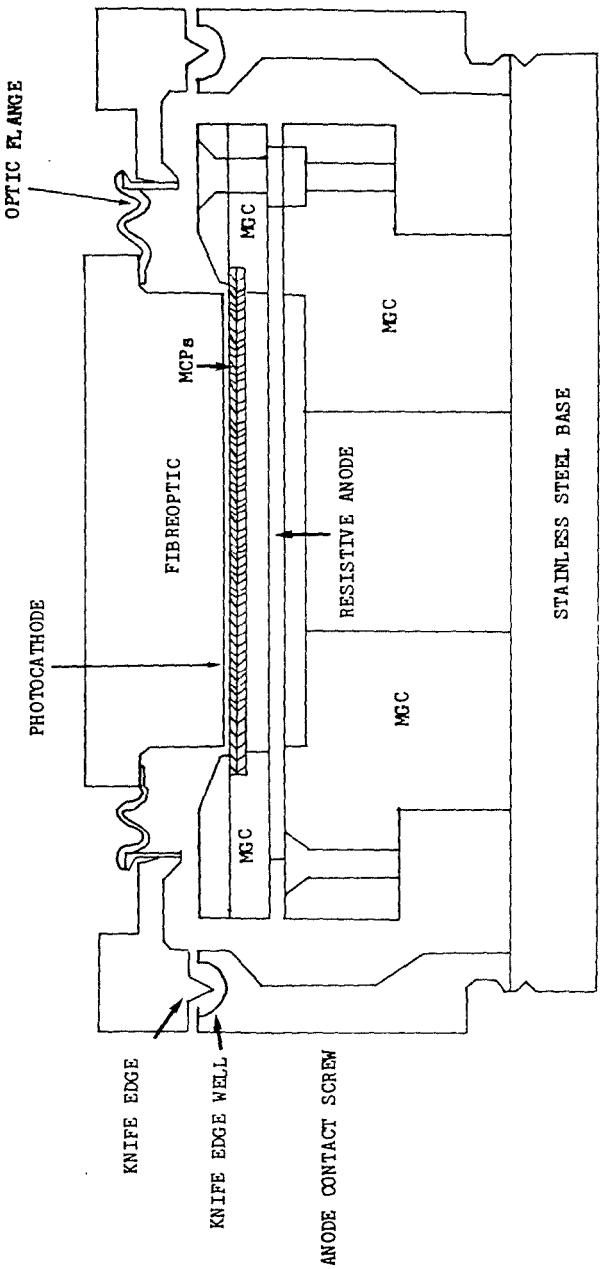

A fibreoptic window was chosen for this tube to enable the optical coupling of the detector to the Leslie Rose Spectrograph in St Andrews. This is because a feature of IPD designs is that the standard glass optics are recessed, with respect to the front face of the tube. This is due to the way the window is mounted in the optic flange. A consequence of this choice is that there is an additional loss of efficiency due to the transmission of the fibreoptic plate. Figure 2-5 shows a graph of the typical transmission performance of the fibreoptic window, supplied by ITL. The photocathode is deposited on the output face of the fibreoptic window and is separated from the input MCP by a gap of 500 μm.

The MCPs used are a Mullard G12-46DT matched pair. These plates are 46 mm diameter plates having an l/d ratio of 80:1. The plates are mounted in a back to back tandem configuration, with no interplate gap. There is a total bias angle of 13^{o} between the plates at the interface. The channel diameters are nominally 12.5 μm with a pitch of 15 μm. Open area ratio is stated as being 60%. The input face of the first plate has an Al_2O_3 layer deposited on its surface. The resistance between electrodes for such plates are quoted by Mullard (1985) as being of the order of 60 MΩ to 250 MΩ and are matched for the two plates.

The resistive anode is of the CAT design and is made of a resistive ink deposited on a ceramic base. The approximate anode dimensions, where the nomenclature is that for figure 2-1(b), are;

Figure 2-5: Diagram showing transmission curve of the fibreoptic faceplate. (ITL)

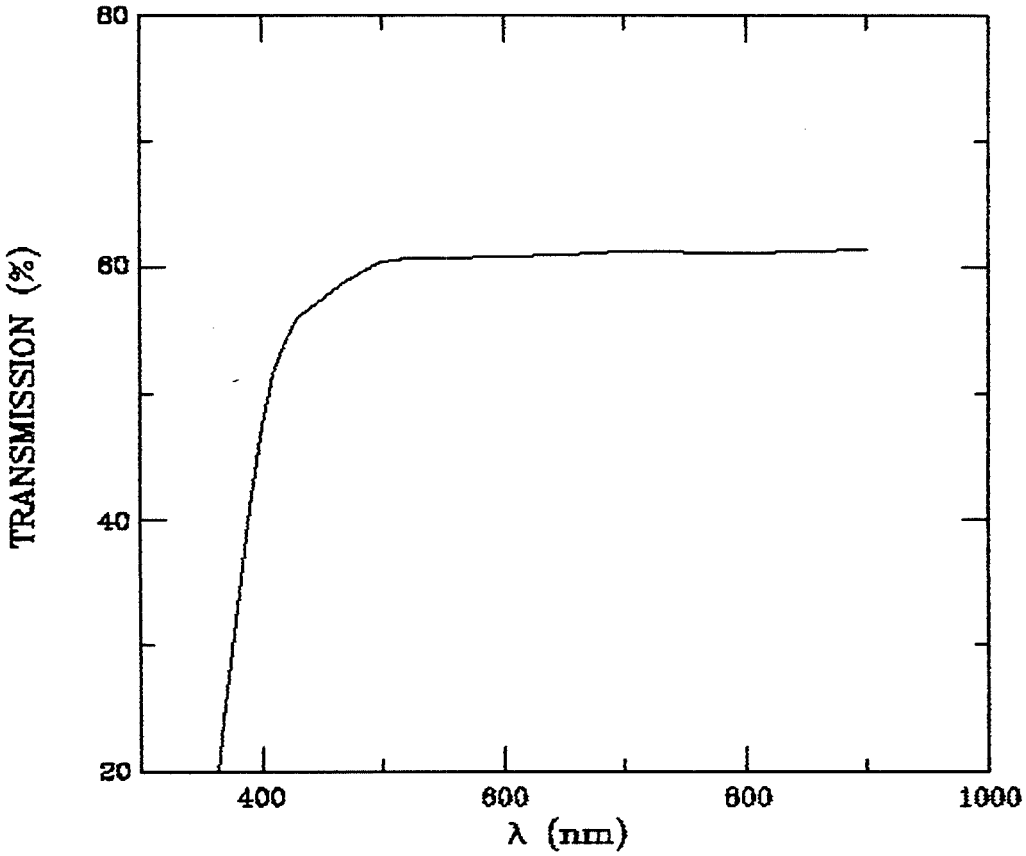

$$d = 5.2 \text{ cm} \quad a = 8.65\text{cm} \quad w = 0.2 \text{ cm}.$$

giving anode parameters

$$d/2a = 0.3 \quad w/d = 0.04 \quad w/a = 0.02 \quad \alpha = 17^{\circ}30'.$$

$$A_G = 25.7 \text{ cm}^2 \quad A_S = 1.1 \text{ cm}^2 \quad A_W = 19.4 \text{ cm}^2$$

For near linear performance Fraser and Mathieson (1981d) recommend that $d/2a > 0.2$ and $w/d \ll 1$, these requirements are met by the anode.

Prior to the manufacture of the tube the double terminal resistance value was measured as $R_2 = 37$ kΩ, which gives a value of $R_{\square} = 158$ kΩ using equation 2.7. With a total anode area of 26 cm^2 and a gap of 5 mm between the output MCP and the anode, the anode capacity is calculated to be of the order of 0.18 pFcm^{-2}.

2.5) IPD Manufacture

The main elements of the IPD's tube manufacture and processing will be reviewed briefly, in order to appreciate their bearing on the detector's final performance and highlight the current technological limits of the process. An IPD tube is assembled from three main component sections, the MCP-anode stack assembly, the window and the tube casing. The need for cleanilness in the treatment of detector components has already been emphasised. Defects such as the hotspots, field emission and dead areas seen on photocathodes and MCPs are often due to particles of dust and other microscopic contaminants. A large part of the process of assembly is therefore done in a clean room environment to minimise the

contamination of components. At all stages of manufacture and processing, measures must be taken to prevent outgassing of adsorbed molecules in detector components lowering the vacuum pressure in the sealed tube. Serious reduction of the vacuum pressure will degrade the photocathode sensitivity and shorten its lifetime.

2.5.1) MCP-Anode Stack

The dimensions of the gaps separating the internal components together with the provisions made for their insulation and contact points are very crucial. The MCPs and the anode are therefore mounted in a stack assembly (figure 2-4), with machinable glass ceramic (MGC) used in the intermediate layers as the insulator. This material may be cut to precise dimensions with machine tools, so the gaps between respective components and the overall height of the assembly may be achieved with machine tool accuracy.

The MCPs must be matched by manufacturer's specification to ensure that, with the back to back configuration chosen, there will be an equal voltage across each plate. When mounted in the MGC support, the MCPs must fit exactly in order to ensure there will be no arcing with the rim, since this would lead to breakdown of the plate. This applies to the MCP contact rings as well, which should be in good contact with the plate electrode surface.

2.5.2) Tube Casing

The three components of the tube casing are made from stainless steel blocks, and comprise the body, the base and the knife edge assembly. Each section is baked in vacuo at 1000°C, in order to remove impurities deep within the components. These impurities would otherwise cause contamination of the photocathode by lowering the final tube pressure. The terminal feed-throughs mounted in the base are chemically cleaned before they are welded in and then leak tested, to avoid porous welds.

When the tube is finally sealed off in vacuo, the seal is formed by a cold indium weld. This is done by closing a knife edge onto a machined well in the tube body containing melted indium. The principle is illustrated in figure 2-4. This indium must be melted into the channel evenly and cut down so that it just fills the well. Several vacuum bakes may be necessary prior to processing to ensure that there is an even layer of the metal in the knife edge well and that there are no gaseous impurities in the indium. Any bubbles formed during the sealing of the tube would lower the vacuum pressure of the tube and contaminate the photocathode.

2.5.3) Window

The optic faceplate of an IPD is assembled from two components, the window and the optic flange. In this case the window is a fibreoptic, frit sealed to a Nicromet 44 flange. The assembly was baked out in O_2 and was then chrome plated to a required resistance value, to provide the photocathode terminal connection. It was then welded to the knife edge surround and baked out again ready for processing.

2.5.4) Photocathode Processing and Transfer

A system similar to that of Van Huyssteen (1976) is used to process the photocathode and then transfer it to the main tube body for sealing. The system is usually pumped down to pressures of 10^{-8} torr and then baked out overnight at a temperature of $200^{o}C$. The MCPs are then scrubbed at a current of ~3 μA for 24 hours. During this period the applied potential is varied slightly to ensure uniform scrubbing of the channel walls.

The tri-alkali photocathode is basically formed by evaporating alternate layers of sodium, potassium and antimony onto the window. Progress is assessed from the photocurrent response to a 3000 K tungsten lamp. After several cycles of this procedure, a final evaporation run is done using caesium to improve the performance of the cathode. This process is done at a lower temperature to allow it to be monitored, since the caesium reaction is very fast. The

colour of the photocathode, caused by optical interference, appears pinkish after the first sodium-antimony cycle changing to gold and then a light grey as further cycles are completed. At the completion of processing, the system is allowed to bake further for several hours prior to sealing.

The processed cathode is then twisted through 90^{o} and lowered by bellows onto the tube body for sealing. It is important at this stage that the two components are parallel in order to achieve a proper seal and maintain a constant gap between the photocathode and MCP. The pressure at this stage is usually of the order of 10^{-9} torr. A schematic diagram of the apparatus is shown in figure 2-6.

2.5.5) Technological Limitations

At the time of processing the system used was designed for processing devices with windows of typically 18 mm to 25 mm. This creates a problem for processing larger photocathode windows, since there may not be uniform evaporation of the alkali vapours on the window. The evaporation should ideally be over an aperture, known as the 'throw', of 2.5x the cathode active diameter to produce uniform evaporation. The cathode uniformity actually obtained will be discussed in chapter 6.

When the tube is sealed off an uncertainty of up to $\pm 150\ \mu m$ may be introduced into the gap value. This arises from the technique used to achieve the knife edge seal and any slight flexure in the optic flange upon removal from vacuo. A uniform change in the value

Figure 2-6: Schematic diagram showing processing apparatus and mechanism for sealing off tube (van Huyssteen 1976).

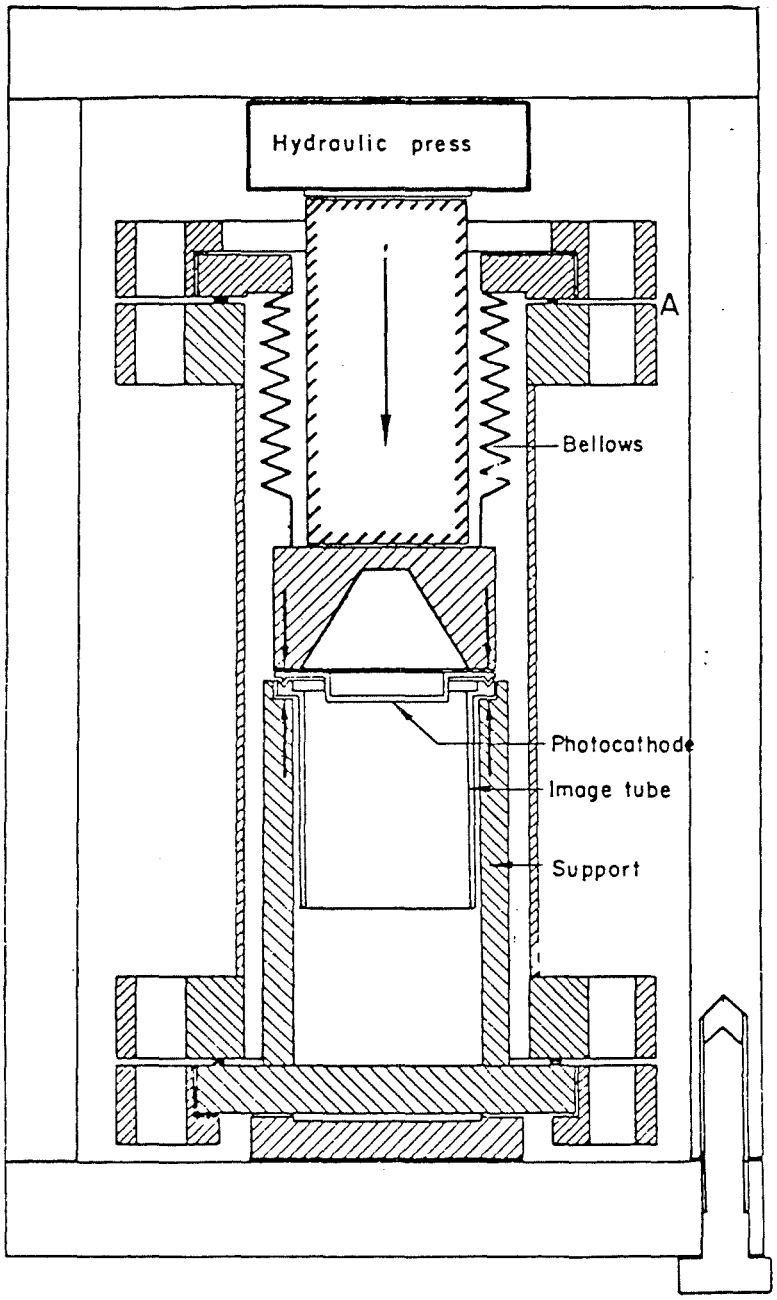

of this gap may cause either an improvement, or degradation of the required resolution contribution from the proximity focussed lens. Non-uniformity will lead to spatial variations in the resolution.

The bakeout procedures necessary in preparation of the tube also lead to the possibility of structural deformation of the MCP at the temperatures encountered (Lyons 1985).

Chapter 3

3.1) Signal Processing Hardware

The pre-amplifiers and signal processing electronics for this IPD system were designed and built by Dr Rees' group at University College London and supplied by ITL with the detector tube. This particular model of electronics had been recently designed (Rees 1983) and now is supplied with 18, 25 and 40 mm active diameter IPD systems by ITL.

In view of the project timescale the alternative approach of designing a processing system from scratch was considered impractical. Using the the existing processing electronics had the advantage of allowing assessment of the performance of the overall commercial system, in line with the CASE objectives.

3.2) Pre-amplifier Circuit Design

The IPD pre-amplifiers perform the function of amplification and shaping of the anode charge pulses. The IPD pre-amplifier circuit has been discussed by McWhirter et al. (1982) and is based on a design by Alexander (1971). Figure 3-1 shows a circuit diagram for the pre-amplifier, with a schematic of the circuit illustrated in figure 3-2. This schematic shows the three main sections of the design and the components which define the circuit gain and pulse

Figure 3-1: Pre-amplifier circuit diagram (courtesy of ITL).

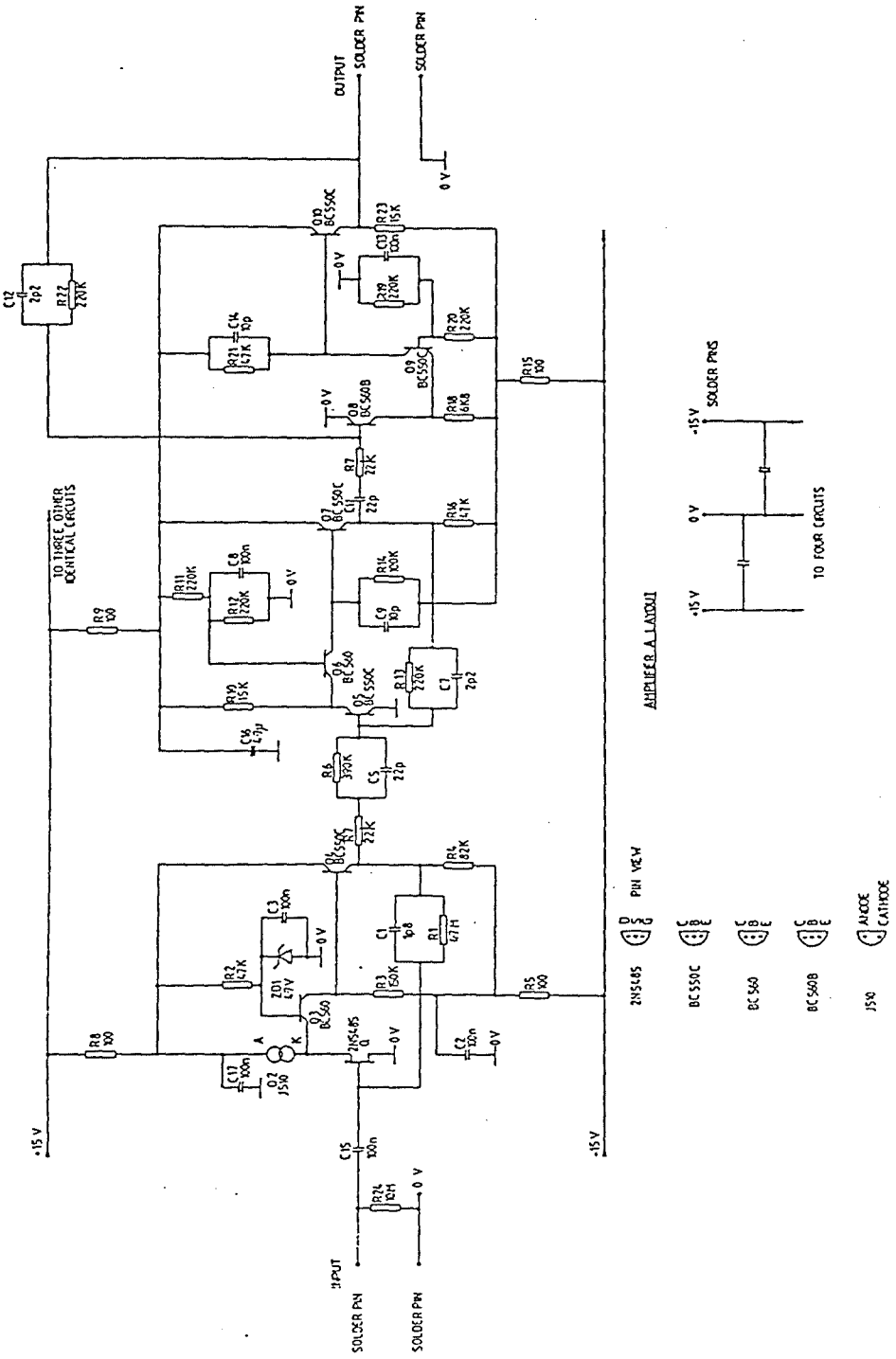

Figure 3-2: Schematic diagram illustrating the operation of the gain and shaping stages of the pre-amplifier circuits.

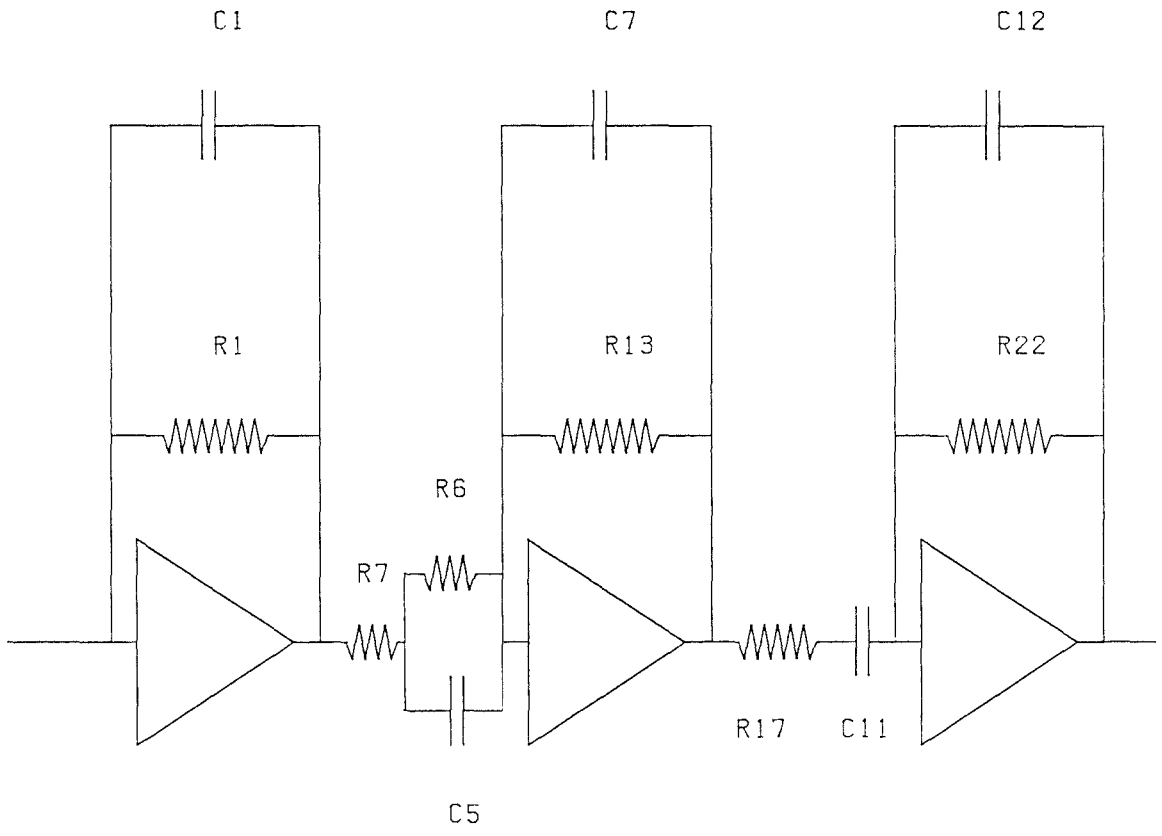

shaping parameters.

Section (i) performs the initial charge to voltage amplification of the anode pulses, having a gain of the order of 2.7×10^{11} VC^{-1}. This gain may be adjusted by modification of the charge amplifiers gain capacitor C_1. The gain may therefore be matched to the size of the charge pulses, determined by MCP gain, arriving from the anode terminals. The following two sections provide further voltage gain and perform the pulse shaping. The pulse shaping employed is double differentiation-double integration (DDDI) with pole zero cancellation of the pre-amplifier decay time constant (ie. R_6C_5), giving a bipolar pulse shape. The purpose of the pole zero cancellation is to ensure there are no baseline shifts in pulses. The time constants of the differentiation-integration shaping circuits in sections (ii) and (iii) are

$$\tau = R_{13}C_7 = R_{17}C_{11} = R_{22}C_{12} \sim R_7C_5. \qquad (3.1)$$

The total amplifier gain expressed as a function of time is

$$\frac{e_o(t_{max})}{Q_D} = \frac{R_3R_5 \times (3\tau - t)t^2 e^{-t/\tau}}{C_1R_2R_4 6\tau^3} \quad \frac{\text{Volts}}{\text{Coulombs}} \qquad (3.2)$$

where τ, the shaping time constant, is 0.5×10^{-6} seconds from (3.1). C_1 is the charge amplifier feedback capacitor and the R are the

voltage gain feedback resistors from sections (ii) and (iii) of figure 3-2. The gain without shaping is therefore

$$\frac{R_3 R_5}{C_1 R_2 R_4} \tag{3.3}$$

Differentiating and solving for the maximum and minimum pulse heights gives the gain for the primary pulse at t_{max} as;

$$\frac{e_o(t_{max})}{Q_D} = \frac{R_3 R_5 \text{ x } 0.127}{C_1 R_2 R_4} \tag{3.4}$$

and the ratio of pulse heights as;

$$\frac{e_o(t_{+max})}{e_o(t_{-max})} = 0.465 \tag{3.5}$$

From (3.2) the zero crossing time is given by 3τ, with the return to <1% of the peak taking 12τ. From an analysis of the pulse height distribution of the anode pulses together with a determination of the height of these pulses, equation (3.4) may be applied to obtain a figure for the charge within single pulses at the anode. Thus the value of the microchannel plate gain may be estimated from this charge figure.

The noise performance of these amplifiers differs from Alexander's design due to the use of different input FET components. McWhirter et al. (1982) report a slightly lower transconductance raising the amplifier noise to the equivalent of 12

Kev (silicon), or 4000 e^- FWHM (1700 e^-rms).

The overload recovery characteristics for these pre-amplifiers is reviewed by Alexander (1971), with typically 25 μs to recover from a 10x overload. With the IPD, large transient input signals often caused one or more of the input 2N5485 FETs to fail. This is in contrast to Alexander (1971) who reports 'rugged' input protection with 2N5564 input FET pairs. The operating conditions giving rise to large transients will be discussed later.

3.3) Pulse Position Processing Methods

Pulse position determination with resistive anodes may be achieved either by the method of pulse amplitude ratios, or rise time analysis of the charge at the anode terminals. The techniques available for both methods of processing have been extensively discussed by Lampton and Paresce (1974). A brief discussion of these methods is important, however, in order to appreciate the problems associated with the pulse position determination and the implications for system performance. It will also complement later discussion of the processing electronics performance and the prospects for signal processing in future large format detector systems.

The pulse position determination electronics must be able to process information at high event rates, free from non-linearities. These include pulse coincidence events, base line shifts and differential non-linearities. Processed images should be free from

spatial non-linearities, such as barrel, or pin-cushion distortion and variable resolution. Other irregularities associated with the design of the circuit, such as fixed pattern noise are equally undesirable.

Of the two methods for determining pulse positions with a resistive anode, one requires the electronic division of two signals, while the other involves the evaluation of the signal arrival times at the anode terminals.

3.3.1) Charge Division

Processing systems utilising the charge division method of analysis usually have several stages in processing. Shaped pulses from the pre-amplifiers are input to sample/hold and pulse peak detection circuitry. The signals are then added as necessary to form the numerators and denominator for the division. The signals are then divided in one of three ways: a) analogue division with subsequent conversion to digital output, b) analogue to digital division, or c) analogue to digital conversion with software division.

This last stage will be the dominant factor determining the overall performance of any design in terms of processing speed, linearity and accuracy. The choice of the method of signal division will involve a compromise between the performance of these three parameters.

3.3.1.1) Analogue Division

Several techniques for signal division by analogue methods have been outlined by Lampton and Paresce (1974). Most of the methods tend to be rather slow and many have limited dynamic range. The logarithmic division method though, has been used by Lampton and Carlson (1979) and more recently by Rees et al. (1980). The numerator and denominator signals are input to logarithm circuits and are then subtracted and input to an exponential circuit. This output signal can then be digitised by an analogue to digital convertor (ADC) to give the position coordinate. These circuits are commercially available in single chip units, but they are relatively slow and errors in the logarithm and exponential circuits will limit accuracy. eg. 0.25% over 100:1 input signal range, with a small frequency response decreasing from 100kHz for a 10V input to 400Hz for a 10mV input (Analogue Devices 1982).

3.2.1.2) Analogue to Digital Division

The successive digital approximation method uses an analogue to digital converter (ADC) in a mode where the signal numerator is converted while the signal denominator is used as the converter's reference input. Accuracy is determined by the quantization error in the conversion. Carpay and Klein (1971) have investigated the technique, reporting a 7-bit ratiometric ADC device having a conversion speed of 5μs per bit.

Hartig et al. (1980) used this method of charge division with a one dimensional resistive anode detector. Using an 8-bit ADC, count rate linearity up to 500Hz was obtained, with circuit dead times of 100μs. For shorter conversion times they report 'a strong preference for conversion to binary numbers containing a maximum number of ones', producing spatial non-linearity. The 100μs allowed for conversion, is required to minimise this effect. The ADC ratiometric method of charge division is currently being used by Paresce (1984), and by Rees (1983) as discussed below.

3.3.1.3) Software Division

This method of charge division involves the analogue to digital conversion of the numerator and denominator signals and then their subsequent division in software by a suitable computer. The quantization errors generated by this method are dependant upon the accuracy of the analogue to digital conversion and the subsequent division in software. The number of bits required to minimise these errors is determined by the dynamic range of the signals and the accuracy required at the low end of the dynamic range.

The technique requires extremely fast analogue to digital conversion of the signals, followed by an interface to a processor able to perform the rapid software division and memory increment. The technique has been used for a Wedge and Strip anode system by Siegmund et al. (1983), who report a count rate ceiling of 5×10^4 cs^{-1}.

3.3.2) Rise Time Delay

Two basic methods exist for the rise time analysis of pulse position. The time difference may be evaluated by the zero crossing method or the leading edge method.

3.3.2.1) Zero Crossing

This method evaluates the difference in the zero crossing time of the appropriately shaped input pulses. Zero crossing is dependant on the duration of the input signals, so for a one dimensional anode, the difference in zero crossing time for signals at each end of the anode will be proportional to position. This time difference can then be digitised to give the pulse position.

The method is intrinsically simple, and can be very fast in operation for anodes with suitable time constants. Use of this method has been demonstrated for a one dimensional anode by Parkes et al. (1974) who demonstrate useful resolution of 40μm in the central 60% of a 20mm field. The technique has been and extended to two dimensional anode systems by Lampton and Paresce (1974).

3.3.2.2) Leading Edge Rise Time

The leading edge rise time method compares delayed pulses to unattenuated, undelayed replicas of these pulses. Again the method is fast, involving simple components such as comparators, with

positional information coming from digitisation of the time value. The method has been discussed and demonstrated by Kinbara and Kumahara (1969).

Most two dimensional resistive anode systems have used one of the charge ratio methods to process signals. An important factor in the popularity of charge division analysis is the relative ease of optimising a charge division system to a particular anode, compared to that of optimising a timing system to an anode's RC parameters. In addition, use of circular arc terminated anodes requires that the charge ratio method of processing be used, in order to achieve near distortionless operation.

Pulse position analysis by timing methods has been shown to give rise to spatial nonlinearity, leading to a positional dependence of resolution. This is demonstrated by Mason et al. (1984), who report a variation in resolution of 70μm to 140μm from the centre to the edge of the anode in Exosat's imaging proportional counter.

3.4) Pulse Position Processing Electronics

The pulse position electronics utilises the charge division method of signal processing, and the successive digital approximation technique. It is an upgrade of the original system, which used logarithmic dividers to perform the charge ratio arithmetic, described by Rees et al. (1982). The circuit diagrams, provided by courtesy of ITL, are shown in figures 3-3(a) and

3-3(b).

A schematic illustrating the signal processing circuit configuration is shown in figure 3-4. The shaped pulses enter the main electronics at A,B,C and D where they are amplified and passed to sample and hold circuits comprised of FET switches. The four input signals are also summed to provide a combined signal which is then passed to upper and lower thresholding and peak position circuits. The threshold circuits are designed to limit processed pulses to those falling within a defined window of pulse heights. Thus large pulses which may represent coincident events are disregarded together with any other signals at a level which would be likely to saturate the system. The low threshold is designed to disregard signals arising from low level noise sources in the detector.

The signal submitted to the lower thresholding circuit causes a high speed comparator to change state at a predetermined level. Outputs from this comparator feed the ratemeter train and the strobe input of the peak position comparator which is fed with the differentiated total charge pulse. The comparator will change state at the crossover point, indicating the peak position of the signal. Output is enabled by the lower threshold strobe pulse and the positive going edge triggers a short monostable delay, the leading edge representing the peak pulse.

Figure 3-3(a): Circuit diagram for the main pulse processing electronics (courtesy of ITL).

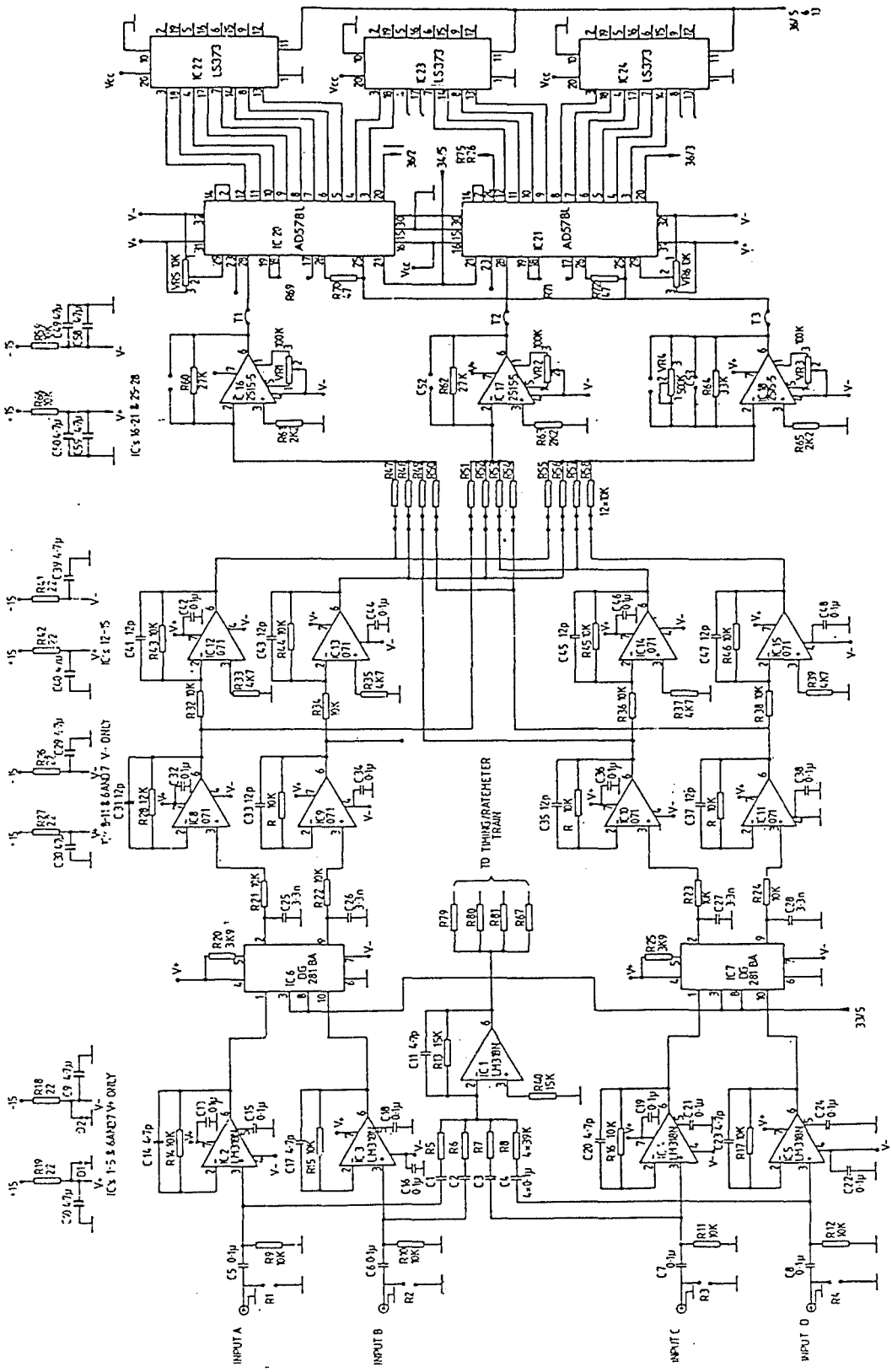

Figure 3-3(b): Circuit diagram for the timing and ratemeter electronics (courtesy of ITL).

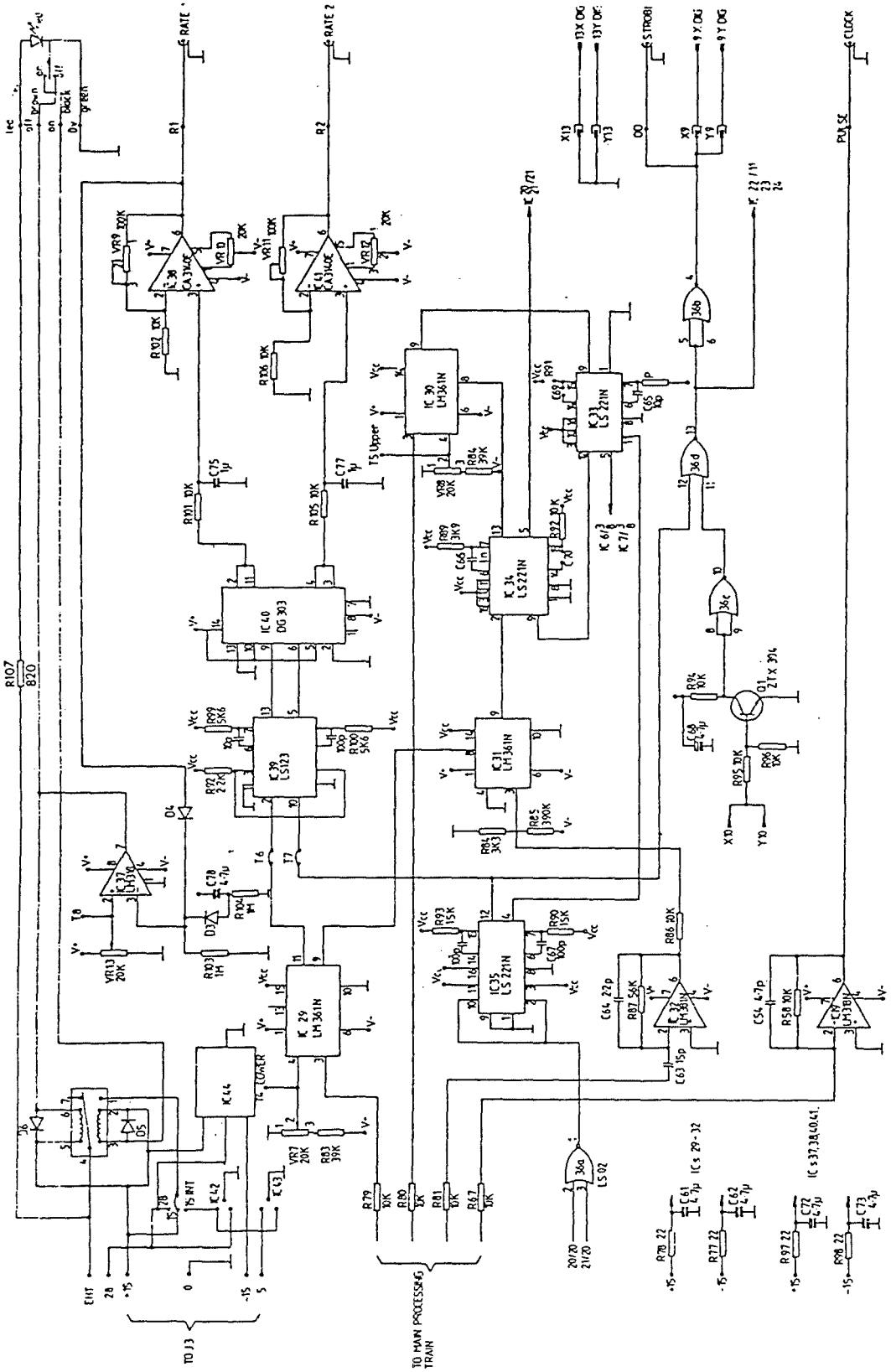

Figure 3-4: Schematic diagram illustrating the circuit operation of the main pulse processing electronics.

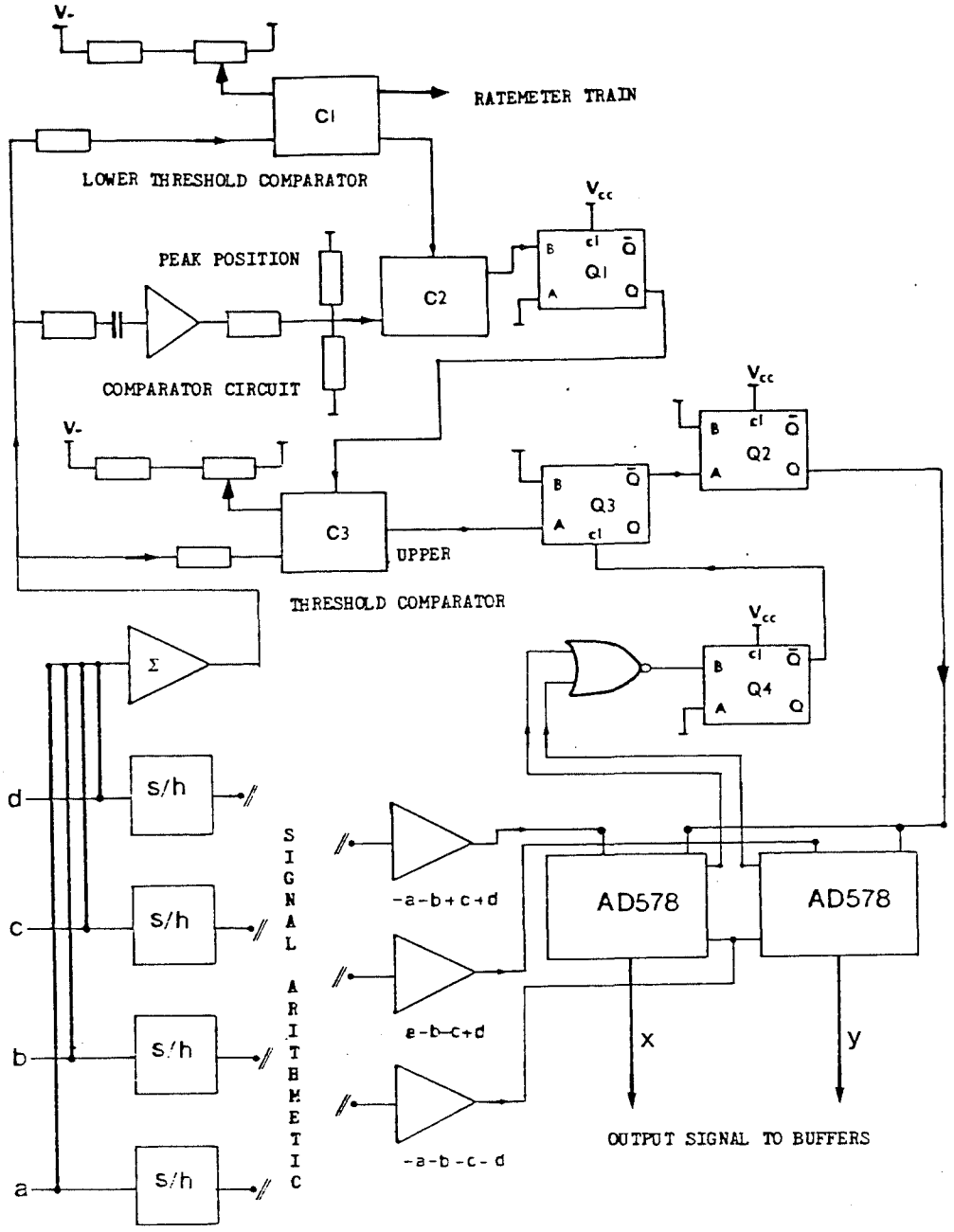

The upper threshold comparator is enabled by this pulse and triggered by pulses which do not exceed the predetermined upper level. This trigger provides a signal for a hold monostable controlling the sample/hold devices and triggers another monostable which enables the 'conversion start' of the ADCs.

The anode signals are then added and subtracted to give the numerators -A-B+C+D, +A-B-C+D and the denominator -A-B-C-D. These are then divided by 12-bit ADCs (AD578), with the denominator used as the reference input to these ADCs. At the completion of both conversions, on the trailing edge of the end of conversion signal (EOC), two short monostables are triggered. One feeds the ratemeter train and the output strobe circuit. The other sends a clear signal to the hold monostable which releases the sample/hold circuits from hold mode, and enables processing of the next pulse train. Figure 3-5 shows the timing diagram for this circuit.

The output buffers are enabled at the end of conversion, providing there is no inhibit signal from the interface. To provide the analogue 'X' and 'Y' positions the digital signals are taken off to two digital to analogue converters (DAC), followed by amplifiers to scale the analogue outputs from 0 to 10 volts.

3.5) Pulse Height Analysis

Following a suggestion by Edwin (1983), it was found that with a simple modification the processing circuitry could also be used to

Figure 3-5: Timing diagram for the main processing electronics with component identifications given in figure 3-4.

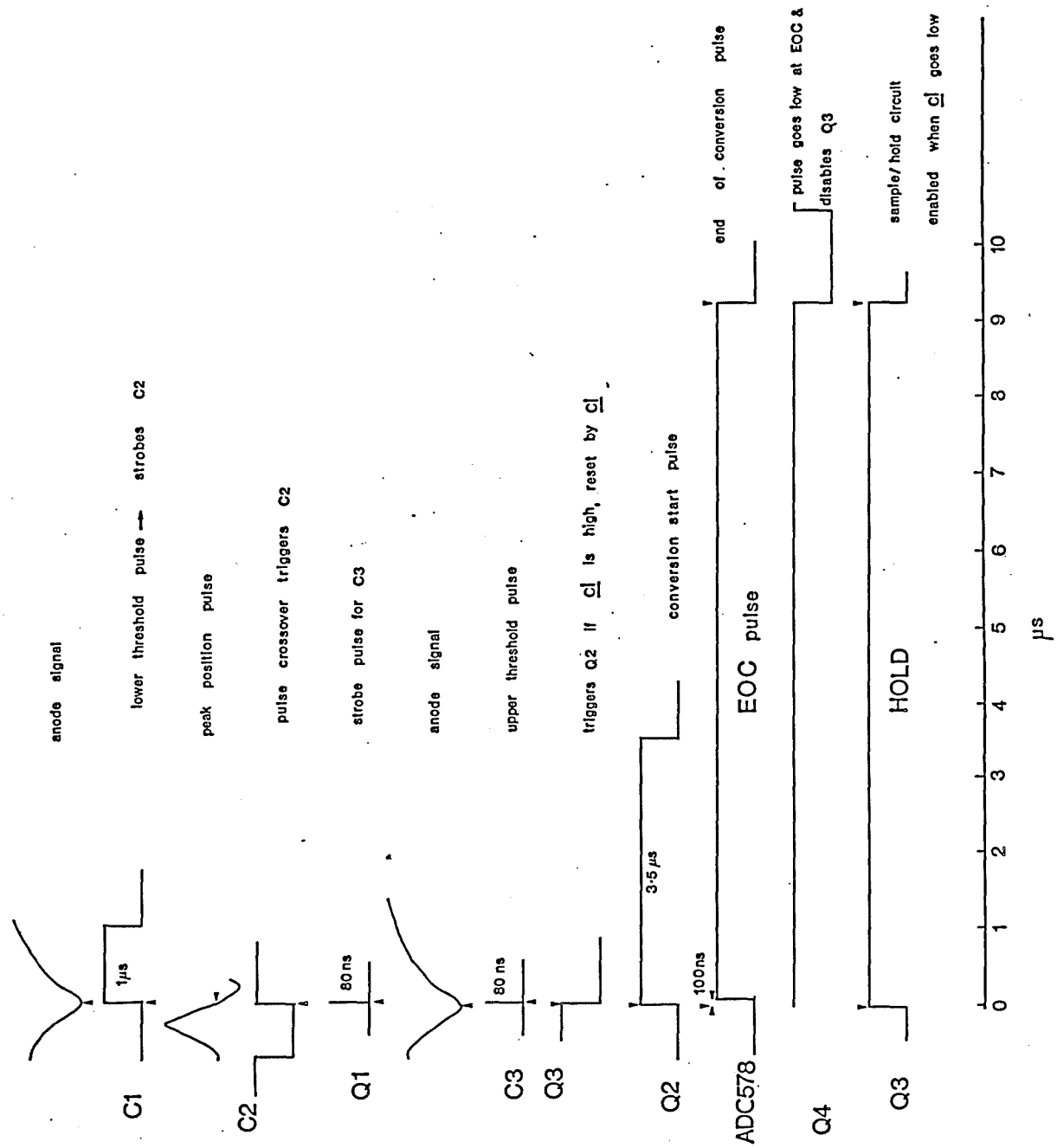

obtain detector pulse height distributions (PHD). The reference pulse of the 'Y' channel ADC, which represents the summed signal, is moved into the comparison input and the T2 input disconnected. The reference is then tied to a fixed ten volts. The ADC output will now give a ratio of the summed pulse heights to the reference voltage providing a convenient pulse height analyser. The modification was implemented with the addition of a few circuit board pins using wire wrap connections.

When operating in this mode pulse height distributions are integrated normally as detector images. Output from the 'X' channel is disabled by writing zeros to appropriate memory locations. The pulse height data will then appear in the first cross-section of the final image, while the remainder of the image is redundant. Typical pulse height distributions obtained with this technique are displayed in chapter 7.

3.6) Analogue Output

The ratemeter train provides outputs corresponding to different measures of pulse rates. Each circuit consists of a monostable followed by an analogue switch and operational amplifier to scale the output signal. The source of the two individual trigger signals, for each of the circuits, has already been established as that of the lower threshold strobe and the trailing edge of the EOC signal. Thus one ratemeter gives the count rate of all pulses passed by the lower threshold circuit, irrespective of subsequent processing, while the other registers the rate of processed events.

Thus in principle the number of large events rejected may be derived from the difference between the two ratemeters.

This circuit also monitors the count rate and if it exceeds a threshold set at 10^5 cs^{-1} the voltage supply for the EHT unit is tripped off. While providing some protection against over illumination, it may not prevent damage to the cathode and so care is still required in operating the detector.

3.7) ADC Operation

The 12 bit ADCs have a nominal conversion speed of 5.6 secs, though this may be slowed down by adjustment of the converters' timing circuits, or decreased by short cycling the converters to 10 bit operation. The grade of chip installed (AD578LN) gives guaranteed 12 bit accuracy for conversion speeds down to 3μs (Analogue Devices 1982). The maximum linearity error at 25^{o}C is quoted at $\pm$ 0.5 LSB (max), with the bipolar offset error of $\pm$ 0.25% FSR max.

The setup of the converters is very critical if optimum performance is to be obtained. The summing amplifiers (shown in figure 3-3 as IC16 to IC18) should be adjusted so that they do not provide an offset voltage to the converters. The lower threshold setting is particularly critical to the converters' operation as a consequence of the converters' internal adjustment arrangements.

In bipolar operation, the AD578 converter inputs an offset voltage to its internal comparator (Analogue Devices 1982), together with a 'zero adjust' voltage level to ensure conversion on the correct part of the transfer characteristic. For low signal levels, when operating in a ratiometric mode, the contribution from the zero adjust will become significant compared with the input signal. This was demonstrated by feeding appropriate signals, which simulated a single image point, into the electronics and varying the zero adjust resistor. The spot on the oscilloscope moves backwards and forwards diagonally from the centre, optimum adjustment being around the level where there is no spot movement. In view of this effect it is necessary to ensure that small pulses are not processed, so the lower discriminator should be set fairly high. In practice it was found that this did not conflict with setting the lower threshold on the valley of the pulse height distribution. The upper threshold setting must also be set so that it will not allow processing of pulses which will saturate the converters. The implications of these requirements, in terms of the loss of valid events, will be discussed in chapter 5.

3.8) Electronics Resolution Test

An estimate of the processing electronics contribution to the system resolution was obtained by investigating the processing of simulated input signals. A signal generator was used to simulate 0.5μs unipolar anode pulses at a count rate of 200 cs^{-1}. Equal signals were input at the equivalent of orthogonal anode terminals

A - C and B - D and then the test was repeated for all four terminals. In both cases, a zero numerator signal is produced and corresponds to an image point in the centre of the anode. The amplitude of the input pulses was also varied to give ADC reference pulses (ie. the denominator signal) ranging from 2 to 12 volts. This gives an estimate of the effect of a variable reference on the ADC conversion precision. To obtain reasonable sampling of the image points a 12 x 10 bit window was selected and the 12 bit cross sectional profiles used for analysis. The profiles obtained were analysed by fitting Gaussians to the profiles, using Starlink software.

The results for orthogonal inputs are shown in table 3.1 and illustrated as histograms in figure 3-6. The procedure was repeated at 15000 cs^{-1} to see if there was any major change in response and these results are shown in table 3.2. The results for four terminal inputs are presented in table 3.3. These results show that within a reference range of 5V to 10V the positional error introduced by the ADCs will be 1 to 2 channels FWHM in 4096. This would correspond to a FWHM of 1 bin in 1024 channels. When the reference voltage is 2 V the accuracy is degraded to ~3 bins FWHM. The 12 V level only appears to be slightly worse than that at 10 V, however the ADCs saturate at 12 V and the effects arising from saturation may introduce unknown errors. High count rates slightly broaden the profiles, although how much of this is due to pulse pileup effects resulting from the use of unipolar pulses is uncertain.

Figure 3-6: Histograms of electronically simulated image points for reference voltages; a) 10 V, b) 5 V, c) 2 V and d) 12 V.

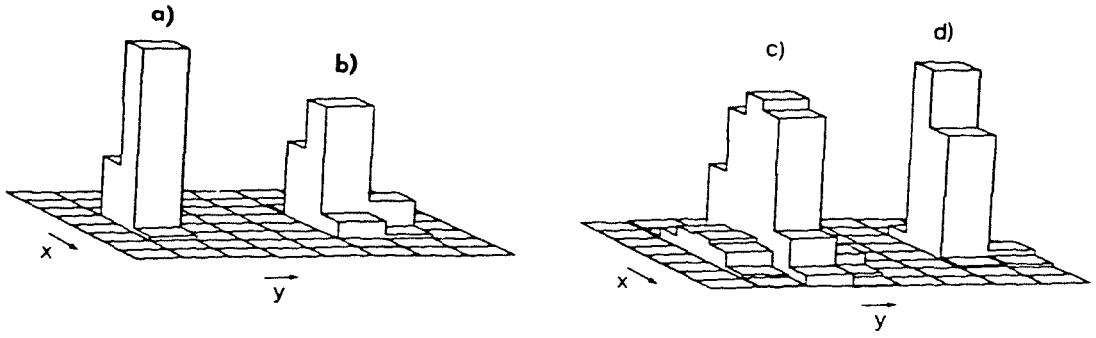

Table 3.1: Simulated image point widths for orthogonal inputs.

(a) 500 cs^{-1}.

Ref. (V)	Width (12 bit pixels FWHM)
10	1.3
5	2.1
2	3.1
12	1.4

Table 3.2: Simulated image point widths for orthogonal inputs.

(b) 15000 cs^{-1}.

Ref. (V)	Width (12 bit pixels FWHM)
10	1.5
5	2.1
2	3.3
12	1.4

Table 3.3: Simulated image point widths for four equal inputs.

(c) 500 cs^{-1}.

Ref. (V)	Width (12 bit pixels FWHM)
10	1.1
5	1.5
2	3.3
12	1.3

The image point location also gives an idealised simulation of real operation, where the voltage levels would be continually changing and the pulses bipolar. The results highlight the need for a good MCP pulse height resolution, since the accuracy of the signal processing is dependant upon the size of the summed pulse from the anode terminals.

3.9) Peripheral Hardware

Figure 3-7 shows the hardware configuration for the system at the telescope. The control computer is some distance from the dome, with about 30m of line necessary for the communication link with the detector. The diagram illustrates the deployment of analogue hardware and the power supply connections for the system.

3.9.1) Power Supplies.

The EHT unit supplied with the system is a Brandenberg 482BN and is mounted in the detector head assembly behind the pre-amplifier circuits. The unit is designed to provide up to 3.0 kV, but it became apparent after some initial work on the system that this was insufficient for a 40 mm device. This is mainly due to the voltage required for a saturated pulse height distribution with two 80:1 (l/d) micro-channel plates. It was also not possible to assess operation at higher proximity focussing voltages than those previously employed on these particular detectors eg. Rees et al. (1980, 1981).

Figure 3-7: Schematic diagram illustrating detector hardware configuration.

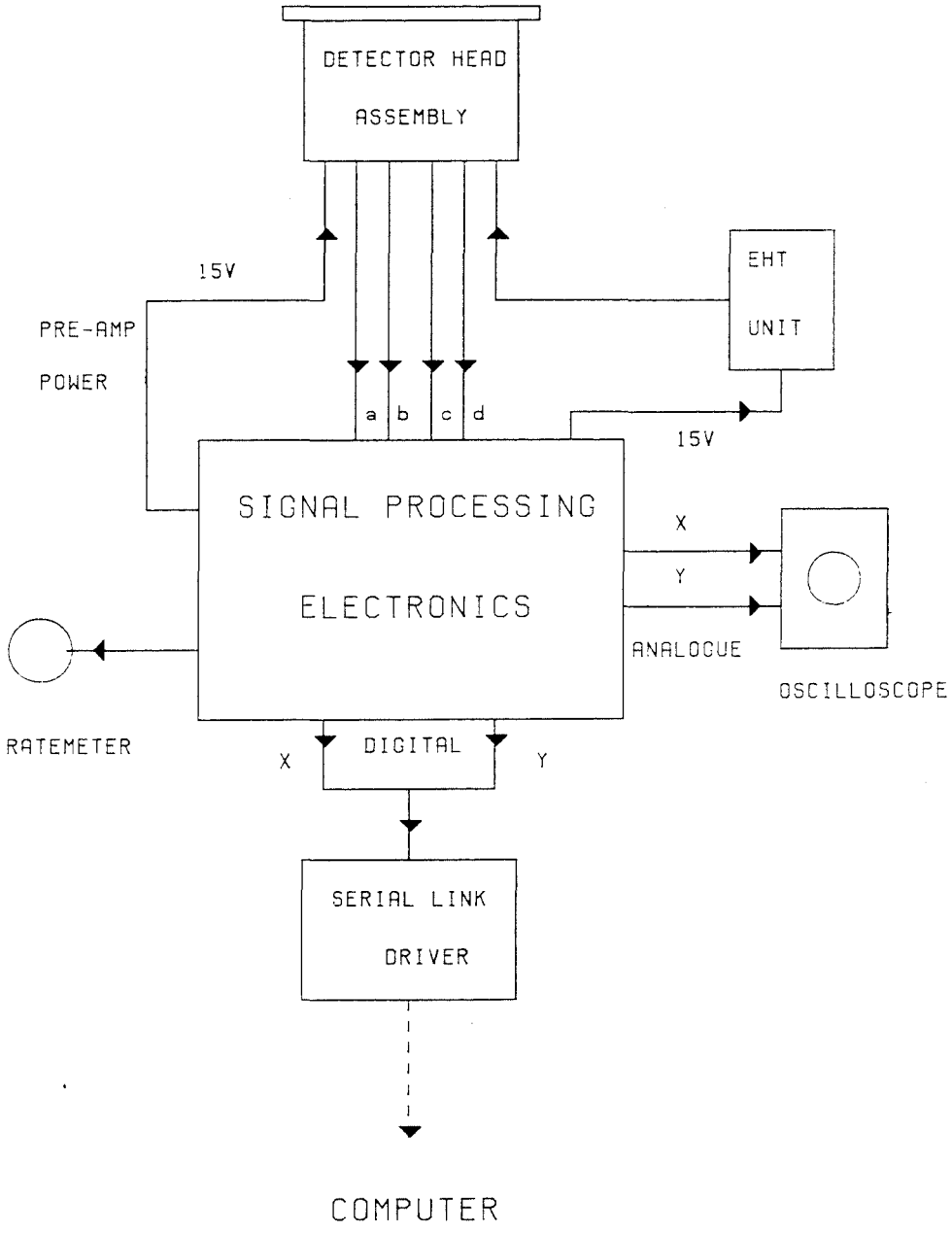

The unit was therefore replaced with a Hunting Hivolt Series-1 module providing up to 4.5 kV. The unit was too large to be placed inside the detector head assembly, so instead it is run in close proximity to the detector head. This module provides the necessary EHT required to run the detector and also incorporates a 'soft-start'. The unit takes a few seconds to achieve its full operational voltage and this is less traumatic in terms of stress on the tube.

Problems with pickup have been reported when the detector head leads, which carry the pre-amplifier signals to the main electronics, are too long (Rees 1982). The main electronics are therefore contained in two units, one holding the power supplies and the other the processing electronics. Thus the smaller processing electronics unit may be mounted on the telescope, close to the detector head, while the other, larger unit, may be positioned further away. Modifications for additional connections have been added to take 15 V rails to the processing electronics and the new external power supply. As mentioned in 3.6 the voltage rail to the EHT unit is tripped at count rates in excess of 100 kHz.

3.9.2) Image Acquisition and Display Hardware

The analogue outputs from the processing electronics are connected to a Tektronix 2213 oscilloscope with a standard short persistence P31 phosphor. This provides a real time display of photon events. The count rate from the detector is monitored by

means of a moving coil meter which may be connected to either of the two ratemeter outputs from the processing electronics.

Digital output from the processing electronics is sent to the control computer via a serial driver, designed and constructed by Mr D. Carr at the University Observatory. This converts the parallel input to serial output by means of a series of 8-bit shift registers. The serial receiver unit, which operates on the reverse principle, is interfaced to the windowing hardware unit. The serial driver units can function at count rates up to 100 MHz and so will not be a limiting factor on the overall system performance.

The windowing unit basically consists of a set of memories, into which are written all the event addresses necessary for a particular window. All incoming data is then rejected if its position does not fall within the window. The location of events falling within the window are then established by mapping the event positions, to determine the memory address to be incremented. The windowing unit is interfaced to the serial receiver and both are mounted on a circuit board fitted in a Camac crate which is directly accessible to the external memory. The control computer and the Camac crate unit are both located in the observatory data processing laboratory and are remotely linked through the serial driver to the detector system at the telescope.

Chapter 4

4.1) Computer System Hardware

The detector system runs under the control of an LSI 11/23 computer. Figure 4-1 shows a schematic layout illustrating the principle peripherals associated with the system. The LSI 11/23 is supported by three 2.5 MByte Winchester disk drives and a nine track dual density magnetic tape unit. A Fisher Controls Camac crate system which includes a Sension Camac external memory provides the interface between the detector electronics and the computer. Users interact with the computer via several VDUs, one of which functions as an operator terminal. The detector system is run from a BBC micro adapted to emulate a Tektronix T4010 graphics terminal, with a monochrome monitor. This terminal is installed in the telescope dome and connected via a line-driver to the LSI 11/23. Hardcopy output may be obtained by linking the terminal to a graphics workstation supported by a Tektronix 4612 hardcopy unit.

4.2) FORTH

The system is programmed exclusively in FORTH (Moore 1974), a language particularly suited to instrumentation control. FORTH is a high level language essentially built around a dictionary of fundamental words, which define the system. Additional words may be defined which are comprised of existing definitions and thus the

Figure 4-1: Schematic layout illustrating the main components of the IPD's computer hardware.

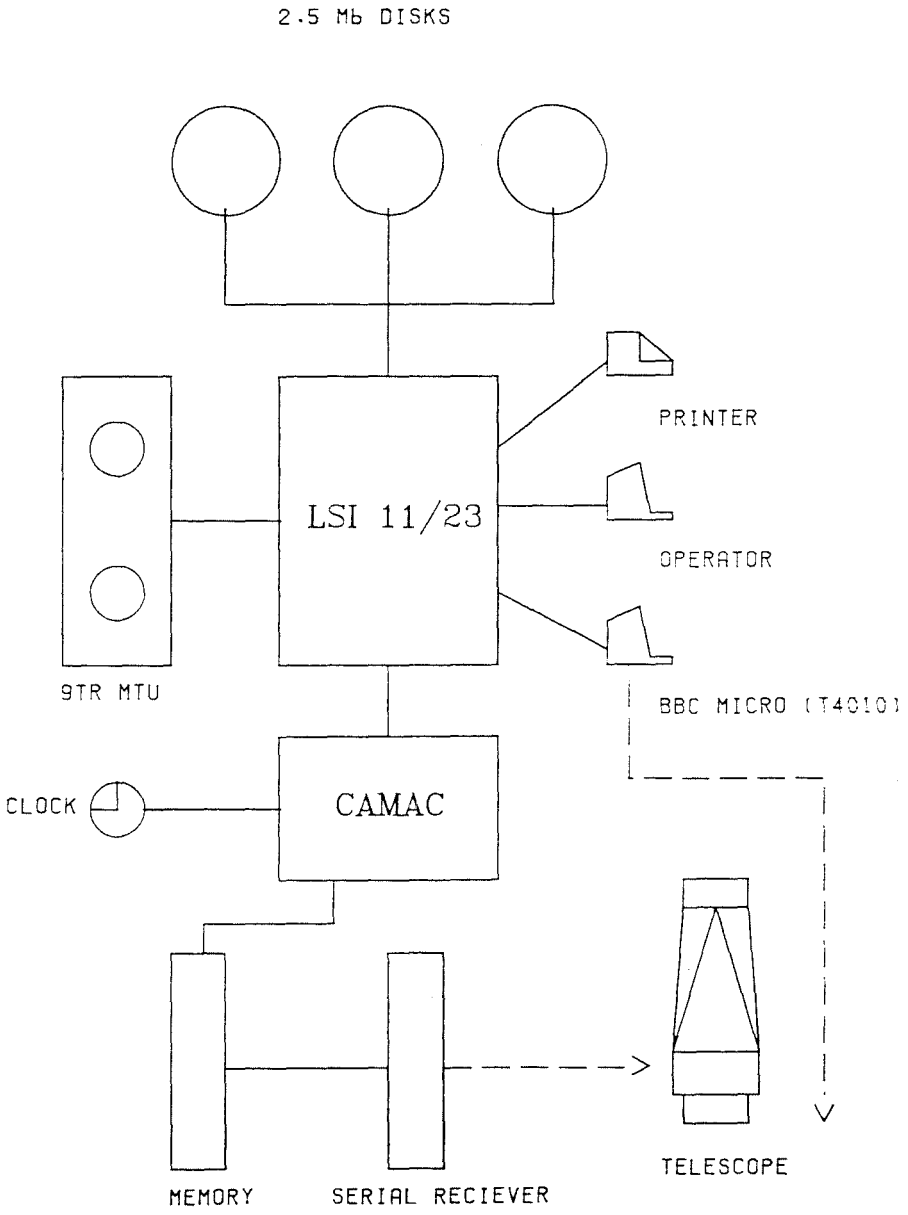

system vocabulary may be readily extended. Extended memory is provided by virtual access to 1024 byte disk blocks, which provide the basic format for all disk areas used by the computer. Parameters for the operations defined in FORTH words are manipulated on a stack using the reverse polish notation (RPN) method of arithmetic.

The flexibility and modularity of the language offers many advantages, including the ease of structured programming and especially the level of interaction possible with instrumentation. Since FORTH has no operating system it has been suggested that it may be more accurately described as a software environment for program development (Wright 1983).

FORTH has been used at several observatories either for direct instrument control (Moore and Rather 1974, Wright 1983) or related software engineering and maintenance applications (Pettini 1983).

The St Andrews FORTH system described by Davenhall et al. (1979) comprises a set of low level packages for graphics, magnetic tape support and Camac control operations. It resides on the first half of the system disk, shown schematically in figure 4-2(a) allowing the remaining space to be allocated to instrument control packages, development work and program work areas. This leaves the two remaining disk drives free for storage of data.

Figure 4-2(a): Allocation of space on the main LSI 11/23 system disk;

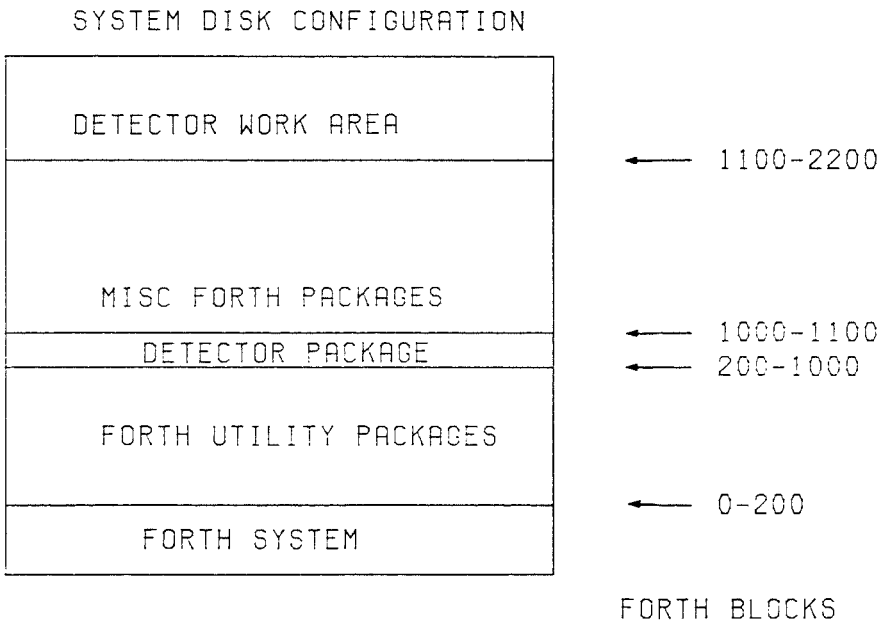

Figure 4-2(b): Storage format of detector images on data disks.

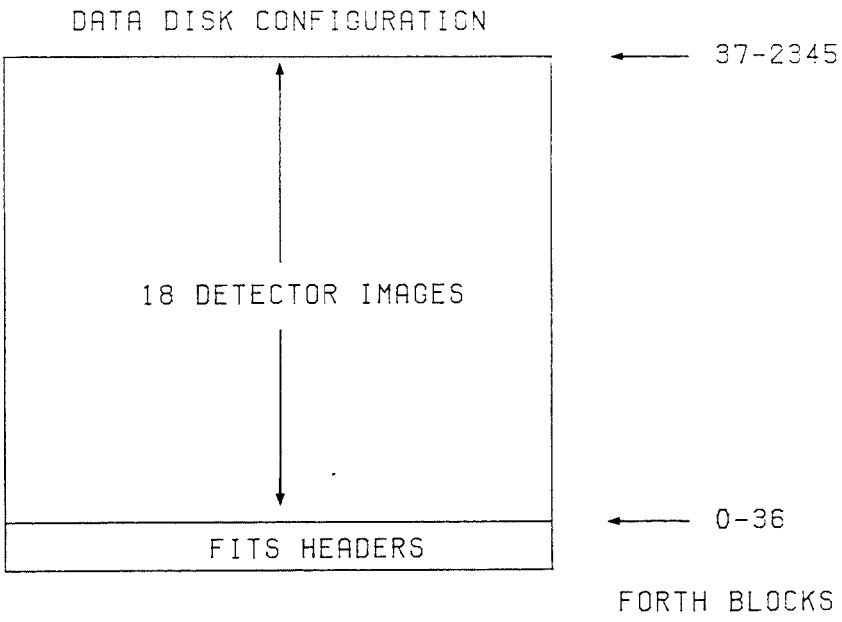

4.3) System Definition

The requirements for the detector control software are similar to those of other spectrographic detector systems, such as the SAAO Reticon detector (Lloyd Evans 1982). These fall into the four main categories of instrument control and monitoring, image display, storage of data, and instrument preparation routines.

The software must be able to set up and control the detector integrations either interactively or automatically and provide real time display of data. On line data reduction has not been considered since this would lead to a conflict of resources with the primary role of instrument control. This is due to the restricted speed and size of the LSI 11/23 computer and the practicalities of observing with a small telescope. The ease of data transfer to Starlink and St Andrews VAX computers negates any advantage in using the LSI 11/23 for data reduction. In addition the facilities of the Starlink system offer obvious benefits in terms of available software libraries, increased processing power and advanced image display terminals.

There are several technical constraints associated with the system which have a bearing on the design of a detector control package.

4.3.1) Hardware Resolution

The detector processing electronics provides a 12 x 12 bit output, allowing up to 4096 x 4096 pixels from the X and Y outputs respectively. The Autonomous Memory Control unit (AMC) in the CAMAC system is only capable of handling 16 bit words in direct memory increment mode. Thus it is necessary to throw away some of the least significant bits of the 24 bit total, output from the processing electronics. This imposes a limit of five pixel format configurations based on the possible combinations of the 16 bits. Figure 4-3 shows the detector pixel formats allowed by this limitation, the first three being interchangeable between the X or the Y axes.

4.3.2) Windowing

With all but the 256 x 256 pixel option there will be a rebinning of data in one axis. Some of the binned resolution may be recovered by the use of a hardware windowing unit designed by Mr D. Carr. This unit which forms part of the serial receiver contains two memories which are used to translate the X and Y addresses of events. The loading of these memories may be predefined, depending on the format required, so that events from only a certain section of the detector are counted and the location of the event recovered by memory mapping. Thus by windowing in only a certain segment of the detector, the full bit resolution possible in either axis may be retained at the sacrifice of some image area.

Figure 4-3: Diagram illustrating the pixel formats available utilising 16 out of 24 bits available from detector electronics.

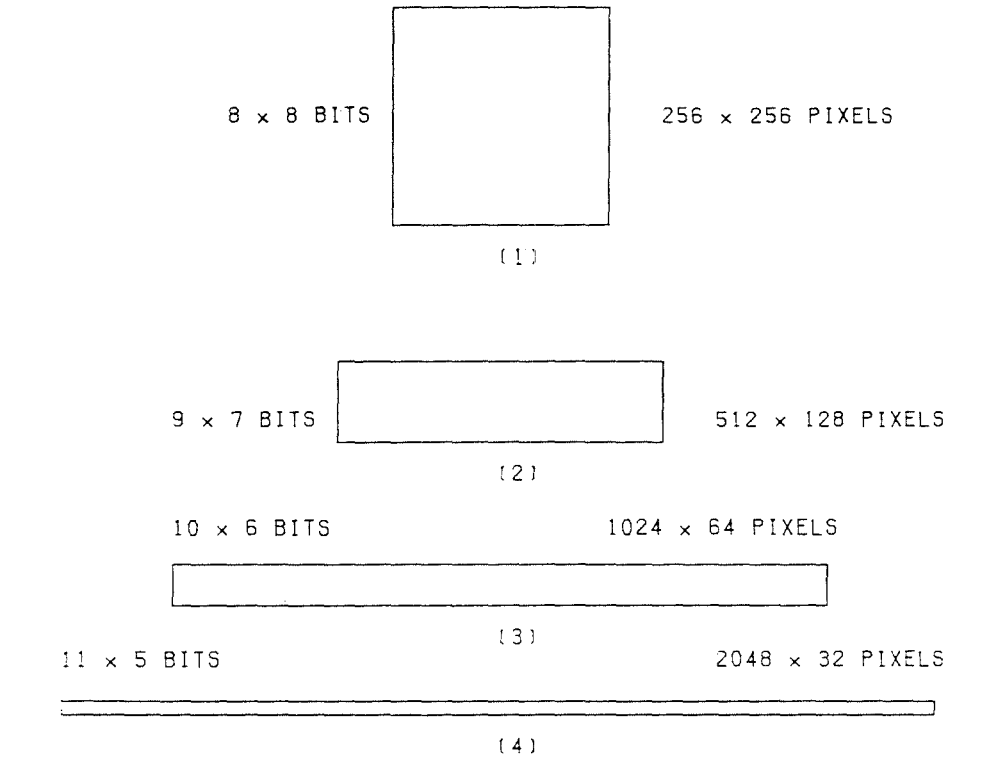

Windowing can only give the resolution available from the output of the detector processing electronics, therefore there are limitations on where the windows may be defined. Considering the detector output in terms of a 4096 x 1024 pixel grid, any of the five formats in figure 4-3 may be placed within this grid.

4.3.3) Dynamic Range

The LSI 11/23 is a 16 bit computer and the dynamic range of detector images will be limited to a maximum of 32768 counts per pixel. Should very long integrations be required, images can be copied to the LSI 11/23 memory and written to tape at pre-determined intervals, to avoid memory overflow.

4.3.4) Image Storage

With the combination of 2^{16} x 16 bit pixels, one detector image will require 128 Kbytes of memory for storage. This means that one 2.5 Mbyte disk, allowing sufficient space for storing image header information, will only hold 18 images. Tape storage of images is therefore an important requirement if any number of images are to be recorded at one time, or if long term storage is required. In addition to the use of tape as a storage medium, it is also required for transfer of data to Starlink and to St Andrews VAX computers so that the chosen format must be compatible with both functions.

4.3.5) Processing Time

The AMC takes 2 μs to increment an event address in the external Camac memory which limits the maximum event rate processed in this part of the system to 5×10^5 counts per second. This does not therefore have a dominant effect on the total processing speed, being 5x faster than the processing electronics.

4.4) Control and Image Display

The detector control package forms a section of the St Andrews FORTH system and is stored on the system disk, as shown in figure 4-2(a). A general work area in the top region of the disk is used to hold header information, observing logs, a calibration image and the Fourier routine's work area. A listing of the package's FORTH code is presented in appendix A, with explanatory information.

The main detector package is based around the St Andrews Forth system's routines and a CAMAC control routine, written by Mr J. Stapleton to increment the external Camac memory. Three additional modules loadable from the main program provide advanced one dimensional graphics and utility routines, for the display of spectra, disk and tape I/O, focus and alignment software. In addition, there is a package of general Fourier routines used by the focus and utility modules.

Using the LSI 11/23 memory to store integrating images it was found that running any other application overloaded and crashed the computer. This problem occurred because the AMC requires 4-5 μs to access the memory and running other applications resulted in a conflict of bus access. Thus the computer could not be used whilst integrating images, pointing to the need for an external memory unit.

With the external memory unit installed, integrations are started by enabling the CAMAC crate AMC, with the external Camac memory being used to integrate the detector images. This arrangement allows the computer to run other instruments through Camac at the same time, such as the Twin Telescope Photometer control system (Bell and Hilditch 1984).

The image being integrated may be copied at any time to the LSI 11/23 memory, where it may be accessed by the image analysis and display routines. Real time non-destructive inspection of the integrated image is therefore possible. Integrations may be halted without copying from external to internal memory or stopped with subsequent transfer to internal memory. Transfers from one memory to the other may be made in both directions, requiring <1 s per transfer. For optimum efficiency, the external memory is erased by wiping the internal memory and transferring it to the external memory. Integrations may either be started and stopped at the terminal, or an integration may be timed automatically for a preset exposure time.

The two dimensional display of images is achieved using a graphics package written by Davenhall (1983) for the analysis of microdensitometer scans of galactic plates. Four basic routines are available at a T4010 graphics terminal which display image data above a given pixel threshold.

Routine GRAY uses single shading to display any pixel above the given threshold and is the fastest of the routines, taking up to 100 seconds to plot an image of 256 x 256 pixels. IDT displays a contour map using one and two lines to shade successive grey levels of the image. DOTLINE and OUTLINE draw either dot or line contours between the threshold level pixels and at predetermined intervals after that. Sections of an image may also be plotted as hidden line isometric projections. These routines are all designed to plot data either directly, from the LSI 11/23 memory, or from image data held on disk. Typical output from the two dimensional display routines, illustrating an image of a USAF resolution chart at two different threshold levels, is shown in figures 4-4 and 4-5.

Upon loading the detector package, a default pixel format of 1024 x 64 is selected, without windowing, but this may be changed to any of the 5 formats shown in Figure 4-3, with the relevant display parameters changed automatically. If it is desired to window in an area of the detector, the window may be set up by cursor settings on a two dimensional plot, or direct input of the window coordinates.

Figure 4-4: A USAF resolution chart displayed at thresholds of 150 and 5 counts respectively, using GRAYSCALE display (a) and b), and IDT display (c) and (d).

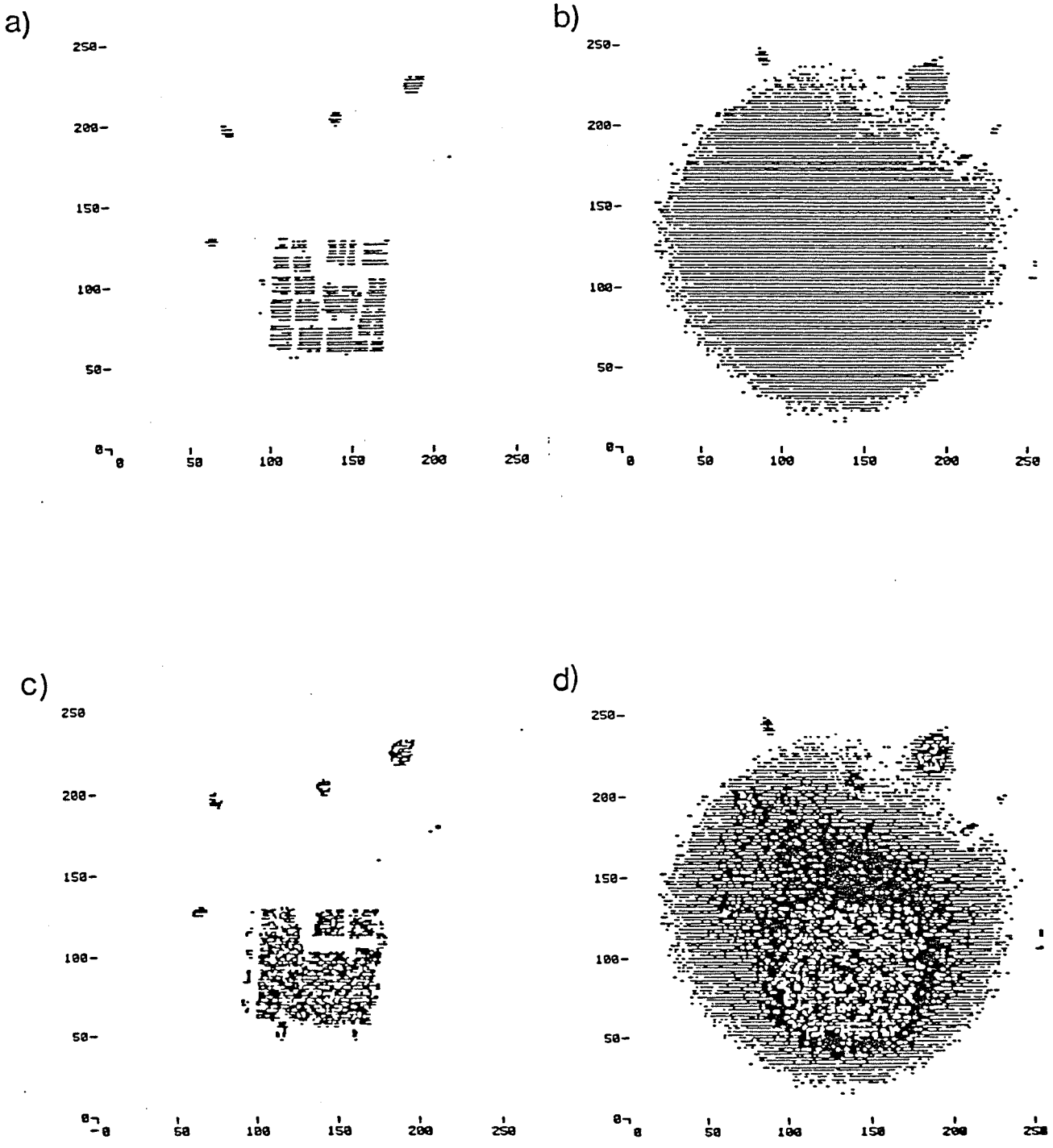

Figure 4-5: A USAF resolution chart displayed at thresholds of 150 and 5 counts respectively, using DOTLINE display (a) and b), and OUTLINE display (c) and (d).

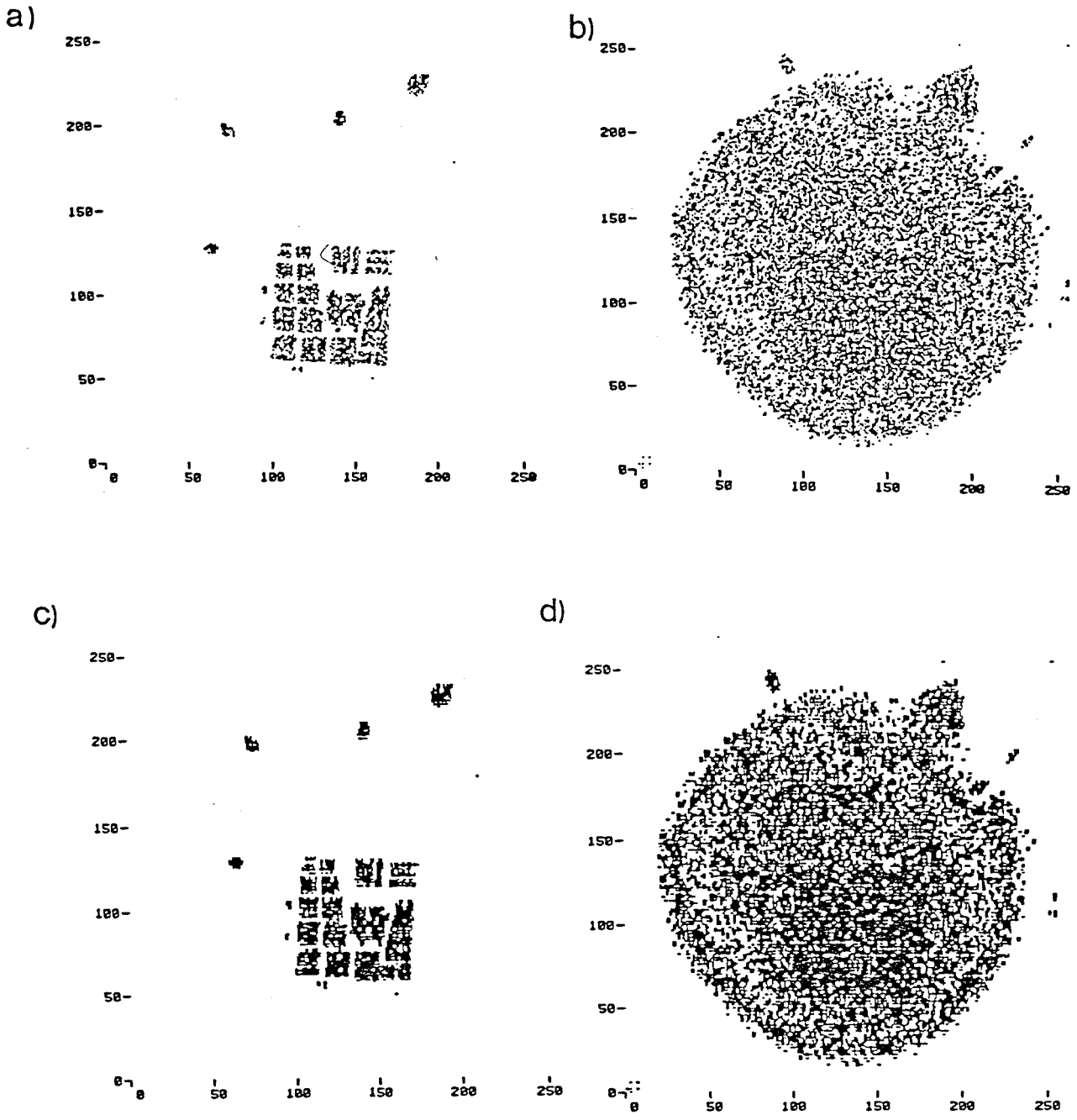

FORTH identifies commands from the first three characters and the word length, and differentiates between case. To reduce danger of accidental input of dangerous system commands, the main package commands were written in lowercase. Thus when the package is running, with the terminal set up appropriately, all commands other than detector package definitions will be ignored. This precaution provides some measure of protection for general users although in the long term, with the conclusion of package development, the use of a FORTH sealed vocabulary for the program would be preferred.

4.5) System I/O

The tape storage routines are again based on the existing St Andrews low level FORTH routines for magnetic tape handling. The format chosen for the writing of tape images was the FITS format (Wells et al. 1981). In this format images are stored to tape as files containing 2880 byte logical records, the first one or more of these records containing FITS header information written as 36 individual 80 character records.

The FITS format was chosen primarily for its portability. A considerable amount of software exists on Starlink facilities for reading and writing FITS files, and simple routines to read FITS files on the St Andrews VAX were easily implemented. The format also stores data in a relatively compact format, allowing typically 140 files to be stored on one standard tape. The header record

format allows a large amount of image information to be stored on the file, in a readily understandable format. Thus images written to tape are in a format suitable both for transfer to another computer and for long term storage, if required.

Table 4.1 shows the FITS header format adopted for the detector FORTH package. It incorporates mainly standard format headers with a few non-standard entries, which are specifically for recognition by the Starlink SPICA package. Users may also create their own FITS header files and use these if required.

While running the I/O package, object names for the FITS headers may be given and a comment of up to 80 characters added. One difference from the standard FITS format is that the data is written with 'reverse byte-swapped' integers, a feature of the DEC series architecture. This format is adopted because all the computers currently used for analysis of images are also DEC series machines. A simple algorithm could be implemented to re-order the byte-swapped integers, should this be necessary.

The tape handling package also incorporates several simple routines for skipping over FITS files already on a tape, for reading headers and for the accounting of images recorded. Whilst images are being written to tape, FITS headers are displayed and a copy may be sent to the printer.

Table 4.1 : Example of a detector system FITS header.

```
SIMPLE   =                    T /
BITPIX   =                   16 /  16 BIT UNSIGNED INTEGERS
NAXIS    =                    2 /  TWO DIMENSIONAL DATA
NAXIS1   =                 1024 /  X AXIS PIXELS
NAXIS2   =                   64 /  Y AXIS PIXELS
BSCALE   =                  1.0 /  SCALING FACTOR
BZERO    =                  0.0 /  ZERO OFFSET
BUNIT    = 'COUNTS'             /  BRIGHTNESS UNITS
DWELL    =                  120 /  INTEGRATION TIME (SECONDS)
TIME-OBS = '23:11:34'           /  INTEGRATION START TIME
DATE-OBS = '11:03:84'           /  DATE OBSERVED
FORMAT   = 'DEC    '            /  BYTE-SWAPPED DATA (SIMPLE=F)
INSTRUME = 'LRT_IPD'            /  ST ANDREWS SPECTROGRAPH+IPD
OBJECT   = 'HD12029'            /  OBJECT IDENTIFICATION
COMMENT  = Radial velocity standard star- obsv 01
END
```

Note: FORMAT and DWELL are keywords recognised by St. Andrews and Starlink software.

Disk storage of images follows the format indicated in figure 4-2(b), with FITS header information stored at the bottom of the disk, followed by 18 image files. The system is designed for optimum speed of storage and access of images, and allows the images to be written directly to tape as FITS files with their original headers at a later time if necessary.

Images may be displayed by recalling them by file number (1-18), to the LSI 11/23 memory, or if necessary, accessing them directly on disk. There is also a facility to write images to disk starting from a given FORTH block number, although this method is slower and less efficient.

4.6) System Utilities

The main core of these routines is geared to the display of imaged spectra and other routines required for astronomical observations. The graphics routines are essentially designed to allow display of one dimensional slices in either direction through an image. For astronomical work a spectrum will be imaged onto the detector window and lie over several cross sections.

The basic one dimensional routines have been enhanced to display one or more summed cross sections with automatic scaling and biassing of the resulting spectrum. The number of cross sections to be summed can be set up manually or by cursor from a grayscale plot of the image. The contents of the LSI 11/23 memory alone or the

external memory (copied into the LSI 11/23 memory) may be displayed as intensity versus bin number in one of three modes. These modes give either histogram, joined line or dot plots with the whole X axis or just a section (minimum of 20 points) being used. Scaling of the images can be either from zero or the minimum, to the maximum number of counts in the selected region. If the number of counts in a summed bin exceeds the 16 bit precision limit, the plot is halted and an error message given.

There is also an option to apply smoothing to the displayed spectra by means of a 3, 5, or 7 point running mean with a triangular window (Bevington 1969) of the form

$$F'(x) = \sum_{i=x-n}^{x+n} w(i)F(x), \qquad (4.1)$$

where n = 1,2 or 3.

This feature was incorporated to provide real time assessment of data and for this reason, the running mean method has been employed. The algorithm is especially suited to the graphics routines, where data points are accessed in memory, manipulated according to a previously defined plotting function, and displayed. Thus it is relatively easy to sum the cross sections for each X axis bin and apply a running mean smooth to the data as the plotting is done. In consequence this method is both fast, requires no work area and does not modify the image in memory in any way. Figure 4-6 shows the terminal display for a spectrum with each of the four filtering options.

Figure 4-6: Stellar spectra of SX Aur showing the spectra displayed for; a) unsmoothed b) 3 point smooth, c) 5 point smooth, d) 7 point smooth.

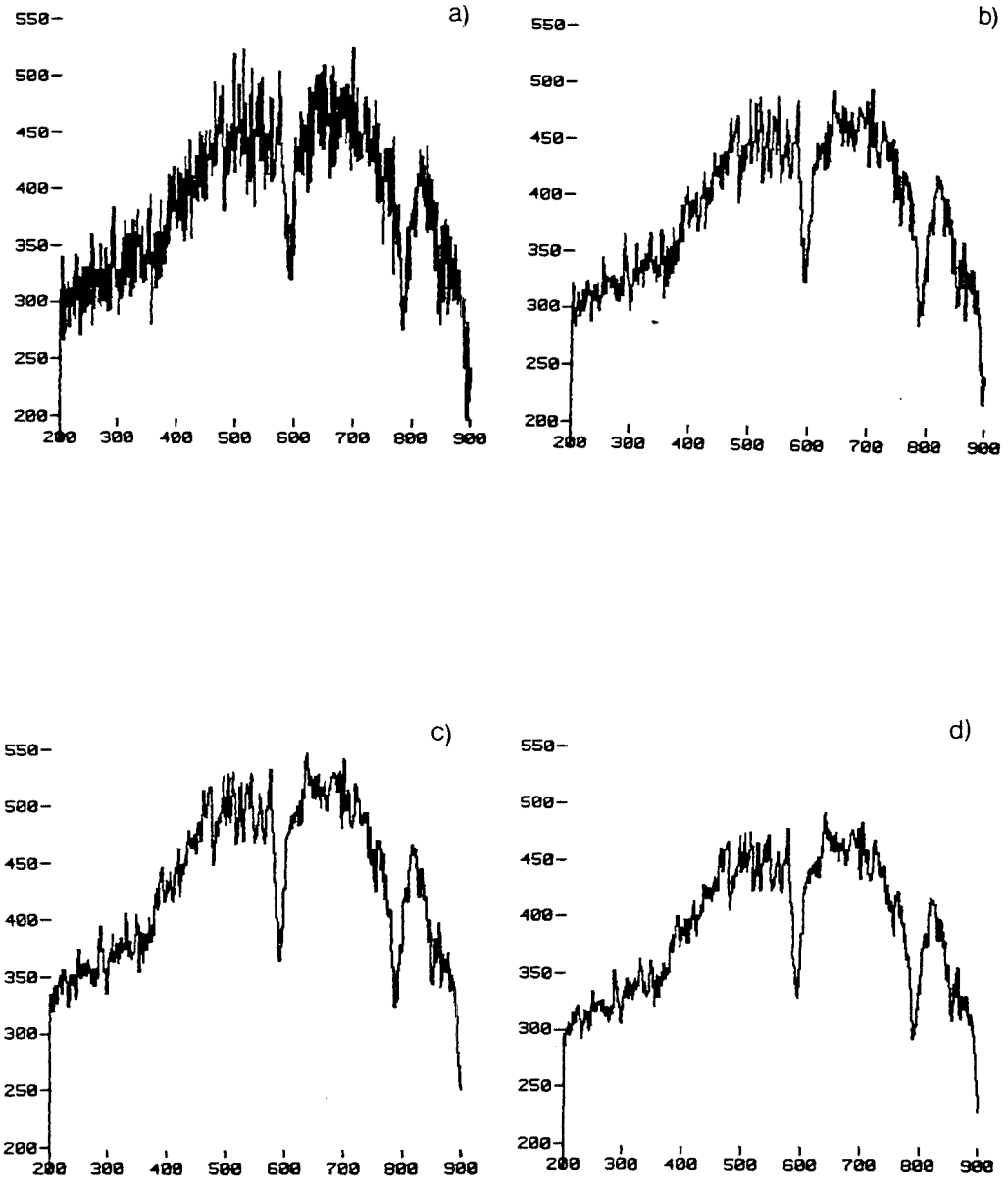

While observing, the user may require to see the build up of a spectrum together with relevant information regarding an integration. There are several FORTH words to give a repeated update of the current image together with a display of the current integration time. The required display parameters may be selected together with a refresh rate for the display. Thus the user may monitor the progress of the observation while guiding the telescope, for instance.

Single or summed cross sections may also be extracted and stored to a section of the package work area or another disk as one dimensional spectra for later use.

The flexibility of such a FORTH programmed system means that sequences of operations may be defined as new words at the users' discretion. Thus an operation such as recording a comparison arc spectrum, for a pre-determined exposure time, labelling the header and writing it to tape or disk may be defined.

4.7) System Preparation

The main routines in this module are those used to prepare for an observing run on the telescope and for alignment of the detector, when it is installed on the spectrograph.

4.7.1) Alignment

When the detector is installed on the telescope it is necessary to align the detector's X axis parallel with the dispersion direction of the spectrograph. For this purpose the detector is mounted on the spectrograph with a special fitting enabling fine rotation of the detector head by means of a micrometer.

The coarse rotation setting may be found by the display of a comparison arc spectrum and adjustment of the detector head until the arc lines are perpendicular to the dispersion direction. Fine adjustments may be obtained by using a routine which cross-correlates selected cross-sections of the arc spectra, to indicate the shift between them due to misalignment. The head assembly may then be rotated to determine a minimum shift between the cross-sections.

4.7.2) Focussing

Prior to an observing session the spectrograph must be focussed. This is best achieved by using the spectrograph's copper-argon comparison arc spectra. The optimum focus may be determined either from the average width of the comparison arc lines, or by using the Hartmann focus shutter. Both methods employ Fourier techniques, either to perform an autocorrelation of an arc spectrum, or the cross-correlation of a pair of Hartmann focus exposures. Because of the extensive use of Fourier techniques in

these procedures a suite of routines was written in FORTH to perform fast Fourier transforms, auto-correlation and cross-correlation of detector data cross sections.

4.7.3) Fast Fourier Transform (FFT)

The discrete Fourier transform of a spectrum of N equally spaced points, where N is a power of two (Wintz and Gonzalez 1977), may be represented by

$$F(u) = \sum_{x=0}^{N-1} F(x)\exp[-2i\pi ux/N], \qquad (4.2)$$

for u=0,1,2,...,N-1.

A FORTH algorithm to implement a FFT for one dimensional spectra was already available (Stewart 1983). A complete routine was written utilising this algorithm, together with routines to extract and prepare data for a FFT (Bendat and Piersol 1971). The data are extracted directly from single or summed cross sections of an image held in the LSI 11/23 memory and written to a work area on the system disk.

The routine is designed to run with any size of array up to 4096 points, the data being extended by zeros if the number of points is not an integral power of two. Typical transform times are 200 seconds for a 4096 point array, 40 seconds for a 1024 point

array and 10 seconds for a 200 point array. Figure 4-7 shows the Fourier transform of an arc spectrum of 512 points.

4.7.4) Cross-correlation

The use of cross-correlation techniques in astronomy has grown in recent years mainly as a method for the determination of doppler shifts in spectra, both in analogue (Griffin 1967) and digital applications (Tonry and Davis 1979).

The cross-correlation function is an expression of the convolution integral. For two real functions g(x) and h(x), whose Fourier transforms are g(u) and h(u), it is defined as

$$c(x) = g(x) * h(x) = \int_{-\infty}^{\infty} g(u-x)h(u)du. \qquad (4.3)$$

For two spectra g(n) and h(n) of N points in length, whose discrete Fourier transforms are G(k) and H(k), where from (4.2)

$$G(k) = \sum_{n=0}^{N-1} g(n)\exp[-2\pi ink/N], \qquad (4.4)$$

the normalised cross-correlation function may be defined as

$$c(n) = S_1 \sum_{m=0}^{N-1} g(m)h(m-n), \qquad (4.5)$$

where S_1 is the normalising factor $1/N\sigma_g\sigma_h$ with σ_g and σ_h the rms of the spectra ie.

Figure 4-7: Diagram showing the discrete Fourier transform of a comparison arc spectra, where the first 512 points are the real part of the transform and the remaining 512 are the reversed imaginary part of the transform.

a)

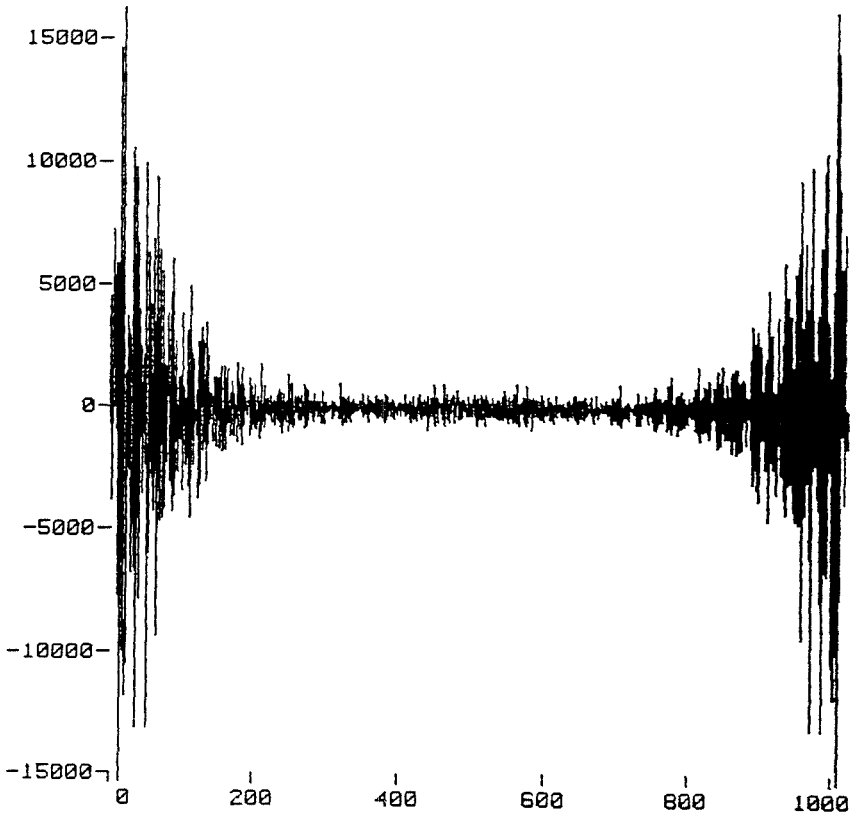

Figure 4-8: Diagram showing the cross-correlation function of two comparison arc spectra.

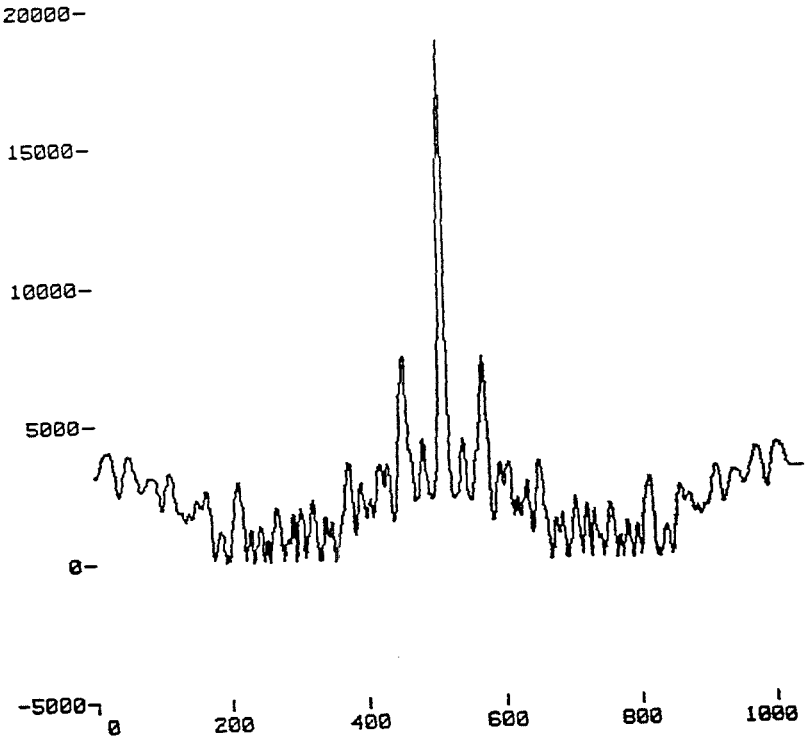

$$\sigma_g^2 = \frac{1}{N}\sum_{n=0}^{N-1} g(n)^2. \qquad (4.6)$$

The function will have a maximum value of one at the point where n is equal to the shift between the two spectra. Thus in principle the technique may be used to obtain the shift between two spectra by determining the point at which the function is at a maximum.

The convolution is best calculated in the Fourier domain where the function reduces to

$$C(k) = S_1 G(k) H^*(k) \qquad (4.7)$$

Thus in the Fourier domain the convolution may be readily calculated as the product of the transform of one spectrum with the complex conjugate of the other. With the availability of an FFT routine the procedure may be easily implemented. The function c(n) is then obtained from the inverse transform of C(k).

The cross-correlation routine written obtains the shift between spectra by first searching for the peak of the function c(n). The function is then rotated, with the array ends wrapped around, so that the peak lies in the central pixel of the array. It is then fitted with a parabola using a routine from McClean (1981) and the FWHM of the peak calculated. The calculated shift and FWHM are displayed and stored if necessary. A typical cross-correlation function of two arc lamp spectra is shown in figure 4-8. Processing speeds are typically 100 seconds for two 1024 point spectra with faster times for shorter spectra or segments of spectra.

The cross-correlation uses four working arrays, two to hold the transforms of the two spectra to be analysed, one for the cross-correlation function and one to hold the rotated correlation function. Autocorrelations are obtained by copying the transform of the spectrum under study to the second transform array. The routines have been tested by analysing detector data with similar routines incorporated in Starlink reduction packages, which will be discussed in due course.

4.8) Alignment Routine

The alignment routine runs as an interactive package, issuing user prompts as necessary. Having been loaded the user is prompted for the cross-sections and sections of the spectra to be correlated. This may be done by using the cursor to delimit the spectra. The user is prompted for a micrometer setting for the detector rotation and then the routine performs an integration, cross-correlates the relevant cross-sections and displays the results. The cross-correlation function may be displayed if necessary. The routine then repeats this sequence until the user is satisfied with the alignment. Results of the tests are held in a table and may be examined at the end of each correlation.

4.9) Hartmann Focus Routine

The focus routine runs as an interactive package, in the same way as the alignment routine. Upon loading the package, the user is

prompted for an arc integration time and allowed to select the section of arc spectrum to be used for the focus test. The observer is then prompted for a focus value and then asked to select the relevant Hartmann shutter dekker setting, an integration is done and then the next shutter setting is prompted for. Having recorded the spectra for the two Hartmann shutter settings, the spectra are cross-correlated and a value for the shift and FWHM are displayed. The user may then continue on to another focus setting and repeat the operation. At the end of each focus test the user may display a table giving the focus data already obtained and if required, change the section of arc being used.

4.10) Autocorrelation Focus Routine

This routine is similar to the previous routine, except that dekker settings need not be changed each time; there is a prompt only for a new focus setting. Again at any time the user may change the limits of the arc spectrum to be auto-correlated, on the basis of the displayed results. The width of the auto-correlation peak is $2^{1/2}$ times the FWHM width of the lines in the spectrum (Gaussian approx.), so the routine can also be used to estimate instrument resolution from unblended arc lines.

4.12) Further Applications

Because of the nature of the FORTH language, the package can be readily extended to include front end packages to run other spectroscopic detectors, such as a Reticon, on the St Andrews

system. With appropriate maintenance the package should also be portable and could be installed on other FORTH based computers, with the addition of suitable hardware interface routines.

4.13) Image Analysis

The analysis of detector images and reduction of observational data has been carried using Starlink software. This approach, as already discussed, is advantageous in terms of the range of software and hardware peripherals available together with the benefits of larger computers.

The two main packages used for the reduction of data were the Starlink ASPIC and SPICA programs. SPICA is a spectral reduction system, and is designed for the analysis of two dimensional images containing spectral data. ASPIC is a set of routines for the handling and reduction of large images from two dimensional detectors. Both programs interface with an advanced raster display colour terminal, for the two dimensional display of images with suitable colour or intensity coding.

Chapter 5

5.1) Photocathode Hotspots

The appearance of field emission hotspots in proximity focussed image tubes arises from the combination of high electric fields and small component spacings. Photocathode hotspots are believed to be a result of microscopic photocathode asperities which cause localised intensification of the electric field leading to field emission. Together with field emission from mounting assemblies, they can be a major problem in proximity focussed tubes (eg. Cromwell et al. 1985). Cochrane and Thumwood (1976) reported hotspots on S20 photocathodes due to breakdown across cathode asperities for field strengths of the order 5.5 $kVmm^{-1}$. Contaminants introduced during processing are thought to be the main cause of these asperities, although whisker growth from the migration of alkali metals on the photocathode has also been proposed (Goodson et al. 1972).

Following delivery of the IPD, initial tests revealed the existence of several field emission hotspots. Lowering the proximity focussing potential below the dead voltage of the input MCP oxide layer (200 V) caused the emission spots to disappear. This confirmed the primary source of these features to be the photocathode. The overall dark noise was very high, with one field emission spot in particular, found to be the main contributor. In

view of the experimental nature of the tube and the timescale for reprocessing it was decided to attempt removal of the hotspots by treatment of the tube. The standard procedures for the removal of hotspots at ITL involve ageing the photocathode and the application of high voltages to the photocathode. Ageing the tube is designed to burn off or stabilise the photocathode hotspots. The application of high voltage is intended to cause field breakdown across the photocathode to MCP gap at the asperity.

Ageing for several hours with a gap voltage of 800 V was found to have little effect upon the main hotspot, although some small spots were neutralised. Applying high potentials across the gap, in order to allow the photocathode to draw a relatively large current was also unsuccessful, with no breakdown occurring. A variation of this technique is to discharge a large capacitor across the photocathode gap and this method was found to be successful in neutralising the dominant field emission feature.

The penalty incurred with such techniques is a possible degradation of the photocathode performance. The two main mechanisms which can cause damage are the lowering of the vacuum pressure within the tube by vaporised material and damage to the input MCP face if a breakdown occurs. Preliminary examination of the tube, following treatment, indicated an area of very low sensitivity in the region where the large hotspot had previously been located, with a corresponding dark spot visible on the photocathode surface. There was no evidence of any major activity which would have indicated serious damage to the MCP. Several

smaller hotspots remained, although less active than their counterparts prior to treatment.

While these features are undesirable, they are not well understood. It is of value to investigate them in some detail, in order to assess the overall effect on the detector performance. Figures 5-1 and 5-2 show Optronix photographs of detector dark noise images obtained at proximity focussing voltages of 300 V and 420 V respectively, after the tube had been operational for a year. The images are photographic reversals and have been scaled to the peak data value in each image. This means that only prominent features such as hotspots are displayed, with the background noise resulting from photographic processing. The MCP potential was adjusted to be 3.35 kV in both cases, so that any differences between images should be due to the photocathode bias alone.

All of the features are evident in both images, but the severity increases at the higher proximity focussing voltage. The largest hotspot, labelled (b) in 5-2, is of particular interest since it shows evidence of channel paralysis in the MCP. Figures 5-7(i) and 5-7(ii) show profiles of the feature at gap voltages of 300 V and 420 V respectively. The profile at a gap voltage of 420 V shows a deep core corresponding to the position of the centre of the profile peak seen in the previous diagram. This indicates that the hollow centre of the hotspot feature appears as the gap voltage increases and is not a photocathode dead area. The profile width at 300 V is ~4.5 bins at FWHM and has a peak count rate of $1\ cs^{-1}pixel^{-1}$, where the pixel size corresponds to 160 μm at the

Optronix Photograph Captions

Figure 5-1: Dark noise image obtained with proximity focussing voltage of 300 V, with integration time of 900 s and pixel format of 256 x 256. Emission features are labelled (a) to (e).

Figure 5-2: Dark noise image obtained with proximity focussing voltage of 400 V, with integration time of 900 s and pixel format of 256 x 256.

Figure 5-3: Dark noise image obtained with proximity focussing voltage of 300 V showing breakdown activity in feature (a). Integration time of 900 s and pixel format of 256 x 256.

Figure 5-4: Dark noise image obtained with proximity focussing voltage of 420 V early in detector tests. Integration time of 900 s and pixel format of 256 x 256.

Figure 5-5: Flat field image obtained with proximity focussing voltage of 420 V, integration time of 900 s and pixel format of 256 x 256.

Figure 5-6: Dark noise image obtained with proximity focussing voltage of 300 V early in detector tests. Integration time of 900 s and pixel format of 256 x 256.

Figure 5-7: Profile of feature (b) at proximity focussing voltages of, (i) 300 V, (ii) 420 V.

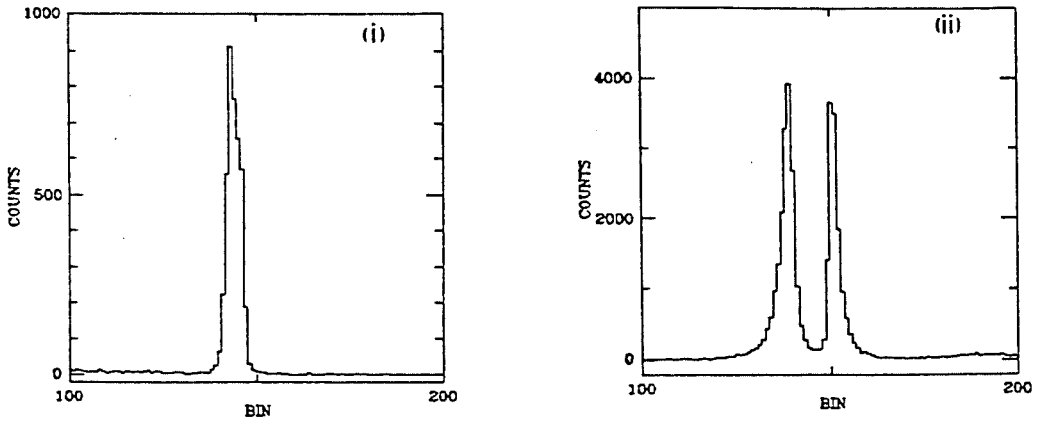

Figure 5-8: Profile of feature (d) at proximity focussing voltages of, (i) 300 V, (ii) 420 V.

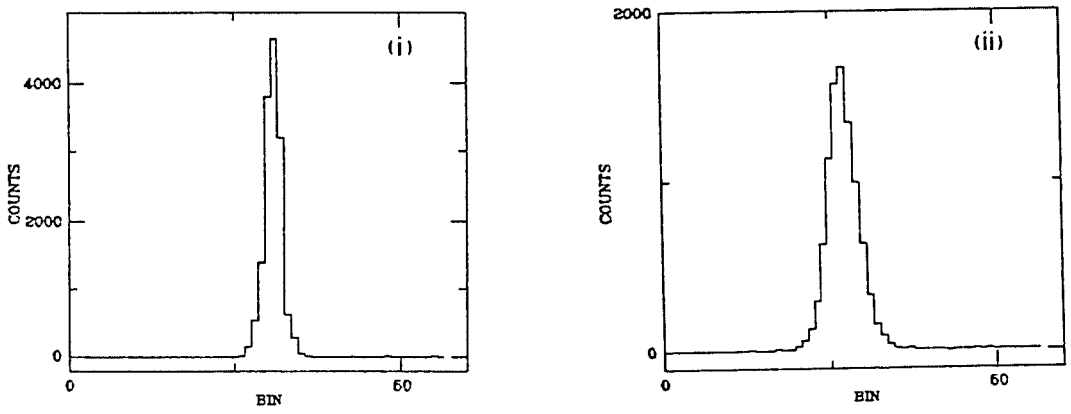

Figure 5-1

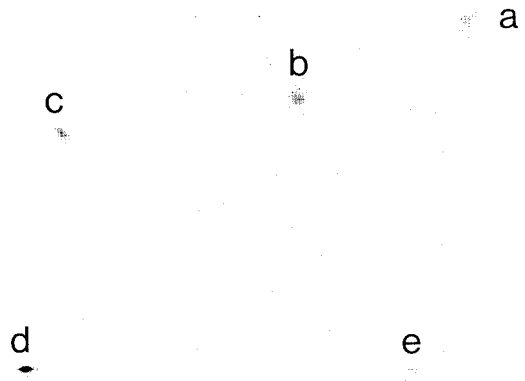

Figure 5-2

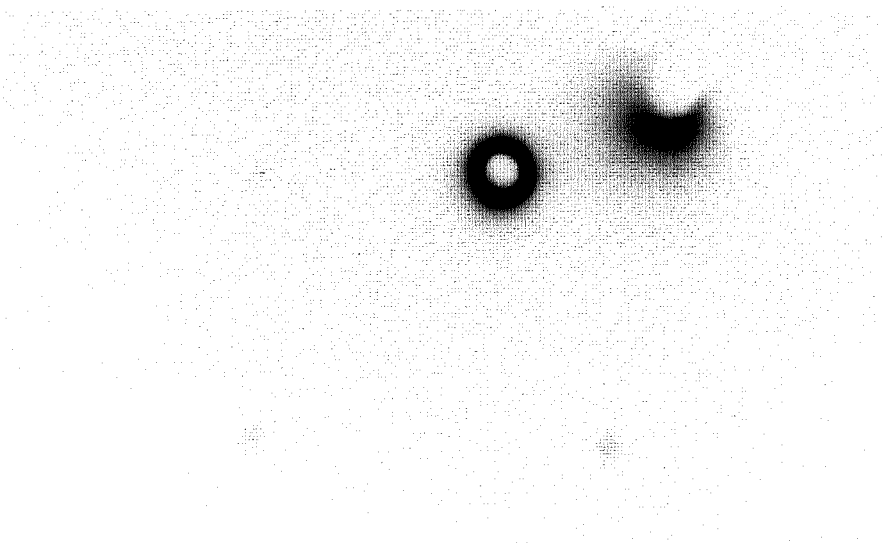

Figure 5-3

Figure 5-4

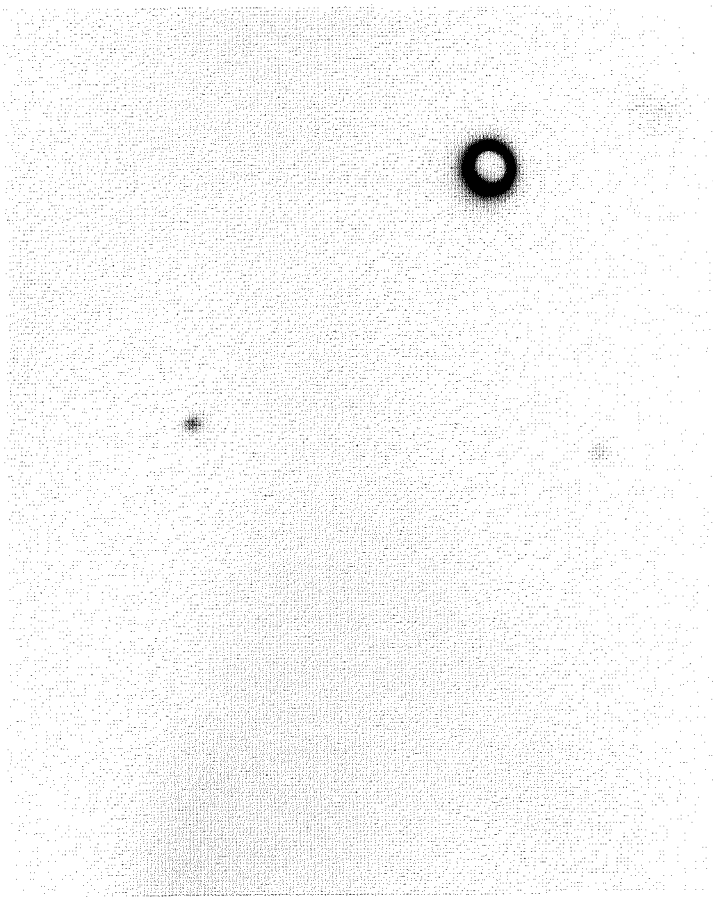

Figure 5-5

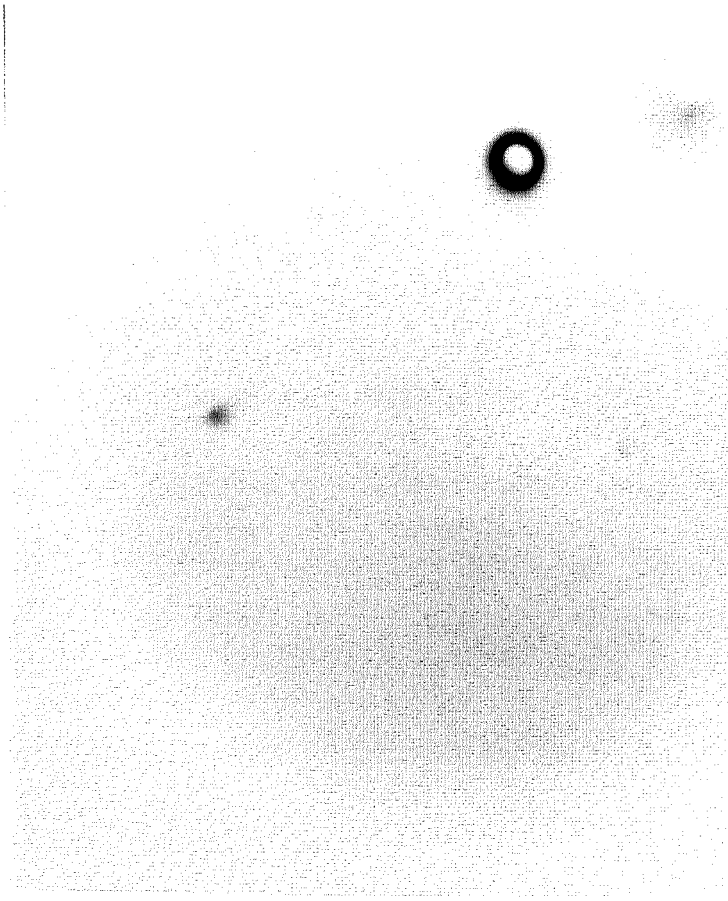

Figure 5-6

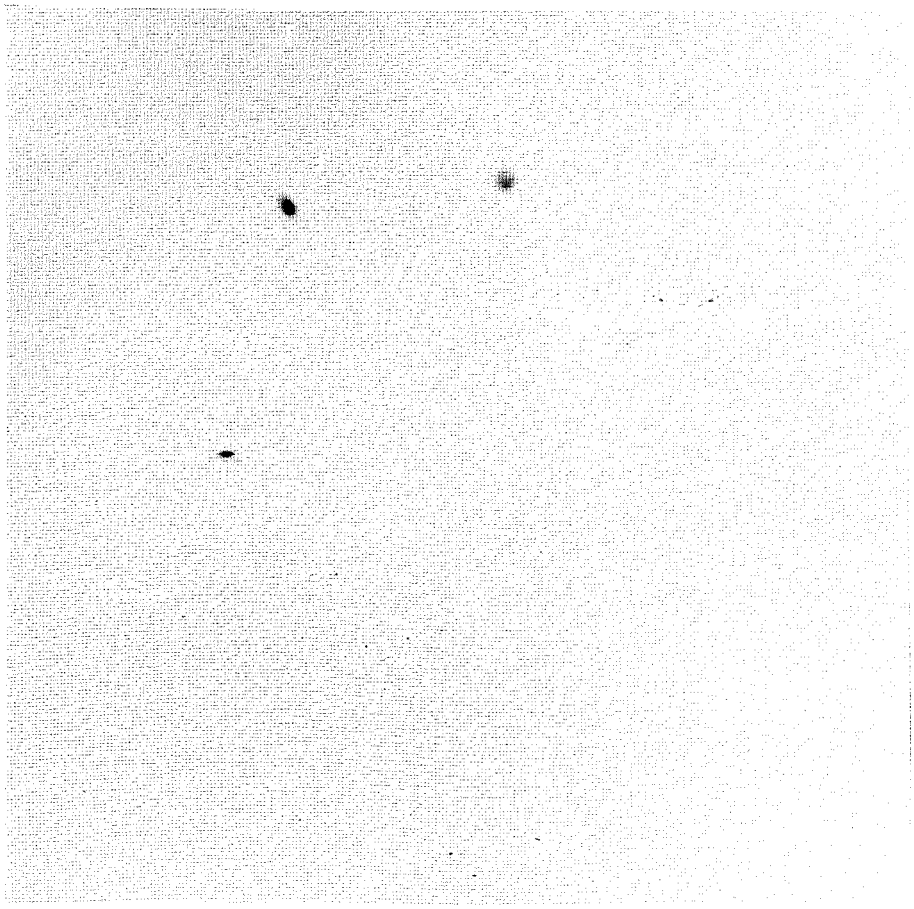

photocathode. The hollow core of the hotspot in 5-7(ii) can be seen to have a flat bottom of ~1 pixel in diameter. Extrapolating from the wings of the hotspot yields a count rate of the order of 30 $cs^{-1}pixel^{-1}$ at the centre of the hotspot. This figure is based on the assumption that there is no channel recovery problem in the wings which is unlikely, and so the figure is probably underestimated. The count rate at the turnover point on the wings is 4.5 $cs^{-1}pixel^{-1}$. The resistive paths between channels will be a factor affecting the replacement of charge in a channel (Gatti et al. 1983, Eberhardt 1981). This could help to explain the large area of the core, if the central paralysed channels are depleting the surrounding channels by this mechanism.

The hotspot feature (a) is the other major feature degrading images at a gap voltage of 420 V. The feature occurs in close proximity to the periphery of the field and may be associated with field emission from the mounting assembly. It is, however, also in close proximity to the location of the hotspot which was removed. Figure 5-4 and 5-6 show earlier detector images where activity from this feature was minimal and illustrate how this feature has increased in severity with detector lifetime. Figure 5-3 shows an image obtained after ~1.5 years of operation when a form of breakdown occurred, while operating with a proximity focussing voltage of 300 V. This activity has the same source as the feature (a) and was observed to 'switch on' for periods of up to several hours, prior to the breakdown. Shorting the photocathode potential to that of the input MCP confirmed that the activity was not originating within the plates themselves. The sharp crescent edge

of this feature in all the images may correspond to a dead area on the photocathode, although in figure 5-3 there is indication of MCP channel saturation around its periphery. Figure 5-5 shows a detector flat field image and illustrates the very low sensitivity observed in this region.

This avalanche activity was removed by running the photocathode at 300 V, for several weeks, with MCPs shorted to ground. While this measure has reduced the activity, above gap voltages of 350 V there is still an increased level of activity giving unacceptable dark noise.

Cochrane and Thumwood (1976) have shown that the physical size of these photocathode asperities is constant and so an increase in the apparent size of the features with voltage must be attributed to the detector behaviour. Figures 5-8(i) and 5-8(ii) show the change in size of hotspot feature (d). The feature is larger and shows broader wings in the image obtained with the 400 V gap potential. The increase in FWHM is coupled with a 50% drop in count rate from the feature. The primary source of this broadening is probably due to a localised drop in MCP gain. This arises from the combination of channel paralysis, possibly compounded with a low gain value resulting from the amount of charge extracted from the channels by the intense point source (Sandel and Broadfoot 1976). Secondaries colliding with the interchannel web will also contribute to the feature broadening. This mechanism will be discussed later in this chapter.

While there are other quieter hotspots, due mainly to the MCPs, the other main photocathode hotspot sources are those labelled (c), (d) and (e) in figure 5-1. While (c) is apparent in dark images at 300 V, it is diminished in intensity at 420 V and is not visible in 5-2. The other two features are asymmetric in shape at 300 V, broadening to a symmetrical profile at 420 V. Table 5-1 gives the image widths of the features labelled in 5-1 for 300 V and 420 V, in the X and Y axis directions of the images.

The activity in all of the hotspots is constantly changing and so the features will vary from image to image. Subtraction of consecutive dark images does not produce good results, usually leaving a residual feature. This is particularly so at the 420 V level where the emission from the two main features is particularly variable. If the detector were to be used for two dimensional imaging, the hotspot areas could not be removed from images completely by subtraction, or flat fielding. For the imaging of spectra, the optimum positions over the area of the photocathode was found to be to either side of the two central features (d) and (e).

To summarize, the advisability of using the techniques discussed above for the removal of hotspots is questionable. The experiences discussed here suggest that damage caused in their removal can lead to large areas of low sensitivity. The effect of hotspots upon detector performance will be discussed further in chapter 7. Existing hotspot activity has been markedly increased

Table 5-1

Photocathode Asperity Widths.

Feature	Width (pixels FWHM)		V_a (V)	
	X	Y		
b	4.0 ± 0.4	3.8 ± 0.5	300	
c	2.8 ± 0.2	2.9 ± 0.1	300	
d	2.8 ± 0.2	1.2 ± 0.1	300	
e	2.6 ± 0.2	0.6 ± 0.2	300	
b	-	-		(i)
c	-	-		(ii)
d	5.0 ± 0.1	4.0 ± 0.1	400	
e	2.6 ± 0.2	0.6 ± 0.2	400	

Pixel Format = 256 x 256 ie. 1 pixel = 156 μm.

Notes: (i) This feature contains core.
(ii) Not present at this voltage.

lend weight to the alkali metal migration theory, if one assumes that this sometimes marked increase in activity is due to additional growth on the asperities. The tube should always be run, therefore, even when not in use. The optimum method for achieving this is to run the photocathode at a moderate potential with the MCPs shorted to ground, in order to maintain the MCP lifetime whilst keeping the photocathode lifetime.

5.2) Photocathode Dark Current

Dark noise from photocathodes is a function of the photocathode material, the applied potential and ambient temperature. Estimates of the detector's intrinsic dark noise are complicated by the pulse threshold discriminators, which reject dark noise events outside preset levels and also the hotspots which add to the level of the background noise. The presence of the proximity focussing field influences the dark emission from the photocathode, since it has the effect of lowering the surface barrier potential of the cathode surface. Thus as the proximity gap potential increases so will the cathode dark noise. Measurements of field enhanced dark emission have been reported by Cochrane and Thumwood (1976) for extended-red S20 photocathodes.

With a proximity focussing voltage of 300 V the overall dark noise at 20^{o}C was typically;

10 $cs^{-1}cm^{-2}$, lower discrimination gain setting = 5.1×10^{6}

49 $cs^{-1}cm^{-2}$, lower discrimination gain setting = 2.8×10^{6}.

With a proximity focussing voltage of 400 V the level increases and

the dark noise was measured as;

115 $cs^{-1}cm^{-2}$, lower discrimination gain = 5 x 10^6 setting,

403 $cs^{-1}cm^{-2}$, lower discrimination gain = 2.8 x 10^6 setting,

506 $cs^{-1}cm^{-2}$, lower discrimination gain = 2.1 x 10^6 setting.

These figures illustrate the increase in dark noise as the lower threshold level is decreased, allowing more events from the negative exponential tail of noise pulses to be processed. There is an order of magnitude increase in dark noise with the increase in proximity focussing field and this is primarily due to the increased hotspot activity. Typically at 300 V the emission hotspots will be contributing 50% to the overall dark noise figure, while at 420 V this figure is 80%. The effect of decreased temperature is to lower the overall dark noise, but not to the degree expected because of the field emission, which appears to be relatively insensitive to temperature. It was found that hotspot free areas of the photocathode show a drop of ~2 from 20^0C to 5^oC.

Figure 5-9(a) shows the variation of dark count rate from start-up over 36 hours with a proximity focussing voltage of 300 V. The temperature variation over this period was minimal. The diagram illustrates a general trend of decreasing dark noise, however there is a large excursion from this trend over a period of 10 hours due to the variable hotspot activity. Over longer periods of operation at 300 V to 350 v this normally stabilises. The diagram in figure 5-9(b) shows the variation of dark noise over a 24 hour period several days after start-up illustrating a general cycling trend due to the temperature variations in the telescope dome of typically $\pm 5^o$C.

Figure 5-9(a): Detector dark noise variation over 36 hours from start-up.

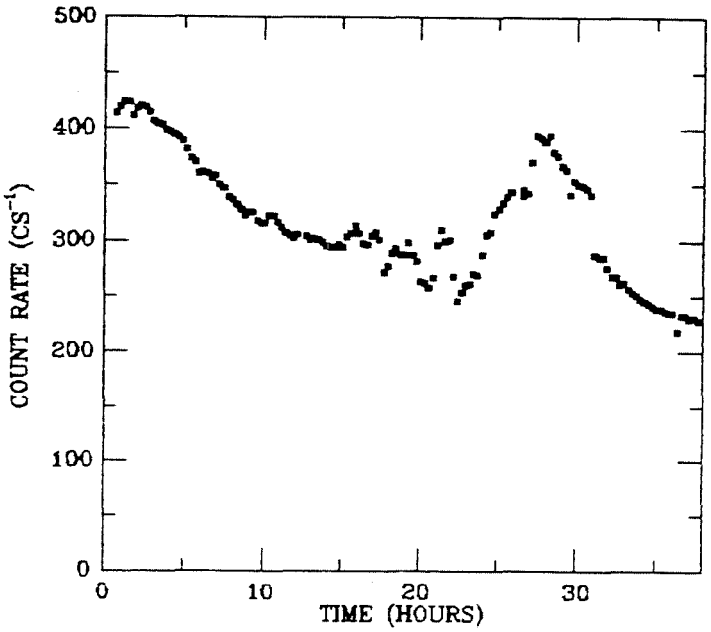

Figure 5-9(b): Detector dark noise variation with telescope dome temperature ($\pm 5^{o}C$).

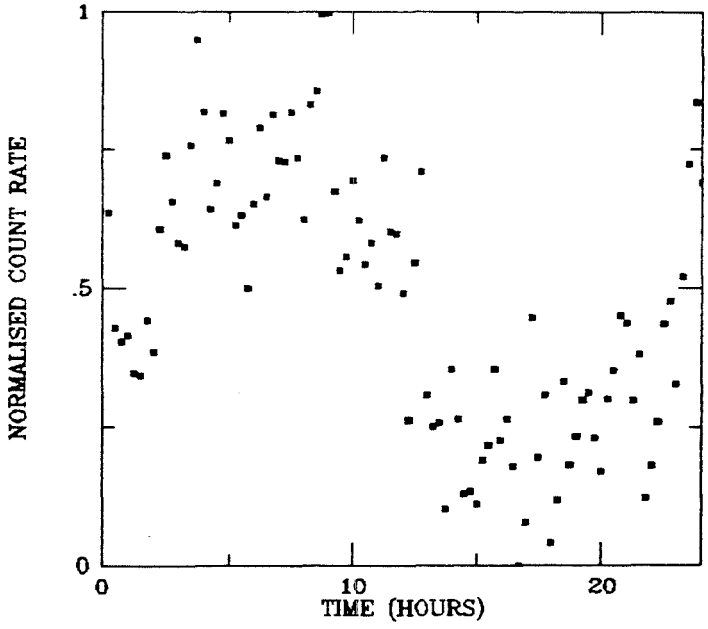

5.3) Photocathode Uniformity

Figures 5-10(a) and (b) show a typical flat field cross section in a raw form, and smoothed using a Gaussian filter over 3 channels. The raw flat field shows evidence of pattern noise and this will discussed in this chapter. The problem of processing the photocathode with an insufficient 'throw' was discussed in Chapter 2 and figure 5-9 illustrates the response drop off towards the edges of the photocathode field. Effectively half of the photocathode active area has a response of less than 50% of the central photocathode area. Thus the usable active area is somewhat less than 40 mm diameter. The large scale photocathode uniformity is poor, with a non-symmetric trend in sensitivity over the field. The Optronix print in figure 5-5, although scaled to the peak count rate, does show the overall photocathode sensitivity variation. The area surrounding the hotspot feature (c) has a very low sensitivity caused by the continous field emission activity and the breakdown event shown in figure 5-3. On the small scale, the cathode also shows considerable variation in reponse which is illustrated in figure 5-11(a). The variation is probably due mainly to the photocathode graininess, with several low sensitivity spots contributing to the non-uniformity.

Detector flat fields are however fairly stable, figure 5-11(b) shows the result of dividing two flat fields illustrating a deviation from non-uniformity of 5% rms, in the central 800 pixels. This also illustrates how the pattern noise in images

Figure 5-10(a): Raw flat field cross section.

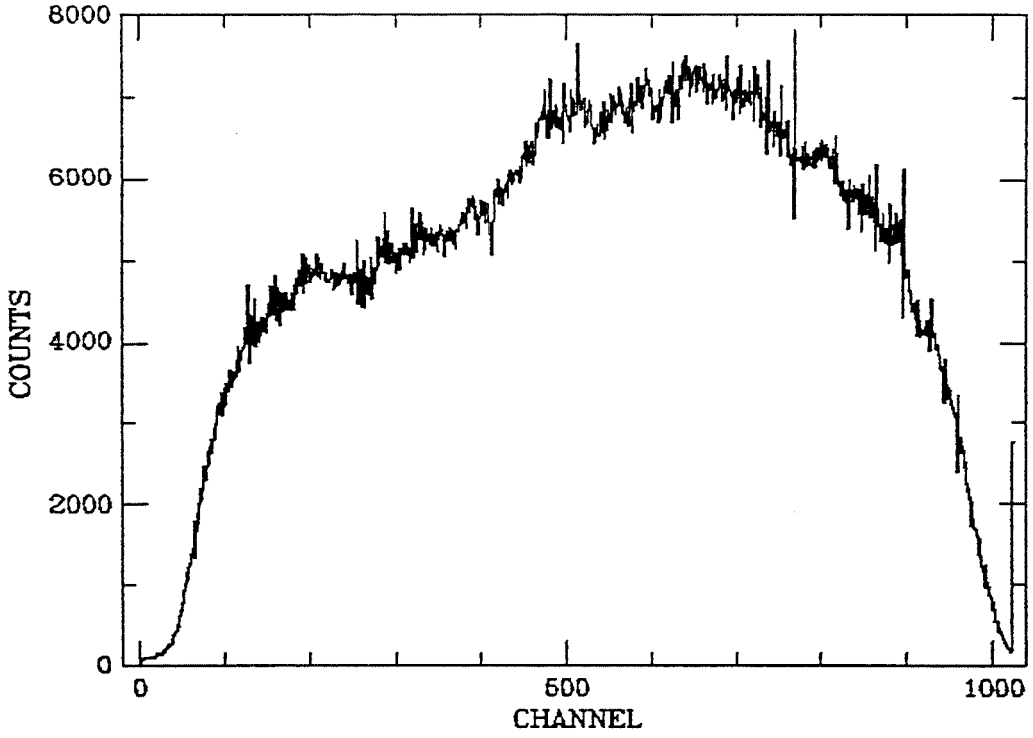

Figure 5-10(b): Flat field smoothed over 3 channels using Gaussian filter.

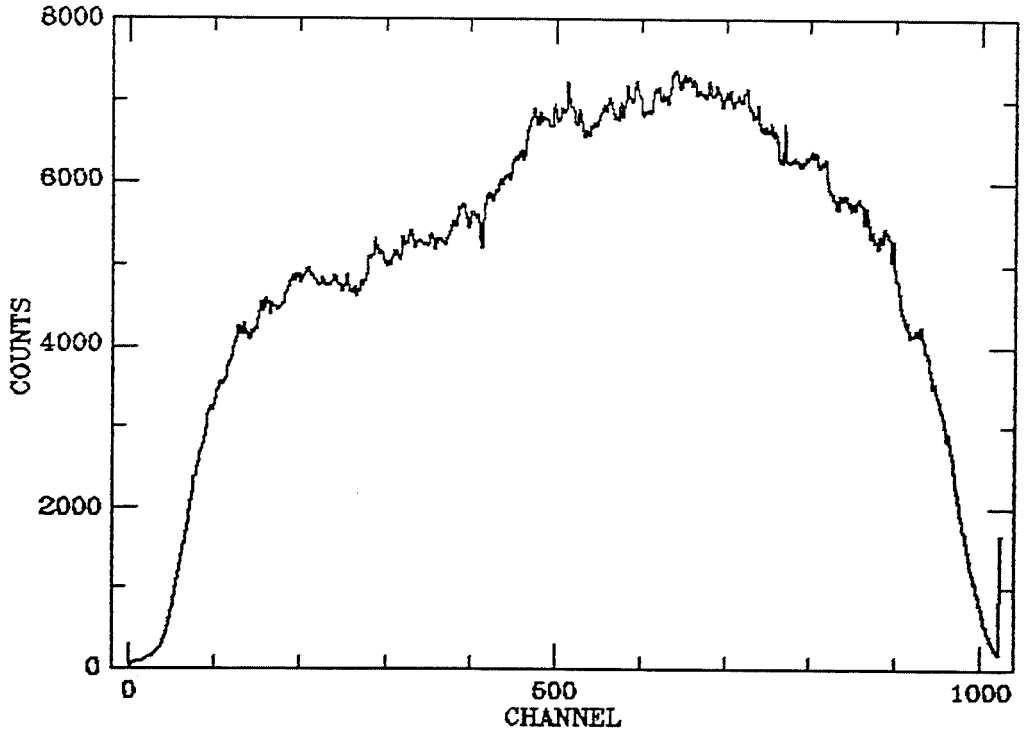

Figure 5-11(a): Rectified flat field (central 800 pixels).

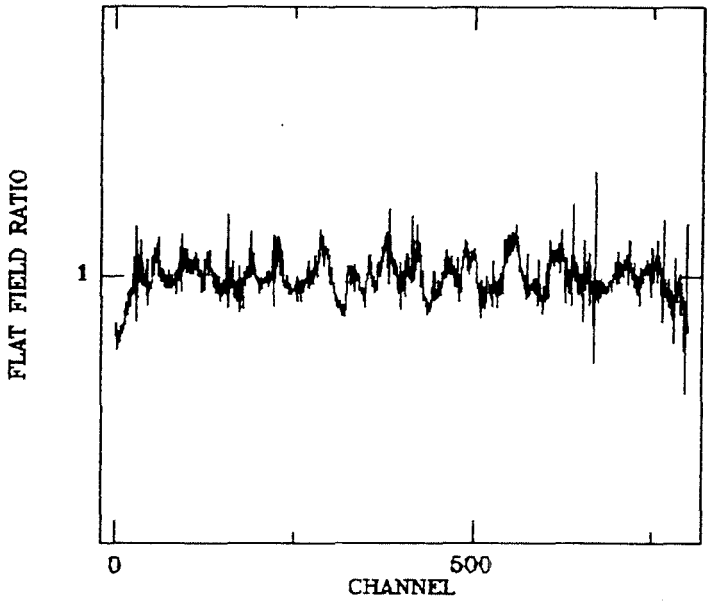

Figure 5-11(b): Diagram showing result of dividing two flat fields.

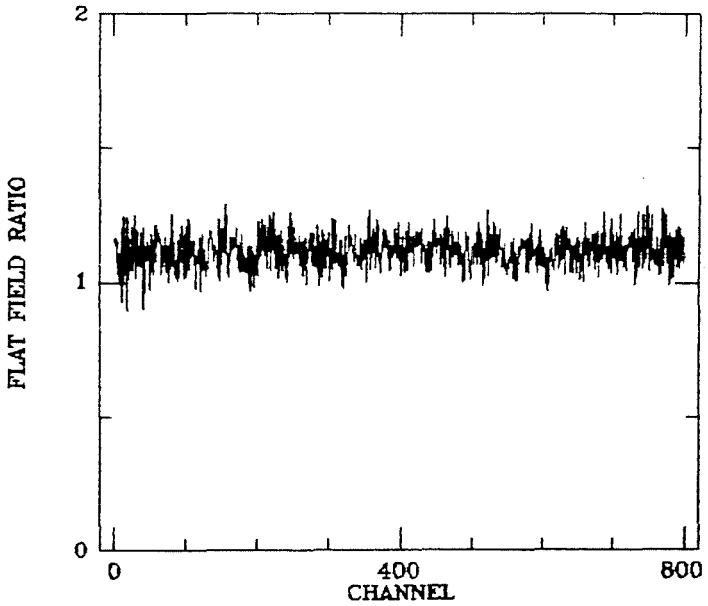

obtained at higher illumination levels cancels. This stability was found to be typical for flat fields obtained with the same pixel format during the course of investigation.

5.4) Electronics

Pattern noise has been one of the main problems experienced with the detector system electronics. Cross sections of flat field images show extraneous features not associated with the detector's imaging characteristics. They are identified by large, single pixel spikes, usually preceded by pixel dropouts of a similar magnitude. Figure 5-12(a) shows a section of flat field illustrating the characteristics of this pattern noise.

The source of the pattern noise is the analogue to digital convertors used for for ratiometric division. Similar effects have been reported by Hartig et al. (1980) and in a different context by Djorgovkski (1984). Analysis of flat field images shows these features to arise in channel locations where there is a major transition from ones to zeros. The most prominent features highlighting this periodicity are:

1111111 - 10000000	Channels 127 - 128,
11111111 - 100000000	Channels 255 - 256,
111111111 - 1000000000	Channels 511 - 512,
101111111 - 1100000000	Channels 767 - 768,
1111111111 - 10000000000	Channels 1023 - 1024.

The rectified raw flat field in figures 5-13(a) and 5-13(b) shows clear evidence of further periodicities in the structure of the

Figure 5-12: Electronic pattern noise at channels 767-768.

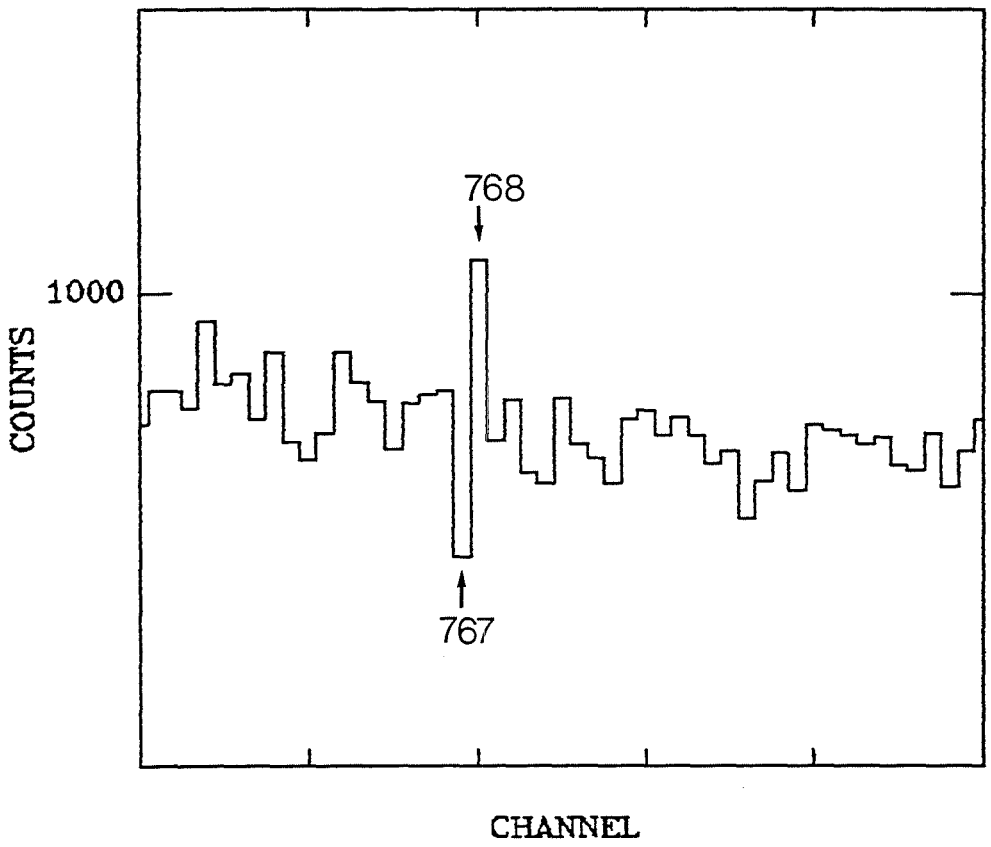

noise. It is clear that the binning bias is not limited just to those channels showing large departures from the mean signal. The power spectra in figure 5-14 confirms that there are a large number of periodicities occurring at lower amplitude levels, with frequencies corresponding to binning bias errors.

When operating ADCs as ratiometric dividers, comparator limitations such as offset voltage, input noise and gain will cause distortion of the transfer characteristic (Analogue Devices 1982). This effect is known as differential non-linearity and is a result of deviations in the step width of the transfer characteristics giving rise to unequal binning during the successive approximation processing. This form of conversion error often results in pattern noise of the type identified in detector images, sometimes referred to as 'skipped codes'. The pattern noise has been observed in other IPD units (McWhirter 1983) and does appear to be intrinsic to the operation of these ADCs for ratiometric division. The pattern noise did not always appear in images and was found to be dependant on several factors.

The analogue to digital converter timing may be controlled by the addition of external components to increase or decrease the conversion speed from the nominal 5.6μs. Short cycling of the chip enables higher conversion speeds to be obtained by reducing the dynamic range of the chip from 12 bits to 10 or 8 bits. Initially the system was run as delivered with the chip set up for 3μs conversion speeds at 12 bits. The pattern noise was particularly severe and so the chip was short cycled to 10 bits operation at the

Figure 5-13: (a) Rectified flat field cross section showing noise periodicity, at 10 bit ADC resolution.

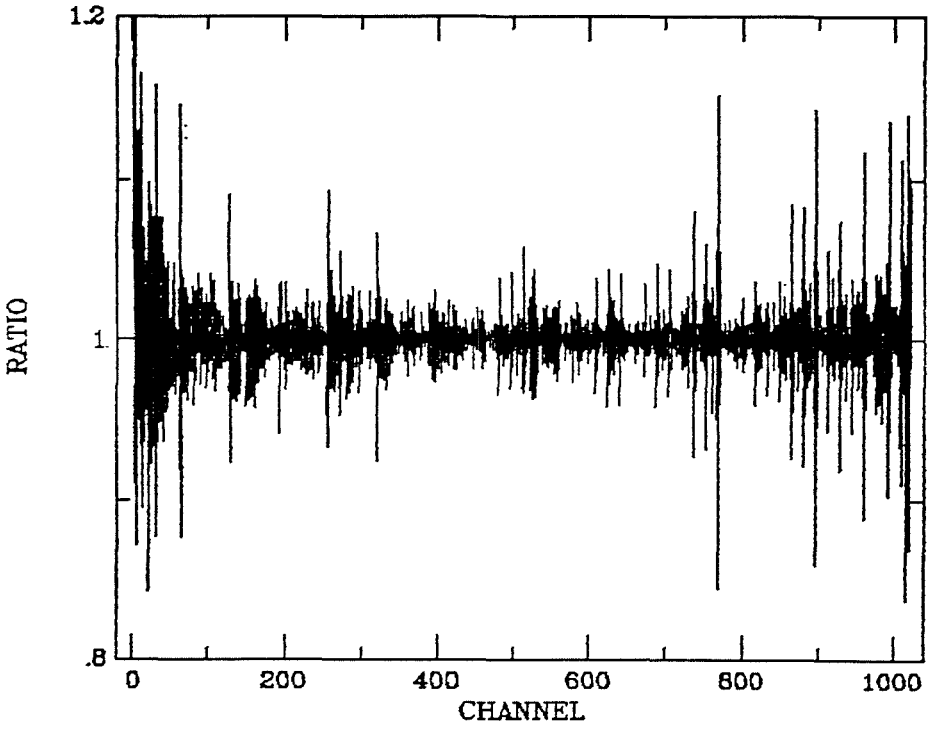

Figure 5-13: (b) Enlarged section of 5-13(a) showing noise structure.

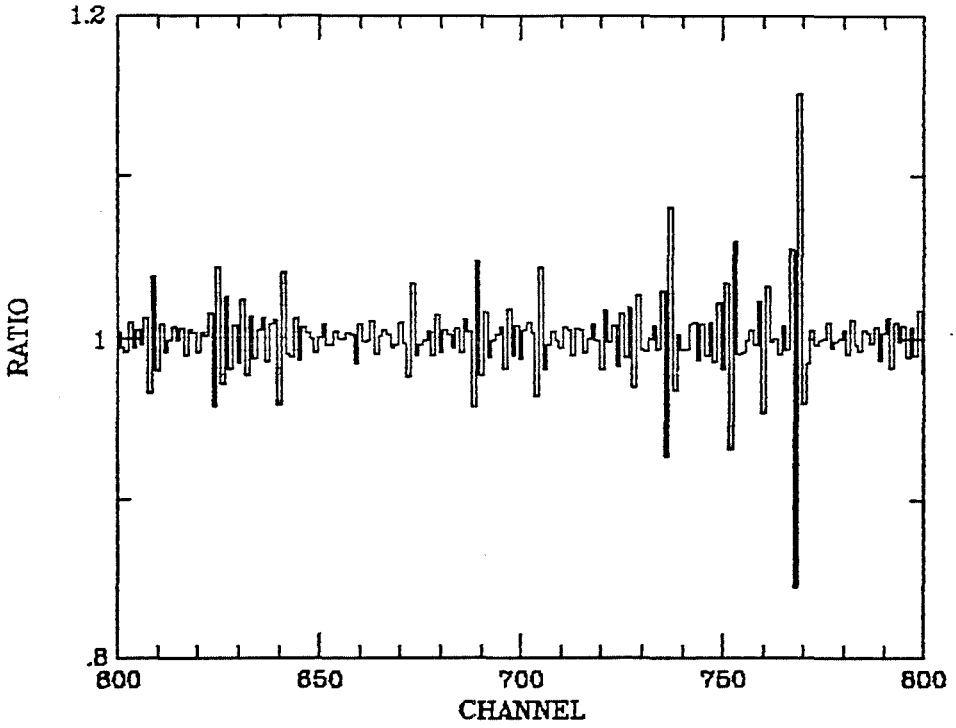

Figure 5-14: Power spectra of 5-13(a) showing periodicity at binning bias frequencies.

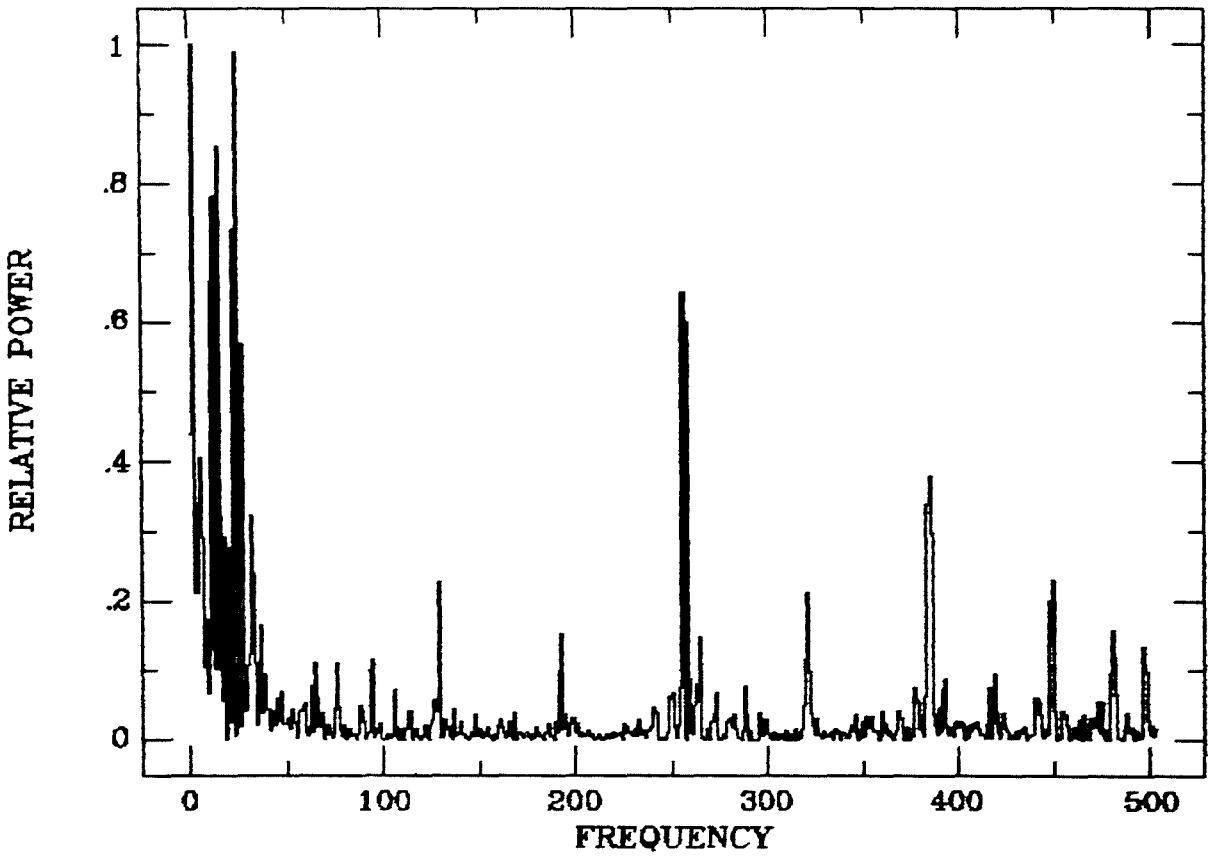

same conversion speed. The optimum performance was obtained with the chip set to operate at 12 bits with a conversion speed of 6μs. Slowing the chip down further was not found to produce any further benefits in the reduction of pattern noise. Since the converters are designed to operate with a fixed 10 V reference, the processing electronics lower threshold was set to ensure that no pulses below the equivalent of a reference voltage of 5 V were processed. The adjustment of the zero offsets of the analogue to digital converters has already been discussed in chapter 3.

The use of higher bit resolutions increases the severity of the pattern noise seen in an image. The large features are seen in images even with 8 bit resolution, although the low level periodicity is less apparent. With less than 8 bits, the pattern noise has not been observed in detector images to date. When the detector system is operated with 10 bit X resolution, giving 1024 pixels, there are 64 Y cross sections and so the periodicity is only seen in the X dimension of the image. If the format is reversed to give 10 bit resolution in Y, the pattern noise is seen in the Y dimension of the image, but not in X.

A significant factor influencing the appearance of pattern noise is the method and degree of illumination of the detector. The pattern noise is always most severe in flat fields where the count rate is fairly high ($\sim 10^4$ cs^{-1}) and the field is uniformly illuminated. It is not usually seen in images obtained with the detector unless the count rate is relatively high. Analysis of the power spectra of detector images, where there was no evidence of

pattern noise, confirmed this to be the case. When the pattern noise does appear, it is repeatable and cancels out when rectified with images obtained under similar conditions. In six flat fields obtained on a number of different occasions, the ratio of the dropout to spike in the feature at channel 768 was found to be 1.41 ± 0.03. Power spectra of flat fields rectified with another were found to indicate only a residual amount of periodicity.

The evidence shows that there is some association between the processing rate of the circuit and the occurrence of pattern noise. Analogue devices state that ADCs used as ratiometric dividers should not have significantly changing reference voltages. The dividers which are classified as being suitable for ratiometric division are all operated at slower conversion speeds than the AD578, which may be significant. It is probable that it is due to an intrinsic property of the ADCs when operated in this mode, such as a settling time associated with the reference voltage circuit.

5.5) Geometrical Uniformity

The geometrical uniformity of the detector was tested by imaging a coarse grid pattern, consisting of 1 mm lines separated by 1 mm spaces, with uniform illumination. Figure 5-15 shows half of the imaged pattern in detail and illustrates the absence of any major geometrical distortion. Other workers (Lampton and Carlson 1979, Rees et al. 1981) have reported some distortion at the periphery of the field. It has not been possible to accurately investigate this, however, since the photocathode sensitivity is

Figure 5-15: Diagram showing image of fringe pattern and demonstrating geometrical uniformity.

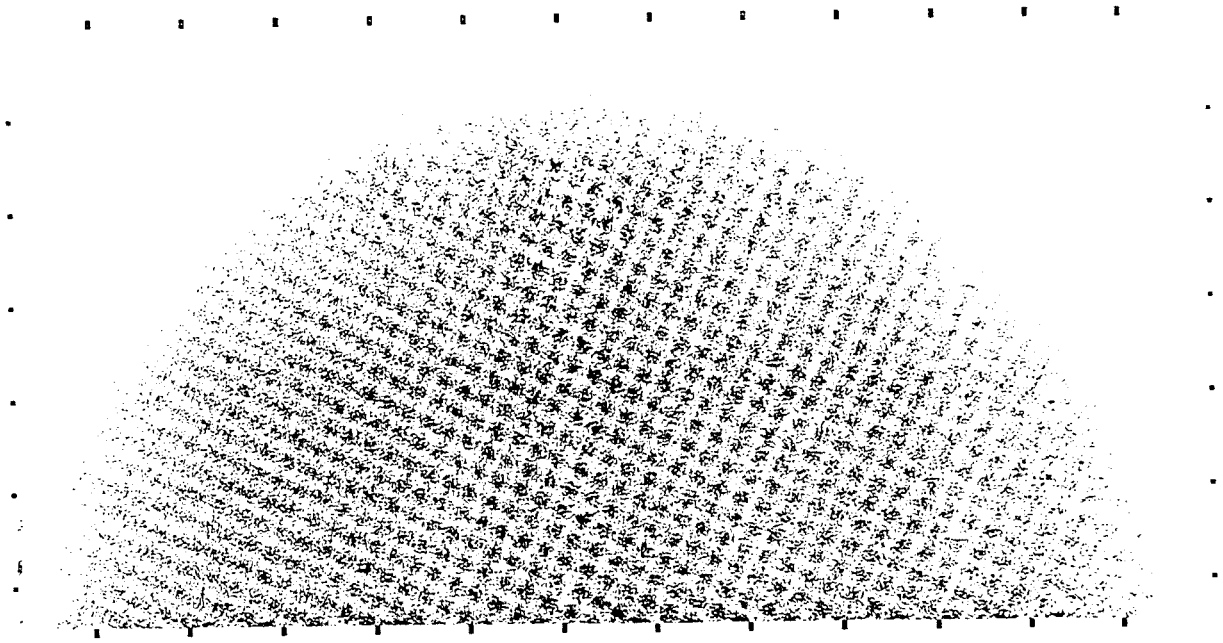

Figure 5-16: Diagram showing image of matrix pattern imaged on central section of photocathode area.

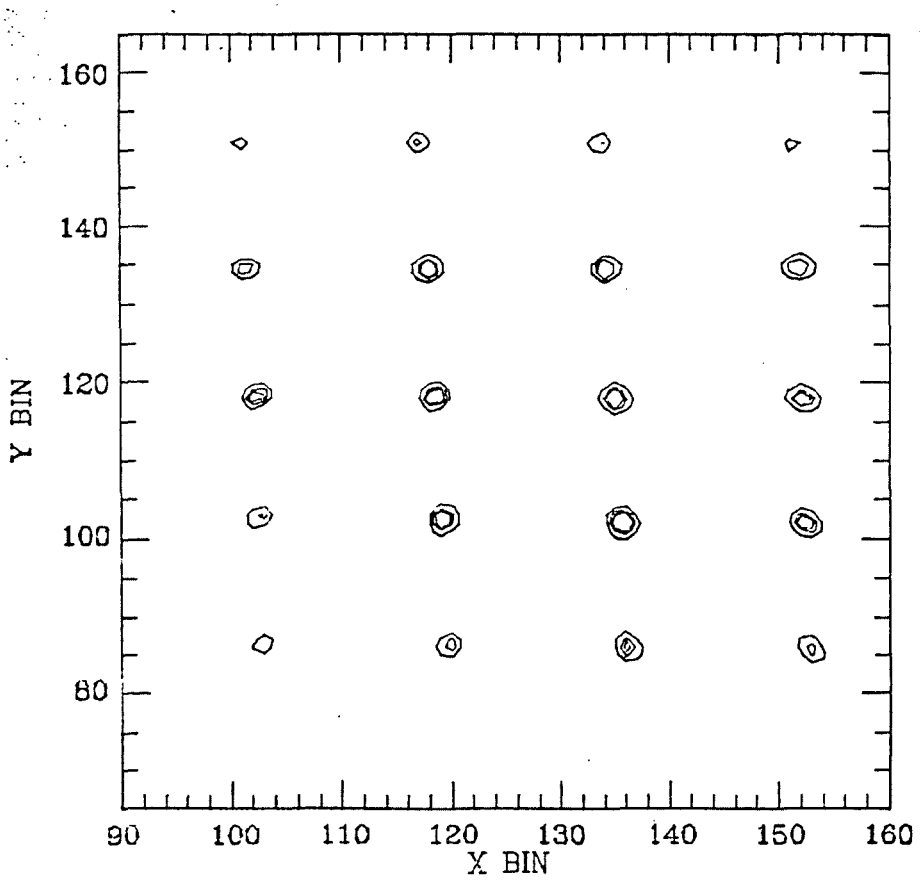

very low at the outer 5% of the photocathode field. This problem is highlighted in figure 5-15 where the edge of the image can be seen to contain little information. Other detector images, such as those of the USAF resolution chart in figure 7-7 also show no signs of any geometrical non-uniformity.

An additional test for geometrical linearity was made using a mask constructed at St Andrews, consisting of 200 μm diameter holes separated by 5 mm, drilled onto thin brass. A contour plot of an image obtained with this mask is shown in figure 5-16. The asymmetrical appearance of some of the holes is a result of the mask preparation technique. Within the uncertainty of the machining errors there is no deviation from uniformity.

5.6) Detective Quantum Efficiency

The detective quantum efficiency of a detector is defined as

$$DQE = \frac{(SNR_{out})^2}{(SNR_{in})^2} \qquad (8.1)$$

and the quantum efficiency of a detector is defined as

$$QE = \frac{(Counts_{out})}{(Photons_{in})} \qquad (8.2)$$

These two quantities give a measure of the efficiency of a detector and are an important consideration if a telescope is to be used to its optimum. For small telescopes, in particular, a high detector DQE will allow the faint limit of operation to be extended. DQEs for MCP detectors have often been quoted in the literature in terms of the photocathode quantum efficiency only, with the MCPs assumed to reduce this value by approximately the value of their open area ratio.

For an IPD the following factors will contribute to the overall DQE of the detector;

(i) Fibreoptic window.

(ii) Photocathode Quantum Efficiency.

(iii) MCP efficiency.

(iv) Resistive Anode time constant.

(v) Pulse processing electronics.

Analysis of the individual components will allow contributions from each component to be assessed and the overall estimate to be compared with experimental results.

5.6.1) Fibreoptic

The loss of signal caused by the fibreoptic was discussed in Chapter 2, with the transmission curve shown in figure 2-5. Typically the transmission losses of the fibreoptic are of the order of 60% in the range 400 nm to 1000 nm.

5.6.2) Photocathode Quantum Efficiency

The photocathode responsive quantum efficiency (RQE) was measured at ITL soon after the processing of the tube. The RQE calculated from the photocurrent generated by the cathode from a series of four calibrated lamps is illustrated in figure 5-17. The response is typical of an S20 photocathode, having its peak sensitivity in the blue. It has not been possible to remeasure the RQE, and the figure may be lower by up to 50% (Lyons 1985). The major source of this drop is the hotspot removal which may have contributed considerably to the degradation of the cathode. The RQE of photocathodes is enhanced by the presence of a high electric field which will lower the surface barrier potential of the material. For S20 photocathodes Cochrane and Thumwood have shown the gain in the region 400 nm to 600 nm to be minimal for field strengths of the order of 4 $kVmm^{-1}$. This is because the sensitivity gain is a function of wavelength with optimum enhancement arising at wavelengths corresponding to the photoelectric threshold. For S20 type photocathodes this will be in the range 700 nm to 900 nm.

With semitransparent photocathodes, some radiation can be transmitted and then reflected back to the photocathode by the MCP surface, causing an increase in the RQE (Pollehn 1974). The increase in efficiency is at the expense of DQE, since a loss of signal to noise is involved. This and other scattering phenomena are often referred to as veiling glare.

Figure 5-17: Photocathode RQE measured using standard lamps at ITL.

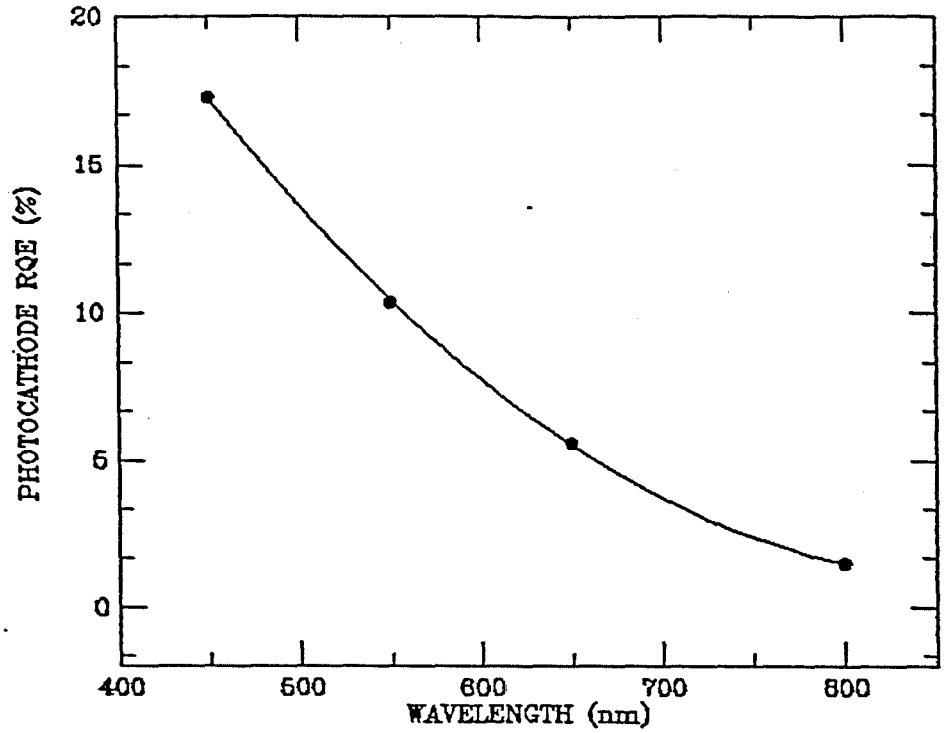

Figure 5-18: Transmission curve for RG0 beta light source filter.

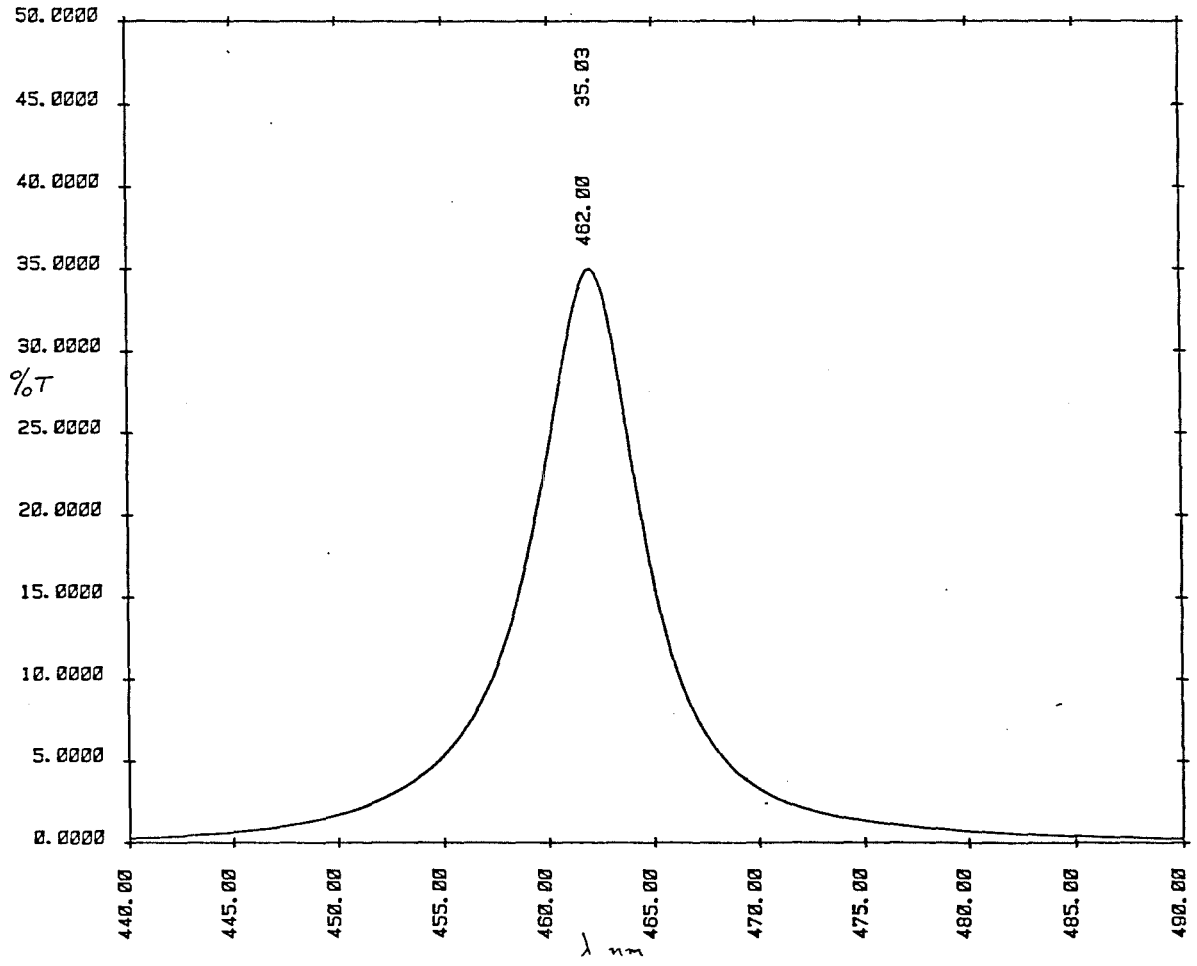

5.6.3) Micro-Channel Plates.

Two major factors will influence the efficiency of the MCPs and their performance within the tube, namely the open area ratio of the plates and the effect of the Al_2O_3 film covering the input plate.

The open area ratio of the plates is the fraction of the plate that will allow electrons to fall into one of the plate channels. This ratio is typically about 55 to 60% for normal MCPs measured geometrically. The effective ratio may be higher due to the contribution of web generated electrons eg. 85% (Eberhardt 1981). Web electrons are secondary electrons which are generated from collisions with the channel boundaries and forced into a channel by the repulsion of the proximity focussing field and the attraction of the channel field. Photoelectrons will also be returned towards the photocathode as a result of reflection at the Al_2O_3 barrier film. Csorba (1979) gives a figure of 10-15% for this loss mechanism. The electrons produced by these two mechanisms will be returned to the MCP input by the proximity focussing field. The distance between the primary collision and the second impact will be determined by the field strength, electron energy and emission angle. Both these mechanisms will result in a lowered DQE, and it is emphasised that the enhanced collection efficiency achieved will result in a degradation in resolution.

The Al_2O_3 film barrier on the input MCP attenuates the energy of the incident photoelectrons and thus reduces δ_1, the secondary electron emission coefficient of the MCP. Each photoelectron loses kinetic energy corresponding to the film 'dead voltage' and there is an associated increase in radial energy resulting from scattering. Photoelectrons with an incident energy of less than 200 V will not penetrate the film, while those with higher energies lose kinetic energy of 150-200 eV from their passage through the film. Csorba (1979) found the maximum value of δ_1 to occur for photoelectron energies corresponding to 800-900 V. Above 1000 V the film appears relatively transparent to electrons, however, the value of δ_1 is reduced by the increase of radial energy of the photoelectrons. This was confirmed by Lyons (1985) in a similar test with Mullard MCPs. For these plates the dead voltage was slightly less than 200 V, with transmissions of 0.25 and 0.15 for cathode gap voltages of 400 V and 300 V respectively.

5.6.4) Resistive Anode

The detection efficiency of the resistive anode is determined by the minimum time window within which two individual input pulses will be determined. This parameter is given by the time constant $(R_{\square}C/\pi^2)$, which is calculated from the anode capacity. Using the anode capacitance density of 18 $pFcm^{-2}$ calculated in Chapter 2, the time constant of the anode is 7.3 ns. Thus up to the normal operating count rate limit of the detector, the coincidence count rate will not cause a significant number of pulses to be lost to

coincidence.

5.6.5) Electronics

The contribution of the electronics, in common with the anode, relates to the maximum number of events that may be processed before the circuit processing deadtime becomes a limitation, causing the loss of valid events. The processing speeds of both the preamplifiers and the signal processing circuitry are sufficient to allow processing of event rates up 10^5 cs^{-1}.

5.6.6) Detector Quantum Efficiency

In order to make an assessment of the quantum efficiency of the detector, a series of measurements were made using a low light level source made in St Andrews to a Royal Greenwich Observatory (RGO) design. The main purpose of the experiment was to obtain an estimate of the losses involved in the detector due to the mechanisms discussed above and to obtain an assessment of the degradation in photocathode sensitivity. The light source was calibrated at the RGO by Dr. R Powell using a secondary photometric standard (Jelley 1982) as a reference. The source response is shown in figure 5-18 and is optimised to the detector's photocathode response. The output flux through the source aperture was $50.9 \pm 4.7\%$ photons s^{-1}, with a central wavelength of 462 nm and a FWHM value of 5.8 nm.

The tests were carried out in a dark box containing an optical bench, using neutral density filters to provide attenuation of the source. The neutral density filters were of the Kodak Wratten gelatin type with a specified uncertainty of ±10% in their density value. For the larger values of filter density this unfortunately leads to large formal errors in the number of photons incident on the detector. Two series of measurements were made with the aperture of the source directly imaged onto the central 2 cm diameter of the photocathode. This was intended to minimise the losses arising from the combination of low photocathode sensitivity and hotspots in the outer area of the detector. For each value of neutral density filter a series of 80 integrations of 300 s were obtained, with dark noise integrations before and after each run of 20 measurements. The dark noise integrations were not always of value, since during the period of these measurements the activity in the hotspot feature (a) (figure 5-1) became very variable, leading to the breakdown seen in figure 5-3. Thus while the measurements were designed to allow for the timescale of temperature variation in the telescope dome, they could not account for hotspot activity on a timescale of minutes.

The results are shown in tables 5-2 and 5-3 for proximity focussing voltages 300 V and 400 V, yielding QE values of 1.96 ± 0.07 and 2.29 ± 0.08 respectively. The results are lower than those found by Lyons and Read (1985) for an ITL 40 mm intensifier of the same basic design operating at an unspecified proximity focussing voltage. It was not possible to remeasure the

Table 5-2

Quantum Efficiency for proximity focussing voltage 300 V.

ND	Incident Photons	Detected Events	Quantum Efficiency
2.0	$5.1 \pm 2.4 \times 10^3$	90 ± 12	1.76 ± 0.86
2.0	$5.1 \pm 2.4 \times 10^3$	63 ± 7	1.24 ± 0.58
2.0	$5.1 \pm 2.4 \times 10^3$	69 ± 7	1.35 ± 0.58
2.0	$5.1 \pm 2.4 \times 10^3$	61 ± 5	1.20 ± 0.57
1.5	$1.9 \pm 0.7 \times 10^4$	368 ± 26	1.94 ± 0.73
1.5	$1.9 \pm 0.7 \times 10^4$	359 ± 6	1.88 ± 0.69
1.5	$1.9 \pm 0.7 \times 10^4$	412 ± 9	2.17 ± 0.80
1.5	$1.9 \pm 0.7 \times 10^4$	406 ± 5	2.14 ± 0.79
1.0	$5.1 \pm 1.2 \times 10^4$	854 ± 15	1.68 ± 0.40
1.0	$5.1 \pm 1.2 \times 10^4$	878 ± 20	1.72 ± 0.41
1.0	$5.1 \pm 1.2 \times 10^4$	779 ± 8	1.53 ± 0.36
1.0	$5.1 \pm 1.2 \times 10^4$	776 ± 16	1.52 ± 0.36
0.6	$1.28 \pm 0.19 \times 10^5$	2444 ± 37	1.91 ± 0.29
0.6	$1.28 \pm 0.19 \times 10^5$	2485 ± 27	1.94 ± 0.29
0.6	$1.28 \pm 0.19 \times 10^5$	2698 ± 48	2.11 ± 0.32
0.6	$1.28 \pm 0.19 \times 10^5$	2762 ± 33	2.16 ± 0.32
0.3	$2.55 \pm 0.20 \times 10^5$	5182 ± 119	2.02 ± 0.17
0.3	$2.55 \pm 0.20 \times 10^5$	5120 ± 53	2.00 ± 0.16
0.3	$2.55 \pm 0.20 \times 10^5$	5227 ± 89	2.05 ± 0.17
0.3	$2.55 \pm 0.20 \times 10^5$	5579 ± 92	2.19 ± 0.18

Table 5-3

Quantum Efficiency for proximity focussing voltage 400 V.

ND	Incident Photons	Detected Events	Quantum Efficiency
1.5	$1.9 \pm 0.7 \times 10^4$	452 ± 25	2.38 ± 0.89
1.5	$1.9 \pm 0.7 \times 10^4$	540 ± 29	2.80 ± 1.10
1.5	$1.9 \pm 0.7 \times 10^4$	435 ± 38	2.28 ± 0.86
1.0	$5.1 \pm 1.2 \times 10^4$	963 ± 58	1.89 ± 0.46
1.0	$5.1 \pm 1.2 \times 10^4$	987 ± 39	1.94 ± 0.46
1.0	$5.1 \pm 1.2 \times 10^4$	1030 ± 64	2.02 ± 0.49
1.0	$5.1 \pm 1.2 \times 10^4$	892 ± 59	1.75 ± 0.43
0.6	$1.28 \pm 0.19 \times 10^5$	3054 ± 66	2.39 ± 0.34
0.6	$1.28 \pm 0.19 \times 10^5$	3105 ± 51	2.43 ± 0.36
0.6	$1.28 \pm 0.19 \times 10^5$	2858 ± 152	2.23 ± 0.35
0.6	$1.28 \pm 0.19 \times 10^5$	3025 ± 150	2.36 ± 0.37
0.3	$2.55 \pm 0.20 \times 10^5$	5688 ± 40	2.22 ± 0.18
0.3	$2.55 \pm 0.20 \times 10^5$	5833 ± 81	2.29 ± 0.18
0.3	$2.55 \pm 0.20 \times 10^5$	6081 ± 81	2.39 ± 0.19
0.3	$2.55 \pm 0.20 \times 10^5$	6336 ± 44	2.49 ± 0.20

photocathode sensitivity individually using calibrated lamps, therefore, the experiment cannot tie down the losses attributable to the collection efficiency of the MCPs alone. The results are, however, reasonably consistent with an increase in transmission of the Al_2O_3 film corresponding to the transmission values of 0.25 at 400 V and 0.15 V at 300 V (Csorba 1979, Lyons 1985).

5.6.7) Conclusions

The results of the QE measurements show that the photocathode sensitivity appears to have dropped since the initial measurement, although the figure is dependent upon the loss estimates. The main uncertainty is the MCP collection efficiency which has been estimated in the literature at between 60% and 85%.

Lyons and Read found the collection efficiency of their intensifier to be 0.59, and attribute this figure to a loss caused by the open area ratio of the plates. Other authors, however, report the collection efficiency to be of the order of 80% - 85% (Eberhardt 1981, Pollehn 1974). The discrepancy could be accounted for by the efficiency of the intensifier phosphor, which Lyons and Read do not discuss. A phosphor efficiency of 70% would be enough to account for the collection efficiency measured. Cromwell (1984) reports measurements for proximity focussed diode intensifiers which indicate that phosphor efficiencies can be as low as 53%.

While the collection efficiency of the MCPs is uncertain, the major loss mechanism within the tube, the Al_2O_3 film, is well understood. Increasing the transmission of the film, however, requires higher proximity focussing voltages of the order of 800 V - 900 V. The problems inherent in using high accelerating voltages have already been discussed in this chapter, however, Allington-Smith and Schwartz (1985) report specifications of 3 $kVmm^{-1}$ fields across photocathode to MCP gaps of 0.2 mm for ITT intensifier tubes.

The low efficiency is obviously an area which requires further investigation in order to make these detectors astonomically competitive. In particular more effort is required to correlate the overall quantum efficiency with the collection efficiency of the plates, since this is an area where design improvements are possible. Once the MCP collection efficiency has been determined, an estimate is required of how any field enhancement of the open area ratio will contribute to degradation of the DQE of the detector. The Al_2O_3 film, however, leaves little room for improvement, other than its removal or operation at high proximity focussing voltages. Possible design improvements which would lead to higher quantum efficiency of the detector will be discussed in Chapter 9.

Chapter 6

6.1) Operation

The detector unit was delivered with a Brandenberg 512 power supply mounted in the head. This unit was unable to supply potentials in excess of 2.9 kV necessary to operate the MCPs at gain saturation. It was replaced with the Hunting unit, described in chapter 3, which was mounted externally. This unit supplies the overall potential required by the detector via an EHT socket which is attached directly to the old internal unit connections.

The potentials across the tube components are set by a resistor chain which divides the EHT across components as required. Thus in order to change individual component potentials, either the overall supply voltage is raised, or the resistor chain is altered accordingly. Provision of three independent EHT supplies would be impractical for the size of the detector head, because of the space available. The use of large external EHT units was found to cause pickup on the preamplifier leads, leading to extraneous features in detector images and artificial pulse height distributions. The pickup problem posed by three separate EHT supplies to bias each individual tube component has therefore been the other major factor ruling out individual component biassing.

The investigations of MCP performance discussed in this chapter were carried out at overall applied potentials of up to 1.75 kV per plate. This limit was imposed on the recommendation of ITL and is based on the manufacturer's plate specifications. Operating the plates at excessively high potentials can lead to plate damage from several mechanisms which would result in the tube having to be reprocessed.

6.2) Gain Determination

In chapter 3 the technique for calculating MCP gain values from the preamplifier response was discussed, together with the method for obtaining pulse height distributions. To determine absolute MCP gain values from the pulse height distributions, it is necessary to calibrate the bin numbers of the distribution in terms of the size of the pulse to which they correspond. This may be easily achieved by relating the lower discriminator cutoff point in the pulse height distribution to the lower discriminator voltage setting.

From figure 3-4 showing the timing circuits for the detector electronics, it can be seen that a summed pulse V from inputs A, B, C and D will be diminished by a factor of 15/39 at the input to the lower threshold comparator. The input impedance of the comparator itself will lower this figure by an additional factor of 2/3. Thus in principle any channel number in the pulse height distribution can be related to the magnitude of its corresponding summed anode pulse and therefore to the MCP gain.

In practice the calibration is obtained by measuring the cutoff points in channel numbers for a number of discriminator voltage settings. A least squares fit to the points gives the parameters necessary to convert a channel number to equivalent discriminator setting. The precision of this technique is determined by the errors in component values and uncertainty in the exact channel of the cutoff point. The errors in component values are dominated by the 20% tolerance values of the charge preamplification capacitors (C1 in figure 3-2), with the resistive components all having 2% tolerance.

The modal gain of a given pulse height distribution is usually defined as the value of the gain at the Gaussian saturation peak (Rogers and Malina 1982). By fitting a Gaussian to the PHD peak, its position in channel numbers of the modal gain can be determined from detector PHDs. This figure may then be related to the actual MCP gain using the procedure outlined.

Initial tests with the system up to this maximum potential indicated that at gains of the order of 5×10^6, the preamplifiers were saturating for a relatively large proportion (10-20%) of real pulses. The gain of the preamplifier charge stage was therefore lowered by changing the value of the feedback capacitor C1, shown in figure 3-2. This adjustment effectively moves the saturation peak of the PHD towards the middle section of the amplifiers' dynamic range, from a previous position where real pulses were being rejected by the upper discriminator.

6.3) Pulse Height Distributions

In order to study the gain saturation characteristics of the MCP configuration, a series of pulse height distributions were obtained at various plate potentials. These distributions were obtained with a uniformly illuminated photocathode giving a nominal output count rate of 3000 cs^{-1} at a lower discriminator level of 0.4 V. In the case of (b) and (c) the discriminator level was lowered to 0.3 V, to resolve the saturation peak. The proximity focussing voltage for these measurements was kept at 300 V, to minimise the contribution of photocathode noise to the distributions.

Figures 6-1(a) to 6-1(f) show the MCP pulse height distributions for overall MCP potentials ranging from 2.85 kV to 3.5 kV. The abrupt cutoff at low bin numbers is due to the lower discriminator. The onset of pulse saturation starts at 2.9 kV, or around 1.45 kV across each of the plates at a gain of 2×10^6 and lies between the values of 3.2 kV and 2.9 kV reported for similar MCP configurations in ITL 40 mm intensifiers by Lyons and Read (1983).

Full saturation occurs around 3.15 kV with a FWHM of 55%. The FWHM values of the distributions displayed in 6-1 are shown in figure 6-2. The diagram indicates that the optimum FWHM value of 45% is obtained between 3.2 kV to 3.4 kV and at potentials above 3.4 kV the saturation peak starts to broaden. This is primarily due

Figure 6-1: Pulse height distribution variation with applied MCP potential.

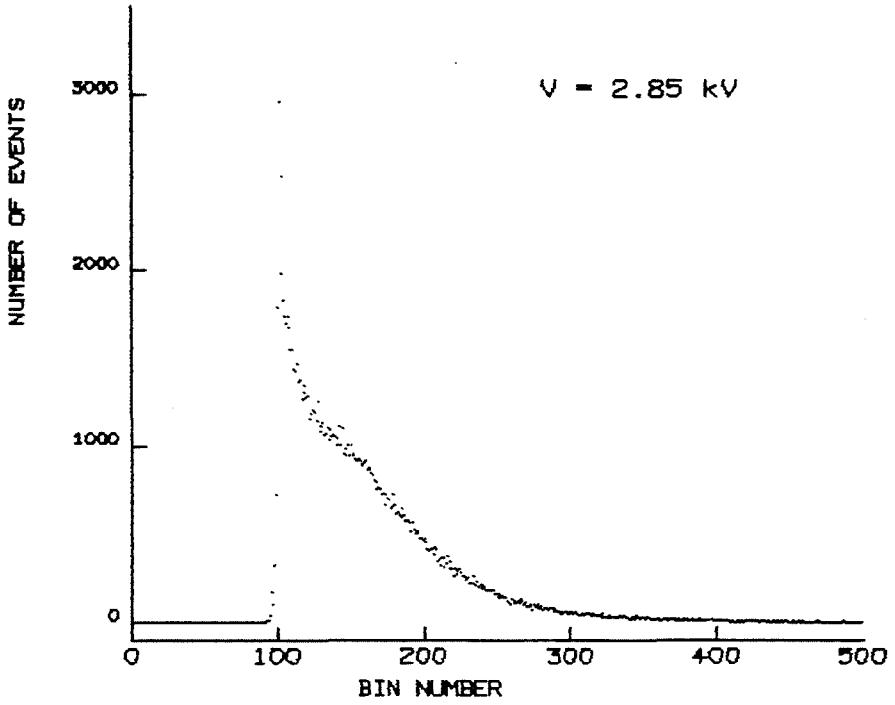

(a) : Discriminator level = 0.4 V

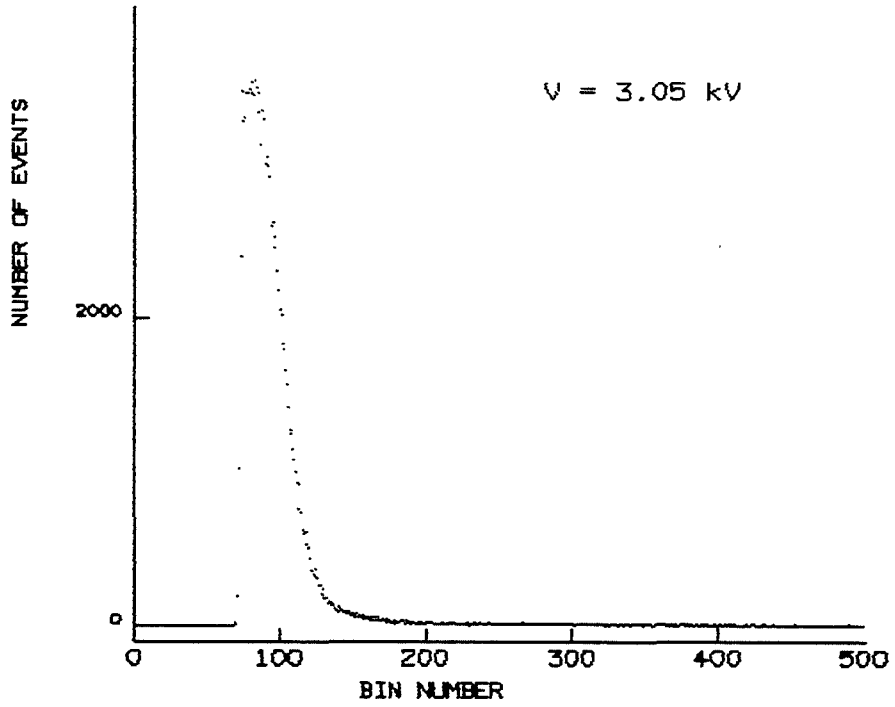

(b) : Modal gain = 2.3×10^6, discriminator level = 0.3 V.

Figure 6-1: Pulse height distribution variation with applied MCP potential.

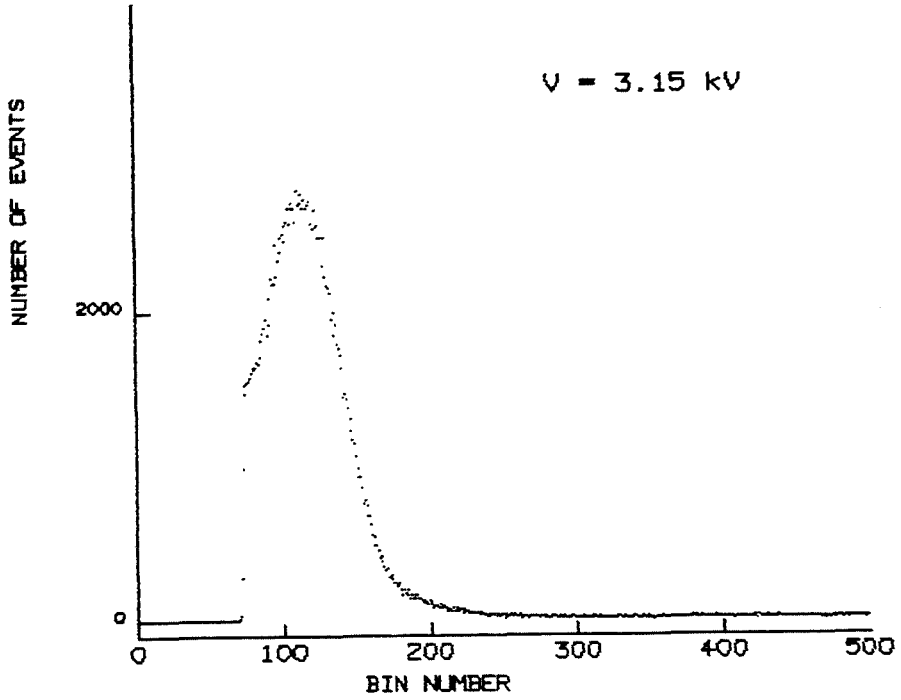

(c) : Modal gain = 3.1×10^6, discriminator level = 0.3 V.

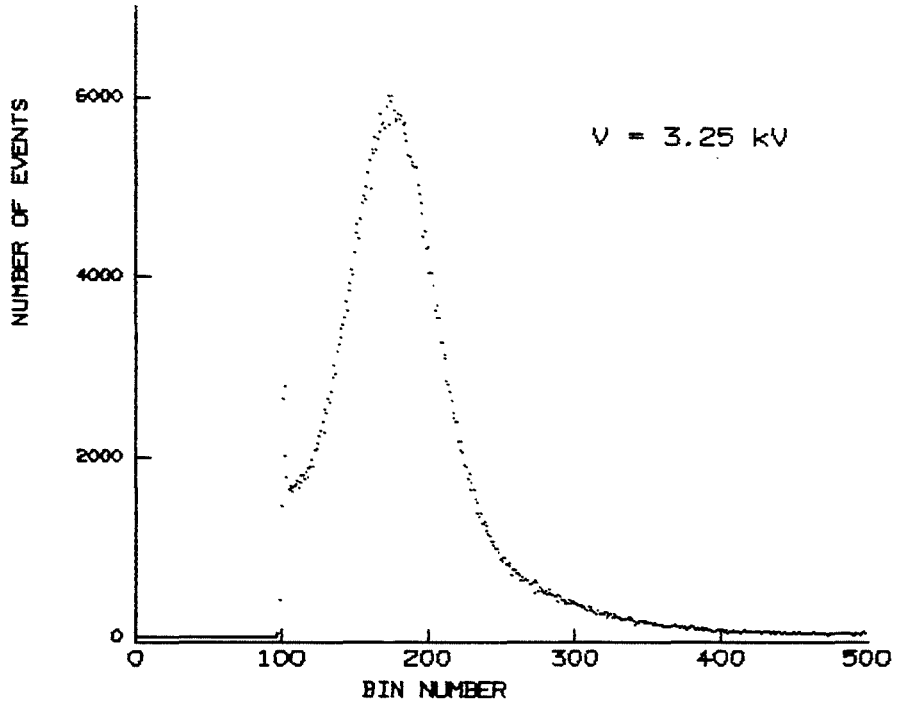

(d) : Modal gain = 4.6×10^6, discriminator level = 0.4V.

Figure 6-1: Pulse height distribution variation with applied MCP potential.

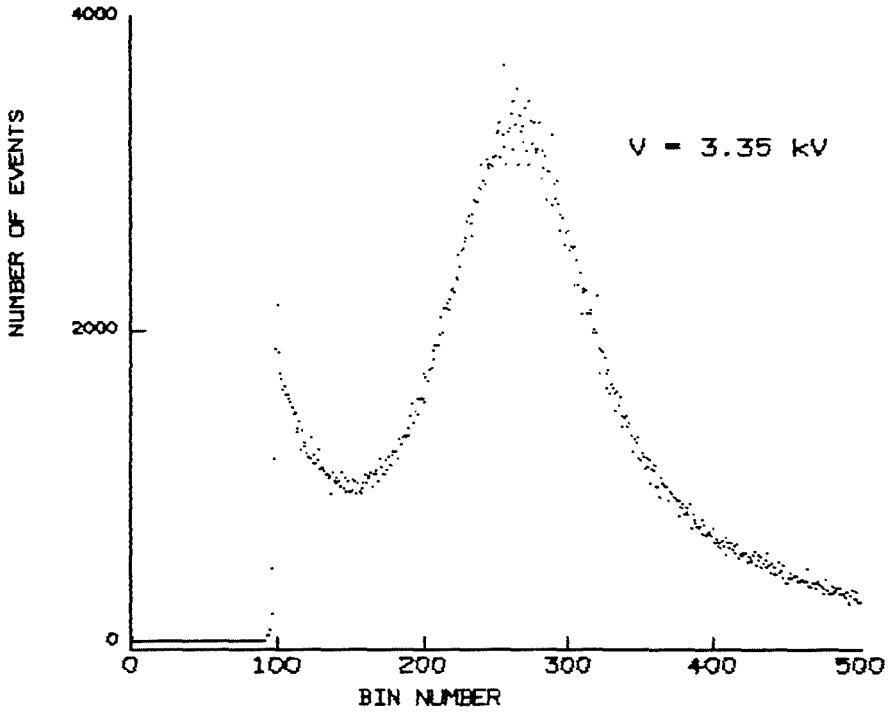

(e) : Modal gain = 5.5 x 10^6, discriminator level = 0.4 V

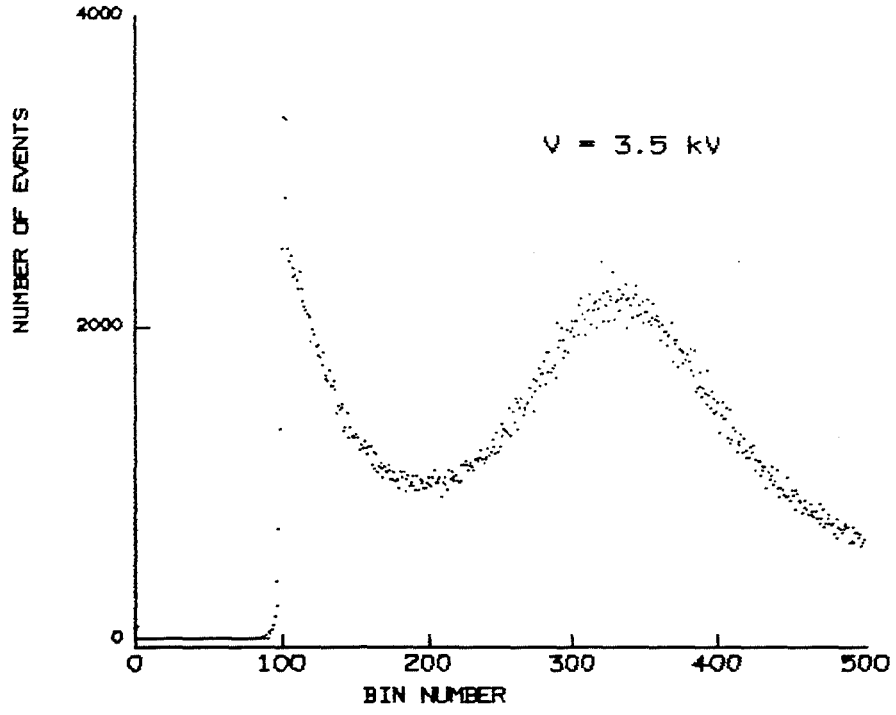

(f) : Modal gain = 8.4 x 10^6, discriminator level = 0.4 V.

Figure 6-2: Pulse height distribution FWHM values for saturated peaks in figures 6-1(c) to 6-1(f).

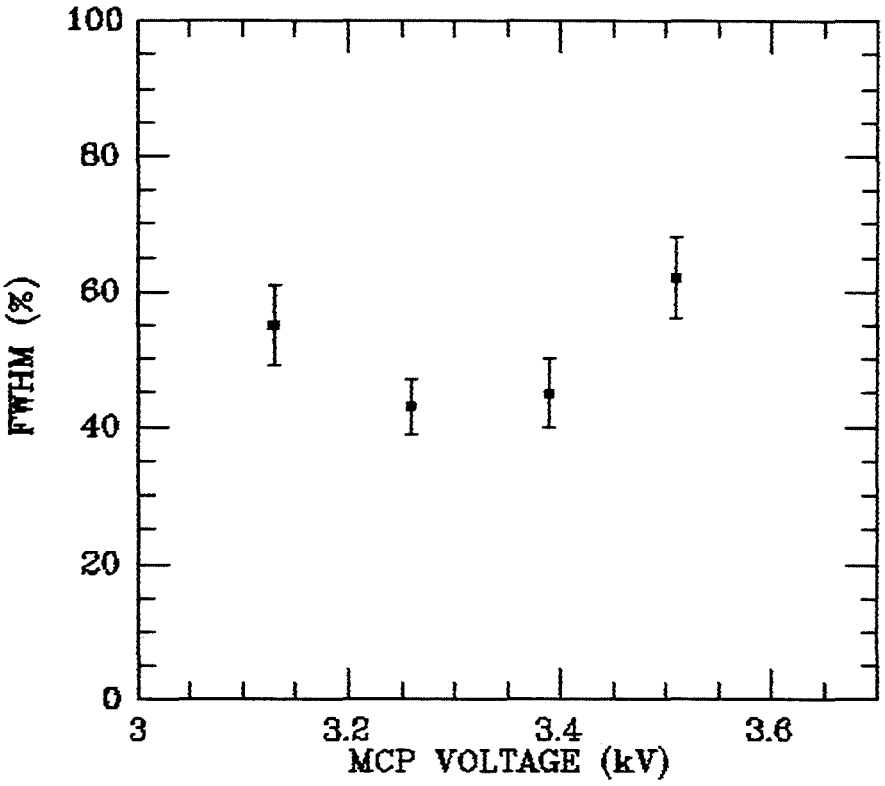

to increased MCP dark noise, caused by increased field emission within the channels. Some ion feedback activity may also be a contributory factor, since the production of further secondaries at the interplate gap could cause broadening of the pulse height distribution. If there were a gap between the plates arising from non-planicity or distortion of the plates, it would result in an appreciable variation in gain values and thus a wide pulse height distribution. The relatively narrow values of FWHM obtained show that there is probably minimal spreading of the charge cloud at the interplate gap above that expected.

Siegmund et al. (1983) report an optimum FWHM value of 32% at 4.5×10^6 for a similar Mullard plate configuration, with a figure of 58% at 10^6. His figures were obtained before sealing off the tube after baking and plate scrubbing. The absence of a noise contribution from the photocathode results in a better pulse height distribution degraded only by MCP noise and may be a factor in the lower PHR value.

The peak to valley ratio follows the same general trend as the pulse height FWHM, giving optimum signal to noise in the region between 3.2 kV and 3.4 kV. The PVR is determined by the output count rate and will be discussed in more detail in a later section.

6.4) Gain

The voltage-gain relationship, for the displayed PHDs and their intermediate MCP voltages, is plotted in figures 6-3 and 6-5(a) with

linear and logarithmic gain scales respectively. Figure 6-3 also shows the absolute calibration errors calculated from the combination of fitting the distributions and the preamplifier component tolerances using equation 3.4. The gain results are in agreement with those of Siegmund et al. (1983) who report an upper limit of 7×10^6. This is around the upper gain value obtained with the IPD at an applied MCP voltage of 3.4 kV, above which the pulse height distribution starts to broaden.

Schimdt and Hendee (1966) found gain to be linearly proportional to the normalised field in the saturated gain regime. Two plates clamped together may be regarded as approximately one plate of length 2 x l, assuming no large discontinuities between the plates. Thus the gain characteristics obtained should show linearity with the applied MCP voltage for fully saturated distributions. Figure 6-4 shows a straight line fit to those gain values showing full saturation and indicates reasonable agreement with the theory.

Evidence for a rapid increase in the level of ion feedback, normally characterised by a sharp turnoff in the voltage-gain relationship, is not apparent. If the broadening of the gain saturation peak at higher potentials is related to the onset of ion feedback, the condition might occur if the MCP potential was taken any higher.

Figure 6-3: MCP gain-voltage relationship where; photocathode to MCP potential = 300 V, count rate = 3000 cs^{-1} and discriminator level = 0.4 V.

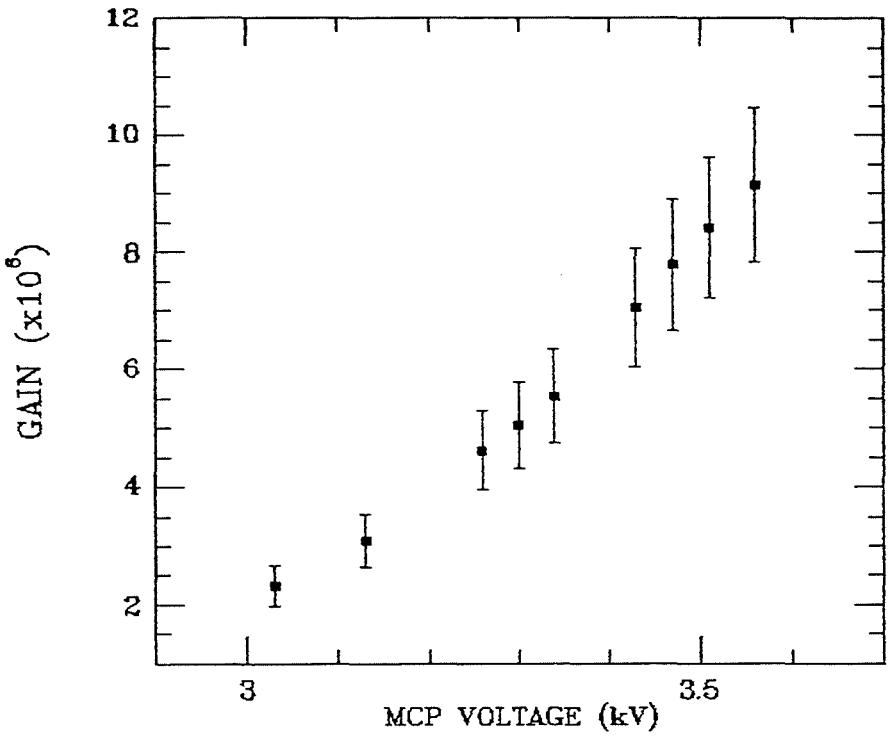

Figure 6-4: Straight line fitted gain characteristic.

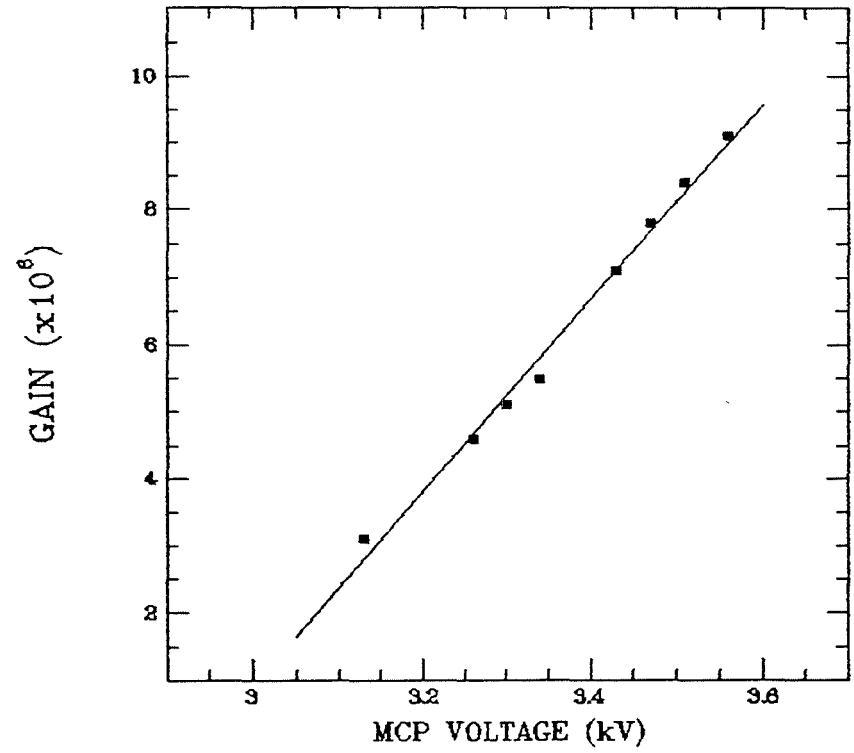

Figures 6-5(a) to 6-5(f) show the gain-voltage characteristics for a number of configurations tested during the device assessment. These characteristics are all related to a particular figure of MCP to anode potential. They were obtained as part of an investigation into the dependence of resolution upon this parameter. The results shows the the MCP gain curve to be reproducible for different tube operating parameters.

The curves in (b) to (f) were obtained over a period of two months and so assuming negligible changes in preamplifier component tolerances over this period, the relative errors between curves should be due to errors in fitting the distributions alone. The data in (a) is that displayed in figure 6-3 and was obtained a year later. When all the gain characteristics are overlaid as in figure 6-6, two features are highlighted.

The voltage-gain characteristics for MCP to anode voltages of 900 and 1000 V appear to give higher gain, by a factor of ~1.5 above the other characteristics for the same MCP potential. The gain characteristic obtained a year after the others gives lower gain values for the same MCP voltages and lies below the main group.

These anomalies are either due to an erroneous value of MCP potential or a real feature of the MCP operational characteristics. The former may be caused by a change of resistance in the voltage divider network for the detector head EHT, or possibly a problem due

Figure 6-5: MCP gain voltage characteristics obtained for different MCP to anode potentials.

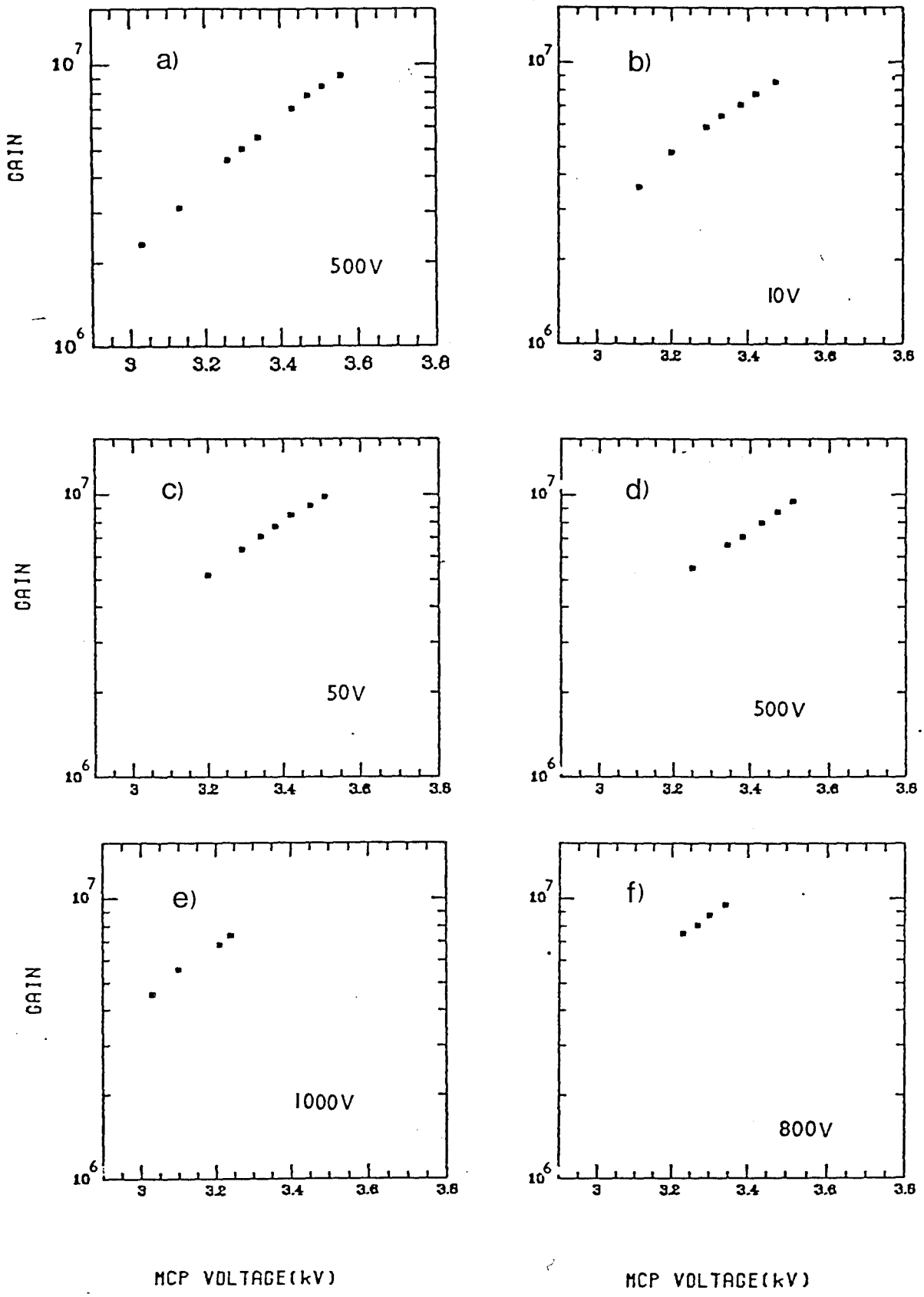

Figure 6-6: Overlaid gain voltage characteristics shown in figure 6-5.

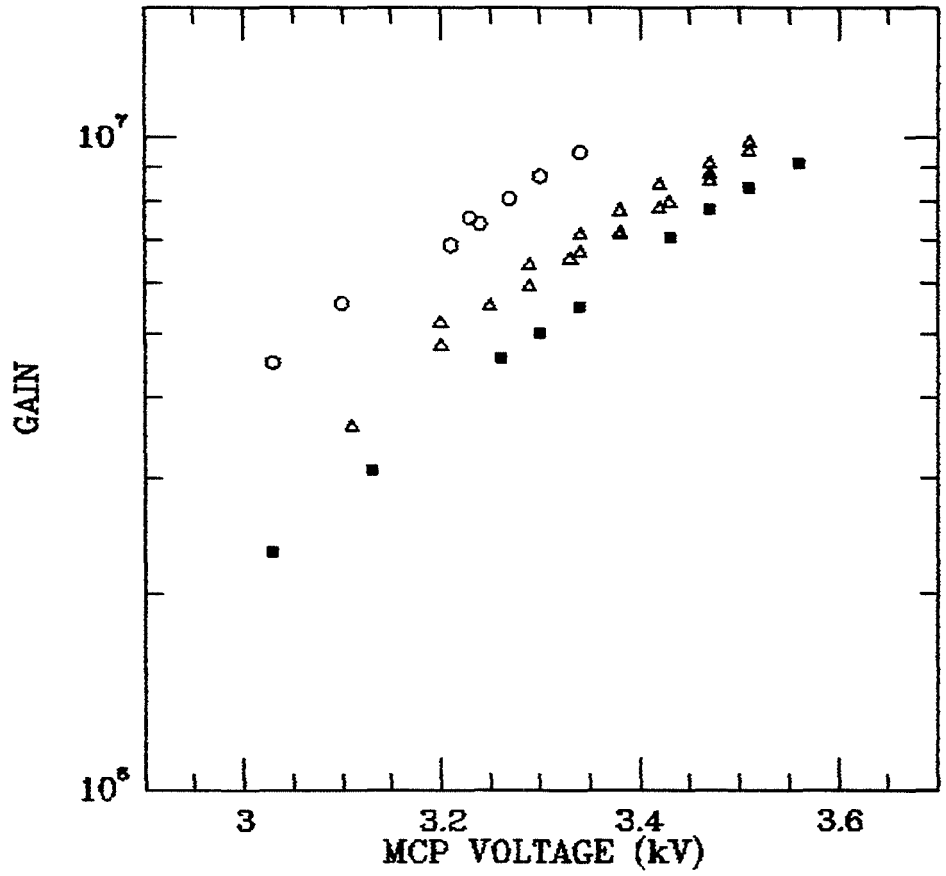

■ Characteristic obtained with anode bias of 500 V (fig. 6-3).

△ Characteristics obtained with anode bias of 10-500 V.

○ Characteristics obtained with anode bias of 900-1000 V.

to operating the EHT supply around its upper limit. It seems unlikely that it is due to a major component failure since a large change in resistance would produce an observable change in the detector performance. The power supply is specified as stable up to overall potentials 4.5 kV and was operated up to this value. The technique used to determine the EHT value was also checked. A consequence of operating with rear end potentials of 1 kV is that overall potentials of up to 5 kV may be necessary. This is obviously in conflict with the unit specification and explains why only four gain points, at lower potentials, were obtained for the two gain curves with high rear end bias.

If this is a real phenomena it may possibly be explained by an interaction with the space charge region at the channel output, due to the high electric field (200 Vm^{-1}). There is, however, no appreciable variation in the pulse height FWHM values obtained for the different gain characteristics. This is an area which requires further investigation with suitable compact EHT units able to supply in excess of 5 kV.

The other important information that can be drawn from the diagram is the apparent drop in gain in the lowest characteristic. The other gain curves were obtained more than a year before the lower characteristic with an estimated extracted plate charge of the order of 10^{11} counts. This figure covers the estimated time for which the detector has been operational at a mean count rate of 10^{3} cs^{-1}. It does not account for the charge extracted by the photocathode field emission features, since this is uncertain and

therefore may be considerably underestimated.

The drop may be due to a change in component values over the year, but is more likely to be due to a drop in the MCP gain. It is unwise to compare this drop in gain with previous MCP lifetime tests due to the experimental nature of the tube and consequently the varied operating conditions to which it has been subjected.

6.5) Dark Noise

The dark current performance of the plates was evaluated by shorting the photocathode terminal to the front MCP terminal. With no accelerating field, any photoelectrons from the photocathode should be stopped at the Al_2O_3 layer on the input MCP. Images for overall MCP potentials of 1.6 kV, 1.65 kV and 1.7 kV were obtained, with a 1024 x 64 pixel format being used for these images. These voltages correspond to the normal operational range of the plate configuration for stable saturated high gains. A lower discriminator level of 0.2 V corresponding to a gain of 1.4×10^6 was used for the signal processing. Figure 6-7 shows three contour plots for images integrated at each of the three potentials. The contour levels have been chosen to highlight both the general background level and the main features of the images. All three images show evidence of hotspot activity arising from channels. This activity increases in intensity with the applied MCP potential. The area seen around cross section 60 correlates with a similar area of activity seen in detector dark noise images. It should be noted that this activity seems to originate around the

Figure 6-7: Contour plots of MCP dark noise for MCP potentials of (a) 3.6 kV, (b) 3.65 kV and (c) 3.7 kV.

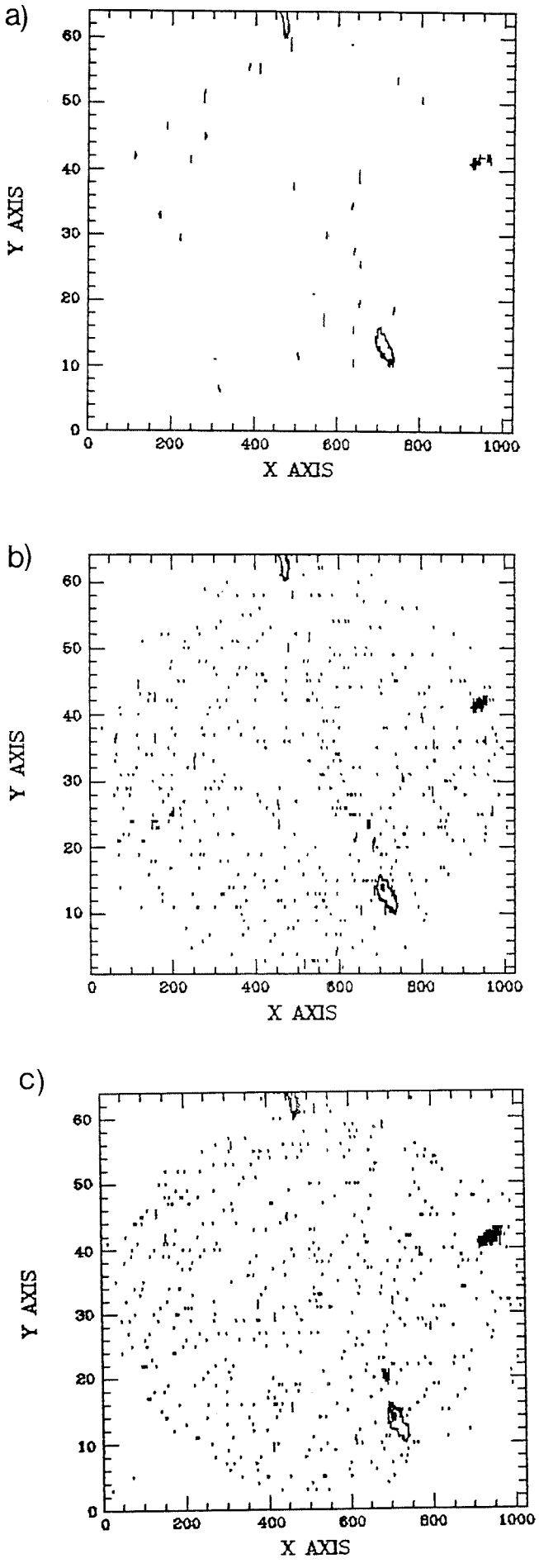

perimeter of the MCP, on the periphery of the area illuminated by the photocathode. This suggests it may be a result of field emission arising from contact with the plate mounting. This could be caused by some degree of plate damage, interaction with the mounting ring, or activity due to residual gas trapped in channels over the contact area (Armentrout 1985). The activity peaks in cross section 64 and has a FWHM of 5 (40μm) channels in this cross section. Comparison with widths of other defects is difficult since the system resolution is very broadened at the periphery of the field.

The area of activity seen at the right hand side of the image around cross sections 40 is on the periphery of the area illuminated by the photocathode hotspot treated by ITL. It seems likely that the process of removing the feature damaged the front MCP slightly, giving rise to this hotspot activity. In detector images this defect is associated with a mild hotspot.

The area of activity seen around cross section 10 is the most intense area of activity in all three of the images and consists of a central peak with broad wings. This area of activity does not correspond to an observed defect in detector dark images. The higher discrimination level for normal operation probably rejects most of the noise from this defect, especially if it is mainly negative exponential noise.

The dark count figures indicate that as voltage increases the hotspots become more active, while there is only a small change in dark count in quiet areas of the plates. The figures for the central hotspot free region are of the order of the 1 $cs^{-1}cm^{-2}$ ($\sim 20^{o}C$), a typical figure for MCPs, after the effect of the lower discriminator cutoff is considered. Overall count rates range from 1.2 $cs^{-1}cm^{-2}$ to 2.2 $cs^{-1}cm^{-2}$ for the displayed images, indicating that the hotspot activity is localised and not a dominant feature of the images.

Figure 6-8(a) and (b) show the dark count pulse height distributions for plate potentials of 1.6 kV and 1.7 kV, respectively. The distribution in figure 6-8(a) for 1.6 kV consists of a noise tail and a small hump, due to the onset of channel saturation. In figure 6-8(b) there is a small peak due to channel saturation with a modal gain of 4.6×10^{6}. The dark noise count rates encountered are not high enough to explain the saturation in terms of the recovery times of individual channels due to high point source count rates. Therefore the activity probably arises from localised gain saturation in channels showing hotspot activity or from some interaction with the mounting hardware, causing field emission. The modal gain of 4.6×10^{6} corresponds to the values in figure 3-2 for operation of the MCPs at an applied potential of 3.4 kV.

Figure 6-8: Pulse height distribution of MCP dark noise.

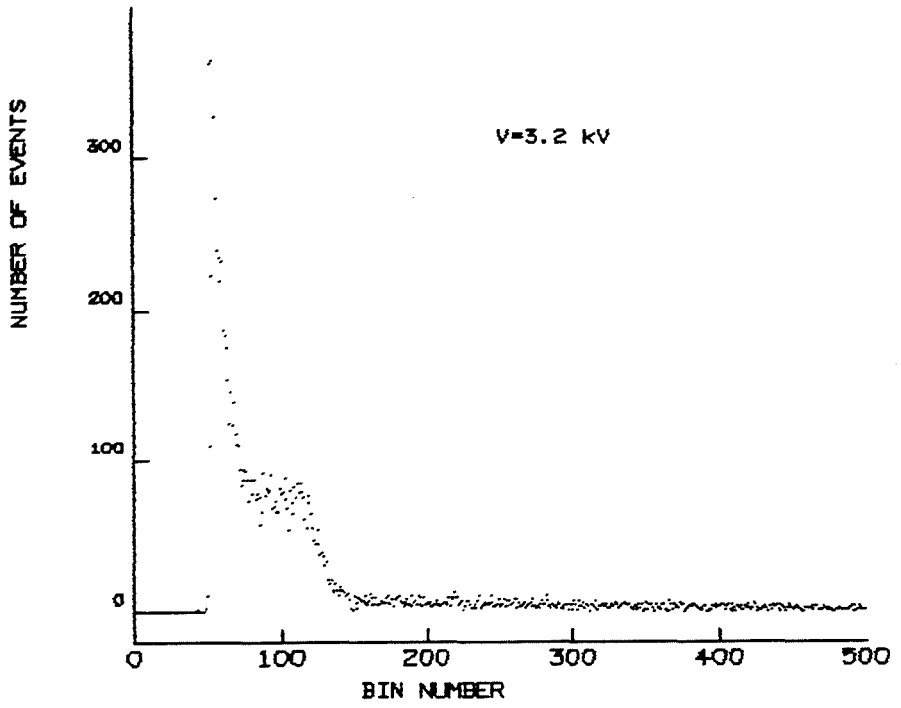

(a): MCP potential = 3.2 kV, Discriminator level = 0.2 V.

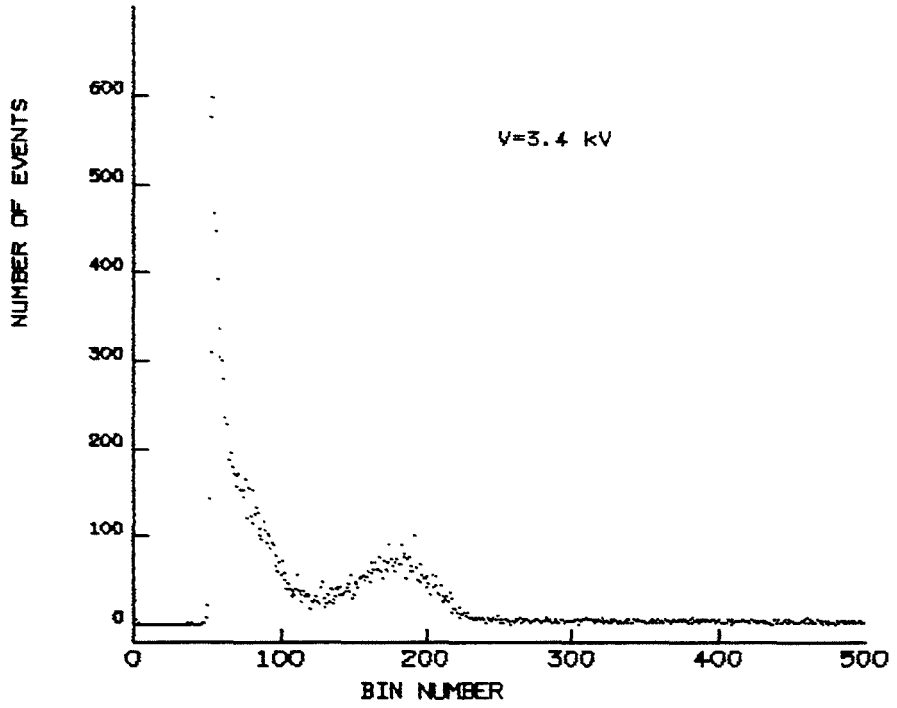

(b): MCP potential = 3.4 kV, Discriminator level = 0.2 V.

With the detector operating in an uncooled environment, the contribution of noise from the MCPs is not serious, in comparison with that from the photocathode. For a cooled tube having a photocathode with minimal cosmetic defects, a noisy MCP would become the principle source of image defects. Siegmund et al. (1984) report that MCP hotspot activity may be significantly reduced by UV scrubbing at high gain, following baking of the plates. Adoption of this scrubbing technique after baking, prior to sealing the tube could provide an improvement in the MCPs imaging performance.

6.6) Count Rate Performance

The relationship between the input and output current of the MCP configuration is an important parameter defining the overall photon counting performance. The variation of gain and pulse height resolution with input current were therefore investigated at proximity focussing voltages of 300 V and 400 V. The tests were carried out in the time period corresponding to the the gain curve shown in figure 6-3. An applied potential of 3.38 kV across the MCPs was used, giving a nominal gain of 6×10^6. The detector was uniformly illuminated with a green LED source and the output count rate determined from the number of detected events. A lower threshold setting of 0.4 V was adopted, corresponding to a gain of 2×10^6 and resulted in an increase in the overall detector dark count of 20%. The setting was chosen due to the limitations of the method for obtaining PHDs. At high count rates the dynamic range of the external memory is exceeded very quickly when all the data is

being incremented in one cross-section. In addition, the large number of low level signals resulting from very low threshold settings cause processing errors in the electronics.

Figures 6-9(a) to 6-9(j) show the evolution of the PHD with increasing illumination levels up to 2×10^4 cs^{-1} for a proximity focussing voltage of 300 V. The dark noise in 6-9(a) is the expected negative exponential shape with a higher tail resulting from the lower discriminator level. The distribution shows a small flattened hump superposed on the negative exponential noise distribution. This will arise from saturation of channels by hotspot noise from the photocathode or MCP defect channels. For 10^3 cs^{-1}, corresponding to 800 cs^{-1} at normal operating levels, there is a poorly defined saturation peak with a FWHM value of 117%, measured as twice its half width half maximum value and a peak to valley ratio of 1.6. This is because of the magnitude of the detector dark noise level with respect to the signal and in figure 6-10 the result of subtracting 6-9(a) from 6-9(b) is shown, highlighting the obscured Gaussian saturation peak. From 2×10^3 s^{-1} onwards the distribution is saturated and has a width of 45%. Figure 6-11 shows the variation of FWHM with count rate and illustrates the poor initial figure which improves to 45% and climbs with increasing count rate, although the change is not appreciable in terms of photon counting requirements. Figure 6-12 shows the PVR to increase with output count rate corresponding to the increase in the ratio of real events to dark noise.

Figure 6-9: Variation of MCP pulse height distribution with output count rate, for proximity focussing voltage = 300 V at discriminator level = 0.4V

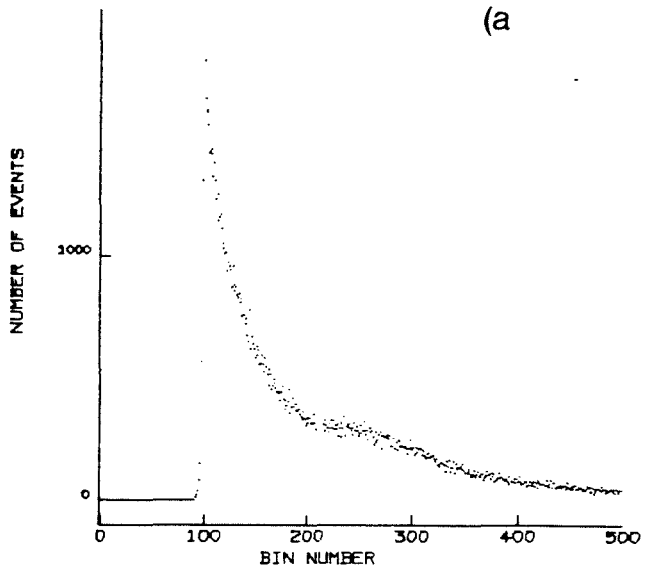

(a) Dark counts.

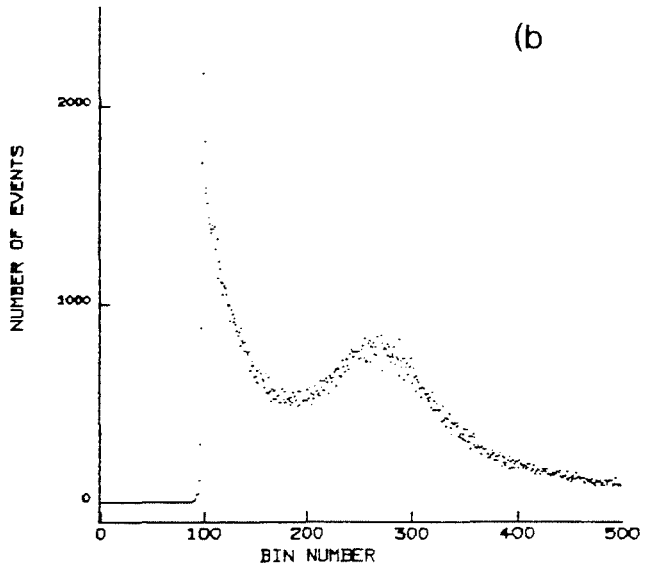

(b) 1000 cs^{-1}.

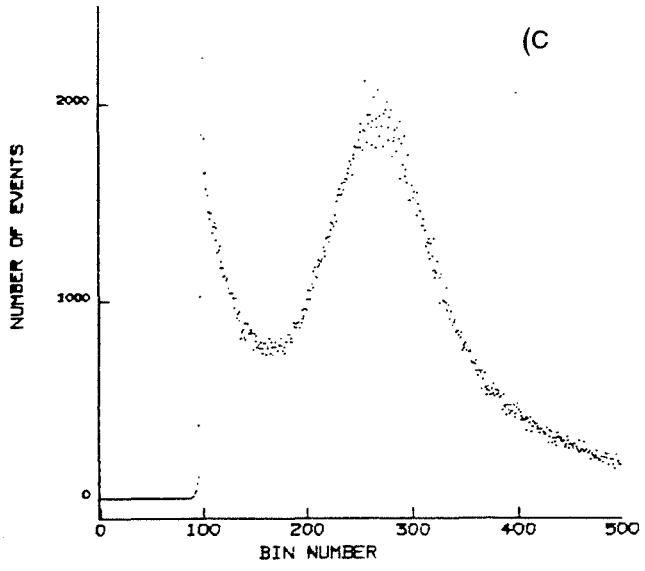

(c) 2000 cs^{-1}.

Figure 6-9: Variation of MCP pulse height distribution with output count rate, for proximity focussing voltage = 300 V at discriminator level = 0.4V

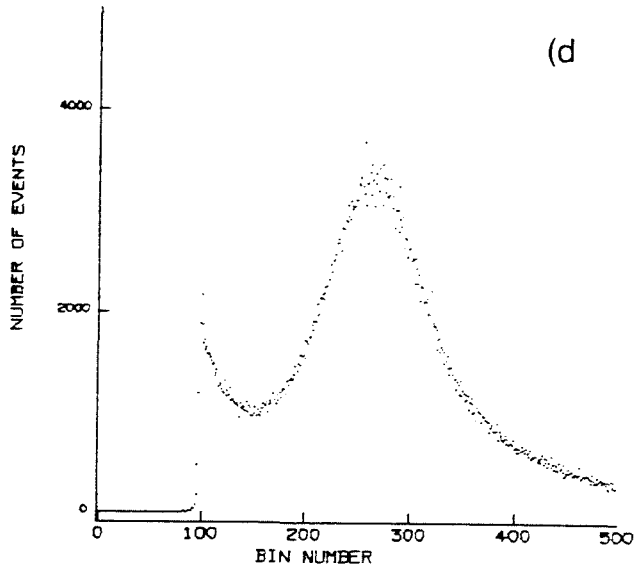

(d) 3000 cs^{-1}.

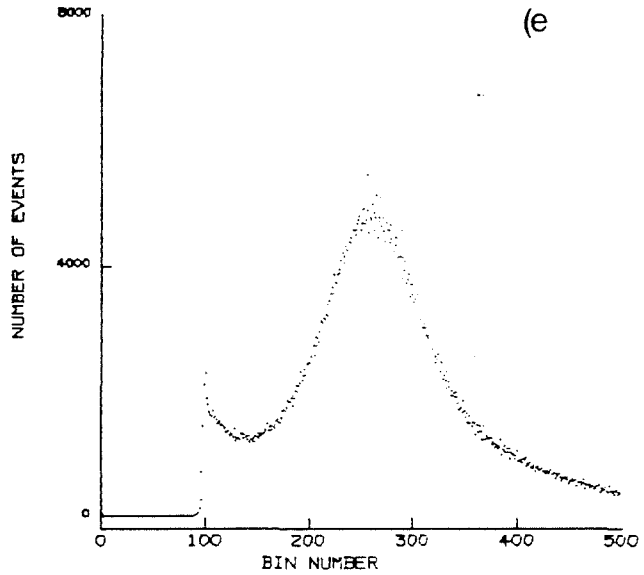

(e) 4000 cs^{-1}.

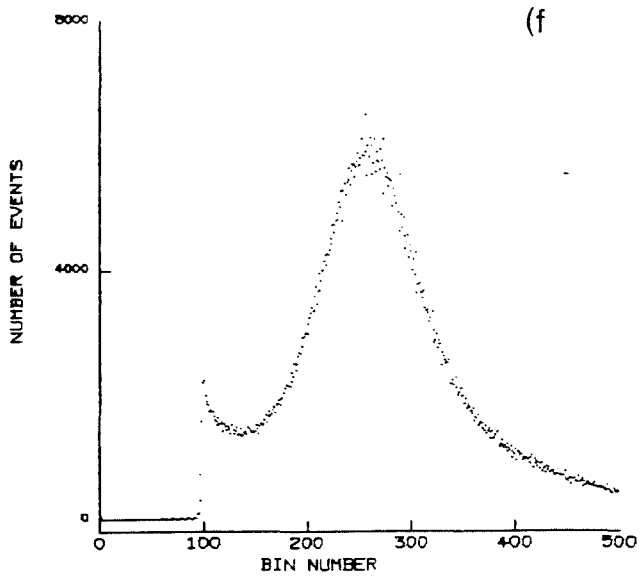

(f) 5000 cs^{-1}.

Figure 6-9: Variation of MCP pulse height distribution with output count rate, for proximity focussing voltage = 300 V at discriminator level = 0.4V

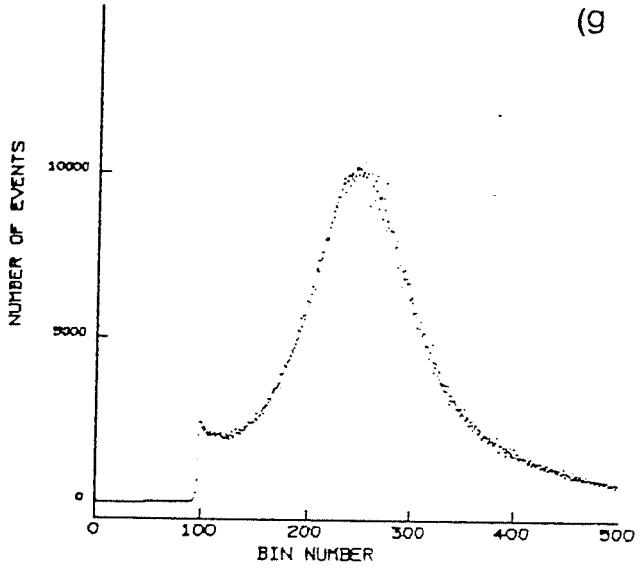

(g) 8000 cs^{-1}.

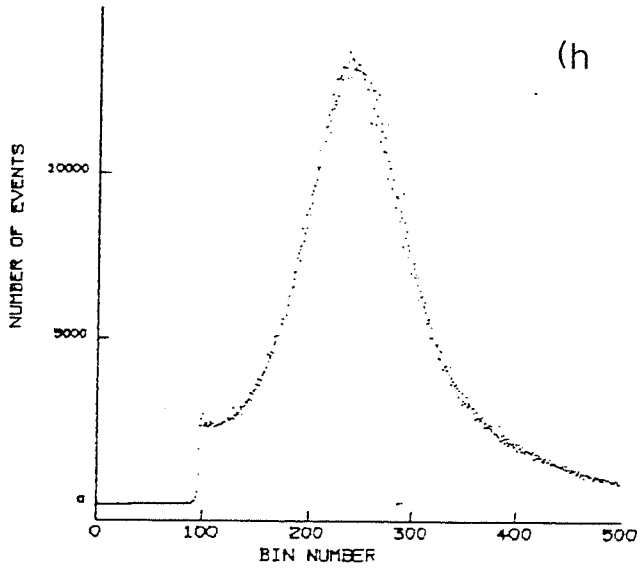

(h) 10000 cs^{-1}.

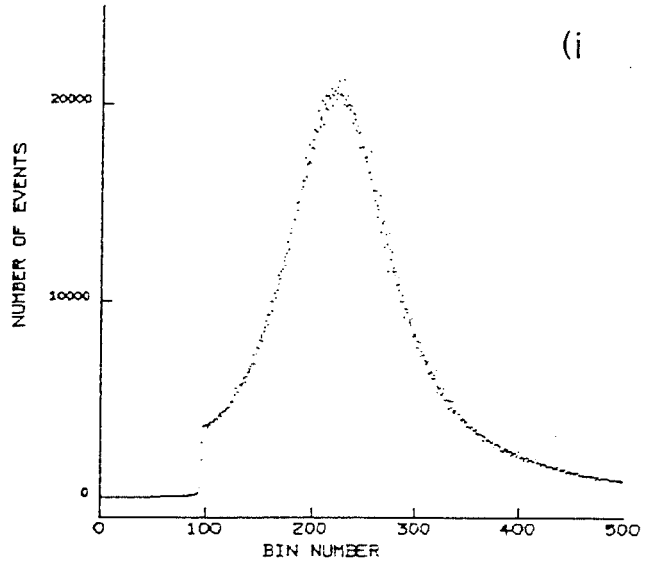

(i) 15000 cs^{-1}.

Figure 6-9: Variation of MCP pulse height distribution with output count rate, for proximity focussing voltage = 300 V at discriminator level = 0.4V

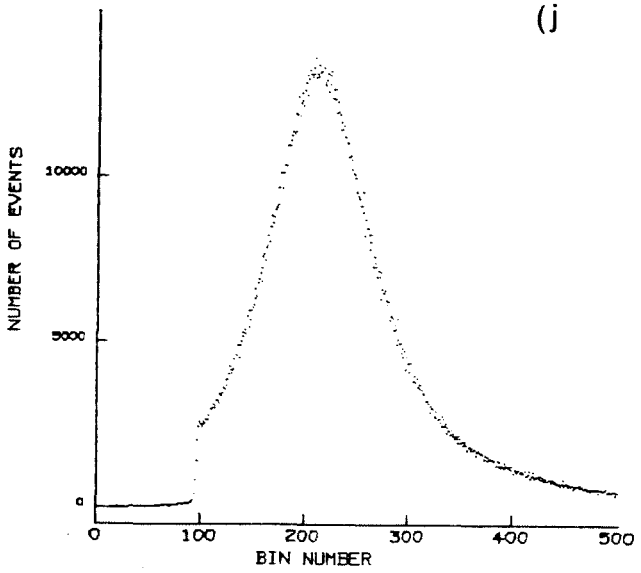

(j) 20000 cs^{-1}.

Figure 6-10: Result of subtracting the dark count pulse height distribution 6-9(a) from low count rate pulse height distribution 6-9(b).

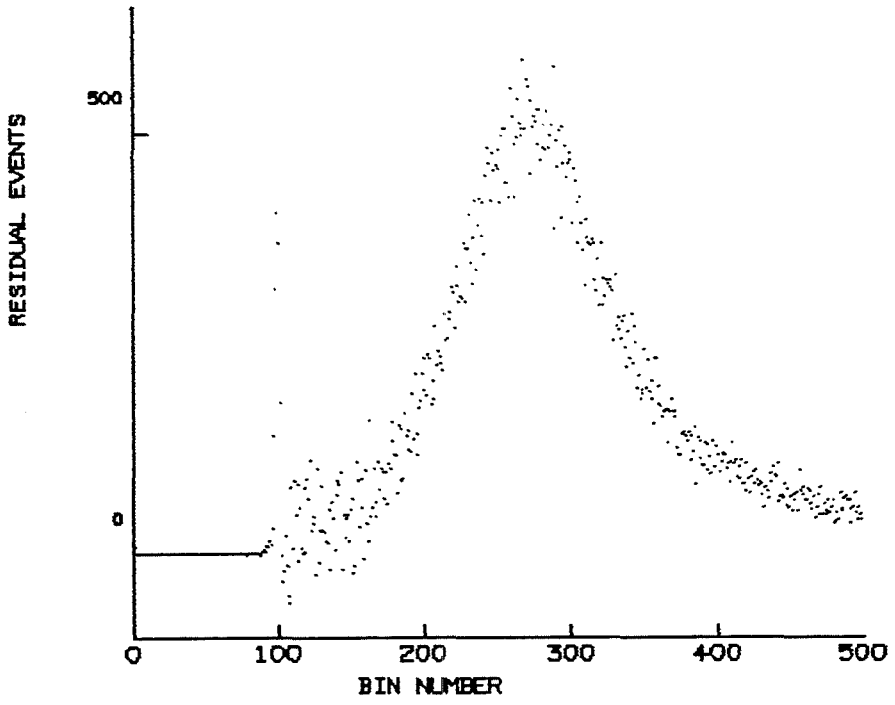

Figure 6-11: Change of saturation peak FWHM with output count rate.

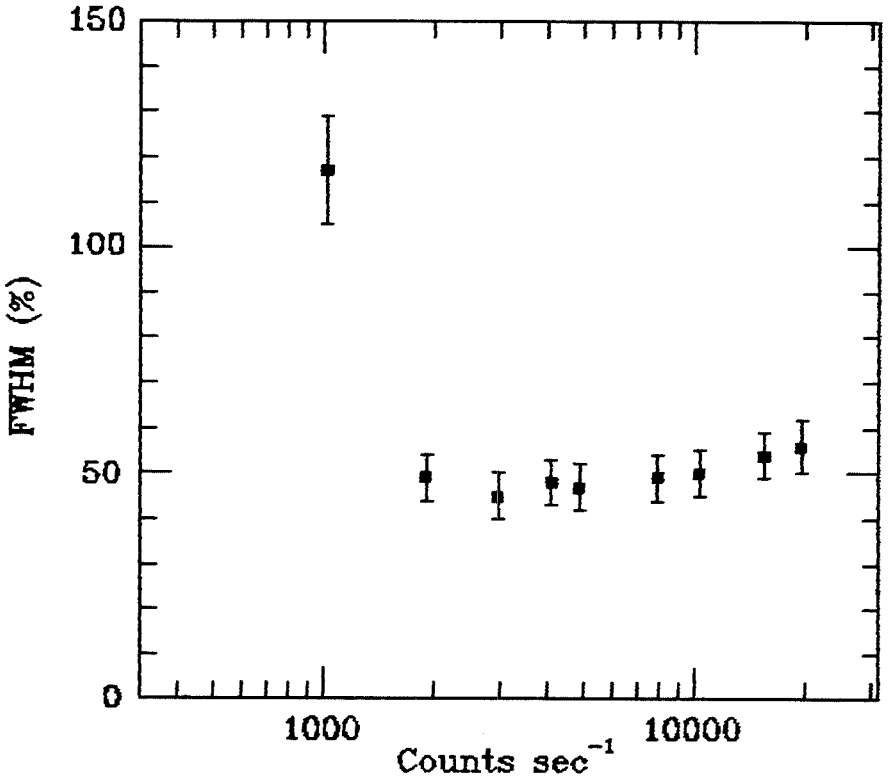

Figure 6-12: Change of peak to valley ratio with output count rate.

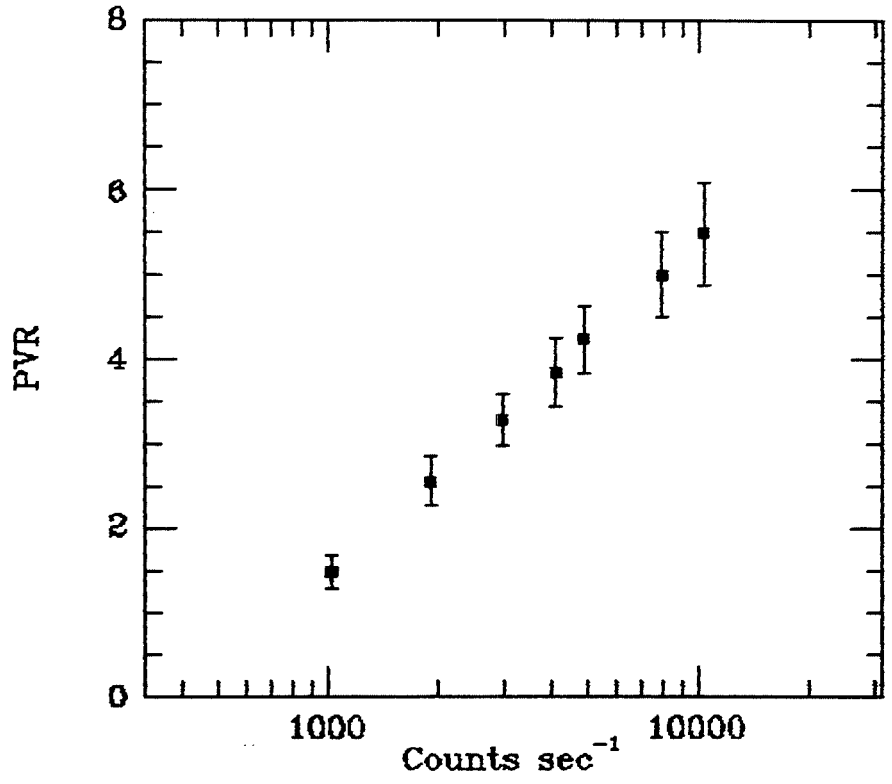

Figure 6-13: Variation of gain with output count rate.

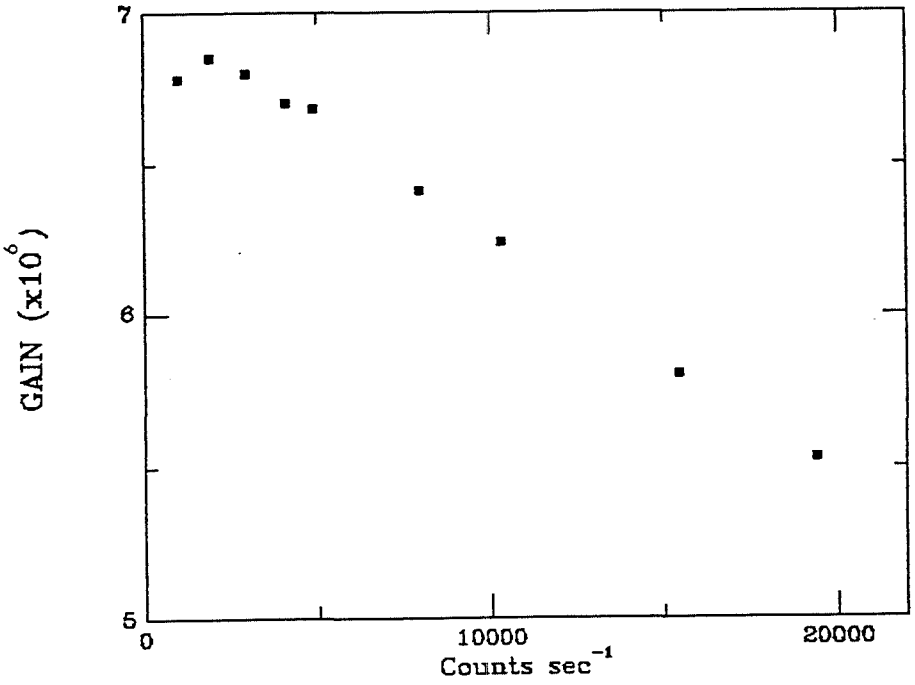

(a) Linear gain scale.

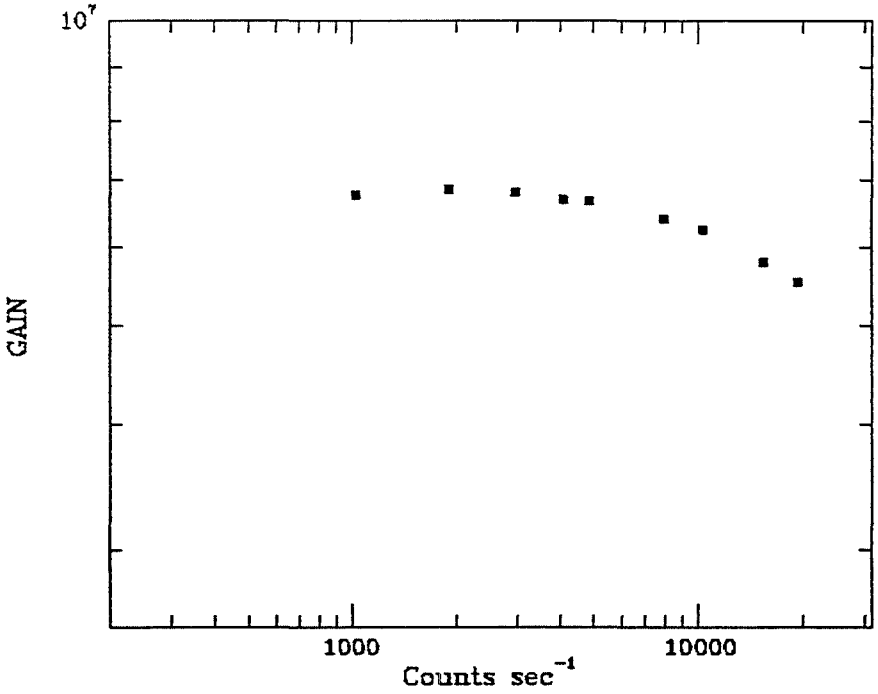

(b) Logarithm gain scale.

Figures 6-13(a) and (b) show the relationship between gain and output count rate, with a drop in gain of the order of 15% over the range 10^3 s^{-1} to 10^4 s^{-1}. Comparison with theory is difficult since precise figures for the input and output charge are required and these are more easily obtained in a demountable system. The main problem is the disparity between the number of pulses detected at the anode and those recorded by the signal processing electronics. High gain pulses below the discrimination level extract charge but are not recorded as events. Mullard (1985) give a typical face to face resistance for these plates as ranging from 60 to 250 MΩ. Taking the value to be 250 MΩ gives an overall count rate ceiling of 6×10^5 before channel recovery time leads to a loss of gain for pulses of 7×10^6 e^-. This figure assumes non-linearity to appear, for a single plate, when the output current exceeds the strip current by 10% and is an order of magnitude higher than the result obtained. If a lower value of MCP resistance is assumed the disparity is even greater.

A more likely explanation is that there is some thermal loading of the output MCP causing a change in bias across the plate configuration and thus lowering the overall gain. The situation arises because the two MCPs are clamped together without an interstage electrode which would allow independent biassing of each plate. The strip power density for a plate at a voltage of 1700 V is 11 mW for an MCP resistance of 250 MΩ and rises to 48 mW for a resistance of 60 MΩ. If a plate heats, it loses resistance, draws more current and thus causes a drop in the current drawn by the

other plate. At the count rates encountered by the system this will lead to the observed drop in gain.

With an increase in proximity focussing voltage to 400 V the problem of dark noise is increased, due to increased hotspot activity and increased photocathode shot noise. This situation is illustrated in figure 6-14 where the general profile remains the same, but the dark count rate has increased by a factor of 10. The slight channel saturation due to hotspots is now also obscured by a higher dark noise level. The variation of PHD with count rate for a proximity focussing voltage of 400 V is shown in 6-15(a) to 6-15(f). The saturation peak is poorly defined below high output count rate levels (~15000 cs^{-1}).

6.7) Conclusions.

The MCP operating parameters discussed show that the overall photon counting performance will, as expected, be degraded by the large amount of spurious photocathode dark noise. The main effect of this noise is to distort the distribution of MCP pulses so that the narrow Gaussian peak required for optimum signal processing is flattened, particularly at low signal levels. The evidence for an underlying Gaussian distribution indicates that a saturated peak would be obtained at low signal levels if the source of noise were not present. The broadening of the pulse height distribution leads to a larger spread of pulse sizes for processing, and thus to a spread in the reference voltage for the ADC units in the processing electronics.

The drop in gain as the output count rate increases means that resolution could be expected to be degraded at these levels. At very high count rates a serious thermal overloading problem could arise and cause irreparable damage to the plates. The inclusion of an interstage electrode together with another feedthrough are, therefore, necessary in order to allow operation of the plates without gain loss as the count rate increases.

Figure 6-14: Comparison of detector dark noise pulse height distributions for proximity focussing voltages of (i) 300 V and (ii) 400 V.

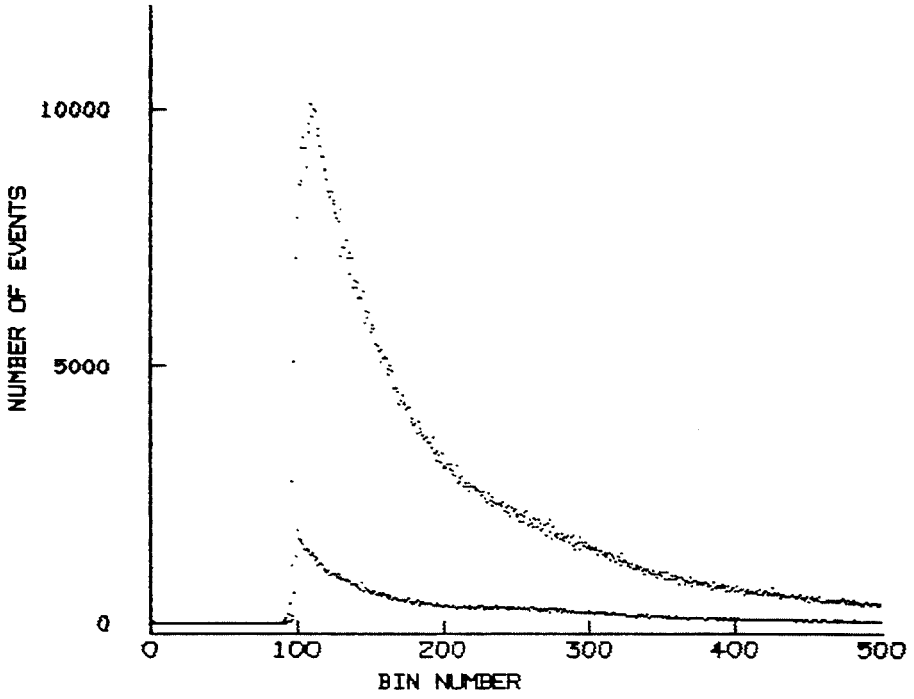

Figure 6-15: Variation pulse height distribution with output count rate for proximity focussing voltage of 400 V at discriminator level = 0.4V.

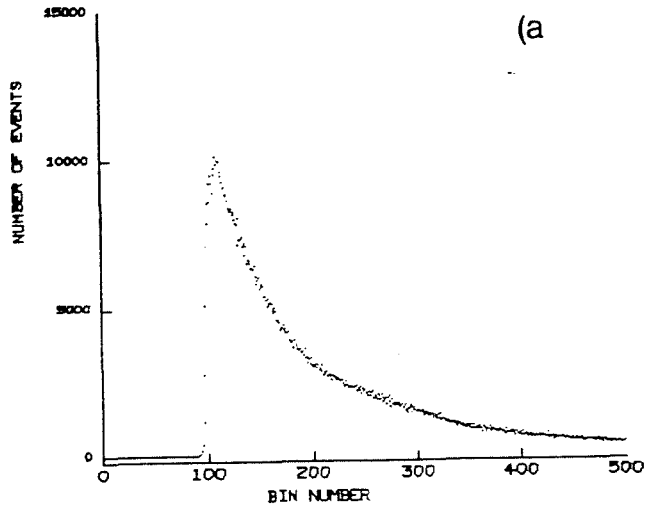

(a) Dark counts.

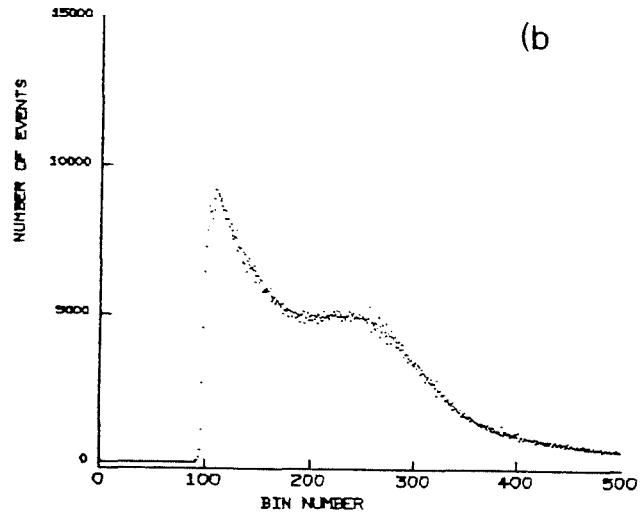

(b) 7000 cs^{-1}.

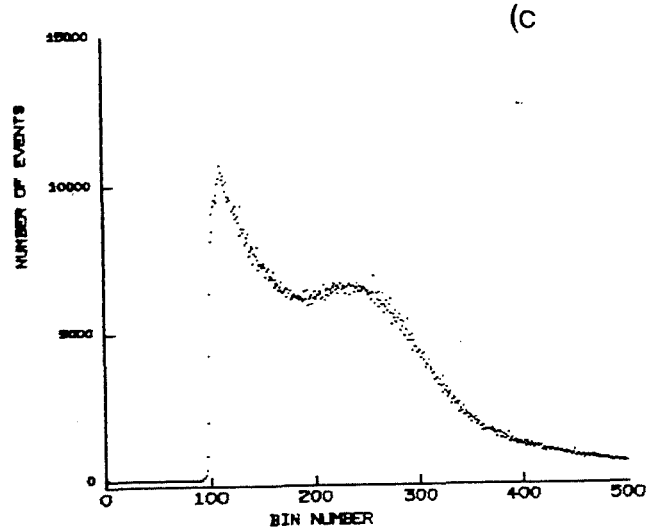

(c) 8000 cs^{-1}.

Figure 6-15: Variation pulse height distribution with output count rate for proximity focussing voltage of 400 V at discriminator level = 0.4V.

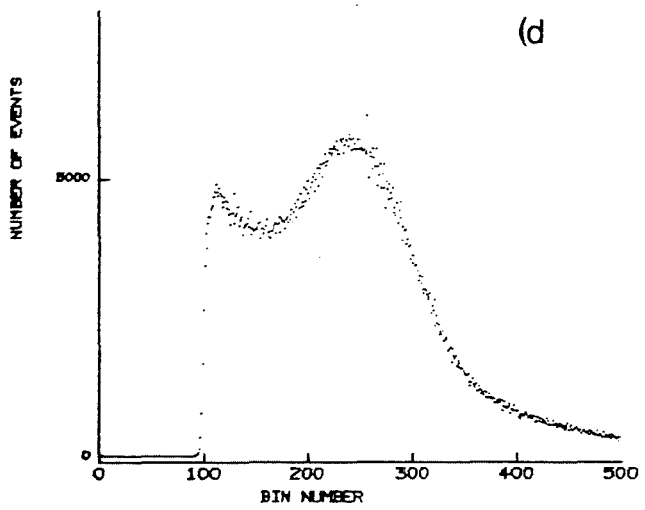

(d) 10000 cs^{-1}.

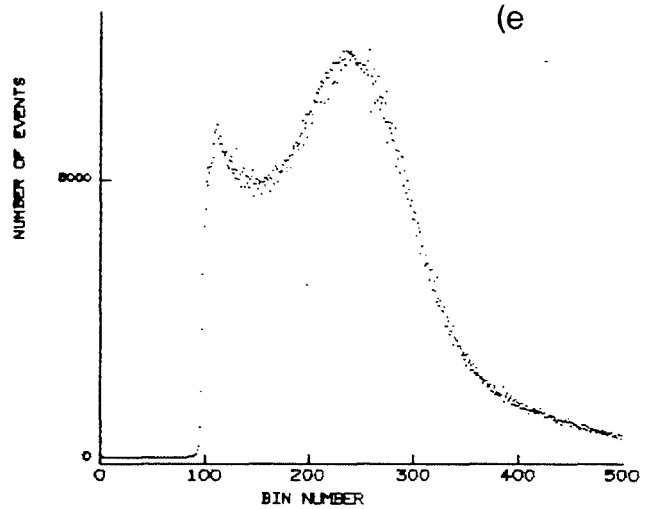

(e) 15000 cs^{-1}.

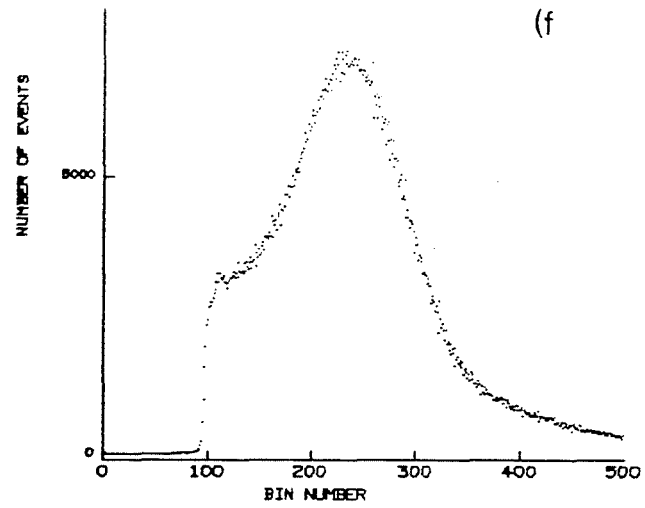

(f) 20000 cs^{-1}.

Chapter 7

7.1) Imaging Theory

The imaging performance of a detector may be analysed by means of linear filter theory applied to optical systems. A system, represented by the operator $S\{\}$, is defined as linear (Dainty and Shaw 1974), if for all inputs $f_1(x,y)$ and $f_2(x,y)$ and constants A and B;

$$S\{Af_1(x,y)+Bf_2(x,y)\} = AS\{f_1(x,y)\}+ BS\{f_2(x,y)\}. \qquad (7.1)$$

As a consequence of this definition, the outputs from a linear system may be considered in isolation as individual elements, with the total system output being a weighted sum of these components. Linear systems are completely specified by their response to an input delta function. In optical systems this is known as the point spread function (PSF). For a linear, stationary system, where the PSF shape is invariant with spatial position, the system may be defined in terms of a convolution where the output is equal to the input convolved with the system PSF. Thus for an output image density at point (x,y) due to a single input point (x_1,y_1), the total input image density will be

$$f(x_1,y_1)\ h(x - x_1,y - y_1), \qquad (7.2)$$

where $h(x - x_1, y - y_1)$ is the system response at the output point (x,y) due to a delta function input at (x_1,y_1).

Therefore, the total image density at (x,y) due to the summation of input points $g(x,y)$ will be

$$g(x,y) = \int_{-\infty}^{\infty}\int f(x,y)\ h(x - x_1, y - y_1)dx_1dy_1. \qquad (7.3)$$

By applying Fourier transforms, this convolution is reduced to

$$G(u,v) = F(u,v)H(u,v). \qquad (7.4)$$

$G(u,v)$ and $F(u,v)$ represent the contributions from each of the input and output image spatial frequencies and $H(u,v)$ is called the transfer function of the system. Working in the domain of spatial frequency makes analysis simpler, since convolution is reduced to multiplication.

Detector PSF profiles are usually Gaussian to a first approximation and are represented in terms of their width, typically the full width half maximum (FWHM) value (ie. 2.345σ). The linear system approach may be extended to give other functions used for the assessment of device resolution.

The line spread function (LSF) may be defined as

$$l(x) = \int_{-\infty}^{\infty} h(x,y_1)\ dy_1, \qquad (7.5)$$

where $l(x)$ is the system's response to an input line function. A detector's LSF is often easier to measure than the PSF, since line widths of arc spectra lines or imaged slit apertures may be easily measured. Within this context the system transfer function is called the optical transfer function. When the PSF is rotationally symmetric the relationships between these functions may be defined in terms of the one dimensional Abell and Hankel transforms (Bracewell 1965). The LSF will be related to the PSF by the Abell transform

$$l(x) = 2\int_x^\infty h(r)(r^2 - x^2)^{-0.5}\, r dr, \tag{7.6}$$

where $h(r) = h(x,y)$ and $r^2 = x^2+y^2$. The optical transfer function $T(\omega)$ is related to the PSF by the Hankel transform

$$T(\omega) = 2\int_0^\infty h(r)J_o(2\pi\omega r)r\, dr, \tag{7.7}$$

and to the LSF by the Fourier transform

$$T(\omega) = \int_{-\infty}^\infty l(x)e^{-2\pi i\omega x}\, dx. \tag{7.8}$$

When the phase and imaginary part of $T(\omega)$ are zero the OTF is completely specified by its modulus, the modulation transfer function (MTF). The MTF may also be defined as the system reponse to an input one dimensional sine wave of spatial frequency and modulation b/a, eg.,

$$f(x) = a + b\cos(2\pi\omega x + x) \tag{7.9}$$

The output will also be a sinusoid of frequency ω, but with a

different modulation. The MTF is thus the ratio of output to input modulation and is dependant on spatial frequency, ie.,

$$MTF = \frac{M_{out}}{M_{in}} \qquad (7.10)$$

where $M_{in} = a/b$ and $M_{out} = \frac{L_{max} - L_{min}}{L_{max} + L_{min}}$.

It should be noted that this will be an approximation to the true performance, if the system is either non-stationary or non-linear. The MTF contributions of its individual elements may be combined by multiplication to give the overall MTF of a detector. This is preferable to consideration of a detector's component PSFs, since they must be combined by convolution to obtain an overall PSF. The MTF therefore provides a convenient method for analysing a detector's resolution, in terms of its spatial frequency reponse. This basic theory allows the derivation of a simple theoretical expression for the MTF which may then be applied to the analysis of detector systems.

Considering a system element to have a symmetric Gaussian PSF defined as

$$P(r) = \frac{1}{\pi \sigma^2} \exp - \left[\frac{x^2}{\sigma^2} \right], \qquad (7.11)$$

the LSF is given by the Abell transform

$$l(x) = \frac{1}{\sqrt{\pi\sigma^2}} \exp-\left[\frac{x^2}{\sigma^2}\right]. \qquad (7.12)$$

The MTF, given by the Fourier transform of the LSF is therefore

$$MTF\ (f) = \exp\ (-\pi^2\sigma^2 f^2) \qquad (7.13)$$

where σ = FWHM/1.66 and f is the unit of spatial frequency, usually defined as line pairs mm^{-1}. With these equations a theoretical MTF may be determined for each individual component of a system, given a value of PSF or LSF. They may then be used to obtain an MTF for the overall system which may be compared with an experimentally determined value for the function.

7.2) IPD Performance

The resolution obtainable with the IPD will be governed by the contributions from the following system elements;

(i) Fibreoptic window of the detector.

(ii) Channel diameter of the MCPs.

(iii) Proximity focussing.

(iv) Resistive anode thermionic noise.

(v) Preamplifier noise.

(vi) Main pulse position electronics errors.

The contribution of each of these components will therefore be discussed for the IPD system in question and a value for the MTF at

5 lpmm^{-1} determined for each component.

7.2.1) Fibreoptic

The fibreoptic window consists of bundles of fibres with a typical diameter of 6 m. The contribution of this element of the system will be minimal compared to the contributions of other system components. Csorba (1981) gives the MTF of a fibreoptic as

$$MTF = 2\,\frac{J_1(2\pi fD)}{2\pi fD}, \qquad (7.14)$$

where J_1 is the first order Bessel function. With the assumption of a Gaussian PSF, this may be written as

$$MTF = \exp-(3.33\ f^2D^2). \qquad (7.15)$$

The derivation of this function assumes round apertures for the fibres and zero crosstalk between adjacent fibres. With an MTF of 0.997 at 5 lpmm^{-1}, the contribution of the fibreoptic window will be minimal.

7.2.2) MCP Channel Diameter

The previous expressions are also applicable to MCPs which present a similar problem (Eberhardt 1981). The detector MCPs have channels of diameter 12.5μm, which gives an MTF of 0.987 at 5 lp/mm using equation 7.15. In this particular system, in common with the fibreoptic, the MCP channel size is not, therefore, a major system

consideration. An example of a situation encountered as the detector's readout resolution approaches that of the MCP channel size is the NASA MOSAIC camera. Weisstrop et al. (1985) have shown simulated images from an MCP-CCD detector where the high resolution CCD images are significantly degraded by both the MCP and fibreoptic stages of the camera.

7.2.3) Proximity Focussing.

The proximity focussing biplanar lens between the photocathode and the first MCP is a major contributor to the value of the overall detector resolution. McWhirter et al. (1982) state this to be the limiting factor in their IPD design, for a 25mm active diameter device. Eberhardt (1977) derives the PSF of a proximity focussed lens as;

$$\frac{P(r)}{P(0)} = \exp \frac{-r^2 V_g}{4L^2 V_r} \qquad (7.16)$$

where L = the photocathode to MCP gap,

V_g = voltage across photocathode to MCP gap,

V_r = mean radial emission energy for photoelectrons,

P(o) = the normalising factor $\frac{V_g}{4L^2 V_r}$

The modulation transfer function for a proximity focussed lens is derived from the Hankel transform of the PSF and may be expressed as

$$M(f) = \exp(-4\pi^2 L^2 f^2 V_r V_g^{-1}), \qquad (7.17)$$

where f is the spatial frequency in line pairs per unit length. The PSF has a variance given by $\sigma^2_{PSF} = 2L^2 V_r V_g^{-1}$, assuming a Maxwellian distribution for the radial emission energies of photoelectrons and so its full width half maximum value may be written as

$$PSF_{FWHM} = 3.33L(V_r V_g^{-1})^{1/2}, \qquad (7.18)$$

where V_r is the average radial emission energy of the photoelectrons.

Figure 7-1 shows the variation of the PSF FWHM with photocathode to MCP gap voltage calculated from equation 7.18 using values of V_r given by Eberhardt (1977) for blue, white and red light. The curves illustrate that in the case of a detector limited only by the proximity focussing, resolution improves with longer wavelengths and higher gap voltages.

Also shown in figure 7-1 are the PSF FWHM variations for the same values of V_r derived from the equations used by McWhirter et al. (1982). Comparison of the two sets of curves show the latter PSFs to be 10μm narrower. This is due to the fact that

Figure 7-1: Theoretical variation of the proximity focussing PSF (FWHM) with gap voltage for Maxwellian and Cosine photoelectron energy distributions.

——— Maxwellian distribution (Eberhardt 1977).
..... Cosine distribution (Csorba 1977).

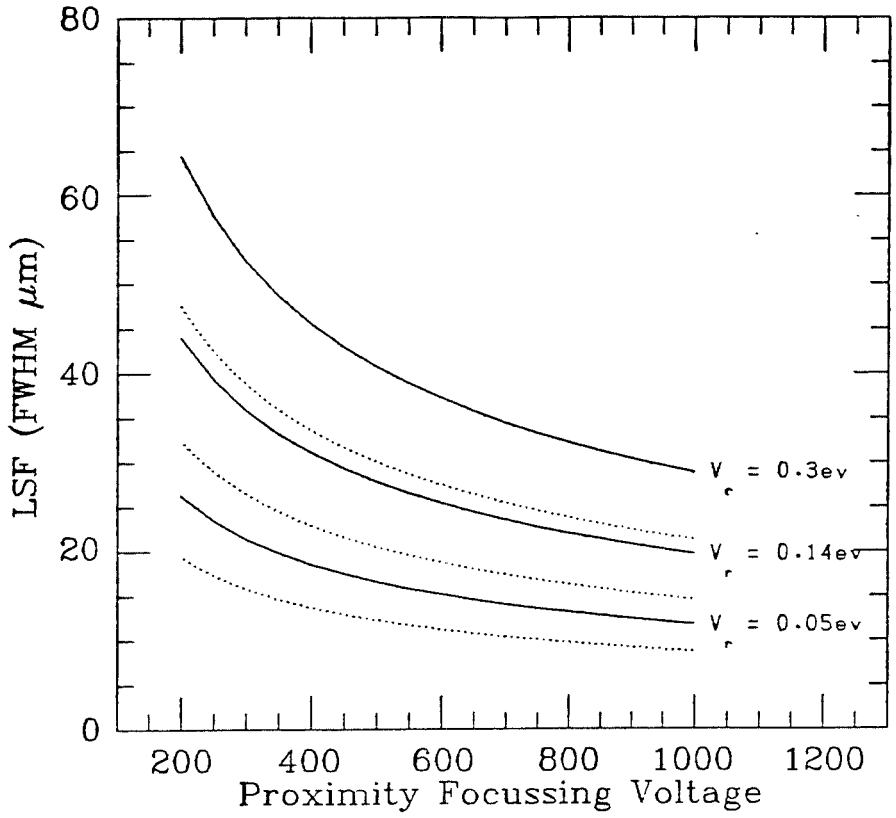

Figure 7-2: Theoretical MTF curves for proximity focused lens with V_r = 0.3 ev at gap voltages of 200 V, 400 V, 600 V and 800 V.

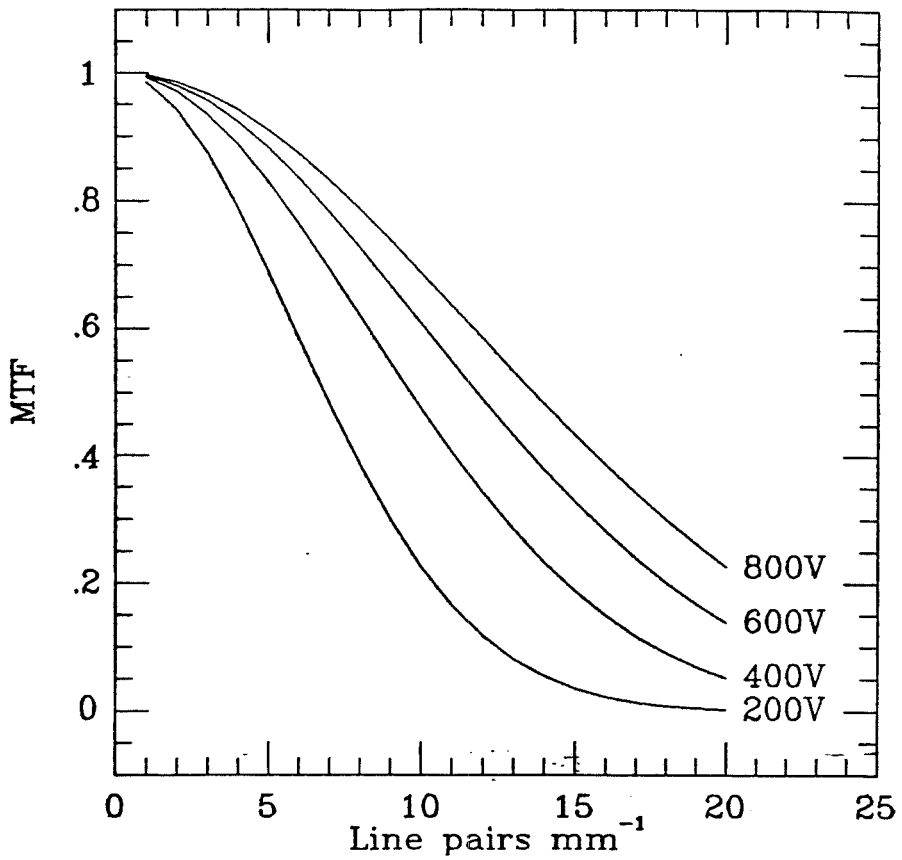

a cosine distribution is employed for the radial emission energy of the photoelectrons as derived by Csorba (1977), where the PSF has a variance of $\sigma^2_{PSF} = 1.48L^2V_rV_g^{-1}$. The graphs show that there is an appreciable difference between the calculated PSF FWHM values for the two different theoretical distributions, particularly at bluer wavelengths with lower focussing voltages. Eberhardt (1977) has studied the distribution of radial emission energies for multialkali photocathodes experimentally and finds it to approximate to a Maxwellian distribution. Csorba (1977), however, states that the distribution is cosine in nature and does not have the long emission tail exhibited by a Maxwellian distribution.

Figure 7-2 shows the predicted MTF curves for a 0.5 mm proximity focussed lens for gap voltages of 200, 400, 600 and 800 volts respectively, using Eberhardt's value of V_r = 0.3 eV for blue light and a Maxwellian distribution. The theoretical advantage of high proximity focussing fields is well illustrated. The disparity between the distributions used is shown by a reduction in MTF from 0.47 to 0.66 at 10 $lpmm^{-1}$, if a cosine distribution is employed. With proximity focussing potentials in the IPD ranging from 300 V to 420 v, the MTF at 5 $lpmm^{-1}$ is 0.78 to 0.84 using a value of V_r = 0.3 eV and the Maxwellian distribution.

The PSF curves in figure 7-1 also disagree slightly with the actual FWHM values obtained by McWhirter et al., who use a value of 0.4 eV for the mean radial emission energy of a photoelectron from an S20 photocathode. The disagreement between authors regarding values of V_r is primarily a result of the varying interpretations of

this parameter. This point is discussed in detail by Eberhardt (1977) and Ezard (1975). S20 (multialkali) photocathodes have a wide range of properties which vary with the processing technique used and the wavelength sensitivity for which they have been optimised (Timan 1985). In particular, much of the work in this field is intended for application to infrared wavelengths, which generally have higher values of V_r, and is discussed in these terms.

An important factor affecting the spatial linearity of the contribution from the proximity focussing resolution is the planar uniformity of the MCP surfaces, especially for larger MCPs. This needs to be considered both prior to and after processing of the detector tube. Lyons (1985) has reported typical variations of the order of 120μm across the surfaces of 40 mm diameter MCPs. Armentrout (1985) discusses the problem of plate arching in large area, mounted, circular MCPs.

Such an effect may give rise to a variation in resolution across the active area of the detector. As shown in equation (7.18), the FWHM of the PSF varies exponentially with the gap width. Thus considering the idealised situation of an arched input MCP creating a difference in the gap of up to 100μm from the nominal figure of 500μm, one would expect a variation in the PSF FWHM of up to 20%. This uncertainty will then be convolved with the PSFs of subsequent stages to produce a larger departure from overall uniformity. There appears to have been little work on this problem, apart from a recent recognition of its existence in the development

of larger format tubes (Jean et al. 1985). Mullard (1985) do not give an estimate of the planicity of their plates.

7.2.4) Resistive Anode Noise

The resolution of a resistive anode was discussed in Chapter 2 and is given by equation 2.6, where the filter time constant T_a is long compared with the anode time constant. The variable ν, the noise form factor is defined as

$$\nu(N,M) = \frac{1}{a}\left[\int_0^\infty \frac{x^{2N-2}}{(1+x^2)^{N+M}} dx \right]^{\frac{1}{2}} \qquad (7.19)$$

for an N times differentiating, M times integrating filter, where 'a' is the peak amplitude of the filter response (Fraser et Mathieson 1981a). Fairstein and Hahn (1965) calculated an expression for 'a', and for the case of a double differentiating, double integrating filter a = 0.131, giving $\nu(2,2) = 2.39$. The results for a calculation of Δx using the anode parameters in Section 2-4, are given in table 7-1 and illustrated in figure 7-3. The figures show the penalty incurred with the use of a large format CAT anode and the need for high gain. The higher thermionic noise figure for this anode is a direct result of the lower anode resistivity, which is necessary in order to maintain a reasonable anode time constant. Thus the resolution for the anode alone, operating with a typical MCP gain of 7×10^6 is 50 μm FWHM, giving an MTF of 0.8 at 5 $lpmm^{-1}$. Table 7-1 shows the variation of the

Figure 7-3: MCP gain - resolution relationship for CAT anode.

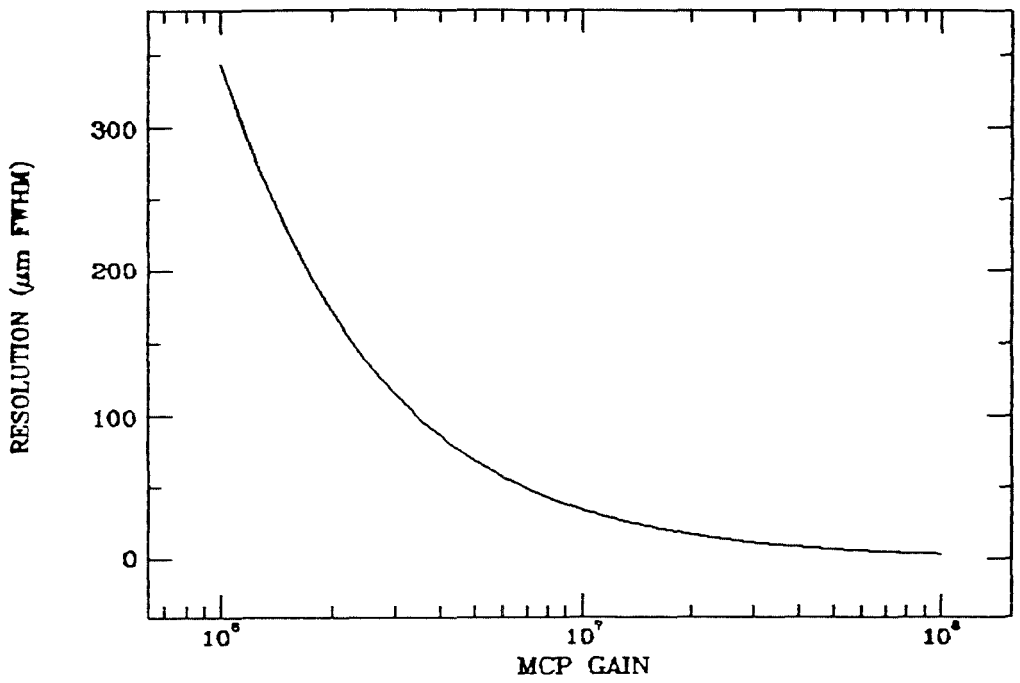

Figure 7-4: MCP gain - resolution relationship for CAT anode and preamplifiers

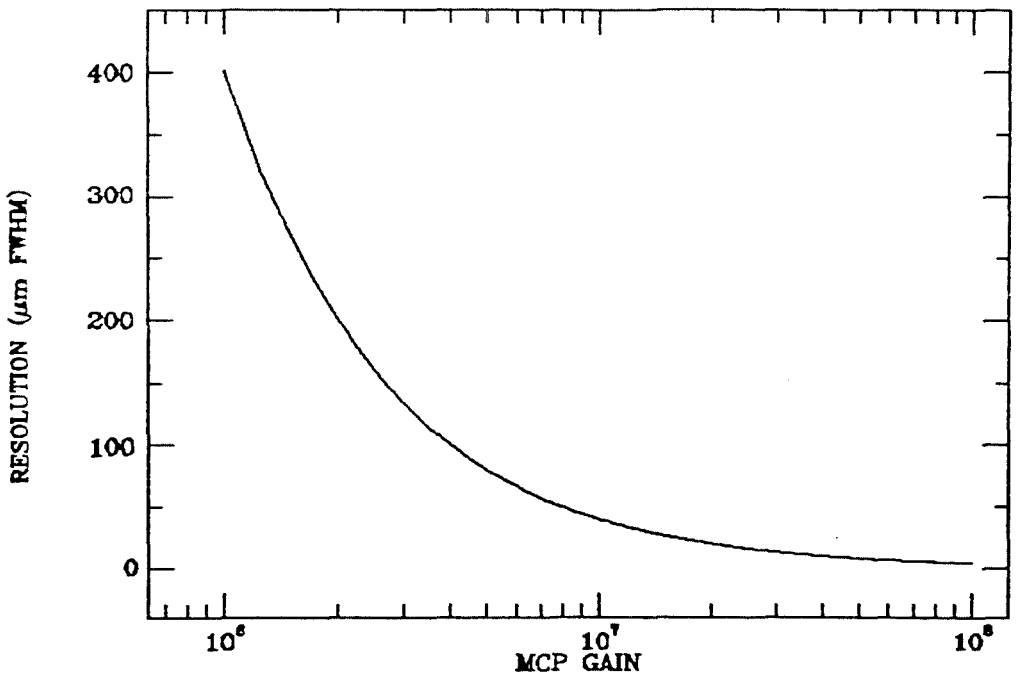

Table 7-1

Theoretical CAT anode Resolution.

MCP Gain	Resolution (μm FWHM)	MTF
2.0×10^6	171.8	0.711
3.0×10^6	114.6	0.309
4.0×10^6	85.9	0.516
5.0×10^6	68.7	0.655
6.0×10^6	57.3	0.746
7.0×10^6	49.1	0.806
8.0×10^6	43.0	0.848
9.0×10^6	38.2	0.878
1.0×10^7	34.4	0.900
2.0×10^7	17.2	0.974
3.0×10^7	11.5	0.988
4.0×10^7	8.6	0.993
5.0×10^7	6.9	0.996
6.0×10^7	5.7	0.997
7.0×10^7	4.9	0.998
8.0×10^7	4.3	0.998
9.0×10^7	3.8	0.999
1.0×10^8	3.4	0.999

anode's PSF and MTF with MCP gain.

It is of interest to investigate the effect that cooling the detector would have upon anode resolution, as a result of a lower anode temperature. Temperatures of $-30^{o}C$ are used typically to reduce photocathode dark noise. A value of T_e = 240 K gives a decrease of 10-15% in the anode's potential resolution resulting from the drop in thermionic noise, giving an MTF = 0.85 at 5 $lpmm^{-1}$. An area which requires further investigation is how the actual resistive properties of the anode change with temperature. Allington-Smith and Schwartz (1984) report that the temperature of CERMET, the material used in the EXOSAT detector shows a negative temperature coeffcient of 2.4×10^{-3} producing a 'zoom' effect in images. There are currently insufficient data on the properties of anodes to be able to generalise with any certainty on their expected performance with temperature.

7.2.5) Preamplifier Noise

The preamplifier noise will provide an additional contribution to the noise of the system. In the case of the preamplifiers this is an appreciable contribution when compared with the anode thermionic noise. The preamplifier noise contribution (Q_p) is added to the anode noise contribution (Q_a) using

$$\frac{(\Delta x)^2}{d^2} = Q_a^2 + Q_p^2 \qquad (7.20)$$

Table 7-2 shows the calculated PSF and MTF values, and they are illustrated in figure 7-4. There is a degradation of the resolution of the order of 15%, which for an MCP gain of 7×10^6 gives a resolution of 57 μm FWHM. This translates to an MTF of 0.75 at 5 $lpmm^{-1}$.

7.2.6) Main pulse position electronics errors.

The contribution of the processing electronics to system resolution was discussed in 3.8. A value of 50 μm FWHM, for a reference voltage of 10 V, was obtained and this gives an MTF = 0.8 at 5 $lpmm^{-1}$. This figure is worse than that of 25 μm claimed by McWhirter et al. (1982) for a system which uses analogue division and which was the predecessor of this IPD signal processing system.

An independent estimate of the combined contributions of the anode noise, preampifier noise and the signal processing unit was obtained using a modification of the technique in 3.8. The upper thresholding comparator was removed and a pulse was input from a pulse generator on the appropriate output line (pin 9), to simulate the conversion enable strobe. The ADC reference was tied to a fixed 10 V line and the system was run with the anode leads connected. Operating in this mode resulted in an image point at the centre of the detector field. The width of this point represented the combined noise contributions. These tests gave a PSF with a FWHM of the order of 45 μm, which was found to remain stable as the trigger rate was increased up to 10^4 cs^{-1}. The electronics resolution tests

Table 7-2

Theoretical combined CAT anode and preamplifier resolution.

MCP Gain	Resolution (μm FWHM)	MTF
2×10^6	200.7	0.027
3×10^6	133.8	0.201
4×10^6	100.3	0.405
5×10^6	80.3	0.561
6×10^6	66.9	0.669
7×10^6	57.3	0.745
8×10^6	50.2	0.798
9×10^6	44.6	0.837
1×10^7	40.1	0.866
2×10^7	20.1	0.965
3×10^7	13.4	0.984
4×10^7	10.0	0.991
5×10^7	8.0	0.994
6×10^7	6.7	0.995
7×10^7	5.7	0.997
8×10^7	5.0	0.998
9×10^7	4.5	0.998
1×10^8	4.0	0.999

discussed in Section 3.8 derived a figure of 50 μm FWHM using a similar technique and thus imply that the figure obtained above should have been of the order of 50 μm or larger. The basic difference between the tests, in terms of the mode of processing signals, is the use of a fixed reference for the latter test. The latter test result also represents a convolution of the anode and preamplifier PSFs and the electronics PSF, while the former represents the signal processing electronics PSF alone. The results indicate, therefore, that the use of a variable reference degrades the system PSF and add weight to the conclusions of Chapter 5 regarding the use of the ADCs as ratiometric dividers.

7.2.7) Detector MTF

To summarise, the MTF contributions to the detector performance at 5 $lpmm^{-1}$ are;

Fibreoptic window of the detector.	0.997
Channel diameter of the MCPs.	0.987
Proximity focussing: 420 V	0.838
Proximity focussing: 300 V	0.781
CAT anode and preamplifiers. (7×10^6)	0.745
Main pulse position electronics errors.	0.799

The MTF curves for the individual elements are shown in figure 7-5. The analysis of McWhirter et al. (1982) concludes that the main limiting factor in a 25 mm IPD design is that of the proximity focussing gap (1.0mm). In comparison, this IPD system is limited by a combination of the three main components, each having approximately equal weight. The improvement in proximity focussing

Figure 7-5: Theoretical MTF curves for individual detector elements.

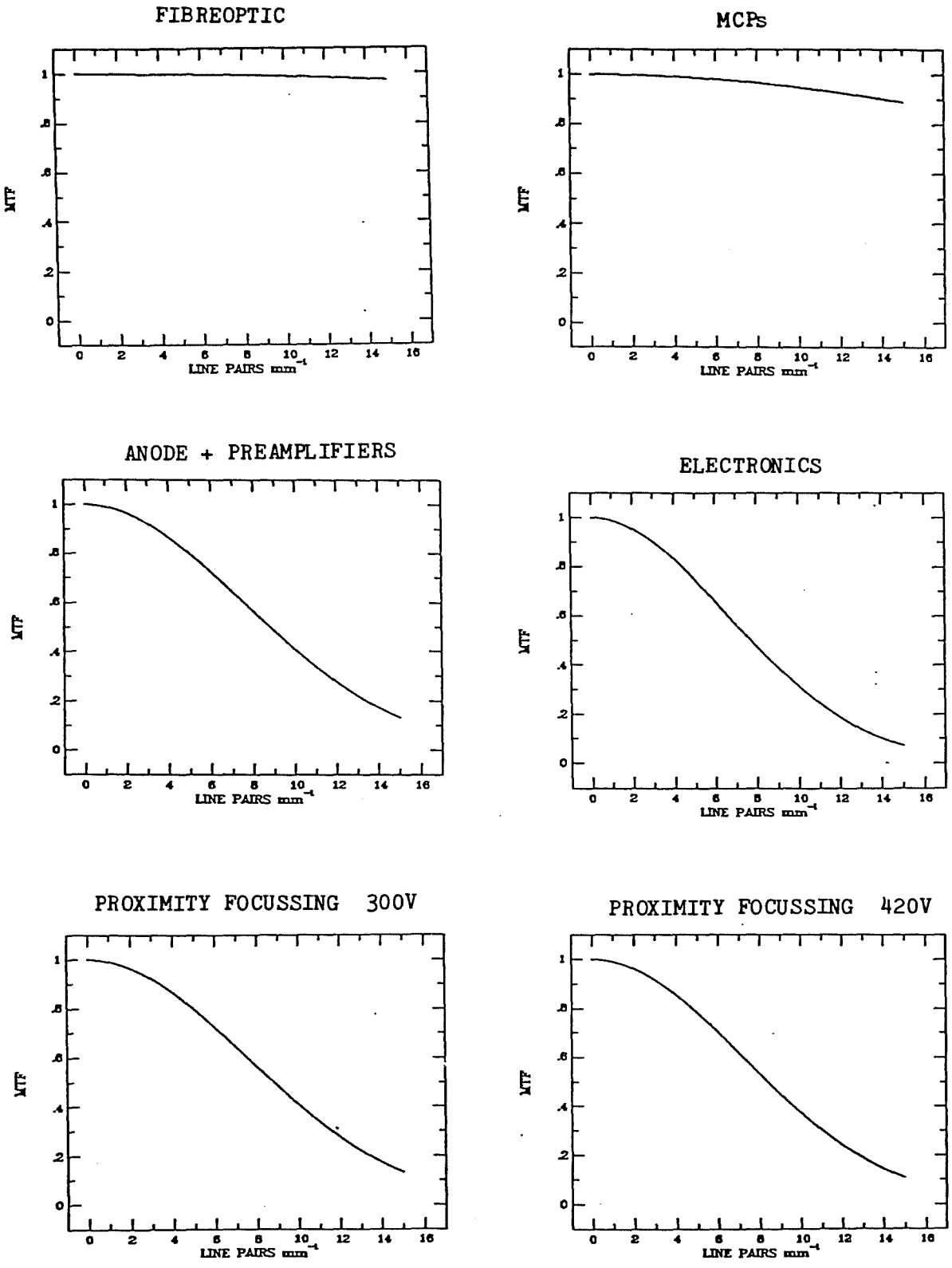

with a smaller gap is offset by the increased thermionic noise of the anode and the more conservative estimate for the electronics. Combining these figures gives values of MTF = 0.39 and 0.44 at 5 $lpmm^{-1}$, for proximity focussing voltages of 300 V and 420 V respectively. This corresponds to detector PSFs of widths 89 μm and 94 μm. Figure 7-6 shows the detector MTF curves for the upper and lower range of MCP operating gains (4-7 x 10^6) at a gap voltage of 300 V.

The most likely sources of errors in this analysis arise from uncertainties in the PSF values derived and the assumption of a linear stationary system. This assumption is not justified if the PSF width varies with image position. A non-linear photocathode to MCP gap, or non-uniformity in the signal processing electronics would both reduce the validity of this analysis. The technique is important, however, since it provides a method for predicting the performance of a detector and its component elements.

7.3) MTF Measurement

The USAF 1951 resolution pattern is a group of square wave bars each representing a series of spatial line frequencies. The chart is used in this experiment consisted of a mask made of iconel, vacuum deposited on a soda glass base. The mask was of high contrast with a relative density difference of greater than 2.0 and a limiting resolution of 230 $lpmm^{-1}$. Figure 7-7 shows the enlarged photographic image of the resolution chart, with line frequency details of the chart given in table 7-3. Estimates of the detector

Figure 7-6: Theoretical MTF curves for IPD operating at gains of 4×10^6 (125 μm) and 7×10^6 (94 μm).

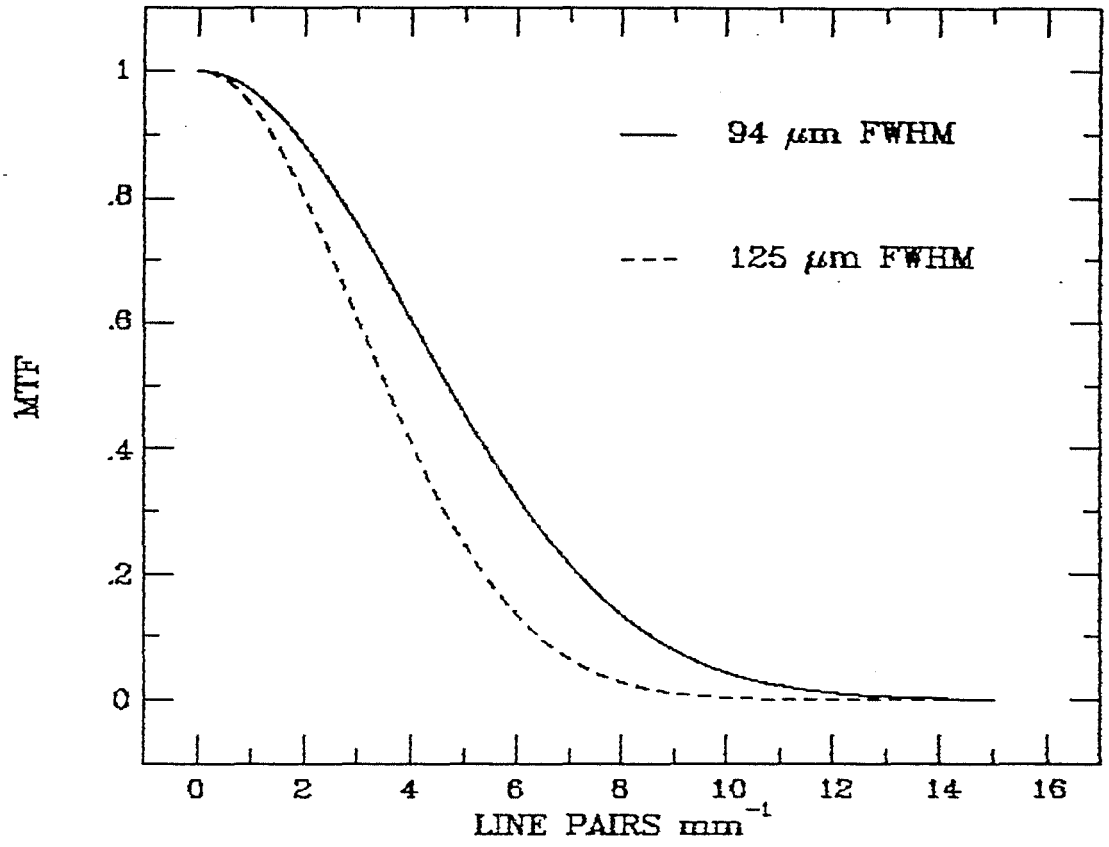

Table 7-1: USAF 1951 resolution chart target formats.

Group Number	Target Number					
	1	2	3	4	5	6
0	1.00	1.12	1.26	1.41	1.59	1.78
1	2.00	2.24	2.52	2.88	3.18	3.57
2	4.00	4.49	5.05	5.67	6.37	7.12
3	8.00	8.98	10.1	11.4	12.8	14.4
4	16.0	17.9	20.2	22.7	25.7	28.5
5	32.0	35.9	40.3	45.2	50.7	57.0

Resolution (line pairs mm^{-1})

Figure 7-1: Photographic enlargement of test USAF 1951 resolution chart.

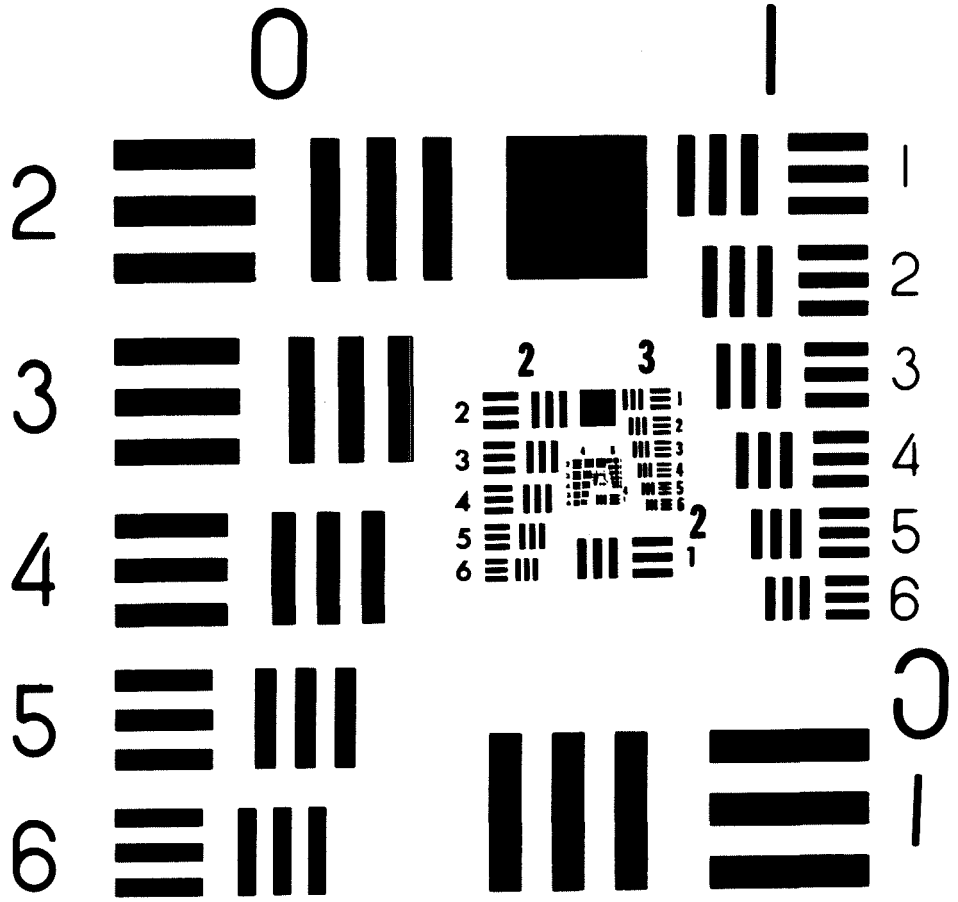

performance were obtained with this chart using two methods;

(i) Visual inspection of digital images of the imaged chart, displayed on a Sigma ARGS terminal can give an estimate of the limiting resolution directly. The displayed image may be zoomed to inspect fine detail. Hence the estimate will be limited by resolution of the detector, or the size of the pixels used to sample the image.

(ii) The resolvable bars of the square wave pattern may be used to obtain a value of the modulation (M_s), at the spatial line frequency of each set of the square wave bars. When a square wave pattern is used to approximate to a sinusoidal input, the modulation M_s is often known as the Contrast Transfer Function (CTF), (Richmond 1976). The value of the MTF may then be obtained from the formula (Coltman 1954),

$$M(\omega) = \frac{\pi}{4}\left(M_s(\omega) + \frac{M_s(3\omega)}{3} - \frac{M_s(5\omega)}{5}.....\right) \qquad (7.21)$$

The measured function may then be directly compared with a theoretical MTF derived for the appropriate system parameters.

The modulation transfer function of the overall detector system was measured at a proximity focussing voltage of 300 V using a pixel format giving an image of 1024 x 64 pixels. The format was obtained using a FORTH word to select a series of sequential image windows

giving mosaic coverage of the pattern with square pixels. The resulting images are then easily inserted into a new image giving a 1024 x 1024 format. Initially a lens was used to image the chart onto the photocathode of the detector. Establishing the exact focus, however, proved to be a problem and images obtained showed evidence of distortion in the imaging optics. In order to avoid these problems the resolution chart was imaged onto a photographic plate, which after processing could be placed in contact with the photocathode. While there was some degradation of resolution in the pattern as a result of this technique, the MTF contribution of the photographic image was not sufficient to affect the determination of the detector's MTF. The chart was contact imaged onto the fibre-optic window using the uniform illumination provided by a green led source, operating at a low current level. The image was centred within the photocathode area.

An Optronix photograph of a typical image of the resolution chart, obtained using the mosaic technique, is shown in figure 7-8. It can be seen that the pattern indicating limiting resolution is (2,6), which from table 7-1 gives a limiting resolution of 7 $lpmm^{-1}$. The modulation for each group of patterns was measured by summing the appropriate cross sections of each pattern to obtain high signal to noise, the images having first been background subtracted. The modulation was then calulated using equation 7.10, assuming that the modulation input was unity. The CTF obtained for the vertical groups of bars down to group (3,1) is shown in figure 7-9. The main feature of the curve is the discontinuity at 4 $lpmm^{-1}$ which indicates the presence of spatial non-uniformity. This effect is

Figure 7-8: Detector image of resolution chart

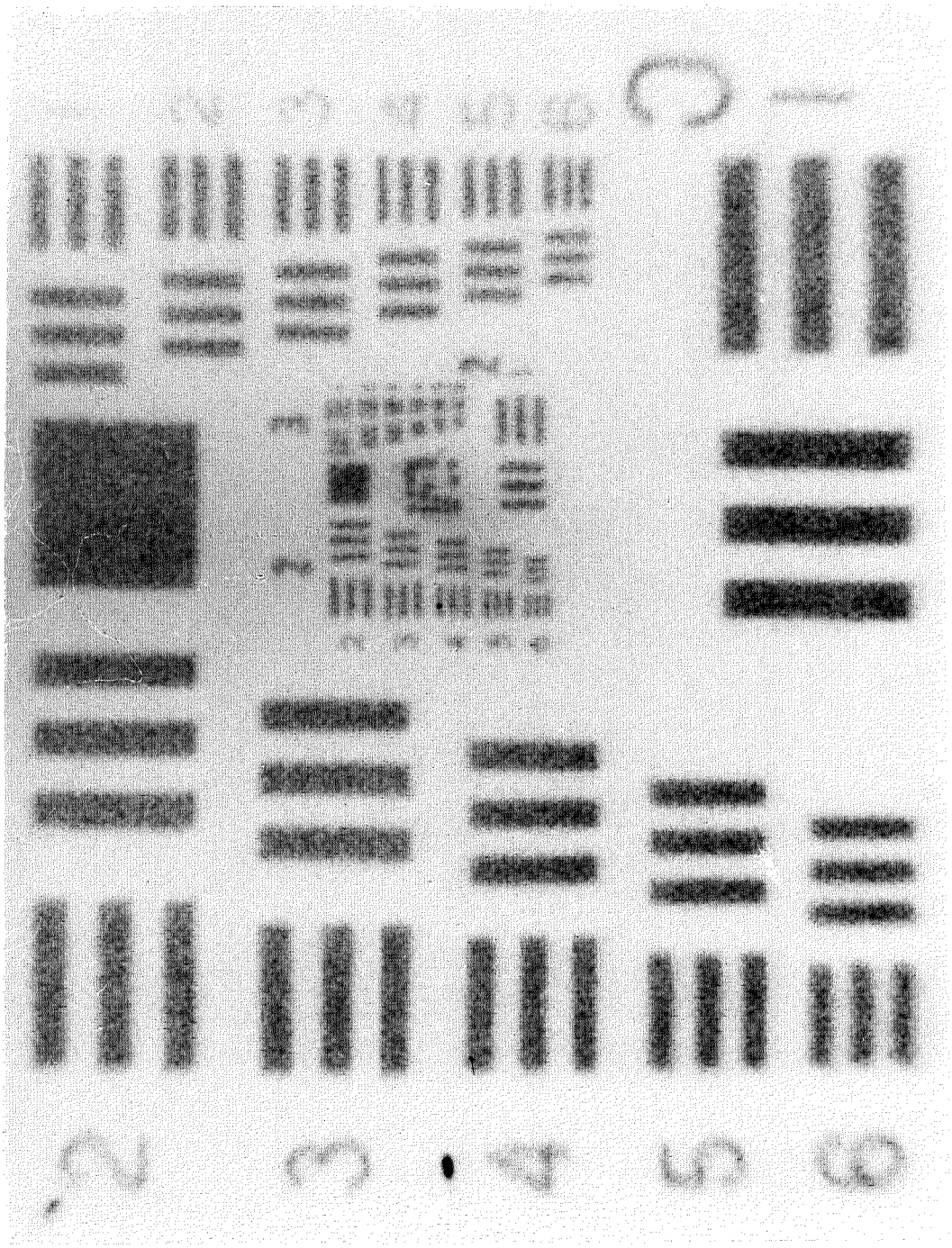

Figure 7-9: Contrast transfer function obtained from measurements of the resolution chart image shown in figure 7-8.

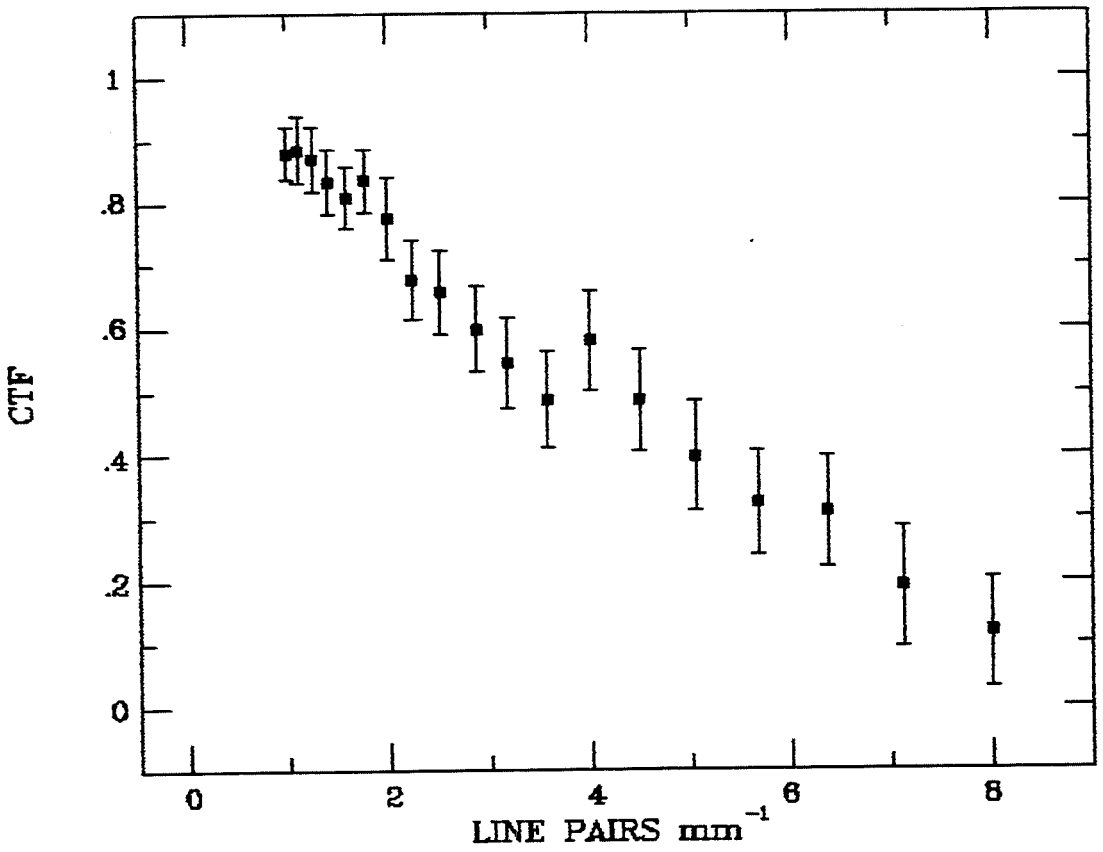

Figure 7-10: Comparision between theoretical detector MTF curve and experimental detector MTF data.

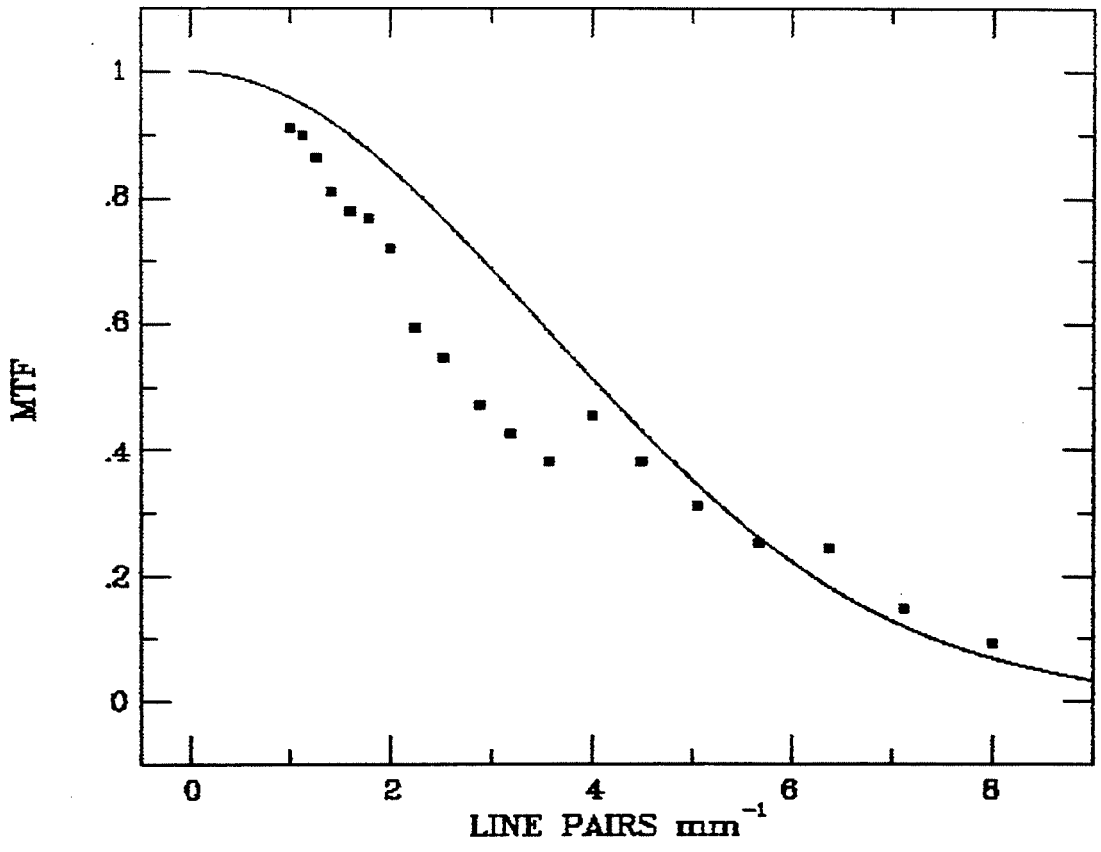

not a result of error in the measurement of these pattern groups, as the two sets of bar patterns at the discontinuity shown in figure 7-11 illustrate. The higher modulation in the pattern at 4.0 $lpmm^{-1}$ is obvious when compared with the pattern at 3.57 $lpmm^{-1}$. Inspection of the chart shows that the pattern group (2,1) is 2 mm from the group (1,6), and closer to the centre of the chart. Also group (2,1) lies closer to the centre of the imaging area.

In order to make a comparision with the theoretical MTF for the detector, the CTF was transformed to the MTF using Coltman's formula in equation 7.21. The intermediate values of modulation required by this formula were calculated by fitting a fifth order, weighted polynomial (Bevington 1969) to the CTF data. It must be stated, however, that the validity of this transformation and the comparison with a theoretical MTF will be limited by the apparent non-uniformity indicated in the CTF. Figure 7-10 shows the theoretical MTF calculated for the detector operating at a gain of 6×10^6 compared with the resolution chart MTF data. The data at frequencies up to 4.0 $lpmm^{-1}$ do not compare well with the MTF curve, while the MTF points below 4.0 $lpmm^{-1}$ lie closer to the theoretical curve. Thus the PSF resolution of the detector seems to lie at a value greater than that predicted. The discontinuity in the curve suggests that the resolution is not constant over the detector's imaging area and that towards the centre, the PSF width may be in reasonable agreement with the theoretical value of 100 μm.

Figure 7-11: Diagram showing the bar pattern profiles at 4.00 $Lpmm^{-1}$ and 3.57 $Lpmm^{-1}$.

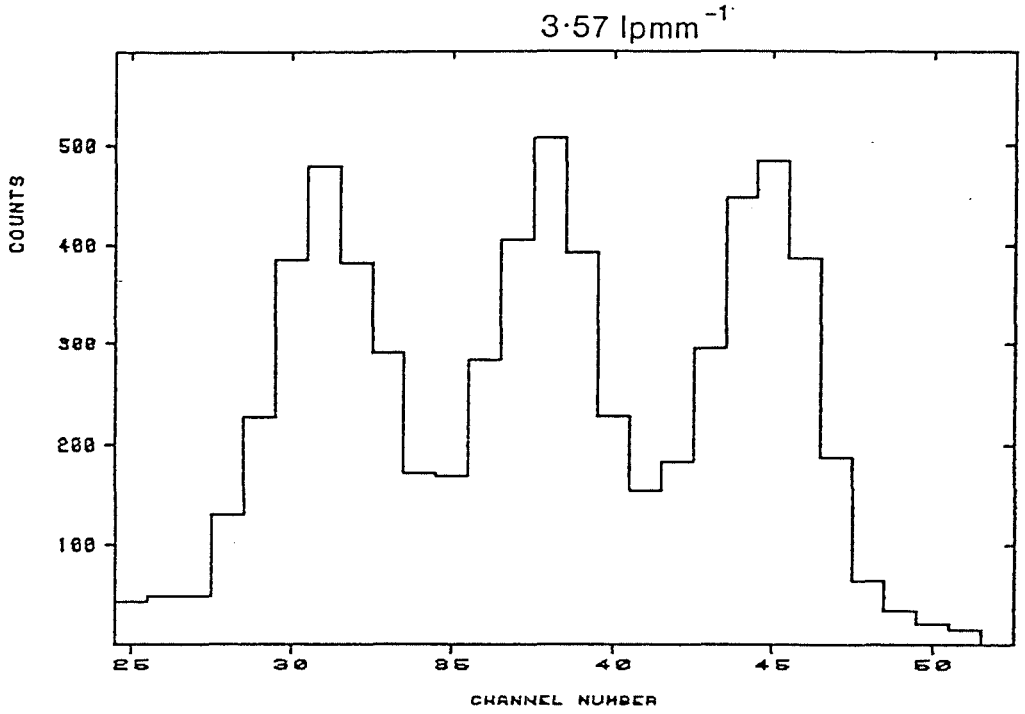

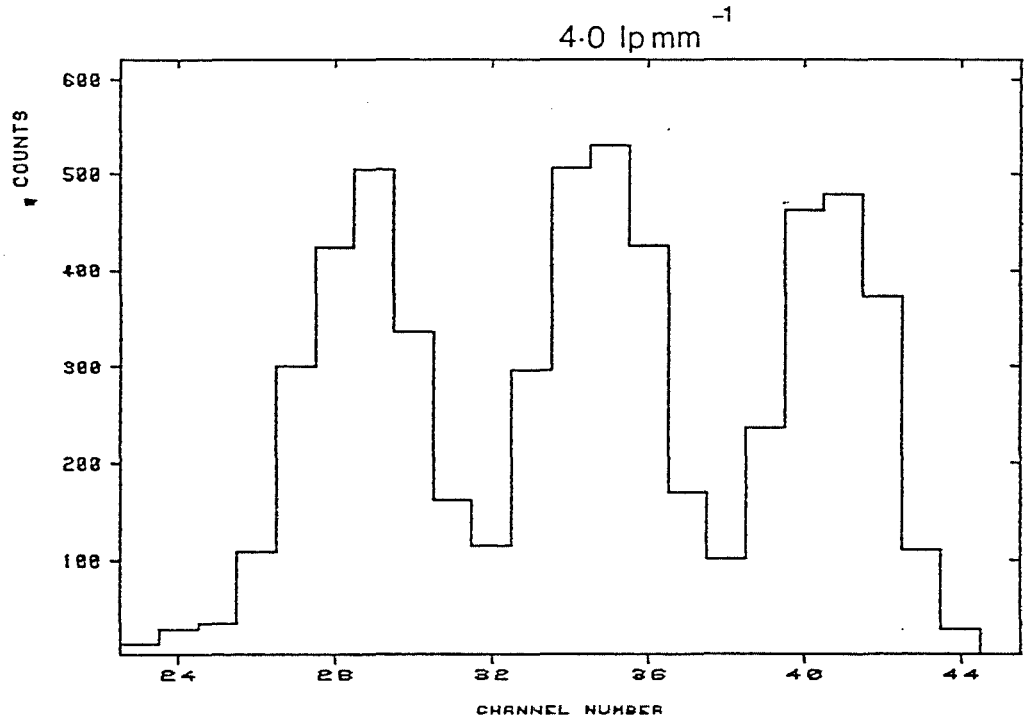

7.4) Arc Spectra.

The spectrograph comparison lamp provides a source of copper-argon arc spectra which are ideal for LSF analysis. Individual lines of imaged arc spectra may be fitted by Gaussians, to obtain FWHM values for the lines. The method is particularly suited to the analysis of detector resolution since arc lines may be examined over a complete slice of the detector's active area, with the exception of the low sensitivity photocathode periphery. Data were also readily analysed, allowing relatively quick testing of a new detector operation configuration. The spectrograph and the problems experienced using it in conjunction with the detector will be discussed in detail in Chapter 8.

The results obtained with the resolution chart indicated that there was some degree of non-uniformity in the detector's resolution. This result was confirmed by examination of comparison arc spectra which show a considerable variation in resolution from the edge to the centre of the imaging area. Figure 7-12 shows a histogram of a calibrated comparison arc spectra. At the usual working dispersion of 30 Å mm^{-1}, the displayed area of spectrum covers the central 800 of a 1024 pixel cross section, giving 40 μm pixels. Arc lines at the edge of the field in figure 7-12 can be seen to be broader in width than those in the central region. The spatially dependant broadening can be seen in figure 7-13, where line widths are plotted as a function of their position on a 1024 pixel cross section. The majority of lines are, to a varying

Figure 7-12: Calibrated histogram of a copper argon arc spectra.

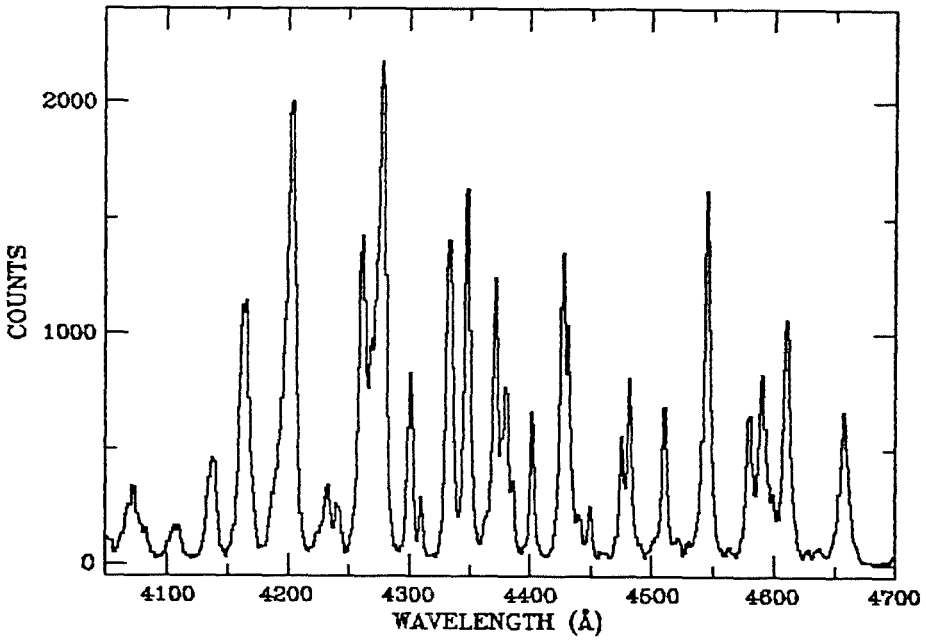

Figure 7-13: Variation of line width with spatial position for unblended copper argon arc lines.

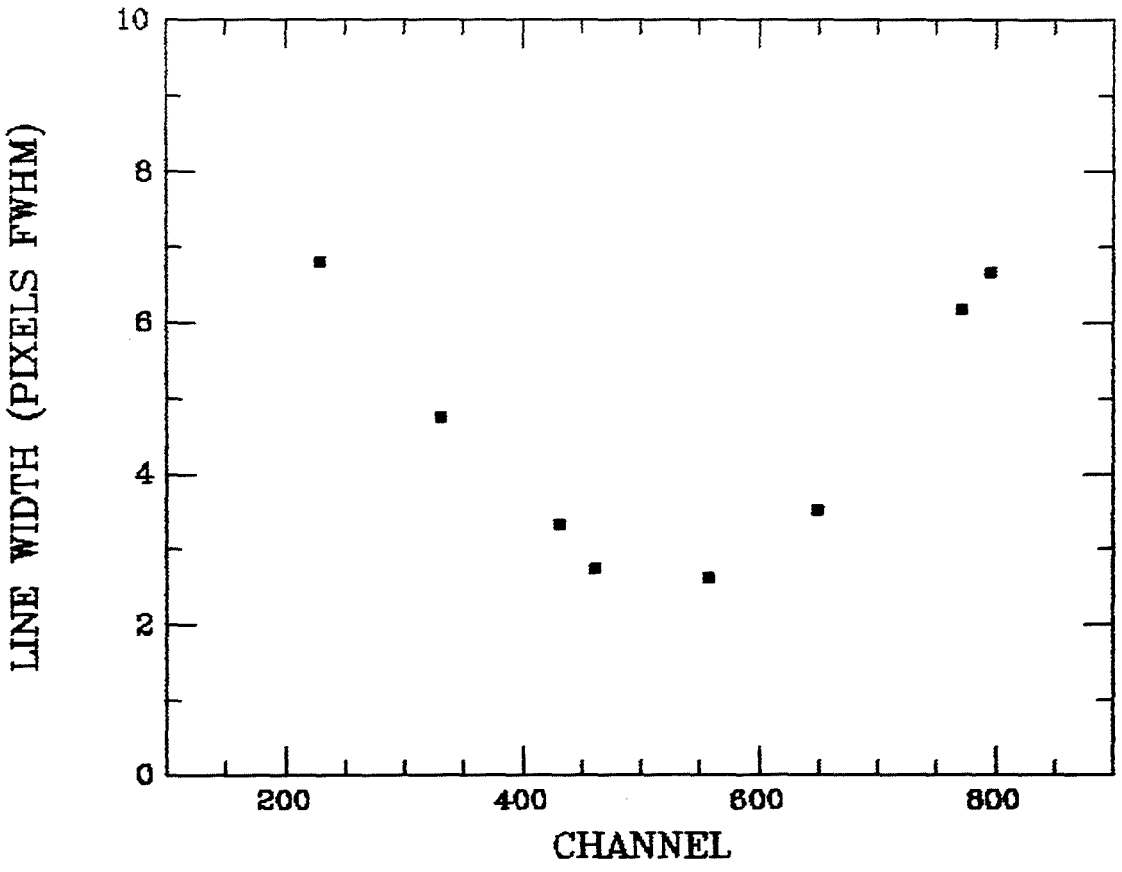

degree, blended and so only those lines which are completely unblended have been plotted. The line widths clearly vary with position, having values ranging from 250 μm to 100 μm. A section of the spectrum is compared with a CCD arc spectrum covering the same spectral range in figure 7-14. The figure highlights the blending of arc lines and it should be noted that some of the arc lines have broad low intensity wings, particularly noticeable in the isolated unblended lines.

The principal parameters affecting resolution which were investigated were the proximity focussing potential, MCP gain and the MCP to anode potential over the ranges;

proximity focussing potential = 300 V - 420 V,

MCP overall applied potential = 3 kV - 3.5 kV,

MCP to Anode potential = 10 V - 1000 V.

While the effects of gain and proximity focussing have been discussed already the latter parameter has not. The potential between the MCP and the anode determines the size of the charge cloud (w_a) arriving at the anode, given by Eberhardt (1981) as

$$w_a = 3.3L_a(V_{mt}/V_a), \qquad (7.22)$$

where L_a is MCP to anode gap, V_{mt} is the average tangential emission of the MCP emitted electrons and V_a is the gap potential. Eberhardt (1981) has estimated V_{mt} to be 0.2 eV for MCPs operating at 800 V. Using this value is sufficient to indicate that gap voltages of 10 - 1000 V will give typical MCP beam widths at the anode in the range 200 μm to 2 mm. Resistive anodes derive position

Figure 7-14: Comparision of detector arc spectra compared with similar section obtained with a CCD detector on the AAT RGO spectrograph (courtesy Dr P.W.Hill).

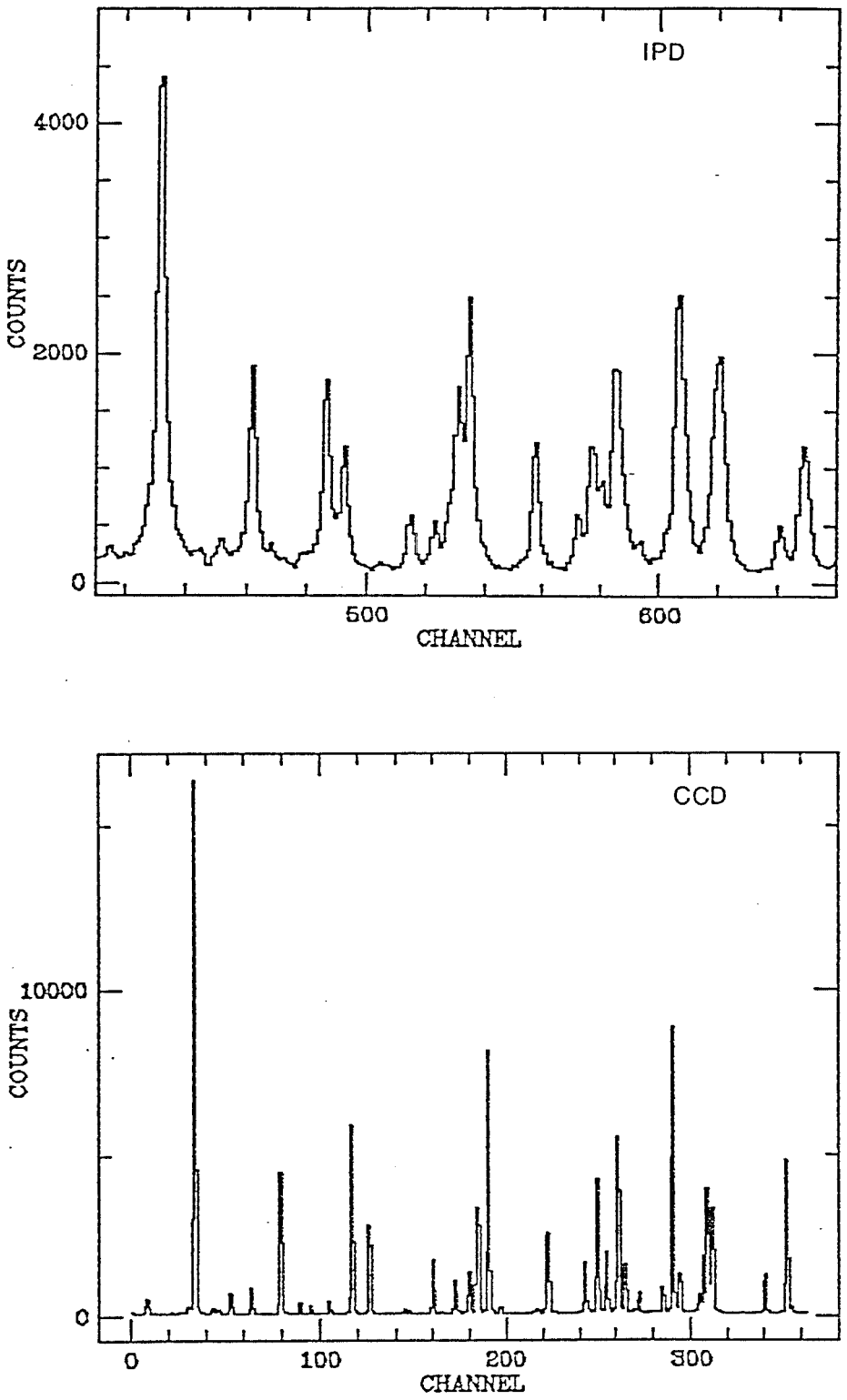

coordinates from the centroid of the incident charge cloud and so resolution should not be dependant on the size of the cloud. Granularity in the anode material on a microscopic scale could, however, cause non-linearity with small incident beam widths.

The MCP to anode potential was tested at voltages of 10 V, 50 V, 100 V, 200 V, 500 V and 1000 V and the parameter was found to produce no measurable improvement in resolution above that obtained with other configurations, when examined with constant values of MCP and proximity focussing potential. Lampton and Paresce (1974) also reported no change in resolution with variation in anode gap potential. At high voltages, no evidence of significant non-linearity was observed in arc spectra.

The MCP and proximity focussing potentials were varied in unison, in order to avoid the necessity of changing the EHT voltage divider resistors before each measurement. It was found that the change in arc line widths was more marked towards the edges of the imaging area than at the centre. Figure 7-15 shows the line profiles of an arc line (λ = 451 nm) in the centre of the imaging area (a) and an arc line (λ = 476 nm) towards the edge of the useful imaging area (b) at the potentials shown in table 7-4. Arc line (a) has a width of approximately 160 μm at the lowest applied potential (corresponding to a gain of 2×10^6), while line (b) is severely broadened with a width of 0.6 mm at the half maximum value. The variation of line widths with applied potential for the two lines is shown in figure 7-16. Both curves show a general trend of decreasing line width, although (a) appears to reach a plateau at

Figure 7-15: Variation of detector line profiles with applied potential for (1) λ = 451.0 nm and (2) λ = 467.4 nm.

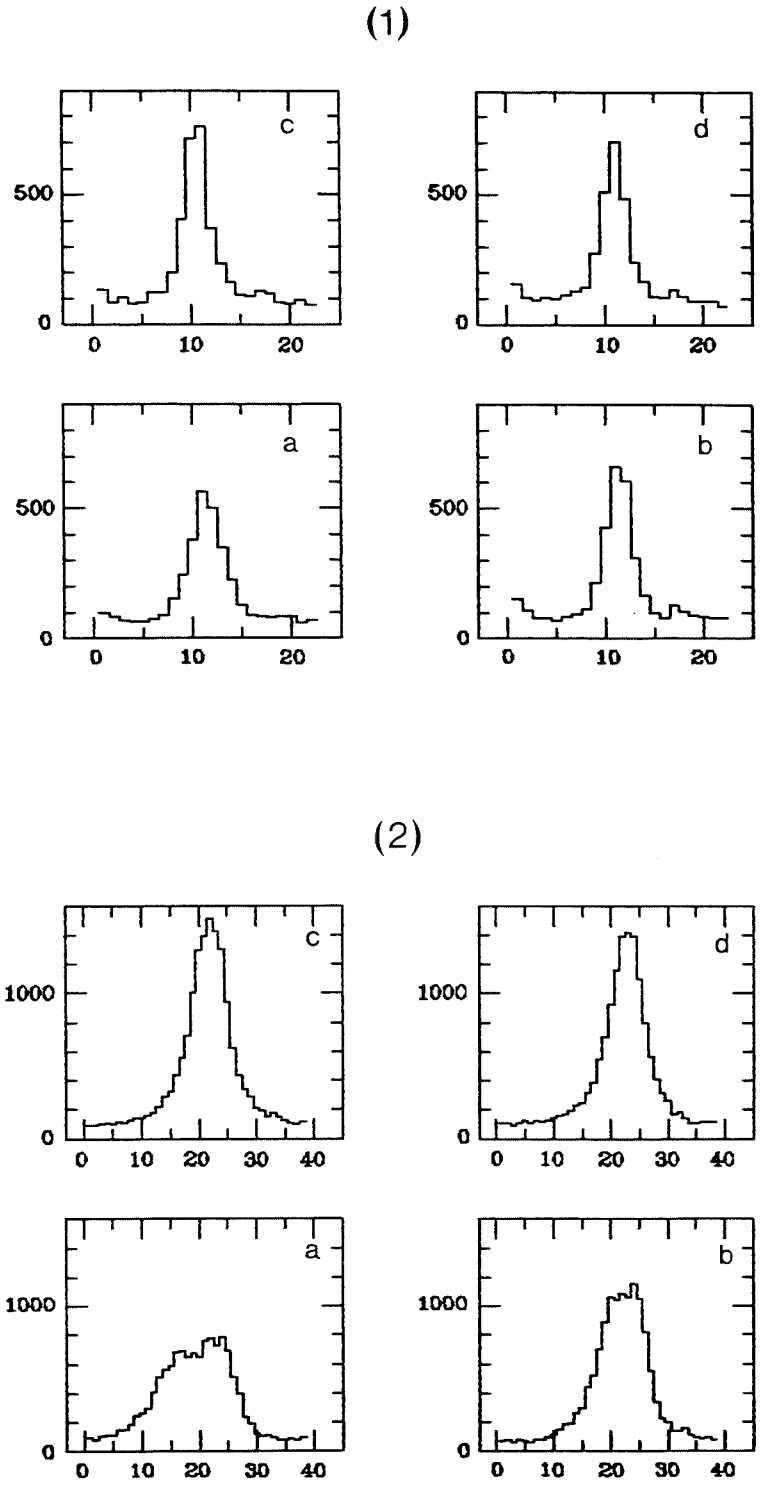

Figure 7-16: Variation of arc line widths with applied potential for (a) λ = 451.0 nm and (b) λ = 467.4 nm.

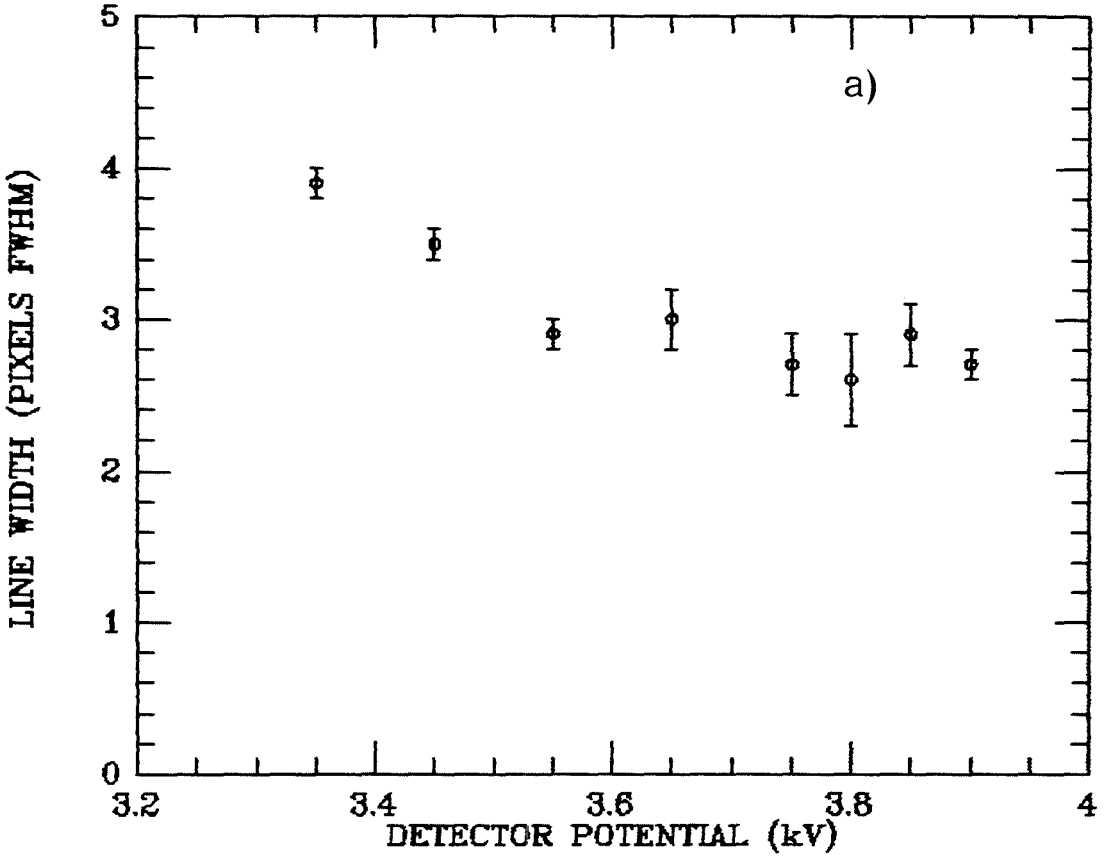

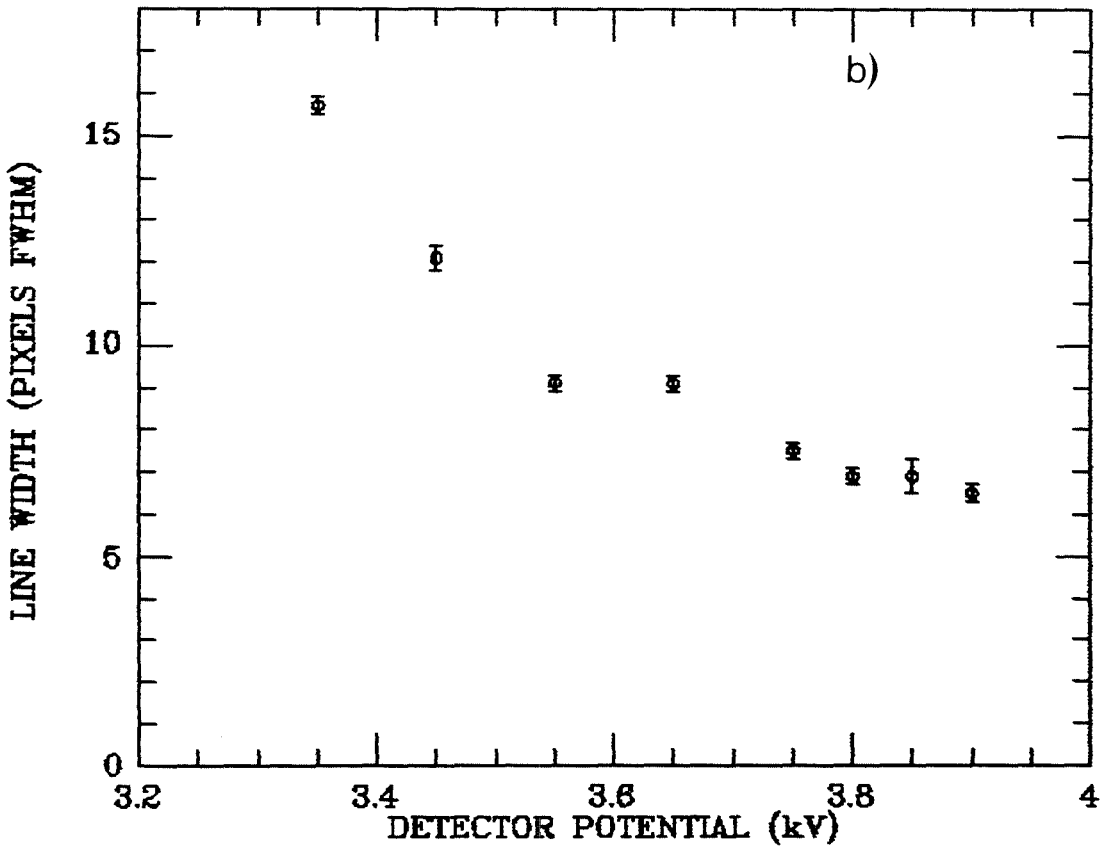

~100 μm FWHM, while (b) has a steeper curve with the width decreasing by 350 μm to its lowest value. The value of 100 μm is in reasonable agreement with the figure derived from theory. Similar behaviour was found for all of the configurations investigated. The trend was found to be generally applicable with the overall change in line width decreasing towards the centre of the imaging area and is illustrated in figure 7-17 for a series of line widths over the spectrum.

The low intensity wings seen in isolated lines are also responsible for the blending of some lines and appear to remain relatively constant over a range of MCP and proximity focussing voltages, although they are generally more extended at the lowest gain values where the line may be much broader. Figure 7-19 shows these wings in the profiles of the arc line $\lambda = 454.5$ nm for the range of applied potentials listed in table 7-4.

In 6.4 it was found that there appeared to be an enhancement of MCP gain for values of $V_a > 800$ V. If this is the case one might expect to obtain decreased line widths at correspondingly lower MCP potentials compared with configurations having lower values of V_a. The line widths obtained for the three configurations tested with a $V_a = 1000$ V were found to approach the limiting values of line widths at lower MCP potentials as anticipated. This effect is shown in figure 7-18 where the line widths obtained are plotted over the results of 7-17. If the two sets of data are considered in terms of the MCP gain values derived in 6.4 then the disparity between the two sets of data is removed. The result provides

Figure 7-17: Variation of arc line widths with applied potential for a series of unblended arc lines.

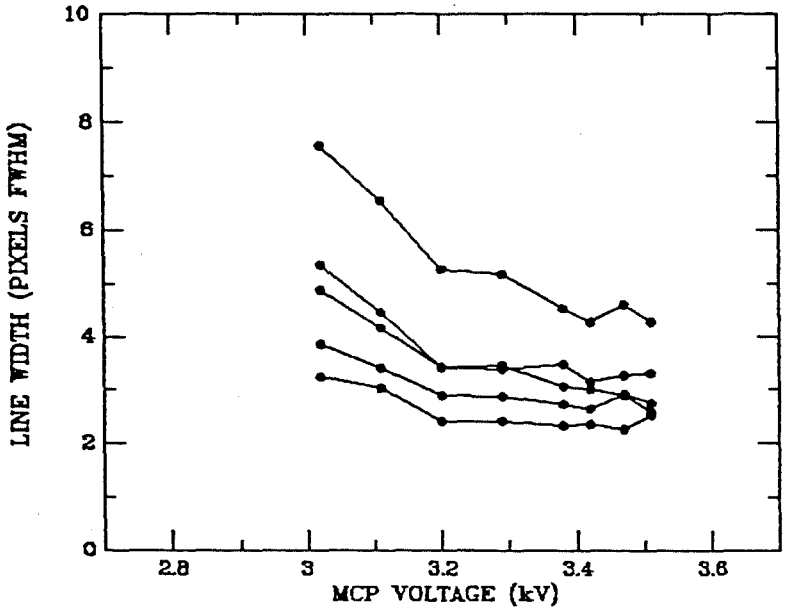

Figure 7-18: Arc line widths for V_a = 1000 V compared with data from figure 7-17.

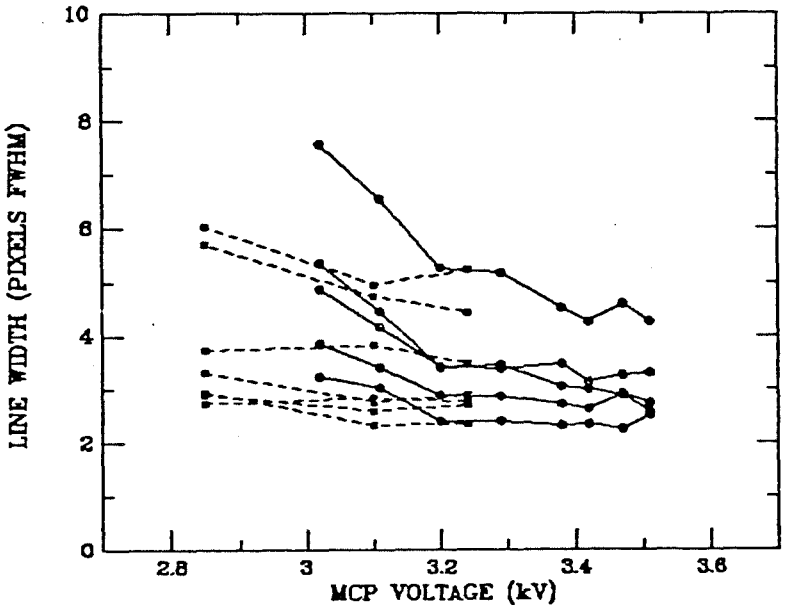

Figure 7-19: Variation of line profile for λ = 454.5 nm over range of applied potentials shown in table 7-4.

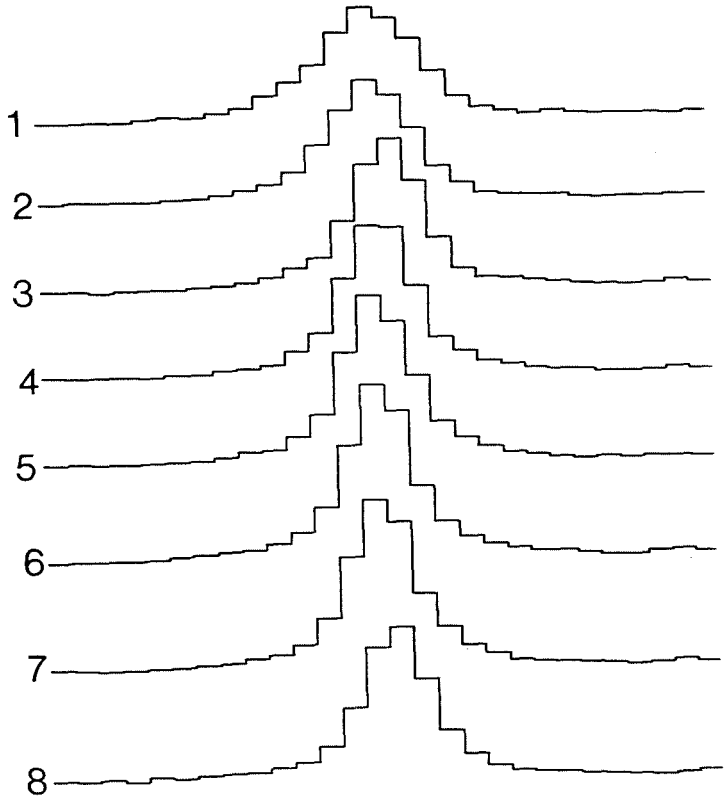

Table 7-4

	V_{tot}	V_{pc}	V_{mcp}	V_a
1	3.35	320	3.01	10
2	3.45	330	3.11	10
3	3.55	340	3.20	10
4	3.65	350	3.29	10
5	3.75	360	3.38	10
6	3.80	365	3.42	10
7	3.85	370	3.47	10
8	3.90	375	3.75	10

further evidence that there is enhancement of MCP gain with the high values of V_a. The alternative explanation is that there is an improvement in resolution with the smaller MCP beam widths. The limited amount of data precludes any further discussion until additional data can be obtained. The operational problems experienced with the EHT unit at these potentials have already been discussed in Chapter 6.

It was shown in 7.2.7 that the expected difference in resolution between proximity focussing voltages of 300 V and 400 V would be 10 m. The applied potential configurations tested showed that as the MCP gain and proximity focussing voltage increased beyond 3.4 kV and 360 V respectively the line widths started to broaden again. At applied voltages in excess of 3.4 kV the FWHM and PVR of the MCP's pulse height distribution start to broaden (figure 6-2). The hotspot noise at proximity focussing voltages of 400 V is considerable and as shown in figures 6-15 severely degrades the pulse height distribution, particularly at lower illumination levels. The combination gives poor pulse height distributions which are not Gaussian and have low signal to noise, which inevitably produce larger errors in the signal processing and a degraded resolution.

7.5) Slit Image LSF

In order to provide independent confirmation of the LSF widths obtained with the spectrograph, a graticule with a 25 μm slit was used to provide a line image from which the LSF could be

independently determined. Images of the slit were obtained at proximity focussing voltages of 300 V and 400 V by placing the graticule in contact with the fibreoptic window and illuminating it with an LED light source. The slit was positioned so as to be close to the centre of the field and the memory was windowed on a central section of the slit.

With the proximity focussing voltage of 300 V, the summed slit width was measured as 130 um from the summed cross sections, with the best cross sections having a width of 110 um. These values are in agreement with those obtained using the spectrograph and reflect the fact that the section of slit upon which the memory was set was not completely centred in the detector imaging area. The values increased to 170 μm and 150 μm respectively for a proximity focussing voltage of 400 V. For the latter measurements the MCP gain was lower giving a predicted theoretical PSF value of 105 μm for the configuration. There remains a disparity between the predicted and the measured values, confirming the result that arc line widths were broader at the 400 V proximity focussing potential.

7.6) Point Source Response

Investigation of the photocathode hotspots indicated that the PSF broadened with increasing count rate. The broadening was confirmed by imaging a fibre of diameter 200 um onto the photocathode surface and increasing the illumination level. The results were obtained for two low illumination levels and for two

images at higher illumination levels where MCP recovery problems are in evidence. Figure 7-20 shows the PSFs obtained together with their cross sectional profiles. The PSFs (a) and (b) represent relatively low levels of illumination where the peak count rates obtained were 0.6 $cs^{-1}pixel^{-1}$ and 1.2 $cs^{-1}pixel^{-1}n$ with a pixel size of 156 μm. Even with this relatively low increase of illumination there is a broadening of the profile from 1.9 to 2.2 pixels FWHM. These figures were derived from a cross section of the image, since it was apparent from the images of the PSF and the widths measured that the images produced by the fibreoptic were not circularly symmetric. With the illumination level increased to a peak count rate of 5.2 $cs^{-1}pixel^{-1}$ the profile broadened to 3.0 $cs^{-1}pixel^{-1}$ and possessed low intensity wings. The illumination level was increased further and a drop in the peak count rate was experienced together with a broadening of the feature to 4.7 pixels FWHM. The illumination level was not raised further in order to avoid the possibility of damaging the detector.

Pollehn (1974) has discussed the dynamics of scattered electrons within proximity focussed tubes and gives the maximum spread of an electron about primary incidence as twice the MCP to photocathode gap. Thus with a gap of 0.5 mm the maximum spread of backscattered electrons would be expected to be 1 mm. The base of the the PSF (d) is 1900 μm giving a spread from the centre of the profile of 950 μm. The extent of the spread is dependant upon the energy of the backscattered electrons and so the halo will be dependant upon the proximity focussing voltage. The increase in scattering at high flux levels is due to increased transmission of photons by the

Figure 7-20: Imaged fibre point spread functions and profiles.

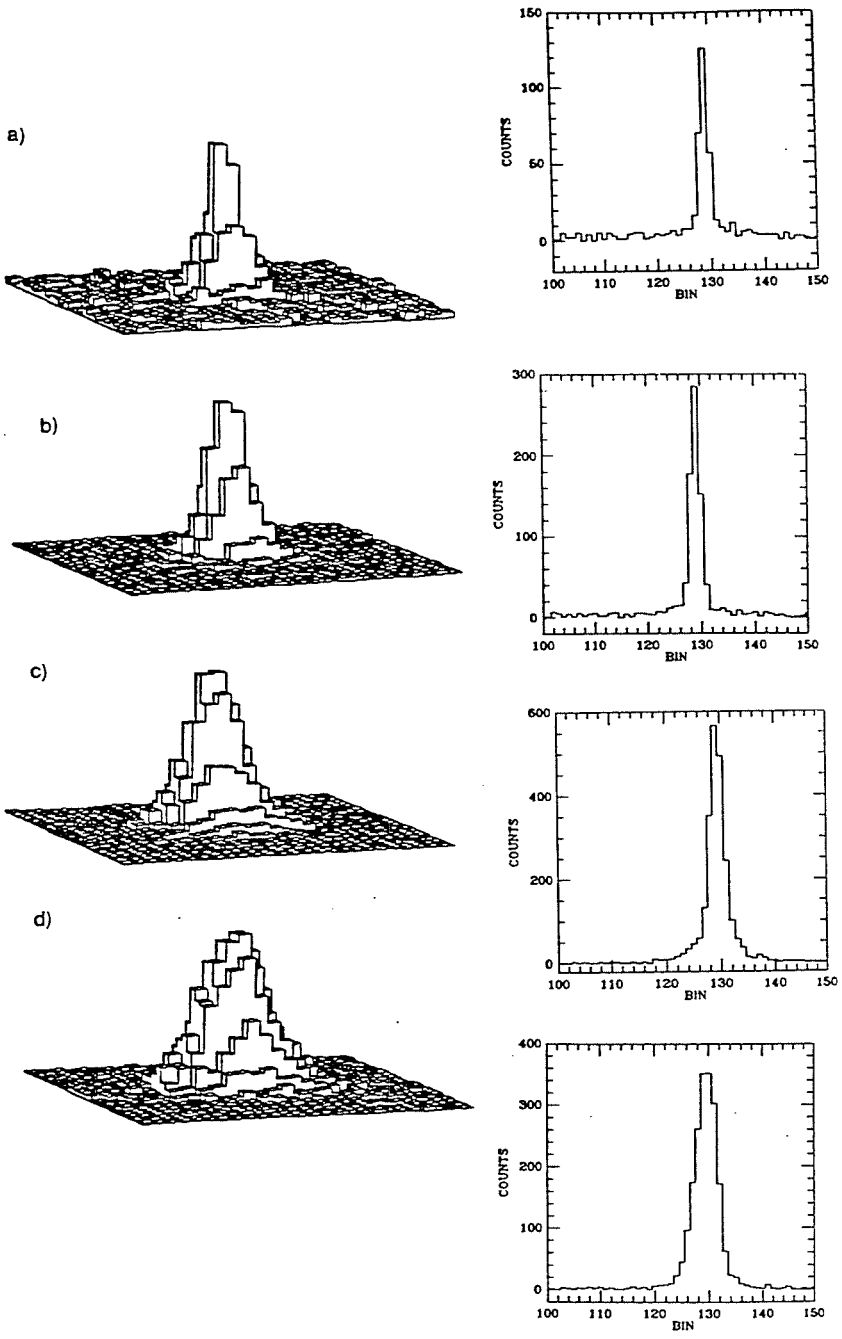

photocathode and a higher degree of electron reflection from the interchannel web and the Al_2O_3 film. The rapid drop of count rate due to channel paralysis in profile (d) means that the broadening will also be caused in part by a localised drop in gain. A drop in gain to 4×10^6 has already been shown to give a theoretical PSF width of 130 μm, and for channel paralysis the gain may be considerably lower. An attempt was made to investigate the MCP gain obtained with these spots, but proved inconclusive because of the low signal to noise in the overall pulse height distributions.

With the two low flux PSFs the base size remains relatively constant with the wings of the profile increasing in intensity and thus lowering the FWHM profile. There should be no drop in gain at these levels and so the broadening should be attributable to the effects of backscattering alone. The contribution of the electronics, however, needs to be considered since it has been shown that at lower illumination levels the signal to noise in the pulse height distribution is low and corresponds to an increase in the gain variation of pulses coupled with a larger change in reference voltage at the analogue to digital converters. Thus it remains difficult to separate the relative contributions.

The scope of this investigation was limited and it requires further experimentation to accurately quantify the change in broadening of the PSF with the level of point source illumination. In particular, future tests should ideally utilise a range of point source sizes, corresponding to a number of different channel groupings combined with a range of proximity focussing voltages.

The exact response of MCPs to point source inputs has been well documented in theory, but there is little experimental confirmation of the theory in the literature.

7.7) Veiling Glare

In order to investigate the veiling glare characteristics of the detector, a technique similar to that of Taylor (1981) was employed. This technique involves masking half of the photocathode area and measuring the percentage difference in illumination one sixth of the photocathode diameter either side of the mask edge. Effective masking of half of the detector photocathode surface was obtained using an opaque masking tape. The veiling glare characteristics were then investigated with several illumination levels at proximity focussing voltages of 400 V and 300 V. One sixth of the photocathode diameter for a 40 mm tube is 6.6 mm. The veiling glare at both proximity focussing voltages was found to be the of order of 1% or less, 6.6 mm from the edge, in agreement with values measured by Lyons and Read (1983) for a 40 mm intensifier. The definition of veiling glare, however, is more relevant to night vision intensifiers than to astronomical requirements and so equivalent measurements were made at 1 mm amd 3 mm from the mask edge. The veiling glare measurements, together with their profiles, are presented in figures 7-21 and 7-22 for several illumination levels, at 1 mm and 3 mm from the edge of the masked region. The profiles have been summed over several cross sections and smoothed using a low pass Fourier noise filter.

Figure 7-21: Veiling glare profiles from edge of masked region for proximity focussing voltage of 300 V.

Veiling Glare Measurements

Count Rate (cs^{-1})	Glare (%)		V_{pc} (V)	No.
	1 mm	3 mm		
1000	-	-	300	1
8000	2.03	0.08	300	2
15000	3.35	1.36	300	3

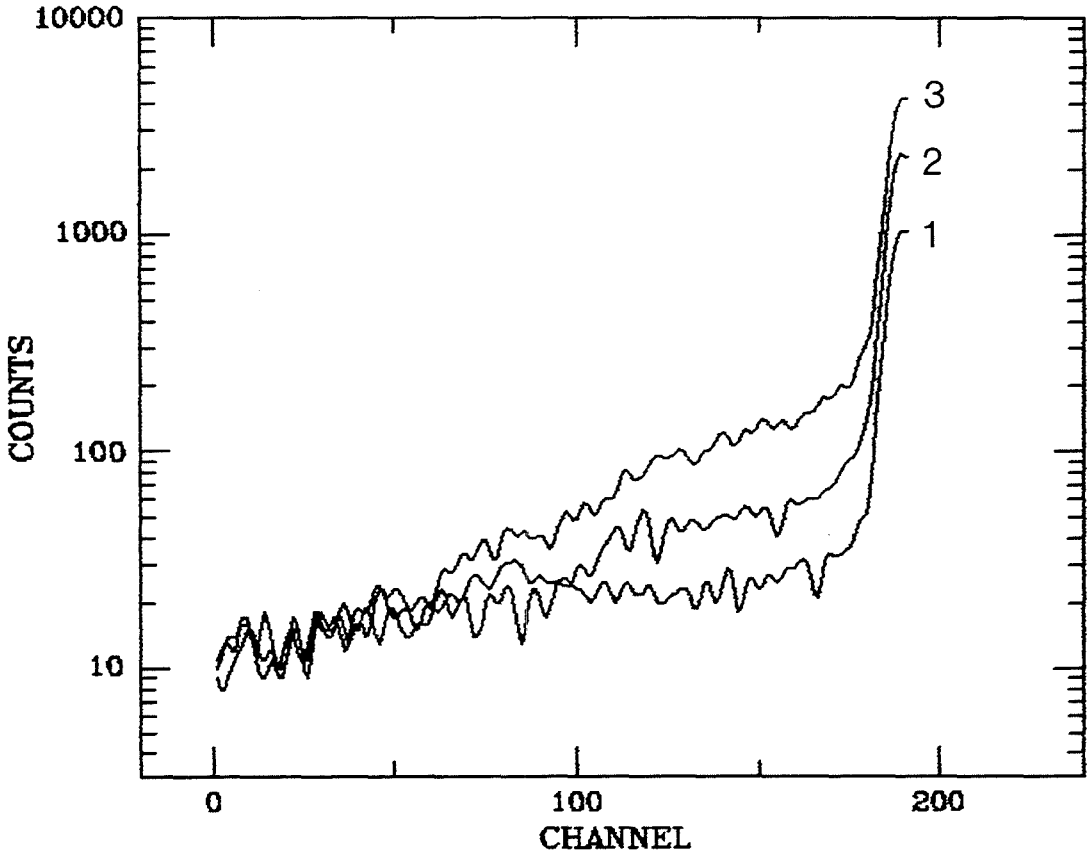

Figure 7-22: Veiling glare profiles from edge of masked region for proximity focussing voltage of 400 V.

Veiling Glare Measurements

Count Rate (cs^{-1})	Glare (%)		V_{pc} (V)	No.
	1 mm	3 mm		
dark	-	-	400	1
3000	2.58	1.25	400	2
6500	4.01	1.11	400	3
8500	4.81	0.98	400	4
13000	6.60	1.84	400	5

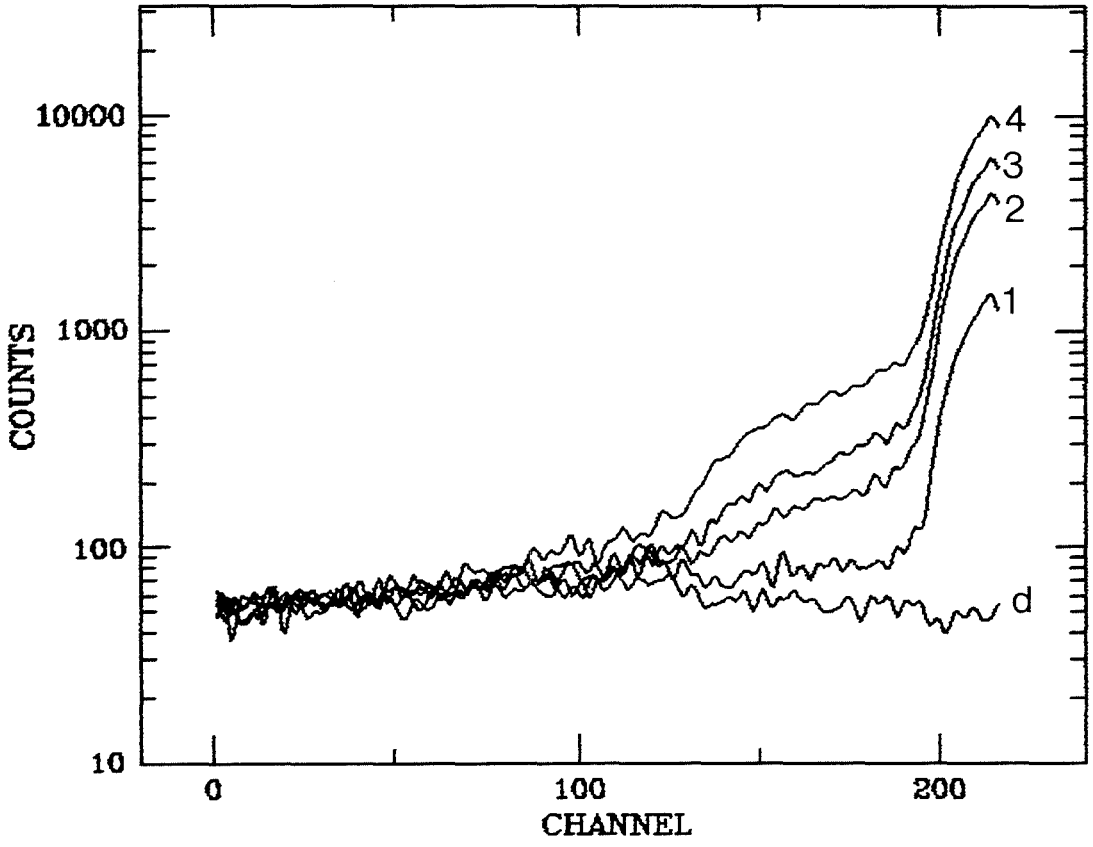

At the higher proximity focussing voltage there is considerably more glare, with a halo extending 1 mm from the masking edge and a broader, low intensity halo extending over 3 mm. In comparison profiles at 300 V have have a relatively sharp cutoff, but the low intensity halo extends over 4 mm. This result can be explained if, as expected, scattered electrons do not travel as far in the focussing field before they are returned to the MCP input.

7.8) Conclusions

The source of the non-uniform resolution can be attributed to two possible causes, a non-linear photocathode to MCP gap or non-linear signal processing. The apparently uniform non-linear variation of resolution across the field could result from either of these two sources. If the effect does arise from a non-uniformity in the gap width, it would have to be a considerable size (> 1 mm, the nominal gap = 0.5 mm), which would be considerably larger than both the errors specified by ITL and the expected degree of any plate arching. In addition this explanation implies that the gap width, had it been uniform, was well outside of specification. The wings seen in the arc lines may arise from light transmitted by the semi-transparent photocathode. At these low light levels this seems unlikely, particularly since they are seen in the low intensity lines as well as the stronger lines. The signal processing electronics remain the most likely source of the non-linear resolution. The cause may be due to the ratiometric operation of the ADCs, or some other mechanism within the signal processing unit

whose magnitude is signal dependent. The various operating problems encountered with the ADCs weigh heavily in favour of the former suggestion. The preamplifier circuits also introduce spatially dependent errors, because of their relative sensistivity variations. Typical variations would not be expected to cause the observed degree of non-linearity.

Chapter 8

8.1) Objectives

One of the principal objectives of the study was to determine the performance of the IPD as a spectroscopic detector, particularly for the study of stellar radial velocities. Therefore, having established the optimum operating parameters for the detector, a programme of astronomical observation was undertaken. The objectives of this study were to establish the precision with which stellar radial velocities could be determined, to establish the stability of the detector and the spectrographic system, and to use the system in an astronomical project.

The first two objectives were achieved by a study of the spectra of a sample of faint IAU radial velocity standards, obtained with the detector system. Information about the system stability was obtained from a study of the comparison arc spectra obtained during these and subsequent observing runs. Following this initial investigation, the instrument was used to obtain time resolved spectra of the short period eclipsing binary system SV Camelopardis, in order to determine the system's mass ratio. This chapter will therefore briefly discuss the spectrograph and problems encountered during commissioning of the detector system and then discuss the results obtained from the observation of IAU standard velocity stars and SV Camelopardis.

8.2) Spectrograph System

The Leslie Rose Telescope (LRT) at the University Observatory is a 0.5 m, f/11 Cassegrain system. The telescopes instruments include a spectrograph based on the design of Richardson and Brealey (1973). The spectrograph is mounted at the Cassegrain focus giving a plate scale of 37 arcsec mm^{-1} The camera employs an off axis f/11 collimator and an f/4.1 Maksutov camera incorporating two corrector lenses and a field flattener. Focus of the spectrograph camera is achieved by the adjustment of the camera mirror position.

The spectrograph is designed for medium and low dispersion spectroscopy and offers a choice of two gratings, giving 600 lines mm^{-1} or 830 lines mm^{-1}, producing dispersions of 80 $\mathring{A}mm^{-1}$ and 30 $\mathring{A}mm^{-1}$ respectively. In the operating configuration used during the period of the detector test runs, neither the grating, nor the grating angle could be changed while the detector was operating. This precaution was necessary to avoid damaging the photocathode with excess illumination. For the period of study a dispersion of 30 $\mathring{A}mm^{-1}$ was used with a central wavelength of 4500 $\mathring{A}$.

The slit and dekker assembly comprises four settings which allow the slit to be fully covered or open and two central settings allowing a single 2 mm slot and two slots of 2 mm for photographic comparison arc exposures. This latter dekker setting was not compatible with possible detector orientations, due to the cosmetic defects, and so was not used. A mask is provided for the Hartmann

focus test. The slit width of the spectrograph is 70 μm, corresponding to 2.5 arcsec on the sky, which gives a projected slit width of 26μm at the detector.

The spectrograph design is very stable and has negligible flexure when operated in the photographic mode. The St Andrews spectrograph of a similar design for the 1.0 m Kapteyn telescope has a reported stability of the order of 1μm per hour of R.A. (Edwin 1985). Similar results have been obtained with the LRT spectrograph in the photographic mode (Hilditch 1984). The detector was located on the side of the spectrograph by means of a specially constructed mounting plate. Following preliminary tests, a micrometer adjustment was added to enable accurate alignment of the detector axis with the dispersion direction for the spectrograph. The signal processing electronics and EHT unit were mounted on the side of the telescope, to minimise the length of the leads from the detector head to the electronics. No problems were experienced with heat transfer from the electronics to the telescope. Figure 8-1 shows the detector mounted on the spectrograph and illustrates the compactness of the system.

The spectrograph comparison lamp is a hollow cathode copper-argon arc. This type of arc lamp provides a large number of lines suitable for spectral calibration purposes in the region 370 nm to 800 nm. Kodak wratten gelatin filters (ND = 3.0) were necessary to reduce the intensity of the arc spectra to an acceptable level for the detector sensitivity.

Figure 8-1: Detector mounted on Leslie Rose Spectrograph

From 750 nm to 1000 nm there are several very intense lines (Norlen 1973) which can cause problems of order overlaps with shorter wavelengths. Prior to the installation of the IPD, the spectrograph was used principally for photographic spectroscopy, and so the effect of second order overlap was negated by the plate sensitivity cutoff.

The system was initially tested using a 2 mm thick BG38 filter, with a typical transmission of 5% at 800 nm, which had been found to be satisfactory during the testing of an intensifier-photographic plate system (Edwin 1983). Copper-argon arc spectra obtained using this filter were found to have several anomalous lines which could not be identified and were dominant at the blue end of the arc spectra.

Figure 8-2 shows a 100 s integration of an arc spectra obtained using a GG400 filter, normally used to remove second order blue overlap for first order red spectra. The lines are due to second order overlap and correspond to the unidentified lines seen in the arc spectrum using a BG38 filter. The wavelengths of the lines have been obtained from Norlen (1973). At the AAO and SAAO observatories $CuSO_4$ filters are used to remove any red ArI lines resulting from order overlaps with the IPCS and RPCS systems. $CuSO_4$ has a sharp transmission cutoff at 600 nm. These filters are usually in the form of a solid crystal or a liquid cell, the latter being rather more complex to install and maintain. Both options are, however, expensive and the crystal filters have relatively short lifetimes

Figure 8-2: Diagram showing Cu-Ar arc spectra taken with GG40 filter showing second order spectral overlap.

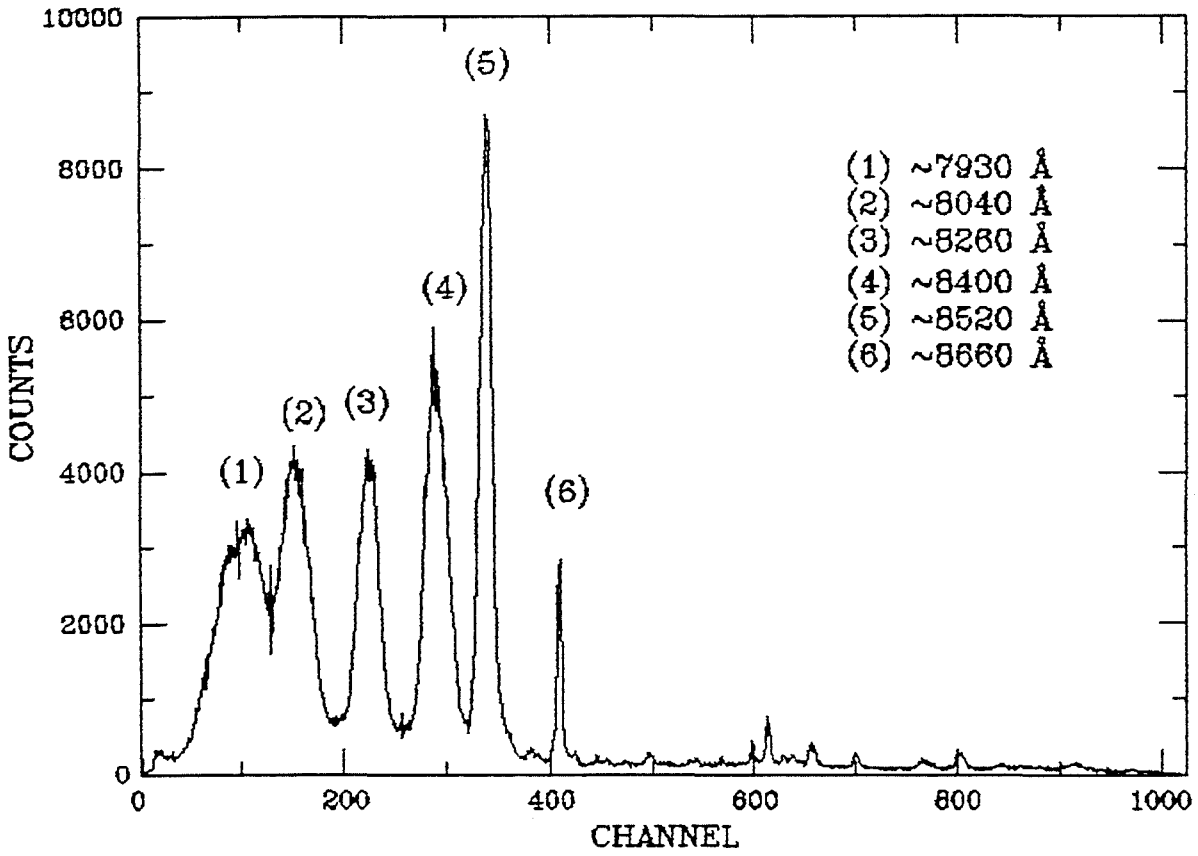

short lifetimes (Lloyd Evans 1984).

A solution to the problem for the St Andrews spectrograph was to use a diffuser cell containing $CuSO_4$ crystals. This arrangement was found to remove second order transmission, but required some experimentation to obtain a suitable thickness of diffuser (5 mm). The main drawback of this technique was that the combination of diffuser, neutral density filters and fibreoptic transmission led to a loss of the weaker arc lines shortward of 400 nm. Although several configurations were investigated it was not possible to obtain a reasonable compromise between the intensity of the lines in the region > 400 nm and the lines < 400 nm. Raw stellar spectra obtained with the detector show calcium H and K lines, indicating that the detector response below 400 nm is still acceptable.

Table 8-1 gives a line list for the copper argon arc lines available in the spectral region of the arc spectra obtained with the detector. The list details the line blends and those lines which were judged suitable for measurement in the calibration of spectra and does not include all the arc lines found in this region. A consequence of the restricted number of lines available is that strong, often saturated lines which are not usually used at this dispersion were of necessity included in the line list. Those lines which were not used for calibration purposes are marked. However, some of the other lines were often discarded because of the poor resulting fit.

Table 8-1

Line (A)	Comment
4806.021	Not used
4764.865	
4657.901	
4609.567	Blended
4589.898	Blended
4579.350	Blended
4545.052	
4510.733	
4481.811	Blended
4474.759	Blended
4448.879	Blended - not used
4400.986 + 4400.0968	
4426.001	Blended
4379.667	Blended
4370.753	Blended
4348.064	
4333.561	
4309.239	
4300.101	
4277.528	Blended
4272.169	Blended - not used
4266.286	Blended - not used
4228.158	Blended
4200.674	Blended - not used
4198.317	Blended - not used
4158.590	
4131.724	
4103.912	

Flat fields for the detector were obtained by illuminating the spectrograph camera system with a green LED (λ = 550 nm). The LED was permanently mounted in the spectrograph with the level of illumination controlled from a simple control potentiometer and an unstabilised supply. This arrangement gives uniform illumination of the detector photocathode and removes the problems of achieving adequate spectral coverage often found in other systems, where a calibration lamp illuminates the slit.

The standard procedure for flat field exposures was to split the total integration time required into a number of hourly segments. The detector control package was then programmed to write the image to tape at hourly intervals and then wipe the contents of the external memory. This technique avoids exceeding the dynamic range of the memory because of high levels of hotspot field emission.

8.2) System Stability

The repeatability of arc exposures was tested by cross correlation of comparison arcs obtained during observing runs. Typical results are shown in figure 8-3, where the shifts were obtained by cross correlating the final processed arc spectra for each stellar spectrum, using the first arc in the run as the template. The correlations were limited to the central 400 pixels of each arc spectrum, thus avoiding most of the broad lines and feature blending which would distort the CCF peak.

Figure 8-3: Correlation between processed comparison arcs on observing runs.

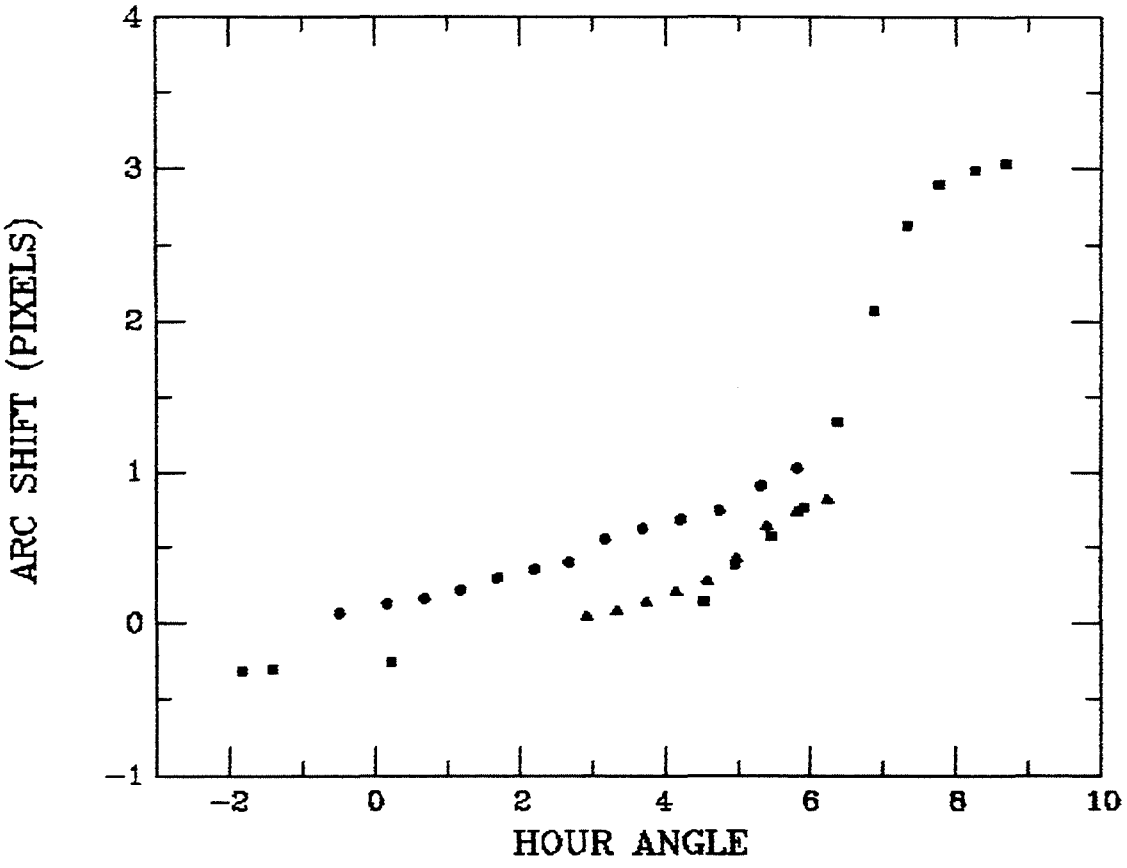

The results show that the registration between consecutive arcs is dependant upon the position of the telescope. The sharp rise in shifts indicates instrument flexure at an hour angle of 6 hours. Figure 8-4 shows the correlation between comparison arcs taken before and after each stellar spectrum for the same series of observations. Registration between these arcs is within 0.1 pixels at hour angles up to approximately 6 hours, where there is an excursion giving a peak shift of 0.5 pixel. The excursion correlates with the zone of flexure in figure 8-3. The system is relatively stable, therefore, with some evidence of flexure at larger hour angles which were found to correspond to declinations of $-10^{o} > \delta > 70^{o}$. The IPD head unit weighs approximately 5 kgs in total and outside the range specified above, it exerts a large moment perpendicular to the axis of the spectrograph.

8.3) Observational Procedures

Prior to an observing run the detector power supplies were checked to ensure that the required voltages were being supplied to the EHT unit and that the proximity focussing and MCP potentials had not drifted. A proximity focussing voltage of 370 V was used, to avoid excessive photocathode hotspot noise and retain good proximity focussing resolution. The MCP applied potential was set at 3.35 kV giving a gain of 6×10^{6}. During the course of an observing run the detector was left running continuously so that hotspot activity would be minimised.

Figure 8-4: Correlation between raw arcs before and after stellar spectrum integration.

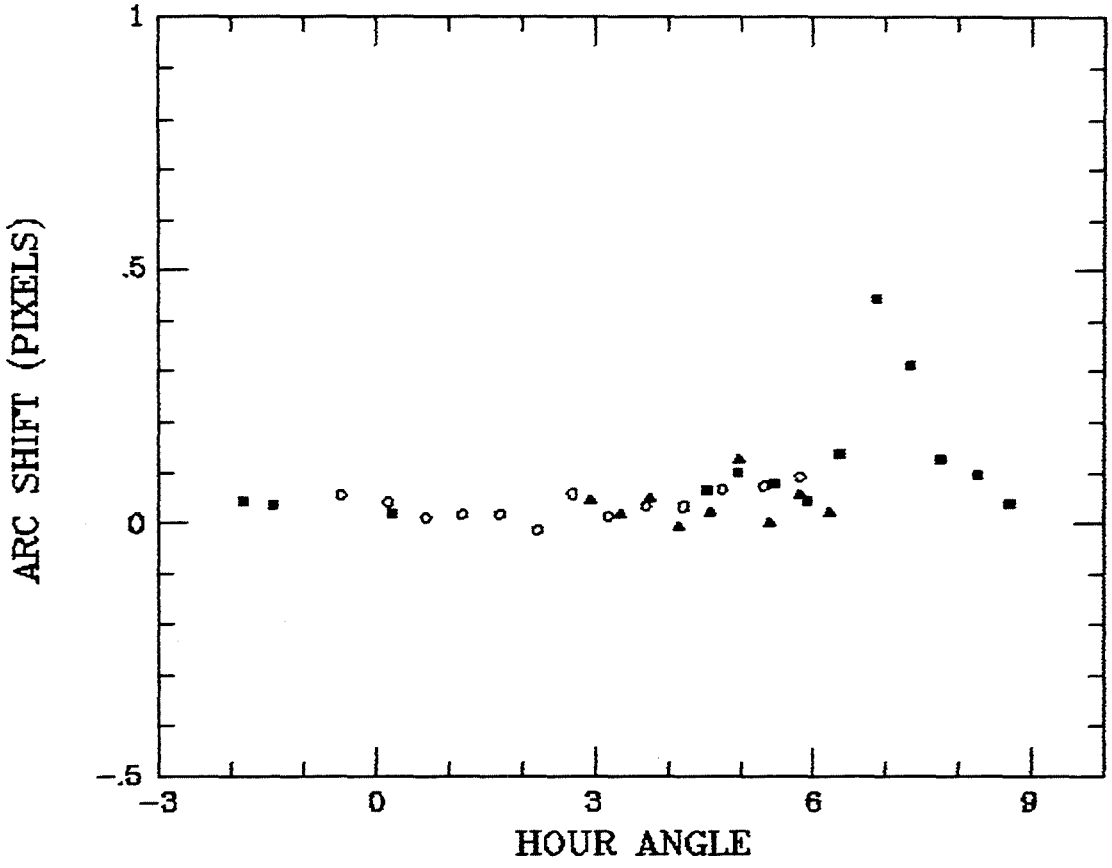

Spectra were imaged onto a central section of the photocathode just below the the hotspot features (d) and (e) shown in figure 5-1. This area lies in the sensitive region of the photocathode. For long integrations some problems were experienced with contamination of the spectra by dark noise from the wings of the two hotspots. An additional displacement of 2 mm was sufficient to remove this contamination. The choice of the software window is determined mainly by the need to exclude hotspots from the images. It was found that the presence of hotspots within the image window could cause premature termination of integrations, due to memory overflow. Specifically localised pattern noise in the area of the hotspots often exceeded the dynamic range of the system in flat field integrations. Windows were therefore selected to cover the area of the spectrum and in this configuration the spectrum typically fell across 10x1024 pixel cross sections.

To allow guiding of the telescope on fainter stars (> V = 7), a Mullard compact image intensifier unit was added to the spectrograph acquisition eyepiece. The addition of the intensifier helped the positive identification of target stars and permitted accurate telescope guiding during integrations. The detector operating package was particularly useful in this respect. The integration display routines give continuously updated plots and image information leaving the observer free to guide the telescope while monitoring the observation's progress.

The detector flat fields were obtained before and after an observing session. The method of illumination meant that the whole detector window was within the illuminated area. The overall flat field count rates were limited to $\sim 10^4$, because of the increasing degree of MCP gain loss above these illumination levels. Consequently, flat field integrations were typically run for 8 - 10 hours during the day, to obtain reasonable image statistics ($\sim 10^4$ counts pixel^{-1}).

Comparison arc spectra were obtained before and after each observation of a stellar spectrum to allow for any shift during the integration period. For continuous observations of the same object, a single arc exposure was taken in between stellar spectra.

8.5) Radial Velocity Measurement

The two principal methods used for the measurement of radial velocities in digitised spectra are the line profile fitting and cross correlation techniques. Line profile fitting involves fitting individual spectral lines with a mathematical function, typically a parabola or a Gaussian. The line characteristics may then be determined from the fit parameters. A major problem with profile fitting arises when it is necessary to fit distorted or blended line shapes. In addition, the technique does not utilise all of the data available, which is a major disadvantage when there are a limited number of lines which can be fitted.

The cross correlation technique provides an alternative method for obtaining the Doppler shift between spectra. The theory of cross correlation is outlined in detail in Chapter 4 and it will be discussed further here in terms of its application to the analysis of stellar spectra. The Doppler shift equation

$$\Delta\lambda/\lambda_o = V/C \qquad (8.1)$$

may be expressed in terms of wavelength shift alone by taking logarithms to give the expression

$$\ln\lambda = \ln[1 + z], \qquad (8.2)$$

where $z = v/c$. Thus the relative velocity of a spectrum calibrated in terms of $\ln\lambda$ may be obtained from the value of $\Delta\ln\lambda$ alone. Cross correlating the spectrum of a radial velocity standard with that of a star of similar spectral type will, therefore, give the relative radial velocity between the two stars. The procedure for cross correlating spectra is in principle the same as that described in section 4.7.4. and is discussed by Simkin (1974). There are, however, several additional techniques associated with the cross correlation of stellar spectra which are of some importance. The template and comparison spectra must both be rectified and suitably noise filtered prior to correlation. Residual low frequency components resulting from the continuum trend and high frequency noise will both cause distortion of the CCF peak which may lead to an incorrect value of velocity. In order to avoid mismatch between

the ends of a spectrum and thus leakage in the FFT, endmasking is usually applied. A typical end masking weighting function is the cosine bell, applied to 5% of the data points at the ends of the data train. For late spectral type stellar spectra the hydrogen lines and the G band are usually omitted from the cross correlation, since these features may broaden the CCF and distort the position of the true peak. The same practice should also be applied to night sky lines and unwanted emission lines, which again may distort the true peak of the CCF. The primary reason for this practice is that the cross correlation function acts as a matched filter and so strong lines will be given more weighting than weak lines.

In view of the detector's limited resolution, the method of cross correlation analysis was adopted as the principle technique to be used in the analysis of stellar radial velocities. This method had two advantages in that there was software available to perform cross correlation of stellar spectra and with the severe line blending expected from this resolution it was unlikely that many lines profiles could otherwise be meaningfully measured in a spectrum.

8.6) Data Reduction

Spectral data obtained with the detector were reduced using the Starlink SPICA package and the REDUCE and VCROSS packages on the Royal Observatory Edinburgh and St Andrews Vax 11/780 minicomputers. SPICA was used to read the raw detector FITS files

from disk and to reduce them to one dimensional spectra suitable for analysis with the REDUCE package. The process of reduction involved flat fielding the spectra and correcting the individual cross sections for any residual non-alignment. A SPICA routine was available which performs the correction by cross correlating arc cross sections and determining the relative shift between them. The cross sections are then aligned using a table of the calculated shifts. The stellar spectra were also noise filtered using SPICA routines.

REDUCE (Hill et al. 1982) is an interactive package designed for the reduction of photographic, Reticon and IPCS spectra. The program uses a modified FITS file convention for the storage of spectra in order to simplify the handling of large numbers of spectra and for economy of disk space. REDUCE comprises a series of modules each designed to perform a certain operation upon the spectral data. The modules used in the reduction of IPD spectra are reading FITS disk files, arc measurement, spectral calibration, wavelength linearisation, rectification of spectra, $\ln\lambda$ wavelength linearisation.

The measurement of comparison arc files is an interactive process based on the standard plate technique of Aitken (1935). Lines from the arc line list are located from their calculated position and are then fitted with parabola over a section of the profile delineated by cursor. Line positions are predicted from the fit and the procedure can be run automatically, using preset cursor settings, once the line position prediction is established. The

resultant series of arc measurement (O-C) residuals may then be displayed and a polynomial fitted to them. Poor arc measurements can be deleted interactively and a new fit made to the data. Figure 8-5(a) shows the result of a typical fit to an arc spectrum with a fifth order polynomial fitted to the data. In figure 8-5(b) the poor arc measures have been pruned and a new fit made to the data. Typical rms values on the fit were in the range 10 to 18 μm, where one pixel is 39 μm. The scatter in the fit indicates that there are probably systematic errors arising from poor arc measurements. The lines fitted to arcs near the ends of comparison spectra often had very large residuals. This was caused by the very poor resolution and sensitivity associated with the periphery of the detector's imaging area.

Wavelength linearisation of a stellar spectrum requires the corresponding arc coefficients and is not possible outside the start and end wavelengths defined by the coefficients. Consequently extrapolation of the polynominal fit is avoided. In common with the other REDUCE options the wavelength linearisation of a series of files may be done automatically using a master file containing the names of files to be processed. The linearisation of stellar spectrum to Lnλ wavelength is achieved in a similar way. Rectification of stellar spectra may be achieved by using a standard continuum file, or by fitting a continuum to each spectrum independently by means of a series of cursor settings. The interpolation routine INTEP (Hill 1982) is used to fit a continuum to the cursor points.

Figure 8-5: REDUCE arc spectra calibration fits, (a) First attempt, (b) final fit.

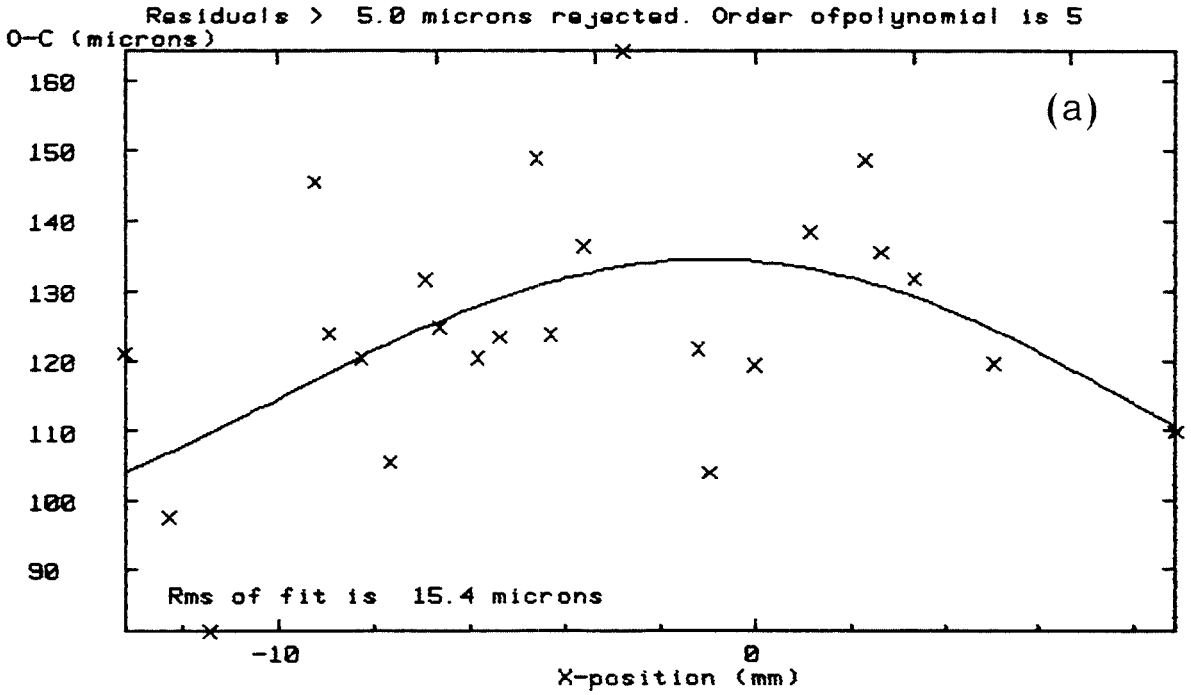

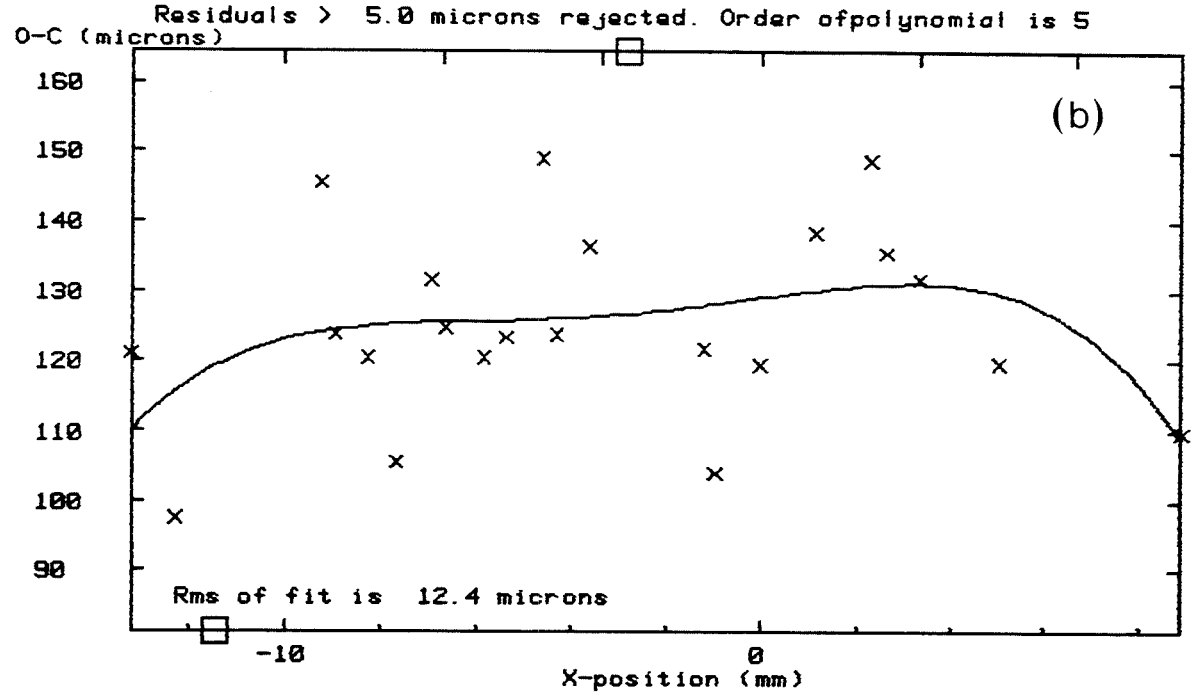

VCROSS (Hill 1982) is used to cross correlate the processed stellar spectra and is a complementary package to REDUCE. The package cross correlates stellar spectra with a given standard and allows the resulting CCF peak to be fitted with a parabola, Gaussian or a Lorentzian function. Several fits may be attempted to one profile in order ascertain the most suitable function. The package may also be used to fit a predetermined function automatically to a series of stellar spectra using the master file structure.

8.7) Detector Spectra

A spectrum of the eclipsing binary V559 Cas is shown in figure 8-6. The system has a magnitude of V = 7.0 and a primary spectral type of B9. This spectrum was obtained with an integration of 300 s. The spectrum illustrates several features of the IPD system. The sensitivity of the detector below 400 nm is illustrated, by the presence of the hydrogen lines in the spectrum. The flat fielded spectrum in figure 8-7 highlights these lines and shows the low signal to noise at the periphery of the detector imaging area. This confirms that the fibreoptic cutoff is not the cause of the loss of arc lines below 400 nm. The exact response of the detector at these wavelengths is difficult to quantify because of the photocathode's non-uniform response. The spike in the region of channel 256 is due to ADC pattern noise. This is one of the few stellar spectra where the presence of pattern noise was immediately apparent. The spectrum of the radial velocity standard HD75935 is shown in figure 8-8. The spectrum has a spectral type of G8V and

Figure 8-6: Raw IPD spectrum of V559 Cas.

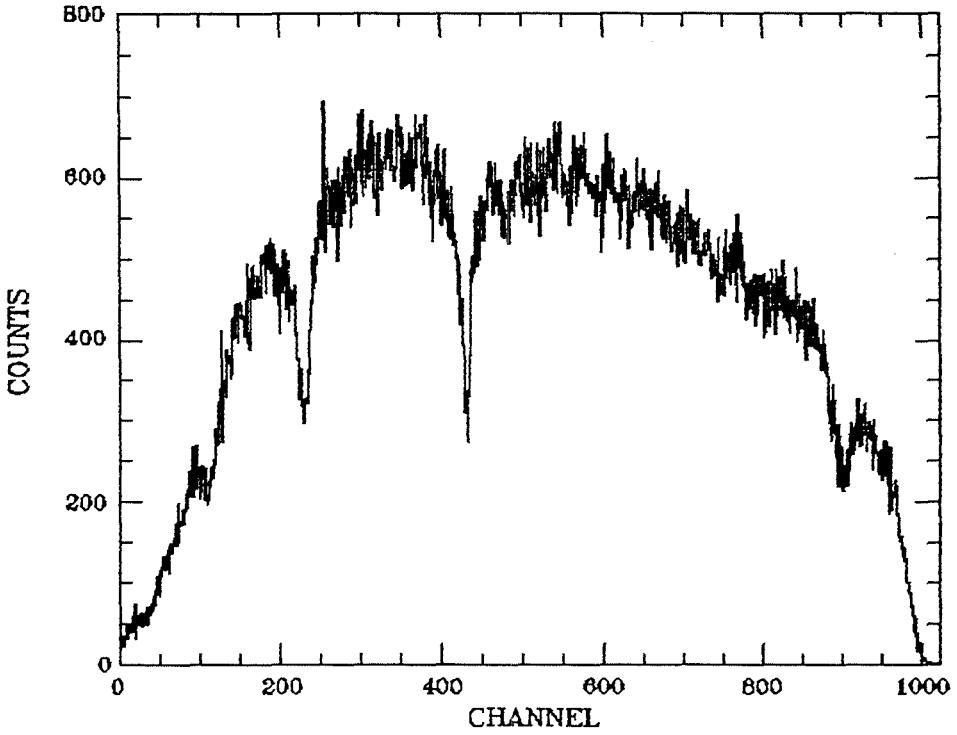

Figure 8-7: Flat fielded raw IPD spectrum of V559 Cas.

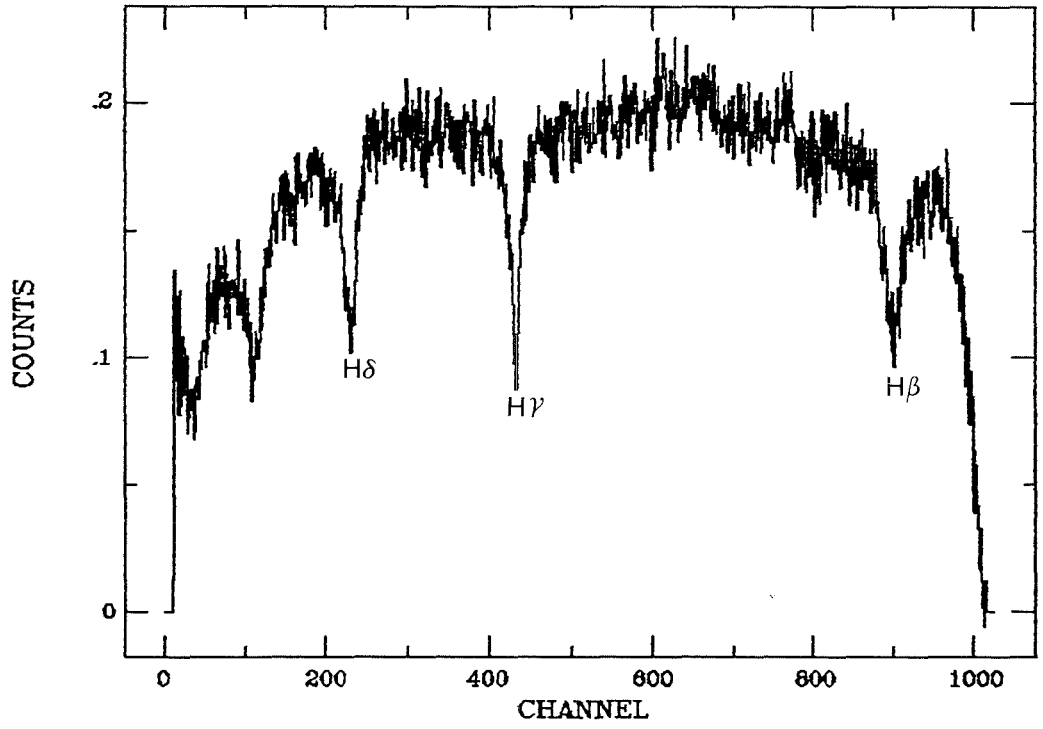

Figure 8-8: Calibrated IPD spectrum of HD75935.

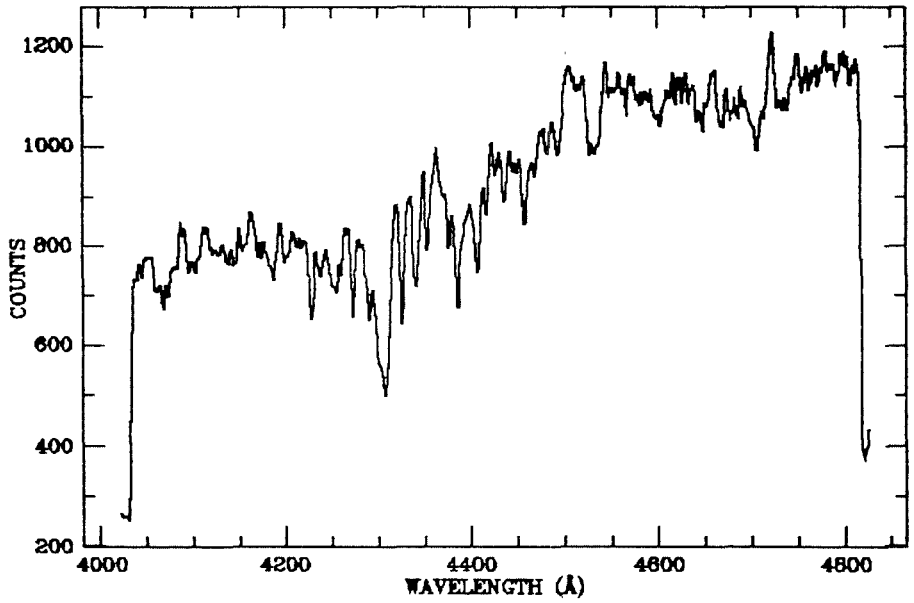

has been truncated at both ends to remove the low sensitivity regions of the photocathode. The problems involved in working with the detector resolution as it stands are well illustrated by this spectrum. While the more prominent features such as Hγ at 434 nm and the G band are fairly prominent, a lot of the metallic lines are severely blended, forming absorption troughs. It is clear that line profile measuring techniques would be of limited value in such a situation and thus confirm the choice of cross correlation as the most appropriate in this situation. The use of the cross correlation technique is not without its own problems, however, since the severe blending of lines will broaden the CCF peak and also cause asymmetries in the CCF peak profile. The measurement of asymmetric CCF peaks using parabolas or Gaussian functions may introduce systematic errors in the determination of the radial velocity of a star.

8.8) Radial Velocity Standards: Observations

The radial velocity standard stars were taken from the IAU lists of faint standards (Pearce 1957, Bouigue 1973) and are shown in table 8-1. They lie in the region of V = 6.45 to V = 9.48 and cover a range of late spectral types from F8V to K5III. Two of the selected stars have been reported as suspected variables by Beardsley et al. (1974) and Fehrenbach and Duflot (1980). Batten et al. (1983) have recommended that they should not be used for high dispersion work. Table 8-2 gives a log of the standard star spectra obtained during the winter of 1984/85. Integration times for the spectra range from 300 s to 2000 s. For the purposes

Table 8.2: IAU radial velocity standards selected for observation.

Star	Sp.	V	(1950)	(1950)	RV (km/s)	
HD12029	K2III	8.96	01 55.8	+29 08	+38.6	
HD23169	G2V	8.75	03 40.9	+25 34	+13.3	
HD29587	G2	7.29	04 38.1	+42 02	+112.4	
HD32963	G2V	8.36	05 40.8	+26 16	-63.1	
HD42397	G0IV	8.68	06 08.5	+25 01	+37.4	
HD65934	G8III	8.87	07 59.1	+26 47	+35.0	
HD75935	G8V	9.35	08 50.9	+27 06	-18.9	
HD86801	G0V	9.48	09 58.7	+28 48	-14.5	
HD90861	K2III	8.36	10 27.1	+28 50	+36.3	
HD102494	G8IV	8.26	11 45.3	+27 37	-22.9	
HD103095	G8Vp	6.45	11 50.1	+38 05	-99.1	(i)
HD112299	F8V	8.66	12 53.0	+26 01	+3.4	
HD122693	F8V	8.74	14 00.0	+24 48	-6.3	
HD126053	G1V	6.27	14 20.7	01 28	-18.4	(ii)
HD140913	G0V	8.81	15 43.1	+28 37	-20.8	
HD213014	gG8	7.7	22 25.8	+17 00	-39.7	
HD223094	K5III	8.97	23 43.9	+28 26	+19.6	

(i) Suspected variable (Beardsley et al. 1974)

(ii) Suspected variable (Fehrenbach and Duflot 1980)

Table 8-3

Radial velocity standard star observations.

OBJECT	(J.D. - 2440000)	OBJECT	(J.D. - 2440000)
HD12029	6027.40215	HD65934	6030.60765
	6027.41932		6092.47364
n = 10	6027.44199	n = 3	6092.49391
	6027.52948		
	6028.40689		
	6028.44558	HD75935	6028.66659
	6028.51780		6033.63630
	6030.52322	n = 7	6092.51684
	6033.34531		6092.53503
	6033.41070		6139.39035
HD23619	6027.49775	HD86801	6030.72313
	6027.61683		5699.49918
n = 6	6028.49041	n = 5	6092.58514
	6028.57310		6142.37544
	6033.43261		6142.35795
	6033.47411		
HD29587	6027.56816	HD90861	6092.60502
	6027.58000		6092.62336
n = 5	6028.60854	n = 3	6084.61256
	6033.45324		
	6033.51281		
HD32963	6028.53138	HD102494	6092.64733
	6028.62077	n = 2	6092.66584
n = 5	6030.56159		
	6033.57286	HD103095	6090.67198
	6033.59899	n = 2	6143.59624
HD42397	6027.59841	HD112299	6090.64938
	6030.58306	n = 4	6141.55812
n = 7	6033.59124		6141.60197
	6091.39633		6141.65582
	6092.43462		
	6092.45374	HD126053	6143.57550
	6117.33706	n = 2	6143.58323
HD122963	6091.72950	HD140913	6141.68225
	6091.74761		
n = 3	6143.65425		

of cross correlation analysis, stellar spectra reduced to 500 points in length were used with a wavelength range 415 nm to 475 nm.

Figure 8-9(a) shows the velocity residuals for the radial velocity standards in the spectral classes F8 to G2, obtained using a standard of each of the four spectral classes. The scatter of velocities in the diagram is considerable. There appears to be no correlation with spectral class, although some spectra show evidence of systematic error which is repeatable over several nights' observations. A similar situation appears to exist for the later spectral types G8 to K5, shown in figure 8-9(b), where there is a similar scatter in the velocity residuals. The resolution of the detector is at best 2.5 pixels FWHM in 1024, with a corresponding velocity dispersion of 180 kms^{-1} at 420 nm. The repeatability of unprocessed arc spectra was shown to be less than 0.2 pixels for most telescope orientations. It would be expected therefore that spectra from the same star might reflect this figure and show a smaller residual velocity scatter. This does not appear to be the case as the series of residuals in figure 8-10 shows. These plots show the radial velocity residuals for a series of spectra where each star in a group has been cross correlated with all the other observations of itself.

There are two main reasons for the radial velocity variations observed, both of which are ultimately due to the resolution of the detector. While unprocessed arc spectra indicate system stability, the calibration of these arc spectra probably introduces systematic

Figure 8-9(a): Radial velocity residuals for spectral types F8 to G2.

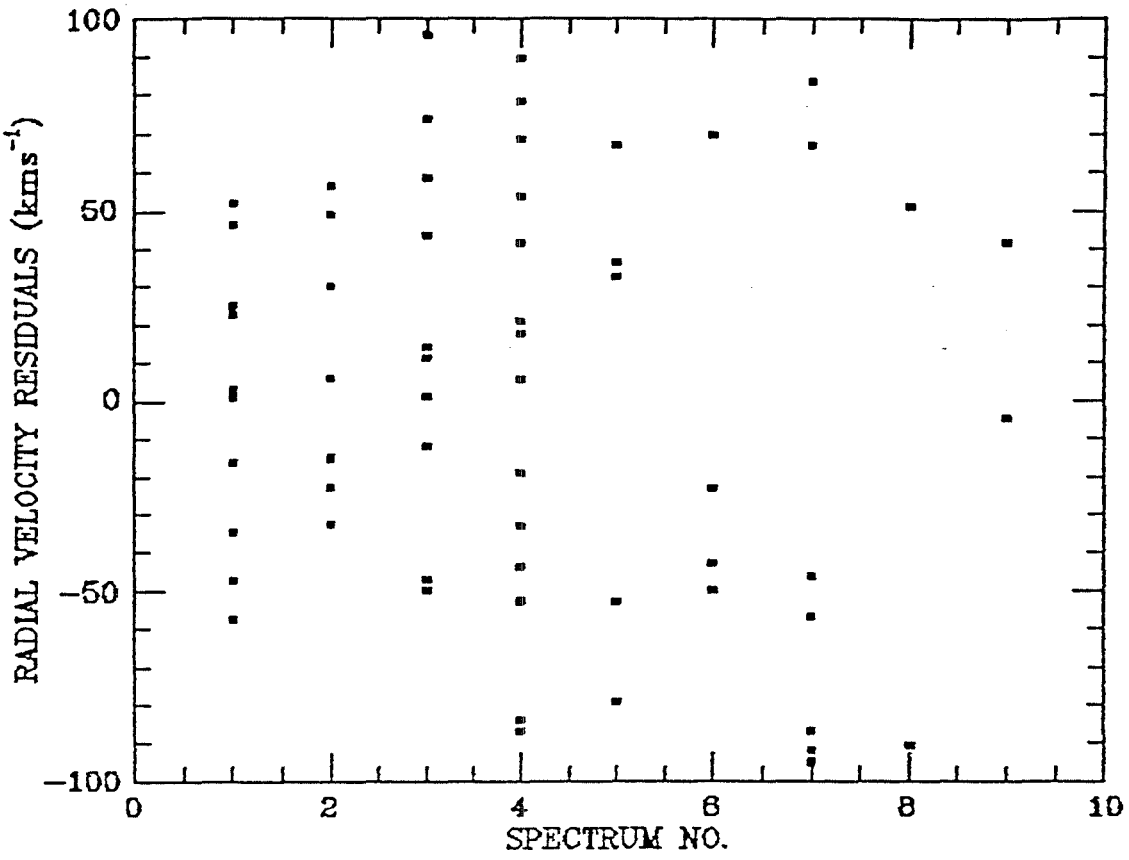

Figure 8-9(b): Radial velocity residuals for spectral types G8 to K5.

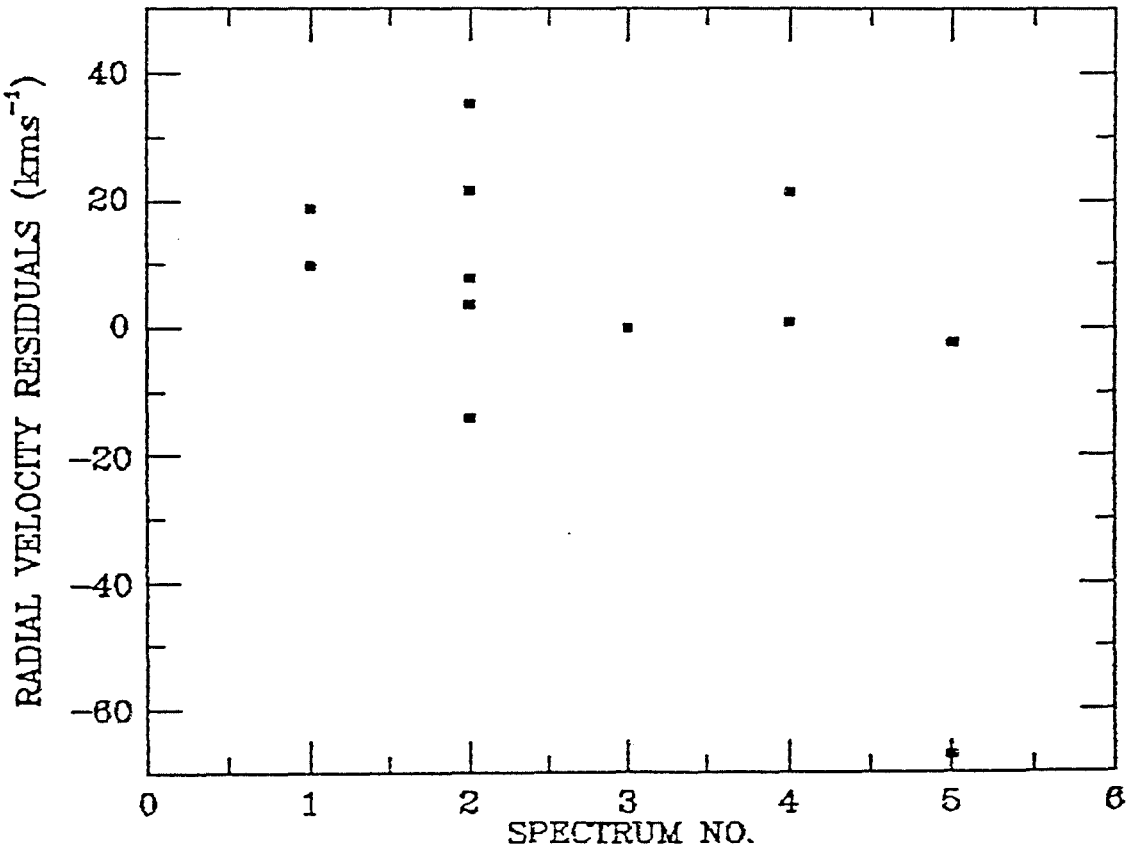

Figure 8-10: Radial velocity residuals for cross correlating spectra from same stars.

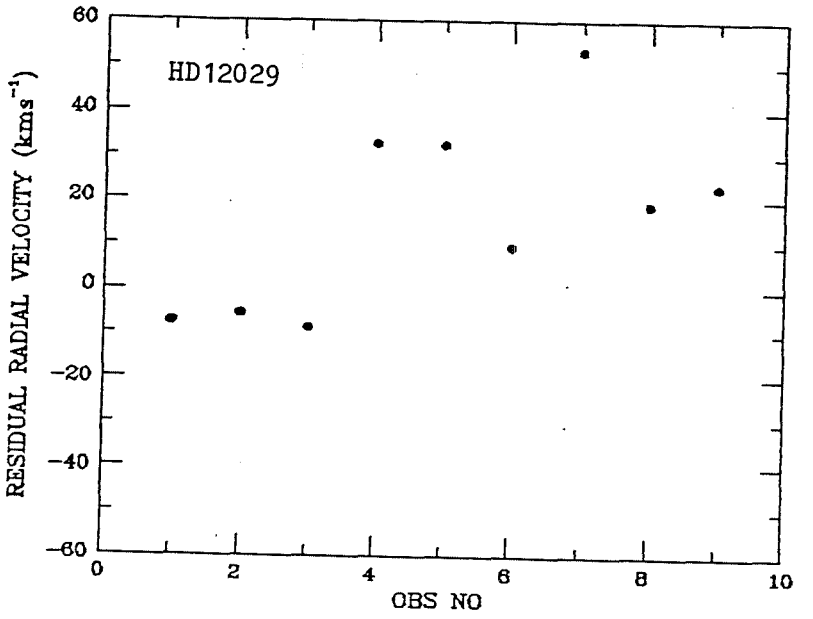

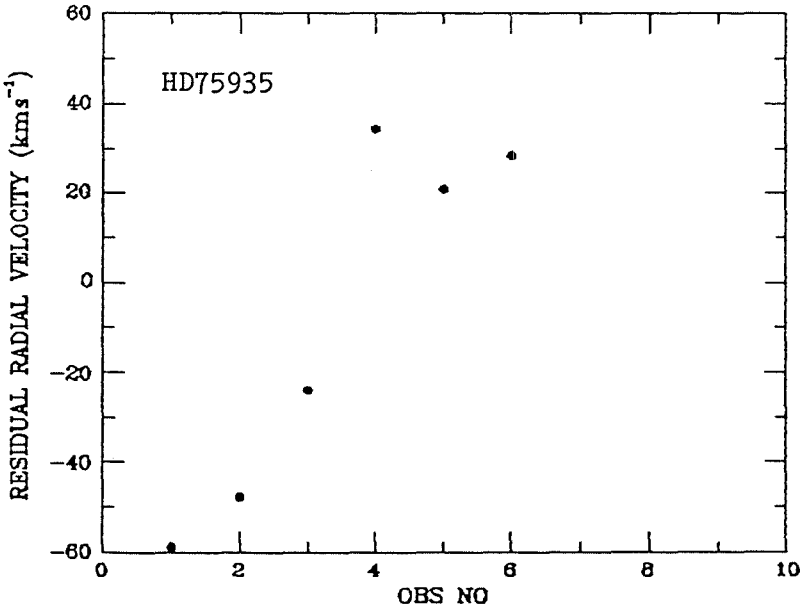

errors into the wavelength linearisation of the stellar spectra. The combination of non-uniform resolution and a large number of blended arc lines introduces a large uncertainty into the accuracy of the arc calibrations. The low resolution also causes considerable blending of stellar spectral lines, particularly in late type spectra and this leads to broad CCF profiles. Figure 8-11 shows typical profiles of CCF peaks and the variation in the velocity obtained for different fitting functions. In the analysis of the spectra, the radial velocity adopted was that from the function giving the lowest error and the optimum fit to CCF profiles. Typical values of the CCF profile widths are in the range of 250 kms^{-1} to 500 km^{-1}. In some cases the CCF peaks are also asymmetric and this leads to considerable errors in fitting any of the functions, when they can be seen not to match the profile.

A technique often used in cross correlation analysis is that of constructing template comparison spectra to improve signal to noise in the cross correlation. This was attempted for several series of spectra. In each case the template was constructed by adding spectra which had been shifted by an amount corresponding to their helocentric velocity correction. The individual spectra were then cross correlated against the template. Figure 8-12 shows the velocity residuals for the application of this technique to the same stars as those shown in figure 8-10. Once again there is little change in the degree of scatter adding further weight to the argument that the results are intrinsic to the detector resolution.

Figure 8-11: Example of CCF peaks.

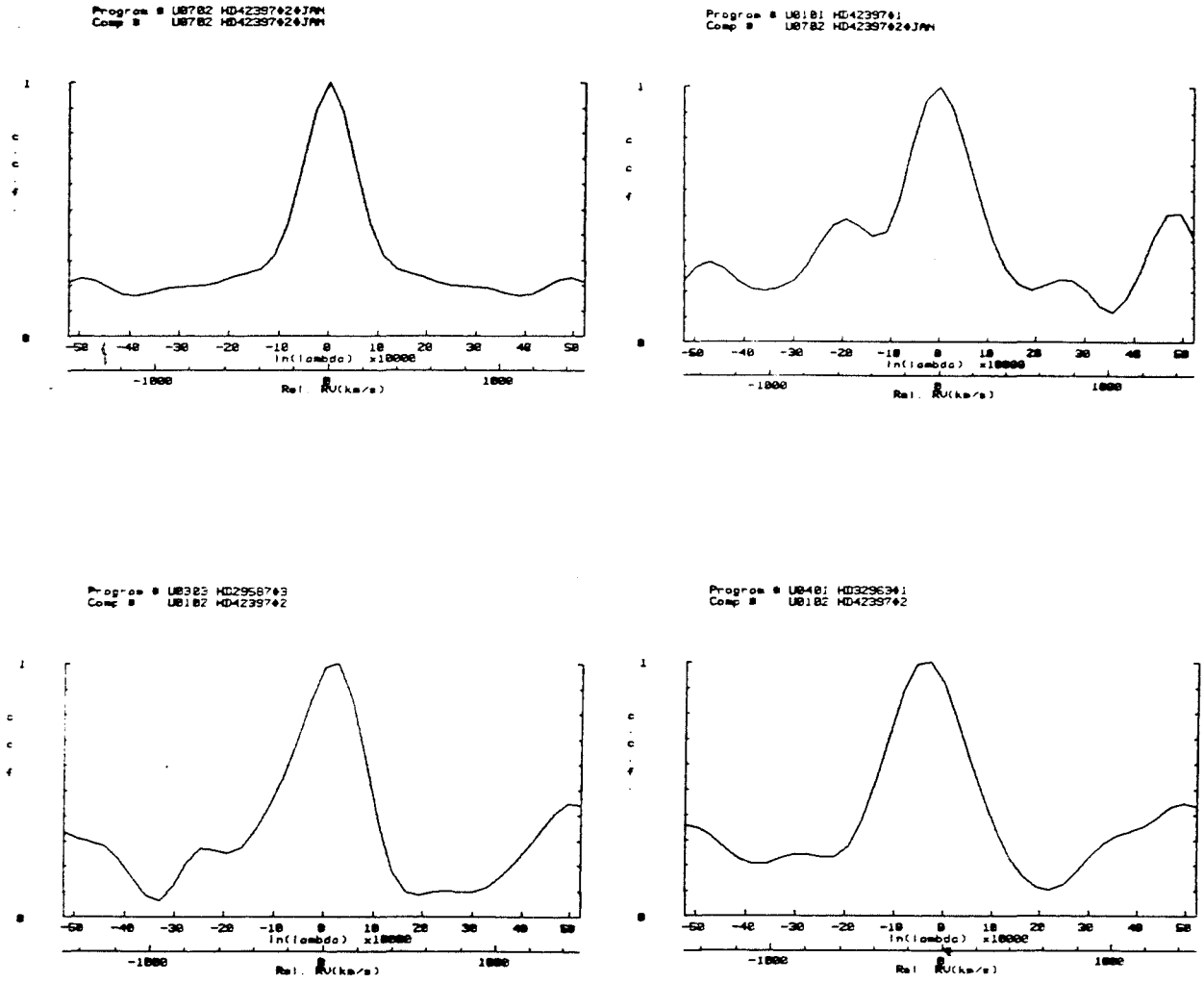

Figure 8-12: Radial velocity residuals obtained usng templates of summed spectra.

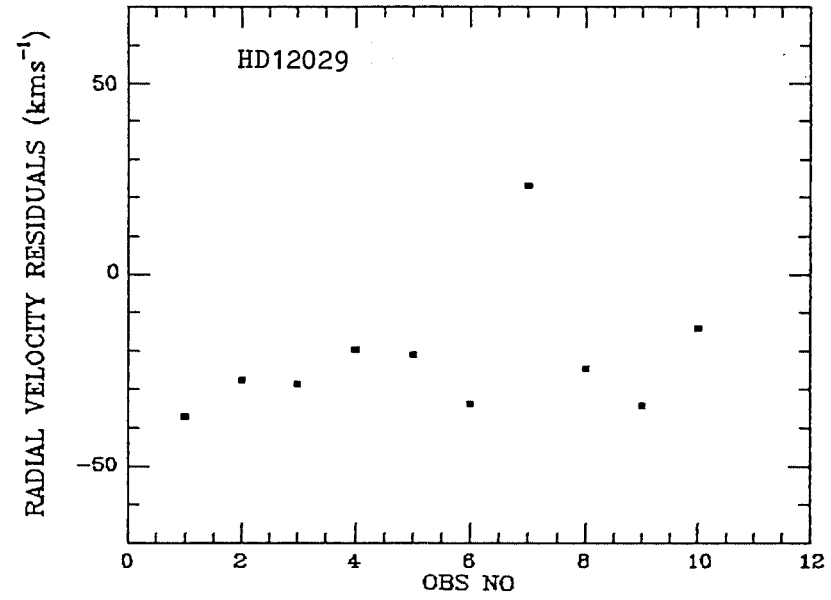

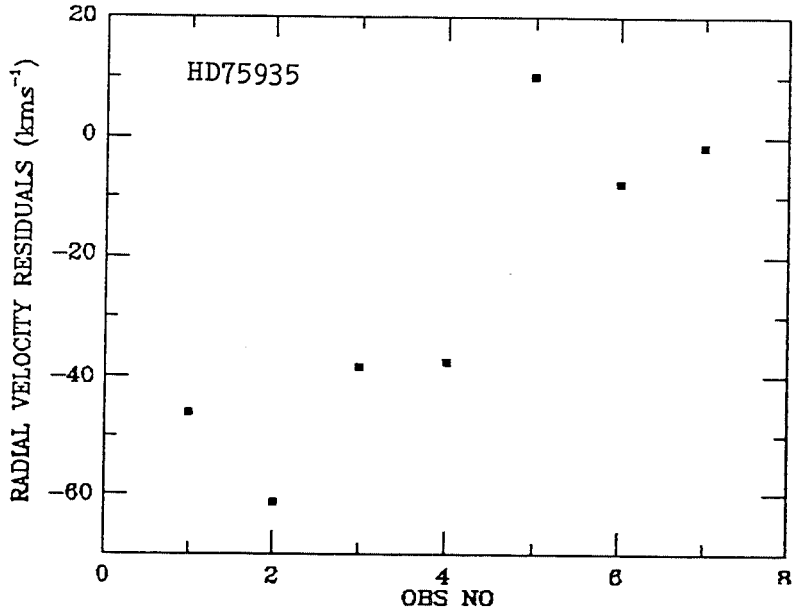

8.9) SV Cam.

SV Cam is an eclipsing binary system of period 0.59 days and was discovered by Guthnick (1929). The system comprises a G3V primary component slightly evolved above the main sequence, with a K4V secondary. SV Cam exhibits a periodic variable light curve apparently due to BY Draconis variability in the secondary component Hilditch et al. (1979). BY Draconis variability (Bopp and Fekel 1977) is thought to be caused by cool starspots covering large areas of the stellar photosphere. Variations in the period of the system can be explained by the eclipsing pair orbiting a third component. Frieboes-Conde and Herczeg (1973) derived a period for the orbit of 72.8 years from an analysis of published times of minima. A revised period of 64 years was proposed by Hilditch et al. (1979). While there is considerable photometric data for the system, spectroscopic data is limited. Hiltner (1953) reported photographic observations where the spectra were obtained with a dispersion of 76 $\dot{A}mm^{-1}$ at Hγ. The spectrograms displayed no evidence of a secondary component spectrum even at mid primary eclipse.

A spectroscopic investigation of SV Cam was undertaken using the higher dispersion of 30 $\dot{A}mm^{-1}$. The primary objective of the study was to derive a mass ratio for the system in order to improve the determination of the orbital parameters calculated by Hilditch et al. (1979) using the LIGHT synthesis program (Hill 1979). Cross correlation analysis has been shown to be particularly successful in deconvolving the velocity component of secondaries in

such systems (McClean 1982). The CCF for such systems when correlated with a standard of similar spectral type to the primary may exhibit a double peak. The separation reaches a maximum at quadrature and the two CCF peaks may be fitted with a double Gaussian function to determine their respective shifts. The separation of the two peaks is dependent on the quality of the spectra and the nature of the system under study. The large radial velocity amplitude of the system was another factor governing the choice of the system, because of the low resolution of the detector.

SV Cam was observed on four separate occasions during the winter of 1984 with two observing runs covering each quadrature. Integration times were restricted to a maximum of 1200 seconds in order to avoid smearing of the spectral features caused by the short period velocity variation of the system. On each observing run, several radial velocity standards of similar spectral type to the primary were also obtained. An ephemeris of the observations of SV Cam are shown in table 8-4.

The radial velocity standards were all correlated with SV Cam and themselves. The internal consistency of the standards was of the same poor standard with the accuracy being nominally the same as that obtained in the previous section. A spectrum comprising two summed spectra of HD86801 was adopted as the template for cross correlation analysis, in the hope that a higher signal to noise would assist in separation of the two component CF peaks. The primary CCF peaks exhibited broad profiles of 200 - 400 kms^{-1}

Table 8-4

Ephemeris of observations for SV Cam

RUN	J.D. - 2440000	Phase	R.V. (kms^{-1})
1	6089.35084	0.607453	29
2	6089.37231	0.643654	11
3	6089.39949	0.689483	36
4	6089.42475	0.732075	110
5	6089.45708	0.786588	141
6	6089.47951	0.824408	98
7	6089.54719	0.938526	126
8	6089.56795	0.973530	10
9	6089.58945	0.009782	-19
10	6089.61233	0.048361	-136
11	6089.63418	0.085203	-102
12	6089.70277	0.200855	-119
13	6089.72271	0.234477	-135
14	6091.42800	0.109829	-70
15	6091.45331	0.152506	-78
16	6091.47474	0.188639	-88
17	6091.49589	0.224301	-149
18	6091.51722	0.260267	-97
19	6091.53634	0.292506	-183
20	6091.55852	0.329904	-144
21	6091.57902	0.364470	-128
22	6091.60075	0.401110	-91
23	6091.62166	0.436367	-60
24	6091.64477	0.475333	-29
25	6091.66775	0.514081	5
26	6091.70839	0.582605	-8
27	6142.47648	0.184570	-126
28	6142.49396	0.214044	-130
29	6142.51152	0.243653	-74
30	6142.53252	0.279061	-98
31	6142.55148	0.311031	-173
32	6142.57010	0.342426	-55
33	6142.59061	0.377009	-67
34	6142.61050	0.410546	-60
35	6142.62825	0.440475	22
36	6142.64911	0.475648	-72
37	6142.66628	0.504599	-15
38	6143.41031	0.759136	69
39	6143.42708	0.787412	60
40	6143.44422	0.816313	76
41	6143.46085	0.844353	151
42	6143.47762	0.872630	61
43	6143.49554	0.902845	29
44	6143.51255	0.931526	62
45	6143.52975	0.960528	44
46	6143.54671	0.989125	94
47	6143.56322	0.016963	4

similar to those of the radial velocity standard cross-correlations. Separation of the primary and secondary components was not observed in the CCF peaks, although some assymetry was present in a number of the CCF peaks. With the width of CCF profiles obtained the result is not surprising, since any secondary peak is likely to be obscured by the primary. The radial velocity curve for the data is shown in figure 8-13, with the velocities listed in table 8-4. Since an accurate time of minima for the system, at the epoch of the observations was not available, the data have been phased using the ephemeris (Hilditch et al. 1979)

$$\text{Pr. Min. (JD)} = 2413895.8807 + 0.59307155\ E.$$

A solution to the radial velocity curve was obtained by a least squares fit to a sine wave (Skillen 1985). The orbit was assumed to be circular since the secondary eclipse occurs at phase 0.5 with primary component symmetry about phase 0.5. The fit yielded the following orbital solution for the primary component of the system:

$$K = 110 \pm 9 \text{ kms}^{-1},$$

$$\gamma = -13 \pm 6 \text{ kms}^{-1},$$

$$a \times \sin i = 0.9 \times 10^{6} \text{ km},$$

$$f = 0.106\ 0$$

Figure 8-14 shows the radial velocity curve with the fitted velocity curve overlaid in the data. The O-C residuals for the system are shown in figure 8-15. There is a large scatter in the data with the standard deviation of the fit sd = 44. Hiltner (1953) gives a graphical solution to the system parameters. His data have been reanalysed in the present study by fitting them in the same

Figure 8-13: Radial velocity curve data for SV Cam.

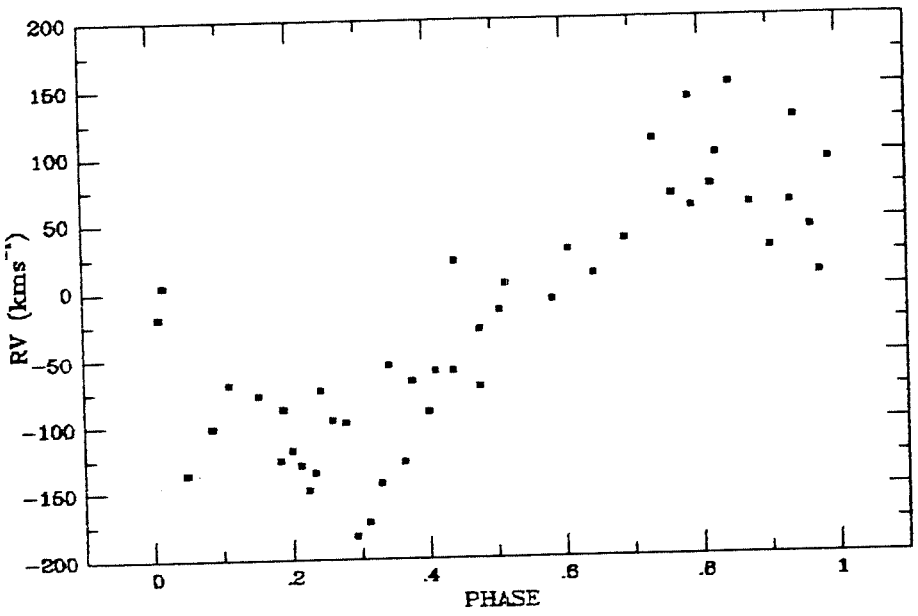

Figure 8-14: Radial velocity curve and fit for SV Cam.

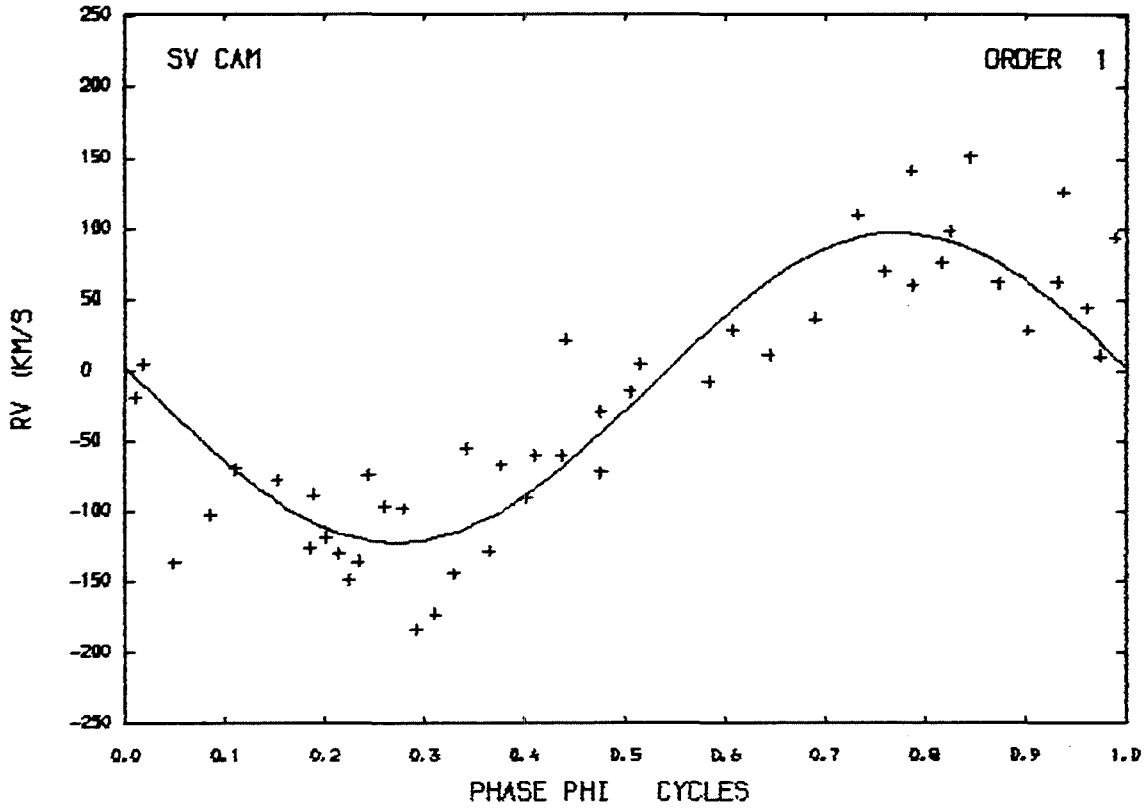

Figure 8-15: O-C residuals to radial velocity curve fit.

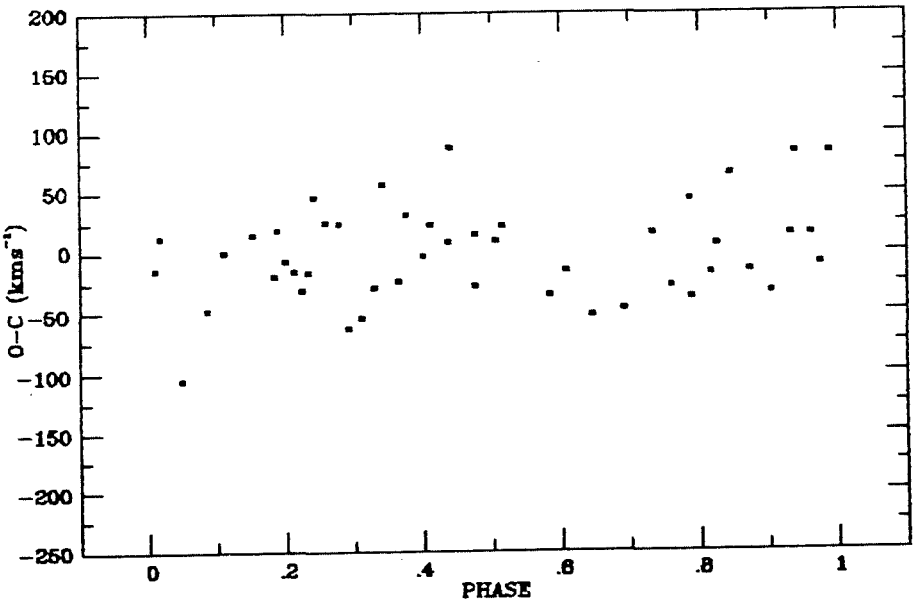

manner as the IPD data with a sine wave. Using the ephemeris above, the results obtained yield the orbital solution.

$$K = 123 \pm 2 \text{ kms}^{-1},$$

$$\gamma = -16 \pm 2 \text{ kms}^{-1},$$

$$a \times \sin i = 1.0 \times 10^{6} \text{ km},$$

$$f = 0.118\ 0$$

Figures 8-15 and 8-16 respectively show the radial velocity curve and the O-C residuals for the fit. The results are in reasonable agreement although the large formal errors for the IPD data are a reflection of the scatter in the radial velocity curve.

While this study has shown the potential of detectors such as the IPD for spectroscopy on small telescopes, it is clear that further work is required at a higher resolution to detect a possible secondary component. An IPD with the improved resolution performance discussed in the summary would be able to achieve this objective.

Figure 8-16: Radial velocity curve and fit for SV Cam., using photographic spectra of Hiltner (1953).

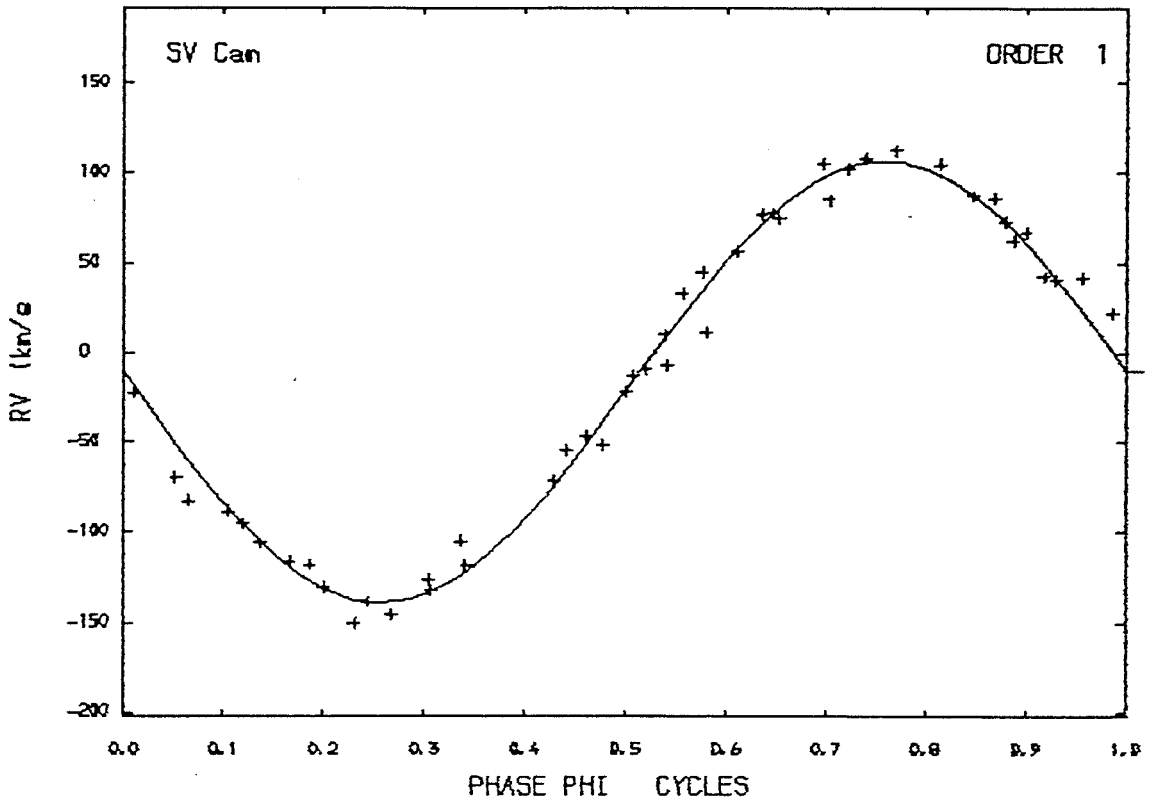

Figure 8-1 : O-C residuals to radial velocity curve fit.

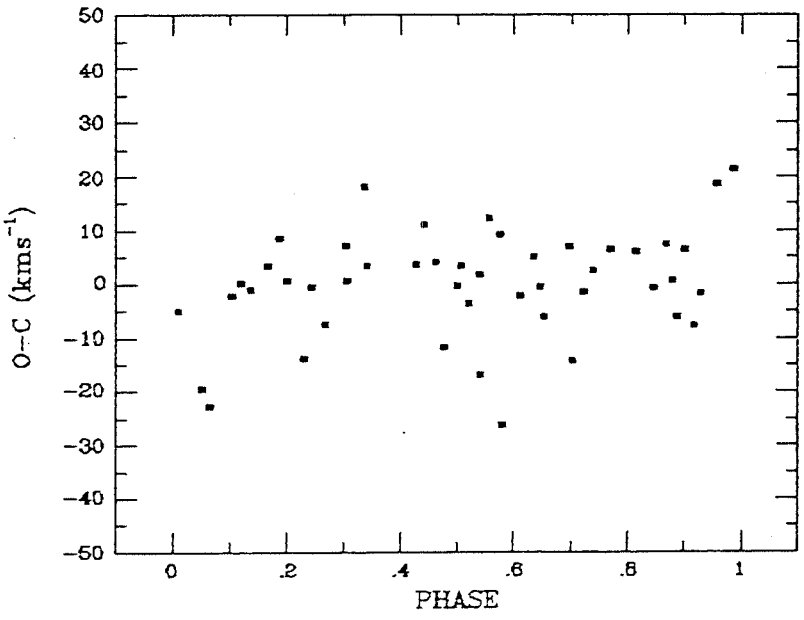

Chapter 9

The radial velocity measurements as expected have a large scatter because of the poor resolution of the detector. The results obtained from the analysis of SV Cam demonstrate the flexibilty of the cross correlation technique as a useful technique for the analysis of stellar radial velocities. The main conclusion to be drawn from the results is that with improved resolution and sensitivity the detector can extend the power of a small telescope considerably. In order to improve the performance of the resistive anode detector performance, the main problems to be addressed are the low, non-uniform resolution and the detective quantum efficiency.

Theoretical analysis of resistive anode operation clearly highlights the importance of achieving high gain, in order to maximise the ratio of MCP signal to the anode and preamplifier noise. This parameter is of particular importance in the larger format CAT anode detectors, where the anode's resistivity is lower, resulting in increased thermionic noise. The resolution of 42 μm obtained by Fermani et al. (1982) for a 25 mm device demonstrates the advantages of working with gains in excess of 10^7. Using the methods discussed in Section 7.2, it can be shown that for a 40 mm detector, MCP gains in excess of 1.5×10^7 will give an anode PSF of < 27 μm (ie. MTF > 0.94 at 5 $lpmm^{-1}$). In order to achieve such

gain figures, a new MCP configuration is required, which produces high stable gains with a narrow pulse height distribution, together with high count rate capabilities and structural stablilty.

The techniques for achieving high MCP gains were discussed in 2.2.1 and require further consideration when applied to the problem of larger format detectors. In order to increase the gain of this particular IPD system, several options need investigation. The use of three clamped l/d = 80:1 plates is the most obvious option, and has been investigated by Siegmund et al. (1984), who report gain values up to 3×10^7 with PHR values of 36%. The count rate capability of an MCP stack compared to a single plate is reduced by a factor dependent on the spread of the pulses at the plate interfaces. For clamped plates, with no interplate spacing, spreading should be of the order of 3 channels at each interface.

A second alternative, with the potential to achieve very high gain, would be to separate either a double or triple clamped configuration by a small gap. Armentrout (1985) suggests optimum gain uniformity is obtained with a clamped pair separated by a gap from a third plate. This arrangement can give high gains in excess of 10^8 and is reported to have a high count rate capability caused by a reduction in the resistance of the central plate due to heating.

The use of mounted plates has advantages in terms of improved electrical contact with the mounting assembly and minimising the probability of damage to the plate during assembly. For large format MCP designs some form of structural support is necessary to prevent arching and distortion of the plates during baking. Jean et al. (1985) report that a planicity of ±20μm can be achieved, for a 40 mm intensifer design, by placing the plates under tensile stress in the mounting assembly. This technique is another area that requires further investigation in order to extend its application to large format multiple MCP configurations.

The potential of curved-channel plates for producing high stable gains also requires consideration, particularly in view of their reported gain and lifetime performance characteristics (Timothy 1981). Curved channel MCPs typically produce gains of 10^6 with PHR values of 30% FWHM, for l/d ratios of 100 to 140. Thus while a single plate would be insufficient, a pair of clamped curved channel MCPs could be expected to produce reasonable gain values. The combination of two such plates could perhaps provide the additional degree of ion feedback protection required to allow the use of an unfilmed input MCP. Before the construction of new sealed tubes, proposed designs should ideally be tested thoroughly in the demountable form to ensure that the MCP configuration chosen will perform to the required specification.

The high gain figure required (ie. > 10^7) could be reduced by using a square or circular resistive anode without the terminating resistors at the boundaries. Fraser and Mathieson (1981a, 1981d) have discussed in detail the techniques for minimising the distortion inherent in these anodes. Rectification of the geometric distortion can be achieved in software using methods such as those reported by Baade et al. (1985) for the geometric rectification of Faint Object Camera images.

The wedge and strip anode is another alternative to the use of CAT anodes. The achievable resolution is limited by the preamplifier noise and partition noise associated with the division of charge. Siegmund et al. (1984), however, report that gains of > 10^7 are still necessary to achieve high resolution with wedge and strip anodes.

The noise contribution of the preamplifiers is another area that requires further investigation in order to improve both the IPD detector's performance and also that of other resistive anode and wedge and strip anode detectors. An initial investigation of some low noise preamplifiers for the IPD has been undertaken. The amplifier's noise performance is specified as 280 e^-rms (660 e^-FWHM) which should increase the anode-preamplifier MTF contribution from 0.75 to 0.81 at 5 lpmm^{-1} for a gain of 7 x 10^6. The amplifier produces unipolar pulses and represents a considerable improvement in performance over the IPD preamplifiers. Initial tests with the amplifiers were inconclusive because of problems associated with

integrating the amplifier's unipolar output pulse with the signal processing electronics. Further work is required to achieve the potential increase in performance. An important point to note in the use of high speed preamplifiers for CAT anodes is that they must be matched to the anode's time constant to maintain anode linearity.

The detector electronics are one of the areas where major improvements would be required to obtain optimum resolution performance from the IPD system. The problems experienced here in operating the ADCs as ratiometric dividers suggest that a new approach to the signal processing electronics is required.

The alternative techniques for signal processing have been discussed in Chapter 3 and involve analogue or software division. Analogue division using the currently available commercial dividers would involve a loss of accuracy and count rate performance although some improvement on the IPD system's existing linearity might be expected. The use of software division requires a fast data acquistion unit which can perform both the signal processing arithmetic and allow analysis of integrating and stored images. In many smaller data acquisition systems this may prove impossible to achieve. Microprocessors are able to perform the necessary operations in dedicated systems, but the operating speeds remain a limiting factor.

An alternative approach which is a compromise between ADC and software division is to use a lookup table to perform the signal division (van Breda 1985). This design would possess the advantages of very high speed operation, with a hardwired approach to the signal processing which allows more flexibility in the data acquisition and analysis. A circuit designed to operate on this principle would have three stages; signal thresholding, analogue to digital conversion and signal arithmetic. Incoming signals would be held at a sample/hold circuit, until enabled by an appropriate signal, when they would undergo thresholding and then be passed to the analogue to digital convertors. Following conversion, signal division is performed by the use of a 'lookup table' memory. The digital memory is loaded with the values of the reciprocals of summed anode signals corresponding to the pixel format required. The address corresponding to the summed anode signal is read and the value is then passed to digital multipliers where it is multiplied with the appropriate signal algorithms. The advantages of this method are that it is inherently more accurate than ratiometric and analogue division techniques. It is also a lot faster since it requires only digital multiplication of signals which can be achieved at higher rates than division. The analogue to digital conversion is also more linear since a fixed reference voltage is used. If a very high rate of conversion is required the use of 'flash' analogue to digital convertors should be considered. In flash convertors, the bit choices are all made at the same time, using $2^n - 1$ comparators, producing an increase in the conversion speed.

The most immediate problem associated with the proximity focussing stage are the field emission hotspots which were a major contributor to the IPDs poor performance. The advantages of analysing the pulse height distributions of the sealed tube have been clearly demonstrated. Pulse height analysis has allowed the magnitude of the hotspots to be assessed and has assisted the optimisation of the detector to minimise their effects. The possibility of plate arching and non-uniformity in the photocathode to MCP gap are important. The effect on the overall detector resolution will be determined by the relative weight of the proximity focussing MTF. In systems where the MTF is of equal weight to other components the effect of any non-uniformity will not be major, while in systems where the proximity focussing is the limiting factor it will be more apparent. With improvements in processing technology, component spacing accuracy and uniformity have improved.

Overall resolution performance in the IPD would be improved if the current 'state of the art' photocathode to MCP gap of 200 μm were achieved. With reported operating voltages of 600 V (Allington-Smith and Schwartz 1984, Pollehn 1980) a proximity focussing PSF of 15 μm (MTF = 0.98 at 5 $lpmm^{-1}$) should be possible.

The IPD photocathode suffers spatial non-uniformity, with a large peripheral area having a very low sensitivity. Recent 40 mm tubes, processed at ITL, with a new plant designed to handle large format tubes, have shown good uniformity. The 'throw' area over the

photocathode has been increased to the required value of 2.5x for optimum processing. In addition manufacturing tolerances have been improved. Little advance in photocathode sensitivities (RQE) can be expected until the III-V technology becomes more widely available. At present the use of III-V technology in astronomical detectors has been limited to photomultipliers.

Sealed tube DQE and QE figures are often discussed solely in terms of the photocathode efficiency and do not consider other losses inherent in these detectors. The attenuating effect of the Al_2O_3 film deposited on the input MCP is an important factor in the assessment of the compact MCP detectors for astronomical spectroscopy. The transmission of photoelectrons is still limited to 0.5 at 600 V (Csorba 1979, Lyons 1985) and thus effectively halves the photocathode efficiency. A possible solution to this problem is to employ higher accelerating voltages of the order of 900 V in combination with larger proximity focussing gaps of 0.5 mm. The value of 0.5 mm is a reasonable compromise between proximity focussing resolution and the travel distance for backscattered electrons. Experiments are required to investigate the possibilty of operating higher fields (1.6 $kVmm^{-1}$) across such gap widths, without incurring the problem of field emission from photocathode asperities.

The use of funneled plates would enhance the collection efficiency of the input MCP and also increase the signal to noise in the system. The larger open area of the plates has advantages in that it reduces the area of the interchannel web and so will reduce

backscattering from primary electron collisions with the web and associated halo effects. The use of funnelled MCPs seems to be limited to night-vision systems at present (Pollehn 1985), where their use has been found to improve intensifier SNR performance as expected.

The loss of resolution with higher count rates also needs further investigation in order to quantify to what degree this is caused by channel paralysis and scattering mechanisms at the input MCP. The tests done with the IPD cannot be regarded as conclusive in view of the problems experienced with the detector resolution and its uniformity. High current plates (low resistance channels), are claimed to operate with point source inputs up to 100 cs^{-1} $pixel^{-1}$ (40 x 40 μm) without channel recovery losses. For spectroscopic applications it would be of limited use if the high point source count rates cause spectral line broadening.

To summmarise, the full potential of resistive anode detectors in astronomical spectroscopy has yet to be realised. This investigation of an IPD has shown that with an improved design, the detector could provide a useful tool for spectroscopic observations on small telescopes. Figure 9-1 shows a theoretical MTF for a detector having a 0.2 mm - 600 V proximity focussing and an MCP gain of 3×10^7. The electronics are assumed to have a PSF width of 20 μm and the characteristics of the low noise preamplifiers are used. The detector would have a PSF width of 31 μm and an MTF of 0.92 at 5 $lpmm^{-1}$. In addition, several important areas have been highlighted which are applicable to the design and operational

requirements of large format proximity focussed tubes.

Figure 9-1: Theoretical MTF curve for a CAT resistive anode detector having 0.2 mm - 600 V proximity focusing, MCP gain = 3 x 10^7, low noise preamplifiers and improved electronics (PSF = 20 m).

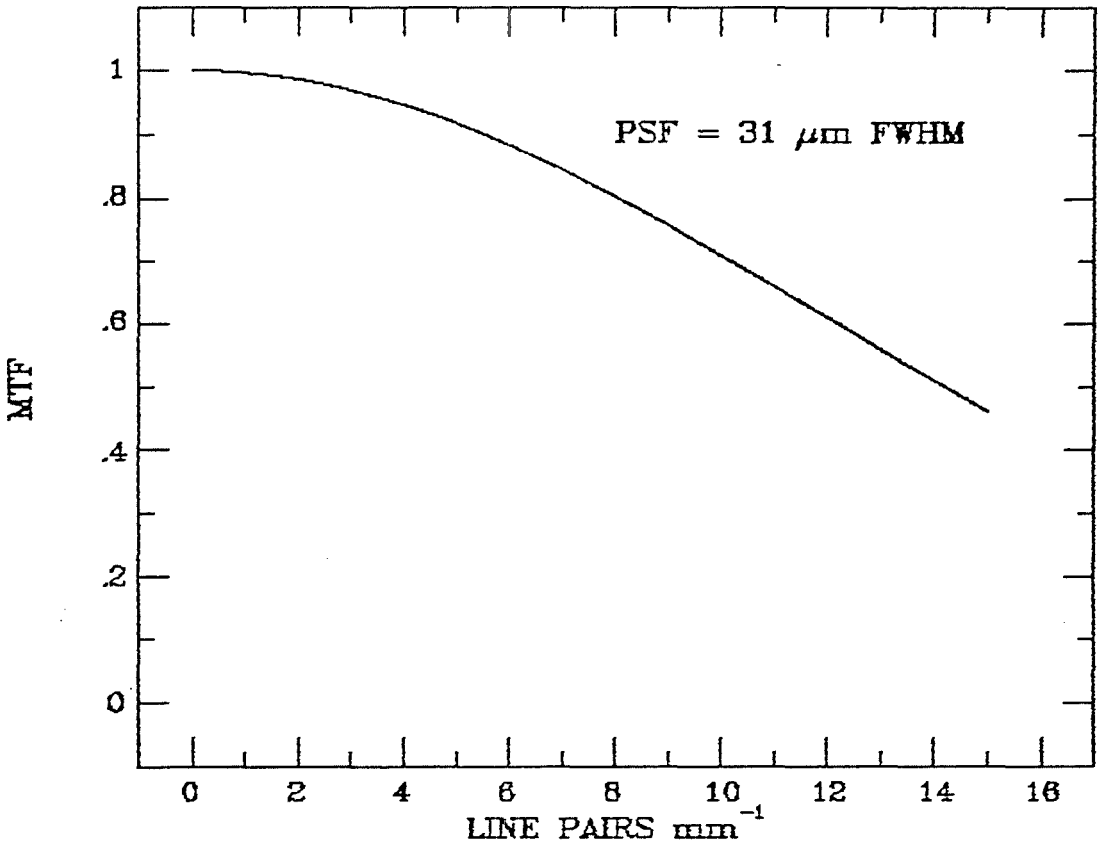

References.

Adams,J. and Manley,B.W. 1965, Electron. Eng. 37, 180.

Allington-Smith,J.R. and Schwartz,H.E 1984, Q.J.R.A.S 25, 267.

Airey,R.W.,D.J.Lees,Morgan,B.L. and Traynar,M.J. 1985, Adv. Elect. Electron. Phys. 64A, 49.

Airey,R.W.,Morgan,B.L. and Ring,J. 1978, McMullan and Morgan p329.

Aikens,R.S.,Harvey,J.W. and Lynds,C.R. 1976, Duchesne and Lelievre p25-1.

Aitken,R.G. 1935, The Binary Stars (McGraw-Hill New York).

Alexander,R.M. 1971, IEEE Trans. Nucl. Sci. NS-18, 264.

Allen,R.G.,Cromwell,R.H.,Liebert,J.W.,Macklin,R.H. and Stockman, H.S. 1983, SPIE Instrumentation in Astronomy V 445, 168.

Analogue Devices 1982, Data Acquisition Databook, Volume 1.

Armentrout,C.J. 1985, Rev. Sci. Instrum. 56, 1179.

Augustyniak,W.M.,Brown,W.L. and Lie,H.P. 1972, IEEE Trans. Nuc. Sci. NS-19, 196.

Baade,D.,Ponz,D. and di Serego Aligheri,S. 1985, The Messenger 41. 7.

Barbe,D.F. 1975, Proc. IEEE 65, 38.

Batten,A.H.,Harris,H.C.,McClure,R.D. and Scarfe,C.D. 1983, Pub. D.A.O 16, no. 12.

Baum,W.A. 1962, Stars and Stellar Sys. II 16, 1.

Beardsley,W.R.,Gatewood,G. and Kamper,K.R. 1974, Ap. J. 194, 637.

Beauvais,Y.,Chautemps,J. and De Groot,P. 1985, Adv. Elect. Electron. Phys. 64A, 267.

Beaver,E.A. and McIlwain,C.E. 1971, Rev. Sci. Instrum. 42, 1321.

Bell,S.A. and Hilditch,R.W. 1984, M.N.R.A.S. 211, 229.

Bendat,J.S. and Piersol,A.G. 1971, Random Data:Analysis and Measurement Procedures (Wiley Interscience).

Bevington,P.R. 1969, Data Reduction and Error Analysis for the Physical Sciences, McGraw-Hill Inc.

Blouke,M.M.,Janesick,J.R.,Hall,J.R. and Cowens,M.W. 1981, SPIE Solid State Imagers for Astronomy 290, 6.

Boerio,A.H. et al. 1966, Adv. Elect. Electron. Phys. 22A, 229.

Bokowski,C.J. and Kopp,M.K. 1970, IEEE Trans. Nuc. Sci. NS-17, 390.

Borkowski,C.J. and Kopp,M.K. 1972, IEEE Trans. Nucl. Sci. NS-19, 161.

Boksenberg,A. 1972, ESO/Cern Conf. Aux. Instr. for Large Telescopes, eds. Lansten,S and Reiz,A. Geneva. p295.

Boksenberg,A. 1976, Duchesne and Lelievre p13-1.

Boksenberg,A. 1975, Image Processing Techniques in Astronomy (D. Reidel, Dordrecht) 59.

Boksenberg,A. and Burgess,D.E. 1972, Adv. Elect. Electron. Phys. 33B, 835.

Bopp,B.W. and Fekel,F. 1977 Ap. J. 82, 490.

Bouigue,R. 1973, Trans. IAU 15A, 409.

Bracewell,R.N. 1965, The Fourier Transform and its Applications, McGraw-Hill Inc.

Boulsteix,J. 1978, McMullan and Morgan p313.

Bowyer,S.,Kimble,R.,Paresce,F.,Lampton,M. and Penegor,G. 1981, App. Opt. 20, 477.

Butcher,H.R. et al. 1982, SPIE Instrumentation in Astronomy IV 331, 311.

Carpay,W.M. and Klein,S.S. 1971 Proc. ISPRA Symp. Nucl. Electronics, Italy, 6-9 May 1969.

Carruthers,G.R. 1976, Duchesne and Lelievre p6-1.

Carruthers,G.R. and Opal,C.B. 1974, SPIE Instrumentation in Astronomy II 44, 127.

Charpak,G. 1977, Nature 270, 499.

Charpak,G. and Sauli,F. 1973, Nucl. Inst. Meth. 103, 365.

Charpak,G.,Bouclier,R.,Bressani,T.,Favier,J, and Zupanicic,C. 1968, Nucl. Inst. Meth. 62, 262.

Choisser,J.P. 1976, Duchesne and Lelievre p27-1.

Cochrane,J.A. and Thumwood,R.F. 1976, Adv. Elect. Electron. Phys. 40A, 441.

Coleman,C.I. 1985, Adv. Elect. Electron. Phys. 64A,

Coltman,J.W. 1954, J. Opt. Soc. Amer. 44, 468.

Crane,P. 1973, Glaspey and Walker p.391.

Cromwell,R.H. 1984, B.A.A.S. 16, No. 4 , 904.

Cromwell,R.H. and Dyvig,R.R. 1972, Adv. Elect. Electron. Phys. 33B, 677.

Cromwell,R.H.,Strittmatter,P.A.,Allen,R.G.,Hege,E.K.,Kuhr,H., Marien,K.H.,Funk,H.W. and Frank,K. 1985, Adv. Elect. Electron. Phys. 64A, 77.

Crowell,M.H. and Labuda,E.F. 1969, Bell Sytem Tech. J. 48, 1481.

Csorba,I.P. 1977, App. Opt. 16, 2647.

Csorba,I.P. 1979, App. Opt. 18, 2440.

Csorba,I.P. 1981, SPIE Assessment of Imaging Systems: Visible and Infrared 274, 42.

Dainty,J.C. and Shaw,R. 1974, Image Science, Academic Press.

Davenhall, A.C. 1983, Ph.D. Thesis, University of St. Andrews.

Davenhall, A.C., Bunclark, P.S., Fraser, C.W., McClean, B.J., Stapleton, J. and Stewart, G.C. 1981 J. Brit. Int. Soc. 34, 145.

Davis, M. and Latham, D.W. 1979, SPIE Instrumentation in Astronomy III 172, 71.

di Serego Alighieri, S., Perryman, M.A.C. and Machetto, F. 1985 Astron. Astro. 149 179.

Diner, D.J. and Westphal, J.A. 1977, Icarus 32, 299.

Djorgovski, S. 1984, Proc. Workshop on Improvements in Photometry NASA CP2350, 152.

Duchesne, M. and Lelievre, G. eds. 1976, Proc. IAU Coll. No. 40 Astronomical Applications of Image Detectors with Linear Response. Paris:Meudon.

Eberhardt, E.H. 1977, App. Opt. 16. 2127.

Eberhardt, E.H. 1979, Appl. Opt. 18, 1418.

Eberhardt, E.H. 1981, ITT Technical Note No 127.

Eccles, M.J., Sim, M.E. and Tritton, K.P. 1983, Low Light Level Detectors in Astronomy (Cambridge University Press).

Eck, H.J., Beaver, E.A. and Shannon, J.L. 1985, Adv. Elect. Electron. Phys. 64A, 148.

Edwin, R.P. 1983, Private Communication.

Edwin, R.P. 1985, Private Communication.

Emberson, D.L., Todkill, A.A. and Wilcock, W.L. 1962 Adv. Elect. Electron. Phys. 16, 127.

Everett, P., Hynecek, J., Zucchino, P. and Lowrance, J. 1982, SPIE Instrumentation in Astronomy IV 331, 151.

Ezard, L.A. 1975, RCA Rev. 36, 711.

Fairstein, E. and Hahn, J. 1965, Nucleonics 23, 54.

Fermani, C., Ruiz, E. Carbon, C.W., Lampton, M. and Paresce, F. 1982 Rev. Sci. Instrum. 53, 570.

Fermani, C., Ruiz, E., Bisiacchi, G.F., Salas, L., Paresce, F., Carlson, C.W. and Lampton, M. 1984, Ast. Astro. 134, 251.

Fehrenbach, C.H. and Duflot, M. 1980, Astron. Astrophys. Supp. 39, 311.

Ford, W.K. jr. 1966, Adv. Elect. Electron. Phys. 22B, 697.

Ford, W.K. jr. 1968, Ann. Rev. Ast. Astro. 6, 1.

Ford, W.K. jr. 1979, Ann. Rev. Ast. Astro. 17, 189.

Fort, B., Boksenberg, A. and Coleman, C.I. 1976, Duchesne and Lelievre p15-1

Fraser, G.W. and Mathieson, E. 1981a, Nucl. Instrum. Meth. 179, 591.

Fraser, G.W., Mathieson, E., Evans, K.D., Lumb, D.H. and Steer, B. 1981b, Nucl. Instrum. Meth. 180, 255.

Fraser, G.W., Mathieson, E. and Evans, K.D 1981c, Nucl. Instrum. Meth. 180, 269.

Fraser, G.W. and Mathieson, E. 1981d, Nucl. Instrum. Meth. 180, 597.

Fraser, G.W. and Mathieson, E. 1981e, Nucl. Instrum. Meth. 184, 537.

Frieboes-Conde, H. and Herczeg, T. 1973, Ast. Astro. Suppl. 12, 1.

Galileo Electro-Optics Corp., Galileo Park, Sturbridge, Mass., USA.

Gatti, E., Oba, K. and Rehak, P. 1983, IEEE Trans. Nucl. Sci. NS-30, 461.

Gear, C.W. 1969, Proc. Skytop Conf. on Computer Systems in Experimental Nuclear Physics., USAEC conf-670301 p552.

Geary, J.C. 1979, SPIE Instrumentation in Astronomy III 172, 82.

Geary, J.C. and Kent, S.M. 1981, SPIE Solid State Imagers for Astronomy 290, 51.

Glaspey,J.W. and Walker,G.A.H. eds. 1973, Proc. Symp. Univ. British Columbia, 15-17 May 1973: Astronomical Observations with Television Type Sensors. Vancouver.

Gilbert,G.R. et al. 1976, Adv. Elect. Electron. Phys. 40B, 699.

Gillingham,P.R. 1983, SPIE Instrumentation in Astronomy V 445, 577.

Ginaven,R.O. et al. 1981, SPIE Solid State Imagers in Astronomy 290, 81.

Goad,L.E. 1979, SPIE Instrumentation in Astronomy III 172, 86.

Goad,L.E. 1982, SPIE Instrumentation in Astronomy IV 331, 130.

Goad,L.E. and Reed,R. 1983 SPIE Instrumentation in Astronomy V 445 176.

Goetze,G.W. 1966, Adv. Elect. Electron. Phys. 22A, 219.

Gonzalez,R.C. and Wintz,P. 1977 Digital Image Processing (Addison-Wesley).

Goodrich,G.W. and Wiley,W.C. 1962, Rev. Sci. Instrum. 33, 761.

Goodson,J.,Woolgar,A.J.,Higgins,J. and Thumwood,R.F. 1972, Adv. Adv. Elect. Electron. Phys. 33A, 83.

Gorham,R.A.,Rodgers,A.W. and Stapinski,T.E. 1982, SPIE Instrumentation in Astronomy IV 331, 490.

Gott,R.,Parkes,W. and Pounds,K.A. 1970, IEEE Trans. Nuc. Sci. NS-17, 367.

Gray,P.M. 1983, SPIE Instrumentation in Astronomy V 445, 57.

Griffin,R.F. 1967, Ap. J. 148, 465.

Guthnick,P. 1929, Astr. Nach. 235, 83.

Hartig,G.F.,Fastie,W.G. and Davidsen,A.F. 1980, Applied Optics 19, 729.

Heckathorn,H.M. and Carruthers,G.R. 1982, SPIE Instrumentation in Astronomy IV 331, 415.

Henry,J.P.,Kellogg,E.M.,Briel,U.G.,Murray,S.A.,van Speybroek,L.P., and Bjorkholm,P.J. 1977, Proc SPIE 106, 163.

Hilditch,R.W. 1985 Private Communication

Hilditch,R.W.,Harland,D.M. and McClean,B.J. 1979, MNRAS 187, 39.

Hill,G. 1979, Pub. D.A.O. 15,.

Hill,G. 1982, Pub. D.A.O. 16.

Hill,G.,Fisher,W.A. and Poeckert,R. 1982, Pub. D.A.O. 16, No 4, 43.

Hill,G.E. 1976, Adv. Elect. Electron. Phys. 40A, 153.

Hiltner,W.A. 1953, Ap. J. 188, 262.

Hiltner,W.A. 1962, Stars and Stellar Sys. II 16, 340.

Hiltner,W.A. and Niklas,W.F. 1962, Adv. Elect. Electron. Phys. 16, 37.

Hobbs,T.I.,Carden,D.A.,Rodgers,A.W.,Stapinski,T.E. and Gorham,R.A. 1983, SPIE Instrumentation in Astronomy V 445, 402.

Hough,J. and Drever,R.W.P. 1972, Nucl. Inst. Meth. 103, 365.

Howes,M.J. and Morgan,D.V. 1979, Charge-Coupled Devices and Systems (New York John Wiley & Sons).

Jean,B.,Boutout,J.P.,Duchenois,V. and Polaert,R. 1985, Adv. Elect. Electron. Phys. 64A, 315.

Jelley,J.V. 1982, Observatory 102, 30.

Johnson,C.B. and Blank,R.E. 1981, SPIE Solid State Imagers for Astronomy 290, 102.

Jones,C.S.,Michon,G.J.,Burke,H.K. and Vogelsong,T.L. 1979, SPIE Space Optics 183, 162.

Jorden,P.R. and van Breda I. 1981 SPIE Solid State Imagers for Astronomy 290 113.

Jorden, P.R, Read, P.D. and van Breda I. 1982, SPIE Instrumentation in Astronomy IV 331, 368.

Kinbara, S. and Kumahara, T. 1969, Nucl. Instrum. Meth. 70, 173.

Kellogg, E.M., Henry, P., Murray, S. and van Speybroek, L. 1976, Rev. Sci. Instrum. 47, 282.

Kellogg, E.M., Murray, S.S. and Bardas, D. 1979, IEEE Trans. Nucl. Sci. NS-26, 407.

Klaasen, K.P., Clary, M.C. and Janesick, J.R. 1982 SPIE Instrumentation in Astronomy IV 331, 376.

Koshida, N. and Hosobuchi, M. 1985, Rev. Sci. Instrum. 56, 1329.

Kron, G.E. 1962, Adv. Elect. Electron. Phys. 16, 25.

Kron, G.E., Ables, H.D. and Hewitt, A.V. 1969, Adv. Elect. Electron. Phys. 28A 1.

Lallemand, A., Duchesne, M. and Wlerick, G. 1960, Adv. Elect. Electron. Phys. 12, 5.

Lampton, M. 1976, Duchesne and Lelievre p32-1.

Lampton, M. and Carlson, C.W. 1979, Rev. Sci. Instrum. 50, 1053.

Lampton, M. and Malina, R.F. 1976, Rev. Sci. Instrum. 47, 1360.

Lampton, M. and Paresce, F. 1974, Rev. Sci. Instrum. 45, 1098.

Lawrence, G.M. and Stone, E.J. 1975, Rev. Sci. Instrum. 46, 432.

Latham, D.W. 1982, Intrumentation for Astronomy with Large Optical Telescopes IAU Coll. 67.

Lauer, T.R., Miler, J.S., Osborne, C.S., Robinson, L.B. and Stover, R.J. 1983, SPIE Instrumentation in Astronomy V 445, 132.

Lelievre, G. 1983, SPIE Instrumentation in Astronomy V 445, 151

Lillie,C.F. and Lawrence,G.M. 1979, SPIE Instrumentation in Astronomy III 172, 321.

Livingston,W.C. 1973, Ann. Rev. Ast. Astro. 11, 95.

Livingston,W.C. 1976, Duchesne and Lelievre p22-1.

Livingston,W.C.,Harvey,J.,Slaughter,C and Trumbo,D. 1976, App. Opt. 15, 40.

Lloyd Evans,T. 1983, Users Guide to Image Tube Spectrograph on 1.9m Telescope at SAAO.

Lloyd Evans,T. 1984, Private Communication.

Lockart,R.F. 1982, SPIE Instrumentation in Astronomy IV 331, 388.

Lorrain,P. and Corson,D. 1962, Electromagnetic Fields and Waves, W.H. Freeman and Company.

Lowrance,J.,Morton,D.C.,Zucchino,P.,Oke,J.B. and Schimdt,M. 1972 Ap. J. 171, 233.

Lynds,C.R. 1975, Q. Rep. K.P.N.O. Apr-Jun 3.

Lynds,C.R. 1971, Ap. J. (Lett.) 164:173.

Lyons,A and Read,P.R. 1983, Private Communication.

Lyons,A. 1985, Private Communication.

Machetto,F. et al. 1982 The Space Telescope Observatory, NASA CP8244, 40.

Mackay,C.D.,Astill,D.M. 1983, SPIE Instrumentation in Astronomy V 445, 140.

Manley,B.W.,Guest,A. and Holmshaw,R.T. 1969, Adv. Elect. Electron. Phys. 28A, 471.

Mason,I.M.,Branduardi-Raymont,G.,Culhane,J.L.,Corbet,R.H.D., Ives,J.C. and Sanford,P.W. 1984, IEEE Trans. Nucl. Sci. NS-31

McClean,B.J. 1981, Ph.D. Thesis, University of St. Andrews.

McClintlock,W.E.,Bazhi,C.A.,Steele,R.E.,Lawrence,G.M. and Timothy,J.G. 1982, App. Opt. 21, 3071.

McCord,T.B. and Westphal,J.A. 1972, App. Opt. 11, 522.

McGee,J.D.,Khogall,A.,Ganson,A. and Baum,W.A. 1966, Adv. Elect. Electron. Phys. 22A, 11.

1966, Adv. Elect. Electron. Phys. 22A, 11.

McMullam,D. and Morgan,B.L. eds. 1978, Preprints of papers presented at 7th Symp. Photo-Electronic Imaging Devices, Imperial College, London.

McMullan,D. and Powell,J.R. 1979, Adv. Elect. Electron. Phys. 52, 315.

McWhirter,I.,Rees,D. and Greenaway,A.H. 1982, J. Phys. E:Sci. Instrum. 15, 145.

Mende,S.B. 1971, App. Opt. 10, 829.

Mertz,L.,Tarbell,T.D.and Title,A. 1982, App. Opt. 21, 628.

Millar,I.C.P.,Washington,D. and Lamport,D.L. 1972, Adv. Elect. Electron. Phys. 33A, 153.

Miller,J.S. et al. 1976, Adv. Elect. Electron. Phys. 40B, 693.

Moore,C.H. 1974, Ast. Astro. (Suppl.) 15, 463.

Moore,C.H. and Rather,E.D. 1974, Ast. Astro. (Suppl.) 15, 497.

Morton,D.C. and Andereck,C.D. 1976, Ap. J. 205, 356.

Oke,J.B. 1981, SPIE Solid State Imagers for Astronomy 290, 45.

Mullard Ltd., Mullard House, Torrington Place, London.

Norlen,G. 1973, Physica Scripta 8, 249.

Opal,O.B.,Feldman,P.D.,Weaver,H.A. and McClintock,W.A. 1979, SPIE Instrumentation in Astronomy III 172, 317.

Osmer,P.S. 1977, Ap. J. 214:1-9

Parkes.W.,Evans,K.D., and Mathieson,E. 1974, Nucl. Instrum. Meth. 121, 151.

Panitz,J.A. and Foesch,J.A. 1976, Rev. Sci. Instrum. 47, 44.

Papaliolios,C.,Nisenson,P. and Ebstein,S. 1985, App. Opt. 24, 287.

Paresce,F. 1984, Private Communication.

Parkes,W.,Evans,K.D. and Mathieson,E. 1974, Nucl. Instrum. Meth. 121, 151.

Pearce,J.A. 1957, Trans. IAU 9, 442.

Pettini,M. 1983, La Palma Observers Guide.

Petrov,P.P. 1982, Instrumentation for Astronomy with Large Optical Telescpes I.A.U. Coll. 67, 299.

Pollehn,H. 1980, Appl. Opt. Opt. Eng. 6, 393.

Pollehn,H. 1985, Adv. Elect. Electron. Phys. 64A, 61.

Rees,D. 1983, Private Communication.

Rees,D.,McWhirter,I.,Rounce,P.A.,Barlow,F.E. and Kellock,S.J. 1980J. Phys. E. Sci. Instrum. 13, 763.

Rees,D.,McWhirter,I.,Rounce,P.A. and Barlow,F.E. 1981, J. Phys. E. Sci. Instrum. 14, 229.

Richmond,J.C. 1976, Adv. Elect. Electron. Phys. 40A, 519.

Richardson,E.H. and Brealey,G.A. 1973, J.R.A.S. Canada 67, 165.

Rogers,D. and Malina,R.F. 1982, Rev. Sci. Instrum. 53, 1438.

Robinson,L.B. and Wampler,E.J. 1972, P.A.S.P. 84, 161.

Rosier,J.C.,Polaert,R.,N'Guyen-Trong,T. and Sidoruk,B McMullan and Morgan p321.

Ruggieri,D.J. 1972, IEEE Trans. Nucl. Sci. NS-19, 74.

Sandel,W.R. and Broadfoot,A.L. 1976, Appl. Opt. 15, 3111.

Schagen,P. 1971, Adv. Image Pickup and Display 1, 1 (Academic Press, New York)

Schectman,S.A. and Hiltner,W.A. 1976, P.A.S.P. 88, 960.

Schmidt,K.C. and Hendee,C.F. 1966, IEEE Trans. Nucl. Sci. NS-13, 100.

Siegmund,O.H.W. and Malina,R.F. 1983, ACS Symp. Series No. 236 Multichannel Image Detectors Vol. 2, 253.

Siegmund,O.H.W.,Clothier,S.,Thornton,J.,Lemen,J.,Harper,R., Mason,I.M. and Culhane,J.L. 1983, IEEE Trans. Nucl. Sci. NS-30, 503.

Siegmund,O.H.W.,Malina,R.F.,Coburn,K. and Warthimer,D. 1984, IEEE Trans. Nucl. Sci. NS-31.

Simkin,S.M. 1974, Astron. Astrophys. 31, 129.

Sims,M.R.,Thomas,H.D. and Turner,M.J.L. 1981, IEEE Trans. Nucl. Sci. NS-28, 82.

Skillen,W.J. 1985, Ph.D. Thesis, University of St. Andrews.

Smith,A.G. and Hoag,A.A. 1979, Ann. Rev. Ast. Astro. 17, 43.

Spicer,W.E. and Bell,R.F. 1972, P.A.S.P. 84, 110.

Stair,P.C. 1980, Rev. Sci. Instrum. 51, 132.

Stapinski,T.E.,Rogers,A.W. and Ellis,M.J. 1981, P.A.S.P. 93 242.

Stewart,G.C. 1983, Ph.D. Thesis, University of St. Andrews.

Stoudenheimer,R.G. 1960, Adv. Elect. Electron. Phys. 12, 41.

Talmi,Y. and Simpson,R.W. 1980, App. Opt. 19, 1401.

Taylor,K. 1981, SPIE Assessment of Imaging Systems: Visible and Infrared 274, 315.

Taylor,R.C.,Hettrick,M.C. and Malina,R.F. 1983, Rev. Sci. Instrum. 54, 171.

Timan,H. 1985, Adv. Elect. Electron. Phys. 63 , 73.

Timothy,J.G. 1981, Rev. Sci. Instrum. 52, 1131.

Timothy,J.G. 1983, P.A.S.P. 95, 810.

Timothy,J.G. and Bybee,R.L. 1975, Rev. Sci. Instrum. 46, 1615.

Timothy,J.G.,Mount,G.H. and Bybee,R.L. 1979, SPIE Instrumentation in Astronomy III 172 199.

Timothy,J.G. and Bybee,R.L. 1981, SPIE Shuttle Pointing of Electro-Optical Experiments 265, 93.

Timothy,J.G.,Joseph,C.L. and Wolff,S.C. 1982, SPIE Instrumentation in Astronomy IV 331, 301.

Trap,H.J.L. 1971, Acta Electronica 14, 41.

Tonry,J. and Davis,M. 1979, Ap. J. 84 (10), 1511.

Tull,R.G. and Nather,R.E. 1973, Glaspey and Walker p171.

Tull,R.G.,Choisser,J.P. and Snow,E.H. 1975, App. Opt. 14, 1182.

Tull,R.G.,Vogt,S.G. and Kelton,P.W. 1979, SPIE Instrumentation in Astronomy III 172, 90.

van Breda,I.G. 1985, Private Communication.

van Huyssteen,C.F. 1976, Adv. Elect. Electron. Phys. 40B, 419.

Vogt,S.S. 1981, SPIE Solid State Imagers for Astronomy, 290, 70

Vogt,S.S. et al. 1978, App. Opt. 17, 574.

Vogt,S.S., Tull,R.G. and Kelton,P. 1978, App. Opt. 17, 574.

Wachtel,M.M.,Doughty,D.D. and Anderson,A.E. 1960, Adv. Elect. Electron. Phys. 12, 59.

Walker,M.F. 1976, Duchesne and Lelievre p37-1.

Walker,G.A.H., Johnson,R. and Yang,S. 1983, Adv. Elect. Electron. Phys. 64A, 213.

Wattson,R.B.,Rappaport,S.A. and Frederick,E.E. 1976, Icarus 27, 417.

Weisstrop,D.,Williams,J.T. and Fahey,R.P. Adv. Elect. Electron. Phys. 64A , 133.

Wells, D.C., Griesen, E.W. and Harten, R.H. 1981, Ast. Astro. (Suppl.) 44, 363.

Westphal, J.A. 1973, Glaspey and Walker p. 127.

Westphal, J.A. and Kristian, J. 1976, Duchesne and Lelievre p19-1.

Wiley, W.C. and Hendee, C.F. 1962, IRE Trans. Nuc. Sci. NS-9, 103.

Williams, J.T. and Weistrop, D. 1983 SPIE Instrumentation in Astronomy V 445, 204.

Wiza, J.L. 1979, Nucl. Instrum. Meth. 162, 587.

Wiza, J.L., Henkel, P.R. and Roy, R.L. 1977, Rev. Sci. Instrum. 48, 1217.

Weiser, H., Vitz, R.C., Moos, H.W. and Weinstein, A. 1976, App. Opt. 15, 3123.

Wlerick, G., Lelievre, G., Servan, B., Cayatte, V., Michet, D., Renard, L. and Horville, D. 1983, SPIE Instrumentation in Astronomy V 445, 143.

Wright, P. 1983, SPIE Instrumentation in Astronomy V 445, 511.

Yamasaki, I., Tamai, N., Kume, H, Tsuchiya, H. and Oba, K. 1985, Rev. Sci. Instrum. 56, 1187.

York, D.G., Jenkins, E.B., Zucchino, P., Lowrance, J.L., Long, D. and Songaila, A. 1981, SPIE Solid State Imagers for Astronomy 290, 202.

Zucchino, P. 1976, Adv. Elect. Electron. Phys. 40A, 239.

Appendix A

Listing of IPD control software.

```
1000
 0 ( Detector - St Andrews IPD Package ..........................)
 1 ( ================================ ..............................
 2
 3
 4
 5
 6
 7
 8
 9
10
11
12
13
14
15
```

```
1001
 0 ( Detector - Working variables ..................................)
 1
 2 EMPTY            0 WARNING !
 3 USERSFLPT
 4
 5 CREATE INTEGRATION_TIME   4 ALLOT
 6
 7 0.0 2INTEGER EXP_START_TIME
 8  10  INTEGER EXP_TIME
 9
10 : 2CR   CR CR ; ( for tidy responses ......)
11 : NEXTCOM   2CR ." ** -------------) "  ;
12 --)
13
14
15
```

```
1002
 0 ( Detector - Spectrum handling and basic graphics ..............)
 1
 2
 3      457 LOAD          ( GRAPHICS. )
 4     1101 LOAD          ( SPECTRUM BASICS. )
 5      460 LOAD          ( 'SPECTRUM DISPLAY PACK'. )
 6      461 LOAD          ( AVPT. ETC. )
 7      453 LOAD          ( ARBITARY PLOTTING. )
 8
 9
10
11 --)
12
13
14
15
```

```
1003
 0 ( Detector - Basic Raster Scan Handling ......................)
 1
 2             VARIABLE XSTEPS                VARIABLE YSTEPS
 3             VARIABLE ROW                   VARAIBLE COL
 4           0 CONSTANT X1                  0 CONSTANT Y1
 5           0 CONSTANT X2                  0 CONSTANT Y2
 6             VARIABLE THRESHOLD             VARAIBLE INTERVAL
 7       11501 CONSTANT GAREA                 1 CONSTANT LINE-SKIP
 8             VARIABLE VAL-SET               0 CONSTANT FOG
 9           0 INTEGER  LX1                   0 INTEGER  LY1
10           0 INTEGER  LX2                   0 INTEGER  LY2
11  : XL   X2 1+ X1 ;     : YL   Y2 1+ Y1 ;
12  FL 30000.0 FCONSTANT CONV              F1 FCONSTANT SKY
13   FL 0.0001 FCONSTANT F.0001     FL 100.0 FCONSTANT F100
14  FL 0.5 FCONSTANT F0.5
15     --)
```

```
1004
 0 ( Detector - Basic Raster Scan Handling ......................)
 1 : GALAXY  ['] GAREA ! ;
 2
 3  442 LOAD  ( CODE DCELL )
 4
 5 : !VALUE DCELL ! UPDATE ;
 6 : STORE COL @ ROW @ !VALUE ;
 7 : VALUE DCELL @ ;
 8 : RAW   ['] VALLE VAL-SET !  ;
 9 : VALUE   VAL-SET @ EXECUTE  ;
10 RAW  VAL-SET @ CONSTANT MODET
11
12
13 : SKIP   ['] LINE-SKIP ! ;
14 : XYSIZE YSTEPS ! XSTEPS ! ;
15   --)
```

```
1005
 0 ( Detector - Basic Raster Scan Handling ......................)
 1
 2       472 LOADER IDT       ( ISODENSITRACING. )
 3       483 LOADER OUTLINE   ( JOINED CONTOURS. )
 4       480 LOADER DOTLINE   ( CONTOURS FROM DOTS. )
 5       464 LOADER ISO       ( ISOMETRIC PROJECTION. )
 6       486 LOADER GRAY      ( PIXELS ABOVE THRESHOLD. )
 7
 8       --)
 9
10
11
12
13
14
15
```

```
1006
 0 ( Detector - Basic Raster Scan Handling ..................... )
 1
 2 : ZOOMSET  X1 := LX1 Y1 := LY1 X2 := LX2 Y2 := LY2
 3     ['] Y2 ! ['] X2 ! ['] Y1 ! ['] X1 !  Y1 X1 DARK
 4     Y2 X1 LIGHT Y2 X2 LIGHT Y1 X2 LIGHT Y1 X1 LIGHT ALPHA ;
 5 : ZOOM COORDS COORDS ZOOMSET ;
 6 : WINDOW X1 X2 ABSCISSA  Y1 Y2 ORDINATE  40 Y CORNER !
 7   X RNG 2@  11 14 */  ) IF 700 Y FRAME !  700 X RNG @
 8   Y RNG @ */ DUP X FRAME ! MINUS 1000 + X CORNER ! ELSE
 9   94 X CORNER ! 906 X FRAME ! 906 Y RNG @ X RNG @ */
10   Y FRAME ! THEN
11   Y2 Y1 - DUP 260 ) IF 4 ELSE
12               100 ) IF 2 ELSE 1 THEN THEN SKIP ;
13 : BACKUP LX1 ['] X1 ! LY1 ['] Y1 ! LX2 ['] X2 ! LY2 ['] Y2 !
14     WINDOW ;
15 --)
```

```
1007
 0 ( Detector - CAMAC Interface ..................................... )
 1 13 CONSTANT UNIT
 2 UNIT 0 2   RNAF RPG
 3 UNIT 0 8   NAF0 ?0
 4 UNIT 0 26  NAF  ENB-PIG     UNIT 0 24  NAF  INH-PIG
 5 UNIT 0 16  WNAF !ADD
 6 UNIT 1 16  WNAF !X          UNIT 2 16  WNAF !Y
 7 UNIT 0  0  RNAF ?X          UNIT 1  0  RNAF ?Y
 8 21 0 16  WNAF WD
 9
10 0-IG      ( SET THE AMC MODE )
11 INH-PIG   ( MAKE SURE NO INTERRUPTS THANK YOU )
12 : HIT    32767 AND  DUP  32768 +  WD  WD ;
13 : ?PG   RPG   INH-PIG   L. ;
14 : GDATA BEGIN  PAUSE  ?0 END   RPG ;
15 --)
```

```
1008
 0 ( Detector - CAMAC Memory Commands ............................... )
 1 12 CONSTANT C_MEM
 2 C_MEM 1 17  WNAF  L_WR_PTR
 3 C_MEM 0 17  WNAF  L_RD_PTR
 4 C_MEM 0  0  RNAF  CMEM@
 5 C_MEM 0 16  WNAF  !CMEM
 6 C_MEM 2 26   NAF  ENB_DMI
 7 C_MEM 2 24   NAF  INH_DMI
 8 C_MEM 12 23 WNAF  CLAMSR
 9 : ?AMC-DONE  BEGIN  PAUSE  RLSR 6 AND 6 = END ;
10 : %AMC-GO    DISK GET   ( STOP DISK CONTENTION )
11       32 0 DO TACTIV DROP  FREEPAGE @ 64 M* ( IMAGE START)
12       I 4096 M* D+  4094 M+  LMAR ( LOAD ADDR. OF END OF BLOCK)
13       2048 WCR-LOAD  CMR-LOAD  ( SET COUNT AND MODE REGS )
14       ARM  ( AND GO )  ?AMC-DONE  LOOP  DISK RELEASE ;
15 --)
```

```
1009
 0 ( Detector - External Memory Read/Write Image ..................)
 1
 2 : m)i  0 L_RD_PTR             ( START AT THE BEGINING )
 3        C_MEM 0 0 BCNAF-LOAD   ( SET UP THE CAMAC COMMAND )
 4        %AMC-GO  ;             ( AND SHIFT THE DATA )
 5 : I)M  0 L_WR_PTR             ( START AT THE START OF THE MEM )
 6        C_MEM 0 16 BCNAF-LOAD  ( SET UP THE CAMAC COMMAND )
 7        %AMC-GO ;              ( AND SHIFT THE DATA )
 8
 9 : iwipe     ANADEX PWIPE TEK  VMEM RELEASE  7 C.
10                      2CR ." **  Image memory cleared " CR ;
11
12 : mwipe   iwipe  I)M   ." **  CAMAC memory cleared " CR
13           7  CLAMSR  ( CLEAR LAM STATUS REGISTER IN CASE )
14          0 0 INTEGRATION_TIME 2! ;
15 --)
```

```
1010
 0 ( Detector - CAMAC Interface - AMC , Exposure Control .........)
 1
 2 : start-exp   ENB_DMI  ( ENABLE COUNTING )
 3             %RT  := EXP_START_TIME  NEXTCOM TIME ;
 4
 5 : runtime   %RT EXP_START_TIME D- 1000. D/ 2CR
 6              ." **  Integration running " D. ." seconds " ;
 7
 8 : halt-exp     %RT    INH_DMI  ( STOP COUNTING )
 9             CR TIME   EXP_START_TIME D- 1000. D/
10             INTEGRATION_TIME D+!   INTEGRATION_TIME 2@
11             2CR ." **  Total exposure of " D. ." seconds " ;
12
13 : stop-exp   halt-exp  m)i  ;
14 --)
15
```

```
1011
 0 ( Detector - CAMAC Interface - AMC , Exposure Control .........)
 1
 2 : %IMAGE   start-exp
 3             CR ." Hit any key to finish "
 4             PAD 1 EXPECT    stop-exp ;
 5 : SECS  CLOCKSPEED M* %RT D+  BEGIN  PAUSE  2DUP %RT D(  END
 6           DROP ;
 7 : seconds  := EXP_TIME ;
 8
 9 : image   start-exp  EXP_TIME SECS   stop-exp ;
10 --)
11
12
13
14
15
```

```
1012
 0 ( Detector - Access Image in Memory ..........................)
 1 OCTAL
 2 CODE VCEL  ( EXPECTS X AND Y COORDS OF PIXEL )
 3    0 XSTEPS MOV    S )+ 0 MUL     ( XSTEPS @  M* )
 4    1 S ) ADD    0 ADC             ( ROT M+ )
 5    2 1 MOV    2 170000 # BIC      ( EXTRACT 12 BIT WORD OFFSET )
 6    2 ASL    S ) 2 MOV             ( CONVERT TO BYTES AND KEEP )
 7    1 007777 # BIC                 ( GET RID OF LOW BITS )
 8    -5 # 0 ASHC    1 FREEPAGE ADD ( GET MAPPING OFFSET )
 9    S -) 1 MOV   NEXT
10 DECIMAL
11
12
13
14
15 --)
```

```
1013
 0 ( Detector - Access Image in Memory ..........................)
 1
 2 : VMVALUE   VCEL  PAUSE  V@ ;
 3 : !VMVALUE  VCEL  V! ;
 4 : D_IMAGE   RAW ;
 5 : V_IMAGE   ['] VMVALUE  VAL-SET ! ;    V_IMAGE
 6    ( DEFAULT TO IMAGE IN MEMORY )
 7
 8
 9
10 --)
11
12
13
14
15
```

```
1014
 0 ( Detector - Generate Image Window in Receiver ..............)
 1   4  INTEGER XB/F      ( X bins per pixel )
 2  16  INTEGER YB/P      ( Y bins per pixel )
 3  16  INTEGER YB                  4 INTEGER XB
 4 1024 INTEGER Y-OFFSET  ( scale factor to offset Y address )
 5   0  INTEGER X-FROM          4096 INTEGER X-TO
 6   0  INTEGER Y-FROM          1024 INTEGER Y-TO
 7   0  INTEGER OYF                0 INTEGER OXF
 8  16  INTEGER OYB/P               4 INTEGER OXB/P
 9
10 : 2**  DUP IF  1 SWAP 0 DO  2*  LOOP  ELSE DROP 1 THEN ;
11
12 : SQWINDOW   X1 X2 ABSCISSA  Y1 Y2 ORDINATE
13              700 700 X FRAME 2!
14              40 300 X CORNER 2! ;   ( A SQUARE PICTURE )
15 --)
```

```
1015
 0 ( Detector - Generate Image Window in Receiver ..............)
 1 : IMAGE-WINDOW  X-TO X-FROM -  XB/P /  XSTEPS !
 2       Y-TO Y-FROM -  YB/P /  YSTEPS !
 3       0 0 XSTEPS @ 1- YSTEPS @ 1- ZOOMSET WINDOW SQWINDOW ;
 4
 5 : LXMEM  X-FROM MINUS 1- !ADD  0  X-TO   X-FROM  DO
 6                 XB/P 0 DO  DUP !X  LOOP 1+  XB/P +LOOP DROP ;
 7
 8 : LYMEM  Y-FROM MINUS 1- !ADD  0  Y-TO  Y-FROM DO
 9                 YB/P 0 DO  DUP Y-OFFSET *  !Y  LOOP  1+
10          YB/P +LOOP  DROP ;
11
12 : CLXMEM  -1 !ADD 4096 0 DO  0 !X  LOOP ;
13
14 : CLYMEM  -1 !ADD 1024 0 DO  0 !Y  LOOP ;
15 --)
```

```
1016
 0 ( Detector - Generate Image Window in Receiver ..............)
 1 : X-BITS  DUP 6 ( IF CR ." **  Min value allowed is 6  ** "
 2           QUIT  THEN
 3           12 OVER - 2** DUP := XB := XB/P
 4           DUP  6  - 2** DUP := YB := YB/P
 5                     2**     := Y-OFFSET
 6           1024 := Y-TO  0 := Y-FROM       ( reset Y window )
 7           4096 := X-TO  0 := X-FROM       ( reset X window )
 8     IMAGE-WINDOW  LXMEM LYMEM  ;
 9
10
11    ( and do setup ........ )
12 --)
13
14
15
```

```
1017
 0 ( Detector - Generate Image Window in Reciever ..............)
 1 : FULL-VIEW    0 0 4096 1024 ZOOMSET SQWINDOW  ERASE AXES ;
 2 : Y_ALL   0 := Y-FROM   1024 := Y-TO ;
 3
 4 : Y-GET    Y-FROM := OYF   YB/P := OYB/P
 5        COORDS  YB/P *  0 MAX OYF + := Y-FROM
 6      COORDS  YB/P *  OYF +  1024 MIN  := Y-TO 2DROP ;
 7 : Y-SET  Y-TO Y-FROM - ( WANT)  YB OVER  1024 */ DUP
 8          0= IF CR ." WINDOW TOO SMALL, MUST BE )" 1024 YB /
 9       , Y_ALL QUIT  THEN := YB/P   1024 YB / YB/P * ( GIVE )
10         SWAP 2/ Y-FROM + OVER 2/ - DUP := Y-FROM  + := Y-TO
11        CR ." RANGE USED IS " CR Y-FROM . ." TO " Y-TO . ;
12 : %H_BAR   X ORG @  2DUP  DARK  X RNG @ +  LIGHT  ALPHA ;
13 : Y-VIEW   Y-FROM OYF -   OYB/P / %H_BAR
14            Y-TO OYF -  OYB/P /  %H_BAR ;
15 --)
```

```
1018
 0 ( Detector - Generate Image Window in Receiver ..............)
 1
 2 : VIEWING-AREA     FULL-VIEW
 3        Y-FROM X-FROM OFF DARK
 4        Y-TO DUP  X-FROM LIGHT   X-TO LIGHT
 5        Y-FROM DUP   X-TO LIGHT   X-FROM LIGHT
 6          CR CR CR ." AXES IN DETECTOR COORDINATES " ;
 7 : %Y-SET     Y-SET  Y-VIEW
 8              CLYMEM   LYMEM  IMAGE-WINDOW  SQWINDOW CR ;
 9 : Y-WINDOW   Y-GET  ." REQUESTED "  Y-FROM .  Y-TO .  %Y-SET ;
10 : YWSET      := Y-TO  := Y-FROM   %Y-SET ;
11 : Y_FULL    Y_ALL   Y-SET   LYMEM ;
12
13 CLXMEM  CLYMEM
14 LXMEM  LYMEM   ( SET UP THE MEMORIES FOR  DEFAULT )
15 IMAGE-WINDOW   12 C.  --)
```

```
1019
 0 ( Detector - Basic Raster Scan Handling extensions ............)
 1
 2
 3 : areset   0 XSTEPS @ X SIZE  0 YSTEPS @ Y SIZE ;
 4 : ras_prep   THRESHOLD ! areset LINEPLOT m)i ;
 5
 6 ( auto plot any of 2-d formats )
 7
 8 : gray     ras_prep GRAY ;
 9 : idt      ras_prep IDT ;
10 : dotline  ras_prep DOTLINE ;
11 : outline  ras_prep OUTLINE ;
12       --)
13
14
15
```

```
1020
 0 ( Detector - assorted responses ..............................)
 1
 2 0 CONSTANT CH   0 INTEGER R1   0 INTEGER R2
 3
 4 : ALPASK   BEGIN KEY [']  CH !
 5            CH R1 = IF 0 1 ELSE CH R2 = IF 1 1 ELSE 0
 6            ZCR ." **  Illegal value re-enter ....."
 7            THEN THEN END ;
 8
 9 : y/n   110 := R1 121 := R2  ."  y or n ? " ALPASK ;
10
11 : cont   ZCR ." **  -)) Hit any key to continue ..."
12              PAD ! EXPECT ;
13
14 --)
15
ok
```

```
1021
 0 ( Detector - Peripherals Loader Block ..........................)
 1
 2    1045 LOADER util
 3    1025 LOADER i/o
 4    1060 LOADER focus
 5    1057 LOADER phd
 6
 7    1 WARNING !
 8  2CR 2CR 2CR
 9 .# **  S E T   L O W E R C A S E   M O D E   N O W  **" 2CR
10 .# **  C L E A R  M E M O R Y --) mwipe"
11      NEXTCOM
12
13
14
15
```

```
1025
 0 ( Detector - I/O Routines for Disc and Tape ....................)
 1
 2
 3 : I/O_PAC ;
 4
 5
 6 2CR  .#  **  Loading I/O Package ** " 2CR
 7
 8
 9
10
11
12 --)
13
14
15
```

```
1026
 0 ( Detector - I/O working variables ............................)
 1 1 TAPES L#LOAD
 2 ( Fits header offsets .......... )
 3 30  64 3 *  +  CONSTANT  X_SIZE_OFFSET   ( NAXIS1 )
 4 30  64 4 *  +  CONSTANT  Y_SIZE_OFFSET   ( NAXIS2 )
 5 30  64 5 *  +  CONSTANT  DWELL2_OFFSET
 6 19  64 6 *  +  CONSTANT  CT1_OFFSET
 7 22  64 8 *  +  CONSTANT  DATE_OBS_OFFSET
 8 30  64 11 * +  CONSTANT  OBJECT_OFFSET
 9 62  64 12 * +  CONSTANT  COMMENT_OFFSET
10
11 CREATE %OBJECT!    18 ALLOT
12 CREATE %FITSCOM!   54 ALLOT
13
14 2201 CONSTANT PROTOHEADER ( Header blocks )
15 --)
```

```
1027
 0 ( Detector - Dumping Images from Memory to Disc ..............)
 1
 2 OCTAL
 3 CODE V)D   ( MOVE 1024 BYTES FROM VM TO DISC BUFFER )
 4   0 S )+ MOV   0 ASR    ( COUNTER INTO WORDS )
 5   -2 340 # MOV  ( NO INTERRUPT THANK YOU )
 6   1  S )+ MOV  ( O/P PTR.)    W S )+ MOV   ( I/P PTR.)
 7   R -) 172344 MOV    172344 S )+ MOV   ( REMAP )
 8   W 40000 # ADD      ( SET UP READY )
 9   BEGIN    1  )+ W )+ MOV    0 SOB     ( DO IT )
10   172344 R )+ MOV    -2  CLR   NEXT    ( TIDY & EXIT )
11
12 DECIMAL
13 --)
14
15
```

```
1028
 0 ( Detector - Dumping Images from Memory to Disc ..............)
 1
 2 : %!BLOCK   PREV 4 + @  0< NOT  IF  DUP PREV 4 + !  THEN
 3     %BLOCK ;   ( A POOR MAN'S !BLOCK )
 4 OCTAL
 5 : IMAGE2DISC  ( WE USE PAGE 2 FOR MAPPING )
 6   20 0 DO    3600 I 200 * +        ( PAGE NUMBER )
 7     10 0 DO  DUP  I 2000 *         ( ADD ALSO OFFSET IN PAGE )
 8       DISC GET   J 10 * I + GAREA +  %!BLOCK  ( BUFF. ADDR.)
 9          2000 V)D                  ( MOVE IT )
10       UPDATE  DISC RELEASE  FLUSH  ( SAVE IT )
11     LOOP  DROP                     ( DUMP PAGE NO.)
12   LOOP ;
13 DECIMAL
14
15 --)
```

```
1029
 0 ( Detector - Create FITS Header ..............................)
 1 0 INTEGER HEAD_BLOCK
 2
 3 : )HEADER   OVER -  HEAD_BLOCK BLOCK +  SWAP CMOVE UPDATE ;
 4
 5 : %XSIZE   XSTEPS @  (.)  X_SIZE_OFFSET  )HEADER ;
 6 : %YSIZE   YSTEPS @  (.)  Y_SIZE_OFFSET  )HEADER ;
 7 : %DWELL2   INTEGRATION_TIME 2@  (D.)  DWELL2_OFFSET  )HEADER ;
 8 : %EXPSTART   EXP_START_TIME  (TIME) CTI_OFFSET    )HEADER ;
 9 : %DATE       TODAY @    (DATE)  DATE_OBS_OFFSET      )HEADER ;
10 : %OBJECT     %OBJECT!  18  OBJECT_OFFSET   )HEADER ;
11 : %FITSCOM    %FITSCOM! 54  COMMENT_OFFSET )HEADER ;
12
13 : PARAMS)HEADER    BASE @  DECIMAL  %XSIZE  %YSIZE  %DWELL2
14               %EXPSTART  %DATE  %OBJECT %FITSCOM  BASE ! ;
15 --)
```

```
1030
 0 ( Detector - Image to Disc ..................................)
 1
 2 : object   PAD 20 BLANK   96 TEXT  PAD %OBJECT! 18 MOVE ;
 3 : fitscom  PAD 56 BLANK   96 TEXT  PAD %FITSCOM! 54 MOVE ;
 4
 5 : HEAD>DISC   := HEAD_BLOCK  PROTOHEADER HEAD_BLOCK COPY
 6              FLUSH PARAMS>HEADER  ;
 7
 8 : ISPACE    1+ GALAXY ;  ( DEFINE DISC SAVE AREA )
 9
10 : i>d  GAREA 1- HEAD>DISC  IMAGE2DISC  ;
11
12
13
14 --)
15
```

```
1031
 0 ( Detector - Header Block to Tape ..........................)
 1
 2 : 1HEAD   ( ASSUMES 1 BLOCK AT GAREA-1 )
 3     PAD 2880 BLANK    ( EMPTY BUFFER )
 4     DISK GET   GAREA 1- %BLOCK
 5     16 0 DO   DUP  I 64 *  +   PAD I 80 * +  64  MOVE   LOOP
 6     DROP  DISC RELEASE
 7     0 := RNUM    PAD 2880 ECMTWRITE ;
 8
 9 --)
10
11
12
13
14
15
```

```
1032
 0 ( Detector - Disc to Tape in 2880 Byte Blocks ..............)
 1
 2 : M_SETUP   GAREA FBLK !
 3       XSTEPS @  YSTEPS @  512 */MOD   SWAP IF  1+  THEN
 4       GAREA + := LBLK   ( COMPUTE LAST BLOCK )
 5       2880 := RL        ( SET RECORD LENGTH )
 6       0 IPTR !   0 OPTR !   0 RECS ! ;
 7 : ?M_SIZE   1C24 IPTR @ -   RL OPTR @ -  MIN ;
 8 : M_FROM    FBLK @  %BLOCK IPTR @ + ;
 9 : M_TO      PAD OPTR @ + ;
10 : M_COUNT   DUP  OPTR +!  IPTR +!
11             IPTR @ 1024 =  IF  0 IPTR !  1 FBLK +!  THEN ;
12 : M_WRBLK   RECS @ := RNUM   PAD RL ECMTWRITE
13             0 OPTR ! ;
14
15 --)
```

```
1033
 0 ( Detector - Disc to Tape in 2880 Byte Blocks ..................)
 1
 2 : BLK_DATA   ( MAY BE BASIS OF BLOCKED TAPE O/P ROUTINE )
 3     M_SETUP  ( THIS IS A BIT SPECIAL )
 4  BEGIN    PAD RL ZERO-MEMORY  ( USE ERASE IF NO GRAPHICS )
 5     BEGIN  DISC GET  M_FROM  M_TO  ?M_SIZE  MOVE  DISC RELEASE
 6            ?M_SIZE M_COUNT
 7            FBLK @ LBLK =   OPTR @ RL =  OR
 8     END   1 RECS +!  M_WRBLK
 9     FBLK @ LBLK =  END   WEOF
10  2CR RECS ?  ." **  Data blocks written to tape "  CR ;
11
12 : D)T  1HEAD  BLK-DATA ;
13        ( THIS NEEDS XYSIZE AND ISPACE TO BE SET )
14 --)
15
```

```
1034
 0 ( Detector - Write Direct to Tape from Memory ..................)
 1
 2 : I)T    GAREA 1- HEAD)DISC  1HEAD    ( GENERATE HEADER )
 3        1920 64 M*   ( FIND ABS ADDRESS OF START OF IMAGE )
 4   45 0 DO  I := RNUM    2DUP  ABSADDRESS 2880 ECMTWRITE
 5            2880 M+  ( MOVE ALONG NOW )  LOOP  2DROP
 6    PAD 2880 ZERO-MEMORY  ( CLEAN OUT THE BUFFER )
 7    3840 ( PAGE NUMBER )  6720 ( OFFSET )   PAD ( BUFFER )
 8    1472 ( BYTE COUNT )   V)D  ( MOVE IT )
 9    45 := RNUM   PAD 2880 ECMTWRITE   WEOF ;
10
11 --)
12
13
14
15
```

```
1035
 0 ( Detector - Image Direct to/from Disc from Memory ............)
 1 OCTAL
 2   0 INTEGER IMAGENO
 3   1 INTEGER S_DRIVE
 4 103 INTEGER I_R/W
 5    VARIABLE S_CYL
 6
 7 : DCOMD  20 * ( HIGH ADDRESS BITS )  I_R/W +  SWAP ;
 8
 9 : DCAC   MINUS SWAP  S_CYL @ 40 * S_DRIVE 40000 * + ;
10
11 : WBB    DISC GET  1 RKCS !   RKDA !  RKDA 2- !  RKDA 4 - !
12                   RKCS !  STOP  DISC RELEASE  4 S_CYL +! ;
13 : SETCYLINDER   IMAGENO 13 * 2 +  S_CYL ! ;
14 --)
15
```

```
1036
 0 ( Detector - Image Direct to/from Disc from Memory ..........)
 1 OCTAL
 2 : I)(D   S_DRIVE IF  ." save image no. " IMAGENO .  SETCYLINDER
 3            360000.  2DUP  DCOMD 60000 DCAC WBB
 4           140000. D+ 2DUP  DCOMD 60000 DCAC WBB
 5           140000. D+       DCOMD 40000 DCAC WBB
 6         IMAGENO 1+ 22 MOD  DUP := IMAGENO  ( MOVE ON - MOD 18 )
 7          0= IF 2CR ." ** Warning disc full ** " 7 C. 2CR THEN
 8    ELSE  CR ." No save disc "  THEN ;
 9
10 ERASE  ( START WITH A CLEAR SCREEN )
11 CR .# Which drive ( of 0-2 ) is the image save pack in ? "
12 CR .# Select 0 (system disc) to disable disc save "
13  ASK  := S_DRIVE  CR ERASE
14 --)
15
```

```
1037
 0 ( Detector - Image Direct to/from Disc from Memory ..........)
 1 OCTAL
 2 : recover   := IMAGENO
 3          S_DRIVE  IF   105 := I_R/W  CR ." Recover from disc "
 4                        I)(D  103 := I_R/W
 5                        CR ." Image now in memory "
 6        ELSE CR ." Cannot get image - no save disc loaded "
 7        THEN ;
 8 : savedisc  DUP 3 ( IF  := S_DRIVE
 9                     ELSE ." Drive no. 0, 1 or 2 only "  THEN ;
10 DECIMAL
11 : i))d  S_DRIVE IF  S_DRIVE 2436 * 1+ IMAGENO +  HEAD)DISC
12           CR ." **  Save to disc as "  I)(D
13     ELSE CR ." Cannot save - no disc defined "  THEN ;
14 --)
15
```

```
1038
 0 ( Detector - Tape Handling Words ..............................)
 1
 2  0 INTEGER TAPIM_NO   2203 INTEGER ISPACE_NO
 3  0 INTEGER OLDTAP_NO
 4
 5 : tapeit   ISPACE_NO ISPACE I)T
 6            ERASE CR ." *** IMAGE FITS HEADER *** " CR
 7            ISPACE_NO LIST CR
 8            TAPIM_NO 1 + := TAPIM_NO
 9            2CR ." **  Save to tape as save image no. "
10            TAPIM_NO . ;
11
12                 ( Write Image to tape ; list FITS header )
13                 (       and increment Image counter......)
14
15  --)
```

```
1039
 0 ( Detector - Tape Handling Words ..............................)
 1
 2 : im_skip   DUP FSFS := OLDTAP_NO ; ( SKip n Images & set )
 3                                     (  images counter...)
 4
 5 : ?images     2CR ." **  " TAPIM_NO .
 6                   ." images written to tape this run "  CR
 7                   ." **  " OLDTAP_NO .
 8                   ." previous Images on tape "  CR CR CR
 9                  ." **  Total of " OLDTAP_NO TAPIM_NO +  .
10                  ." Images saved on tape " CR CR
11                   ." **  Total of " IMAGENO .
12                   ." Images written to disc "  ;
13
14 : shutdown  OFF-LINE REWIND ?images ;   ( Shut off Tape-drive )
15      NEXTCOM
```

```
1045
 0 ( Detector - Graphics routines , smoothing & utilities ........)
 1
 2
 3          : GRSU-PAC ;
 4
 5
 6
 7
 8
 9
10   2CR  .#  **  Loading Graphics Utility PacKage ** " 2CR
11
12 --)
13
14
15
```

```
1046
 0 ( Detector - Utilities and Loader BlocK .......................)
 1
 2 0 INTEGER LLIM  1023 INTEGER  ULIM  0 INTEGER BIAS-ON
 3 1 INTEGER XST  1 INTEGER XEND  ( start & end xsects )
 4 0 INTEGER MN_Y  0 INTEGER MX_Y  ( max and min for scaling )
 5 0 INTEGER  EXLIM     0 INTEGER BLOCKFAC  10 INTEGER GRATE
 6 0 CONSTANT NLINE     0 CONSTANT XY
 7
 8 : erase   ERASE ; ( require for lowercase keywords )
 9 : axes   AXES ;
10 7 :P XYPLOT NLINE XY IF SWAP THEN VMVALUE ;
11 : slice  ['] NLINE  !  ;
12 : xplot  0 ['] XY ! 7 APLOT ;  : yplot  1 ['] XY ! 7 APLOT ;
13
14 : SPT    0 XEND 1+ XST DO OVER I VMVALUE + LOOP ;
15 -->
```

```
1047
 0 ( Detector - Extracting slices from Rasters ..................)
 1   0 CONSTANT COLUMN
 2 : LIGHT-UP 2DUP JOIN ;
 3 : EXTRACT CR   ( USE THE VECTOR POINTER [] FOR ROW/COL SELECT )
 4  ." DESTINATION BLOCK OF EXTRACTED SLICE; " ASK SPECTRUM CR
 5  () IF ." VERTICAL "  ELSE  ." HORIZONTAL "  THEN
 6      ." SLICE TO BE EXTRACTED; " ASK ['] COLUMN ! CR
 7  ." PLEASE WAIT - EXTRACTION PROCEEDING. " CR
 8  () IF  YSTEPS @ 0 DO COLUMN I VALUE I PT ! UPDATE  LOOP
 9    ELSE  XSTEPS @ 0 DO I COLUMN VALUE I PT ! UPDATE  LOOP
10    THEN FLUSH ." EXTRACTION NOW COMPLETE. " CR ;
11
12 --)
13
14
15
```

```
1048
 0 ( Detector - Graphics extensions ............................)
 1
 2 : SCVAL   DUP MN_Y ( IF DUP := MN_Y THEN DUP
 3               MX_Y ) IF DUP := MX_Y THEN DROP ;
 4
 5 : AXSET    MN_Y 0( IF 0 := MN_Y  CR  ( no -ve vals )
 6             ." ** Warning Pixel rollover " THEN
 7              MX_Y MN_Y = IF  CR  ( no data ? )
 8              ." ** Illegal axis limits.....exit routine "
 9                QUIT  THEN   ( stop plot if so )
10                MN_Y MX_Y OVER - 10 / MX_Y + Y SIZE ;
11
12 : bias   2CR ." ** Graphics bias on/off -- " y/n
13              IF 1 := BIAS-ON ELSE 0 := BIAS-ON THEN ;
14 --)
15
```

```
1049
 0 ( Detector - Graphics extensions ............................)
 1
 2 : 1AXRANGE   0 := MX_Y BIAS-ON IF LIMITS SWAP DROP NLINE
 3                       VMVALUE := MN_Y ELSE 0 := MN_Y THEN
 4                 LIMITS DO I NLINE VMVALUE SCVAL LOOP ;
 5
 6 : 2AXRANGE   0 := MX_Y BIAS-ON IF LIMITS SWAP DROP SPT SWAP
 7                          DROP := MN_Y ELSE 0 := MN_Y THEN
 8                 LIMITS DO 0 XEND 1+ XST DO
 9                                 J I VMVALUE + LOOP SCVAL LOOP ;
10
11
12 : xmod   X SIZE  ;   : ymod   Y SIZE  ;
13
14 --)
15
```

```
1050
 0 ( Detector - Graphics extensions ..............................)
 1
 2 : 1D_SCAL   1AXRANGE AXSET ;
 3 : 2D_SCAL   2AXRANGE AXSET ;
 4
 5 : xset   := XST  := XEND ;
 6
 7 : xsects   CR ." Lower xsect : " ASK := XST
 8          ."   Upper xsect : " ASK := XEND ;
 9
10 : delay   2CR ." **  Enter refresh rate in secs "  ASK
11            1 OVER ) OVER 100 ) OR
12             IF ." **  Out of bounds try again .... " DROP CR
13             ELSE := GRATE THEN ;
14
15 : refresh   GRATE SECS ; --)
```

```
1051
 0 ( Detector - Running Mean Smoothing ..........................)
 1
 2
 3 : 3TRI   SPT 2* SWAP 1- SPT SWAP 2+ SPT SWAP DROP + + 4 / ;
 4
 5 : 5TRI   SPT 4 * SWAP 2 - SPT SWAP 1+ SPT 2* SWAP 2 + SPT
 6          2* SWAP 1+ SPT SWAP DROP + + + + 9 / ;
 7
 8 : 7TRI   SPT 8 * SWAP 3 - SPT SWAP 1+ SPT 2* SWAP 1+ SPT
 9          4 * SWAP 2+ SPT 4 * SWAP 1+ SPT 2* SWAP SPT SWAP
10          DROP + + + + + + 22 / ;
11
12
13 -->
14
15
```

```
1052
 0 ( Detector - Running Mean Plotting ...........................)
 1
 2 : ENPTMISS   LIMITS 2 UP + -ROT 1- SWAP - X SIZE ;
 3 : ENPTRESET  LIMITS 2 UP - -ROT 1- SWAP + X SIZE ;
 4
 5  8 :P  SX1PLOT SPT SWAP DROP ;   ( normal plot )
 6  9 :P  SX2PLOT 3TRI ;   ( 3 pt running mean [tri win] )
 7 10 :P  SX3PLOT 5TRI  ;  ( 5 pt running mean [tri win] )
 8 11 :P  SX4PLOT 7TRI  ;  ( 7 PT running mean [tri win ])
 9
10 : XSECTSPLOT   8 APLOT  ;
11 : 3PTPLOT   3 ENPTMISS  9 APLOT 3 ENPTRESET ;
12 : 5PTPLOT   5 ENPTMISS 10 APLOT 5 ENPTRESET ;
13 : 7PTPLOT   7 ENPTMISS 11 APLOT 7 ENPTRESET ;
14
15 --)
```

```
1053
 0 ( Detector - Graphics extensions ..............................)
 1
 2 : smooth   2CR ." **  Enter 0 - 3 ) " ASK
 3                  := BLOCKFAC  ;
 4
 5 : ?smooth   2CR ." **  Enter ........ " CR
 6             ."     0 ==) No smoothing " CR
 7             ."     1 ==) 3 pt running mean smooth " CR
 8             ."     2 ==) 5 pt running mean smooth " CR
 9             ."     3 ==) 7 pt running mean smooth "
10           CR smooth ;
11
12 : IMSPEC    BLOCKFAC DUP 0 = IF XSECTSPLOT THEN
13                      DUP 1 = IF 3PTPLOT   THEN
14                      DUP 2 = IF 5PTPLOT  THEN
15                          3 = IF 7PTPLOT THEN ; -->
```

```
1054
 0 ( Detector - Graphics extensions ..............................)
 1
 2 : /disp   1D_SCAL ERASE AXES xplot ;
 3 : //disp  2D_SCAL ERASE AXES IMSPEC  ;
 4
 5 : /mdisp  m)i /disp ;                    ( from V_mem )
 6 : //mdisp m)i //disp ;                   ( from Ex_mem )
 7
 8 : /ref    BEGIN refresh 12 C. NEXTCOM runtime 2 SECS
 9                               /mdisp (DEV) 32 = END ;
10 : //ref  BEGIN refresh 12 C. NEXTCOM runtime 2 SECS
11                               //mdisp (DEV) 32 = END ;
12
13 : mastpic     300 Y CORNER !  94 X CORNER !
14               900 X FRAME ! ERASE ;
15 --)
```

```
1055
 0 ( Detector - Arc exposure control..............................)
 1
 2 : arc-exp   2CR ." **  Enter ARC integration time : " ASK
 3             50 OVER ) OVER 2000 ) OR  IF 2CR
 4             ." ** %-ERR - Out of bounds value -) " . 2CR
 5             ELSE := EXP_TIME THEN ;
 6
 7
 8
 9
10 NEXTCOM
11
12
13
14
15
```

```
1056
 0 ( Detector - Pulse Height Distributions ......................)
 1   60 INTEGER PHD_TIME
 2
 3 : XMEM_SET -1 !ADD 4096 0 DO 1 !X LOOP ; ( set XMEM to zeroes )
 4
 5      ( now do window set up..set plot to dot & zero x mem )
 6
 7 : PHDINIT  6 X-BITS SQWINDOW  512 1024 X SIZE ERASE
 8                   mwipe DOTTY  1 slice XMEM_SET ;
 9
10      ( and now word to get image , write to tape & plot...)
11
12 : PULSE_GET PHD_TIME seconds image tapeim 7 C,
13                    ERASE axes yplot ;
14 ( and do it.......)
15
```

```
1060
 0 ( Detector - Focus routines ..................................)
 1
 2
 3               : FOCUS ;
 4
 5
 6
 7
 8
 9
10  2CR   .# **  LOADING FOCUS PACKAGE ** "  2CR
11
12   1067 LOAD
13 --)
14
15
```

```
1061
 0 ( Detector - Focus startup procedures.........................)
 1 0 INTEGER ATTP     75 FARRAY FCLIS
 2
 3 : FC@2   2411 := FLAREA =MN FCLIS 2@ 2410 := FLAREA ;
 4 : FC!2   2411 := FLAREA =MN FCLIS 2!D  2410 := FLAREA ;
 5
 6 : foc_setup   BEGIN arc-exp XEND XST 2CR
 7                    ." **  XSECTS limits =" , ." to " ,
 8                    ." reset " y/n IF xsects THEN
 9                    2CR ." **  Delimit arc ( window ) " y/n
10                    IF mwipe image channel THEN
11                    2CR ." **  Limits satisfactory" y/n   END
12               2CR ." **  Clear focus data array" y/n
13               IF 75 0 DO I F0. FCLIS 2!D LOOP
14               0 := ATTP THEN ;
15 --)
```

```
1062
 0 ( Detector - Focus routine results [ more to come ].............)
 1
 2 : foc_data   erase 2CR ." **  FOCUS-) focus test results"
 3                    2CR ." **  FOCUS      SHIFT      WIDTH" CR
 4                ATTP 1+ 1 DO I DUP 1 SWAP FC@2 F.
 5                                DUP 2 SWAP FC@2 F.
 6                                    3 SWAP FC@2 F. CR LOOP ;
 7
 8
 9
10 --)
11
12
13
14
15
```

```
1063
 0 ( Detector - Focus routine ....................................)
 1 : fokus   BEGIN ATTP DUP 24 ) IF DROP 0 THEN 1+ := ATTP
 2              2CR ." **  FOCUS-) Set SLIT to DEKKER 1 " cont
 3              2CR ." **  FOCUS-) Enter focus setting : "
 4                  FASK 1 ATTP FC!2
 5              2CR ." **  FOCUS-) HARTMANN mask in " cont
 6                 mwipe image //mdisp 1four erase
 7              2CR ." **  FOCUS-) HARTMANN mask out " cont
 8                 mwipe image //mdisp 2four erase cross
 9                 XSHF 2 ATTP FC!2  FWHMVAL 3 ATTP FC!2
10              2CR ." **  FOCUS-) Inspect focus data ? " y/n
11                 IF foc_data THEN
12              2CR ." **  FOCUS -) Reset limits ? " y/n
13                 IF foc_setup THEN
14              2CR ." **  FOCUS-) Continue ? " y/n NOT END ;
15 : foc   foc_setup fokus ; NEXTCOM
```

```
1067
 0 ( Detector - FFT routines : variables.........................)
 1
 2 ( declarations .....................)
 3 2345 INTEGER FOURIERBLOCK   ( start block for fourier data )
 4 2048 INTEGER NN             ( 2* number of points in data  )
 5 1024 INTEGER FPR            ( number of points in data     )
 6    1 INTEGER ISIGN          ( forward or reverse transform )
 7
 8 ( Transform calculation variables .............)
 9  VARIABLE ISTEP  VARIABLE MMAX  VARIABLE MZ
10 1 ISTEP !  1 MMAX !  0 MZ !
11
12  FVARIABLE THETA  FVARIABLE WSTEPR  FVARIABLE WR
13  FVARIABLE WIM
14  F1 THETA 2!  F1 WSTEPR 2!  F1 WR 2!  F1 WIM 2!
15 --)
```

```
1068
 0 ( Detector - FFT routines : variables ..........................)
 1
 2 2335 INTEGER SP_AREA
 3
 4 F0. 2INTEGER DDIFF  F0. 2INTEGER  SPSUM
 5 F0. 2INTEGER MN     F0. 2INTEGER  XCMAX  F0. 2INTEGER XCMN
 6 F0. 2INTEGER XSHF  -1 INTEGER XCPK  0 INTEGER ANG
 7
 8 : FDATA   ['] FOURIERBLOCK  !  ;
 9
10 : MMAX@    MMAX @ ;
11 : 8DUP     4 0 DO 6 2UP LOOP ;
12
13 --)
14
15
```

```
1069
 0 ( Detector - FFT routines : access complex numbers.............)
 1
 2 ( handling data from complex disc array )
 3
 4 : FOURPT   1- 4 1024 */MOD FOURIERBLOCK + BLOCK + ;
 5
 6 : DATA@   FOURPT 2@ ;
 7 : !DATA   FOURPT 2! UPDATE ;
 8
 9 : 2DATA@   FOURPT 4@ 2SWAP ;
10 : !2DATA   FOURPT >R  2SWAP R> 4! UPDATE ;
11
12 : CLEARDATA    DO F0. F0.  I 2* 1+ !2DATA LOOP ;
13 --)
14
15
```

```
1070
 0 ( Detector - FTT routines :Transform code [ GJS ].............)
 1
 2  ( do the transform..............)
 3
 4 : TRANSFORM   NN 2 DO I 2* ISTEP ! F2 PI F* ISIGN I *
 5       FLOAT F/ 2DUP  THETA 2!   F.5 F*  FSIN F**2 F2 F*
 6       FMINUS WSTEPR 2! F1 WR 2! F0. WIM 2! I MMAX !
 7       I 1+  1 DO  NN 1+  I DO      I  MMAX +!
 8 MMAX@ 2DATA@ WIM 2@ F* 2SWAP WR  2@ F* 2SWAP F-
 9 MMAX@ 2DATA@ WR  2@ F* 2SWAP WIM 2@ F*       F+
10 I 2DATA@ 2>R   2SWAP  2R>  8DUP 2SWAP F- 2>R  2SWAP F- 2R>
11 MMAX@ !2DATA F+ 2>R   F+ 2R>   I !2DATA  0 I - MMAX +! ISTEP @
12   +LOOP     WR 2@ 2DUP 2DUP WSTEPR 2@ F* F+ THETA 2@  FSIN WIM
13           2@ F* F- WR 2! WIM 2@ 2DUP WSTEPR 2@ F* F+ 2SWAP THETA
14           2@ FSIN F* F+ WIM 2!     2 +LOOP  I +LOOP ;
15  --)
```

```
1071
 0 ( Detector - FFT routines :arrange data.....................)
 1
 2 ( re-order data for transform ..........)
 3
 4 : DATAARRANGE NN 1+  1 DO
 5                            MMAX@ I ) IF
 6 MMAX@ 2DATA@ I 2DATA@ MMAX@ !2DATA I !2DATA
 7               THEN         NN 2/  MZ !
 8               BEGIN MMAX@  MZ @ ) IF  [SWAP]
 9                       MZ @  MINUS MMAX +! MZ @ 2/  MZ !
10                        MZ @ 2 ( END   THEN
11                       MZ @ MMAX +!
12                   2 +LOOP FLUSH ;
13
14 --)
15
```

```
1072
 0 ( Detector - FFT routines :setup transform.....................)
 1
 2 : FOURIER   := ISIGN 1 MMAX ! DATAARRANGE 1 MMAX ! TRANSFORM ;
 3
 4                        ( transform data ..........)
 5
 6
 7 : +TRANS   2CR ." **  Computing transform ........ "
 8             -1  FOURIER   NEXTCOM ;
 9
10 : -TRANS    2CR ." **  Computing inverse transform ........"
11              1 FOURIER  FI NN 2/ FLOAT F/ NN 1+ 1 DO
12              2DUP I DATA@ F* I !DATA LOOP 2DROP NEXTCOM ;
13
14 --)
15
```

```
1073
 0 ( Detector - FFT routines :prepare data .....................)
 1 (  get the data into the fourier work area........)
 2
 3 : QTC   2 1024 */MOD SP_AREA + BLOCK + ;
 4 : GFIX   MULT F* FIX ;
 5 : QTC@   QTC @ ;  : !QTC   )R GFIX  R) QTC ! UPDATE ;
 6 : WKZERO    2048 0 CLEARDATA ;  ( clears 4096 pts in Im array )
 7 : WKPREP    WKZERO  ULIM 1+ LLIM - DUP
 8              16 ( IF 2CR ." **  Insufficient points " QUIT THEN
 9              2048 ) IF 2CR ." **  Array too large " QUIT THEN ;
10
11 : FILLOUT   ULIM 1+ LLIM - 4096 16 DO I OVER 2DUP
12             =  IF LEAVE THEN ) IF I DUP := FPR ?* := NN
13          2CR  ." **  Extending channels to " I .
14                    LEAVE THEN  I +LOOP DROP ; --)
15
```

```
1074
 0 ( Detector - FFT routines : prepare data.....................)
 1
 2 : IVALS-SET   LIMITS SWAP DROP SPT DUP
 3               := MN_Y   := MX_Y  ;
 4
 5 : FOU-INIT   IVALS-SET 2AXRANGE MX_Y MN_Y - FLOAT := DDIFF ;
 6
 7 : FOURPRIME   F0. := SPSUM FOU-INIT ULIM 1+ LLIM DO
 8               C XEND 1+ XST DO J I VMVALUE + LOOP MN_Y -
 9               FLOAT DDIFF F/ 2DUP ['] SPSUM F+! F0.
10                I LLIM - 2* 1+ !2DATA LOOP
11               SPSUM ULIM 1+ LLIM - FLOAT F/ := MN ;
12
13 : MNSUB   ULIM 1- LLIM DO I LLIM - 2* 1+ DATA@
14           MN F- I LLIM - 2* 1+ !DATA LOOP ;
15 --)
```

```
1075
 0 ( Detector - FFT routines , COSBEL ........................)
 1
 2 0 INTEGER BELNO
 3
 4 : 5%BEL   ULIM 1+ LLIM - 20 /  := BELNO ;
 5 : BEL_PT   DO I 1 - FLOA1 PI/2 F* BELNO FLOAT
 6               F/ FSIN 2DUP F*
 7               I LLIM - 2* 1+ DATA@ F*
 8               I LLIM - 2* 1+ !DATA LOOP ;
 9
10 : COSBEL   5%BEL BELNO 1+ LLIM BEL_PT
11            ULIM 1+ ULIM BELNO - BEL_PT ;
12
13 --)
14
15
```

```
1076
 0 ( Detector - FFT routines : Cross correlate data.............)
 1
 2 288 LOAD   ( load system imaginary number routines )
 3
 4 : XCORR    2377 FDATA WKZERO FPR 0
 5            DO I 2* 1+ 2345 FDATA 2DATA@ FMINUS 2SWAP
 6               I 2* 1+ 2361 FDATA 2DATA@ 2SWAP
 7            C* 2SWAP I 2* 1+ 2377 FDATA !2DATA LOOP
 8          2CR ." **  Cross correlation completed " NEXTCOM
 9              -TRANS ;
10
11
12 --)
13
14
15
```

```
1077
 0 ( Detector - FFT routines , rotate xcf function ..............)
 1
 2 : xpk    F0. := XCMAX  F0. := XCMN   -1 := XCPK
 3          FPR  0 DO I DUP 2* 1+ DATA@ 2DUP XCMN
 4             F< IF 2DUP := XCMN THEN 2DUP XCMAX
 5             F) IF := XCMAX  := XCPK ELSE 2DROP DROP THEN LOOP
 6             XCPK 0 < IF 2CR ." **  XCORR-ERROR-no peak found "
 7              2CR QUIT THEN
 8                     XCPK 1- DUP FPR 2/ ) IF
 9                    FPR - := XCPK ELSE := XCPK THEN
10                    FPR 2/ XCPK -  := ANG  ;
11
12
13 --)
14
15
```

```
1078
 0 ( Detector - FFT Routines ....................................)
 1                          ( Rotate the CCF thru ANG )
 2 : f_rot   ANG 0= NOT IF
 3          ANG 1+ 0 DO 2377 FDATA FPR ANG - I + 2* 1+ DATA@
 4                      2393 FDATA  I 2* 1+ !DATA LOOP THEN
 5                      2377 FDATA 1 DATA@
 6                      2393 FDATA ANG 2* 1+ !DATA
 7          FPR 1+ ANG ) IF
 8             FPR ANG 1+ DO 2377 FDATA I ANG - 2* 1+ DATA@
 9                       2393 FDATA I 2* 1+ !DATA LOOP THEN ;
10
11
12 --)
13
14
15
```

```
1079
 0 ( Detector - FFT command words ..............................)
 1
 2 : fou_pr  WKZERO FOURPRIME MNSUB COSBEL FILLOUT ;
 3 ( one day I might put in an IFOU )
 4
 5 : 1four    2345 FDATA fou_pr ;
 6 : 2four    2361 FDATA fou_pr ;
 7
 8
 9
10
11 --)
12
13
14
15
```

```
1080
 0 ( Detector - FFT : plotting and data inspection routine [GJS]..)
 1
 2 ( data output and plotting words ..................)
 3
 4 0 CONSTANT R/AMP
 5
 6 : prfour   DO CR I DUP . 2* 1+ 2DATA@ 2SWAP 2DUP F.
 7              2SWAP 2DUP F. AMPLITUDE F. LOOP ;
 8
 9 3 :P TR_PLOT 2* 1+ 2DATA@ R/AMP 0= IF AMPLITUDE ELSE
10         2DROP THEN PFIX ;      : RFPLOT 3 APLOT ;
11
12 : fplot   0 ['] R/AMP ! RFPLOT ;
13
14 : iplot   1 ['] R/AMP ! RFPLOT ;
15 --)
```

```
1081
 0 ( Detector - Disc array definitions ..........................)
 1 2410 INTEGER FLAREA
 2  VARIABLE AP                  0 AP !
 3
 4 :ORPHAN + 1024 /MOD FLAREA + BLOCK + ;
 5 : FARRAY AP @ SWAP  1+  4 * AP +! CONSTANT
 6        DOES)  @ SWAP 4 *  ADOPT ;
 7
 8 : !D ! UPDATE ;
 9 : +!D +! UPDATE ;
10 : 2!D 2! UPDATE ;
11 : F+!D F+! UPDATE ;
12
13 --)
14
15
```

```
1082
 0 ( Detector - Parabola fitting : preparation ..................)
 1 : 2INT    2INTEGER  ;
 2 9 FARRAY MATRX    3 FARRAY CONST    3 FARRAY SOL
 3
 4 5 INTEGER PT-S  515 INTEGER UPLT   510 INTEGER LWLT
 5 F0. 2INT SX  F0. 2INT SX2  F0. 2INT SY  F0. 2INT SDRES
 6 F0. 2INT DIS F0. 2INT X+   F0. 2INT X-  F0. 2INT X'
 7 F0. 2INT X0 F0. 2INT Y'  F0. 2INT PEAK
 8 F0. 2INT FWHMVAL  F0. 2INT 1HF_MAX  F0. 2INT 2HF_MAX
 9 : FZERO   9 0 DO F0. I MATRX 2!D LOOP
10          3 0 DO F0. I CONST 2!D F0. I SOL 2!D LOOP ;
11
12 : =MN     1- 3 * + 1-   ;
13 : MX@2    =MN  MATRX  2@  ;
14 : MX!2    =MN  MATRX  2!D  ;
15 : MX+!    =MN  MATRX  F+!D  ; --)
```

```
1083
 0 ( Detector - Solve matrix for parabola fit [BJM] ..............)
 1 : GAUSS/SOLVE    4 2 DO  4 2 DO
 2                   J I MX@2  J 1 MX@2  1 1 MX@2 F/ 1 I MX@2
 3                             F* F- J I MX!2 LOOP
 4                      I 1- CONST 2@  I 1 MX@2  1 1 MX@2 F/
 5                      0 CONST 2@ F* F- I 1- CONST 2!D LOOP
 6                   3 3 MX@2 3 2 MX@2 2 2 MX@2 F/ 2 3 MX@2
 7                             F* F- 3 3 MX!2
 8                      2 CONST 2@  3 2 MX@2  2 2 MX@2 F/
 9                      1 CONST 2@ F* F- 2 CONST 2!D
10                      2 CONST 2@  3 3 MX@2 F/ 2 SOL 2!D
11                      1 CONST 2@  2 3 MX@2 2 SOL 2@ F* F-
12                      2 2 MX@2 F/ 1 SOL 2!D 0 CONST 2@
13                  1 2 MX@2 1 SOL 2@ F* F- 2 SOL 2@ 1 3 MX@2
14                  F* F-  1 1 MX@2 F/ 0 SOL 2!D   ;
15 --)
```

```
1084
 0 ( Detector - Fit parabola to points in complex array.............)
 1
 2 : points   PT-S 2/ DUP FPR 2/ DUP ROT 1+ + := UPLT
 3                                      SWAP - := LWLT FZERO
 4       UPLT LWLT DO I LWLT 1- - FLOAT := X'
 5                    I 2* 1+ DATA@ := Y'
 6                    X' F4 FPWR 1 1 MX+! X' F3 FPWR 2DUP
 7                    1 2 MX+! 2 1 MX+! X' F**2 2DUP 2DUP 2DUP
 8                    1 3 MX+! 2 2 MX+! 3 1 MX+! Y' F*
 9                    0 CONST F+!D X' 2DUP 2DUP 2 3 MX+! 3 2
10                    MX+! Y' F* 1 CONST F+!D Y' 2 CONST F+!D LOOP
11            PT-S FLOAT 3 3 MX!2 GAUSS/SOLVE
12             1 SOL 2@ F2 0 SOL 2@ F* F/ FMINUS
13             PT-S 2/ 1+ FLOAT F- := X0
14         X0 XCPK FLOAT F+ 2DUP := XSHF
15                  NEXTCOM ," Shift = " F.  ; -->
```

```
1085
 0 ( Detector - Errors for parabola fitting .....................)
 1
 2  : XCAL 2 SOL 2@ 2SWAP F- 0 SOL 2@ F* F4 F* 1 SOL 2@ F**2 2SWAP
 3 F- 2DUP := DIS F0. F) IF 1 SOL 2@ FMINUS 2DUP DIS FSQRT 2DUP
 4 2ROT 2SWAP F+ -2ROT F- 0 SOL 2@ F2 F* 2DUP 2ROT 2SWAP F/ := X-
 5 F/ := X+ THEN ;
 6
 7 : ERROR F0. := SX F0. := SX2 F0. := SY
 8 UPLT LWLT DO I 2* 1+ DATA@
 9 XCAL DIS F0. F) IF F1 SY F+ := SY I FLOAT X0 F( IF X+ ELSE
10 X- THEN I  PT-S + FLOAT PEAK F- F- 2DUP SX F+ := SX F**2 SX2 F+
11 := SX2 THEN LOOP SY SX2 F* SX F**2 F- FSQRT SY F/ := SDRES ;
12
13 --)
14
15
```

```
1086
 0 ( Detector - find FWHM of CCF in complex array.................)
 1
 2 : fwhm     FPR DUP 2/ 1+
 3                   DO I 2* 1+ DATA@ 2DUP XCMAX F0.5 F* F< IF
 4                     I FLOAT 2SWAP XCMAX F0.5 F* 2SWAP F-
 5                     I 1- 2* 1+ DATA@ I 2* 1+ DATA@ F- F/ F-
 6                   := 1HF_MAX LEAVE ELSE DROP THEN LOOP
 7              0 FPR 2/ 1-
 8                   DO I 2* 1+ DATA@ 2DUP XCMAX F0.5 F* F< IF
 9                     I FLOAT 2SWAP XCMAX F0.5 F* 2SWAP F-
10                     I 1+ 2* 1+ DATA@ I 2* 1+ DATA@ F- F/ F+
11                   := 2HF_MAX LEAVE ELSE DROP THEN -1 +LOOP
12                   1HF_MAX 2HF_MAX F- := FWHMVAL
13            NEXTCOM ." FWHM = " FWHMVAL F. ;
14
15 --)
```

```
1087
 0 ( Detector - FFT command words ..................................)
 1
 2
 3 : cross    2345 FDATA +TRANS 2361 FDATA +TRANS XCORR
 4             xpk f_rot  points fwhm ;
 5
 6
 7 --)
 8
 9
10
11
12
13
14
15
```

```
1088
 0 ( Detector - setup limits for FFT..............................)
 1
 2
 3 : xdlim   BAR BAR 2DUP < IF SWAP THEN 2DUP
 4             - 20 < IF ERASE 2CR ."  ** X1 must be > 20* X2 "
 5                     QUIT THEN SWAP  2DUP
 6             := ULIM := LLIM  X SIZE ;
 7
 8 : chansel   BEGIN 2CR ." ** Reset to default axes " y/n
 9                 IF areset THEN //mdisp xdlim cont //mdisp
10                   ERASE 2CR ." **  Channels " LLIM . ." to "
11                   ULIM . ." selected - repeat " y/n NOT END ;
12
13
14
15
```